
The Central Mozambique
continental margin -
Its tectonic evolution as the centrepiece
of the initial Gondwana break-up

DISSERTATION

in partial fulfilment of the requirements for the degree of
doctor rerum naturalium (Dr. rer. nat.),

submitted to the Department of Geosciences at the
University of Bremen, Germany, by

CHRISTIAN OLAF MÜLLER

Alfred Wegener Institute
Helmholtz Centre for Polar and Marine Research
Bremerhaven, 04 April 2017

Assessors:

PROF. DR. WILFRIED JOKAT

University of Bremen / Alfred Wegener Institute
Department of Geophysics
Am Alten Hafen 26
27568 Bremerhaven - Germany

PROF. DR. CORNELIA SPIEGEL

University of Bremen
Department of Geosciences
Klagenfurter Straße 4
28359 Bremen - Germany

Date of defence:

09 June 2017

Statutory Declaration

Christian Olaf Müller
Wacholderweg 25
27578 Bremerhaven
Germany

I hereby declare that I

1. completed this dissertation without unauthorized external assistance,
2. used no other sources, references or material than those cited and
3. that I have explicitly marked all material which has been quoted either literally or by content from the used sources.

Bremerhaven, 04 April 2017

Christian Olaf Müller

Abstract

A consolidated knowledge of the formation and dispersal of the former supercontinents reveals important evidence for the earth's climate and biosphere in the past and contribute to the prediction of their future evolution. Nowadays, a main objective is the investigation of the initial break-up of the continental assembly of Gondwana that serves as a constraint for its subsequent dispersal and the evolution of all oceans and seas in the southern hemisphere. Evidence of the early rifting stages are expected at the margins of Southeast Africa and East Antarctica, whereas the latter one is difficult to access, due to its remote position and ice coverage. To understand the driving forces and the chronology of the break-up and of the massive volcanism additional detailed knowledge of the crustal setting along the margins of Southeast Africa is required.

Therefore, a new geophysical dataset was acquired with the RV Sonne in the northern Mozambique Basin at the beginning of year 2014. This comprises a deep seismic sounding profile across a so-far unknown structural high, the Beira High. Additional gravity and magnetic data were systematically recorded across the entire northern Mozambique Basin. Based on velocity, amplitude, density and magnetic modelling, a geological model of the continental margin of Central Mozambique was prepared. A new compilation of all available magnetic data in the Mozambique Basin reveals information about the age of the sea floor, which serves as constraint for the reconstruction of the initial Gondwana break-up.

The study depicts a continental origin of up to 23 km thick and partly highly intruded crust at Beira High. In the adjacent coastal areas of the south-western part of Central Mozambique, 7 km thin crust is observed, which is covered by more than 11 km thick sediments and implies the continuation of the continent-ocean transition towards onshore Mozambique. This is in clear contrast to the narrow transition observed in the north-eastern part of the margin and reveals a clear asymmetric crustal setting as supposed for the conjugate margin in the Riiser-Larsen Sea in Antarctica and consequently suggests a complex break-up scenario.

The presence of a pronounced high-velocity lower crustal body is interpreted as magmatic material, which underplates the crust and extends about 200 km from the Central Mozambican margin towards the Mozambique Basin and testifies for the massive vol-

canism during the break-up. The distribution of further volcanics along the entire margin clearly depicts the continuation of the north-eastern branch of the Karoo Large Igneous Province and are mainly emplaced between 177-157 Ma. The magmatism in Southeast Africa seemed to be continuous throughout the initial break-up, which points to the presence of either a mantle plume or a thermal anomaly as source of the giant magmatism. An additional late stage of rift-volcanism mainly affected the margin of Dronning Maud Land and causes the difference in the magnetic signature of the conjugate margins.

The tracing of continuous fractures throughout the Africa-Antarctica Corridor leads to the reconstruction of a tight Gondwana fit prior rifting, which reveals several geological links between the plates. A main structure of the East African-Antarctic Orogen extends from the Namama Shear Zone in Central Mozambique across the Orvin Shear Zone towards the Forster magnetic anomaly in Dronning Maud Land. During the initial Gondwana break-up at 182 Ma, Beira High started to separate from West Gondwana along this suture until it demerged as well from East Gondwana by a rift jump.

The investigation of further partly unknown tectonic structures along the western and southern coast of Mozambique revealed a possible oceanic origin of the southern part of the Mozambique Coastal Plains, due to similarities of the magnetic signature to the oceanic crust south of Beira High as well as the tentative identification of magnetic spreading anomalies. The subsequent emplaced Mozambique Ridge moved southwards as part of a micro plate during an additional active spreading centre in the Northern Natal Valley. The resulting reconstruction of the initial Gondwana break-up in the Africa-Antarctica Corridor accounts for all present-day available geological, geophysical and geodynamic constraints and might serve as a basis for the investigation of the subsequent dispersal of Gondwana.

Zusammenfassung

Fundiertes Wissen über die Bildung und den Zerfall von früheren Großkontinenten unserer Erde liefert wertvolle Hinweise über das Klima und die Biosphäre der damaligen Zeit und lässt uns Aussagen über deren zukünftige Entwicklung treffen. Ein besonderes Augenmerk liegt hierbei auf dem initialen Aufbruch des letzten Großkontinents Gondwana, welcher ursächlich für den weiteren Zerfall und somit für die Entstehung der heutigen Ozeane und Meere in der südlichen Hemisphäre ist. Hinweise aus der frühen Öffnungsphase werden unter anderem vor der Küste von Südost-Afrika und der Ost-Antarktis vermutet, wobei letztere durch ihre exponierte Lage und mächtige Eisbedeckung nur schwer zugänglich ist. Um Rückschlüsse über den Ablauf des Aufbruchs und die Ursache des begleitenden massiven Vulkanismus ziehen zu können, sind weitere Kenntnisse des geologischen Aufbaus entlang der Küste von Südost-Afrika erforderlich.

Zu diesem Zweck wurde Anfang des Jahres 2014 im nördlichen Mosambik-Becken ein neuer geophysikalischer Datensatz mit der FS Sonne aufgezeichnet. Dieser umfasst ein tiefenseismisches Profil über einer, der Küste vorgelagerten, tektonischen Struktur unbekanntem Ursprungs, dem Beira High. Zusätzlich wurden systematisch Schwere- und Magnetikdaten vor der gesamten Küste von Zentral-Mosambik erhoben. Im Zuge dieser Dissertation wurden Geschwindigkeits-, Amplituden-, Dichte- und Magnetikmodellierungen durchgeführt, die als Basis für ein geologisches Modell des Kontinentalrandes von Zentral-Mosambik fungieren. Eine neue Kompilation aller verfügbaren Magnetikdaten im Mosambik-Becken ermöglicht zudem Aussagen über die Altersverteilung des Meeresbodens, welche als Randbedingung für eine Rekonstruktion des frühen Gondwana-Aufbruchs dient.

Die Ergebnisse zeigen einen kontinentalen Ursprung, der bis zu 23 km mächtigen und teils stark intrudierten Kruste des Beira High. Im angrenzenden Küstenbereich wird hingegen 7 km dünne Kruste von mehr als 11 km Sedimentgestein überlagert, was eine Fortsetzung der Kontinent-Ozean-Übergangszone bis ins Festland Mosambiks andeutet. Dies wiederum steht im Gegensatz zu einer schmalen Übergangszone im Nordost-Teil des Kontinentalrandes von Zentral-Mosambik und verdeutlicht eine Asymmetrie in dessen Krustenaufbau, wie sie auch am konjugierenden Kontinentalrand in der Riiser-Larsen See in der Antarktis vermutet wird und deutet folglich einen

komplexen Aufbruch an.

Der starke Vulkanismus während des Aufbruchs wird unter anderem durch eine magmatische Unterplattung der Kruste bestätigt, die sich in Form eines identifizierten Hochgeschwindigkeitskörpers rund 200 km vom Kontinentalrand bis ins Mosambik-Becken erstreckt. Entlang des gesamten Kontinentalrandes von Zentral-Mosambik findet sich eine Vielzahl weiterer Hinweise auf magmatische Gesteine, die vor 177-157 Millionen Jahren entstanden. Sie repräsentieren die Fortsetzung des nordöstlichen Astes der vulkanischen Großprovinz in Südost-Afrika (Karoo LIP) und deuten, in Zusammenbetracht mit älteren Studien, auf einen kontinuierlichen Magmatismus während des Aufbruchs hin, dessen Ursache sowohl ein Mantel-Plume, als auch eine thermische Anomalie sein kann. Eine zusätzliche späte Phase des Rift-Vulkanismus scheint die Küste von Dronning Maud Land in der Antarktis beeinflusst zu haben, wodurch die konjugierenden Kontinentalränder unterschiedliche magnetische Signaturen aufweisen.

Durch die Nachverfolgung von Bruchzonen im gesamten Afrika-Antarktis-Korridor ergab sich in der Rekonstruktion einer enger Fit der Kontinentalplatten vor dem Gondwana-Aufbruch, worin sich Platten-übergreifende geologische Strukturen erkennen lassen. Dabei zeigt sich als eine Hauptstruktur des ostafrikanisch-antarktischen Orogens die Verbindung der Namama Scherzone in Zentral-Mosambik über die Orvin Scherzone in der Antarktis hin zur „Forster magnetic anomaly“. Während des initialen Aufbruchs vor etwa 182 Millionen Jahren begann sich das Beira High entlang dieser Suture von West-Gondwana zu trennen bis es sich durch einen Riftsprung ebenfalls von der heutigen antarktischen Platte separierte.

Die Untersuchung weiterer tektonischer Strukturen entlang der West- und Südküste Mosambiks ergab einen möglichen ozeanischen Ursprung des südlichen Teils der Küstenebenen Mosambiks. Hinweise darauf lieferten ausgeprägte Ähnlichkeiten zur magnetischen Signatur der ozeanischen Kruste südlich des Beira High sowie tendenziell interpretierte magnetische Spreizungsanomalien. Der anschließend entstandene Mosambik-Rücken ist während der Aktivität eines weiteren Spreizungszentrums im heutigen nördlichen Natalbecken als Teil einer Mikroplatte weiter nach Süden gewandert. Das, aus dieser Dissertation, resultierende Aufbruchmodell des Afrika-Antarktis-Korridors berücksichtigt die heutig bekannten Informationen aus Geologie, Geophysik und Geodynamik in dieser Region und kann als Grundlage für die Untersuchung des weiteren Zerfalls von Gondwana dienen.

Contents

Abstract	I
Zusammenfassung	III
Contents	V
List of Figures	VIII
List of Tables	XI
List of Abbreviations	XII
1 Introduction	1
1.1 Why is the ancient Gondwana still important?	1
1.2 Geological setting of a volcanic rifted margin	3
1.3 Geophysical investigations at the continental margin of Central Mozambique and in the Mozambique Basin	5
1.4 Research questions of this thesis	10
2 Data acquisition, processing and modelling	13
2.1 Seismic refraction data	13
2.1.1 Acquisition and processing	14
2.1.2 Ray tracing vs. FD-amplitude modelling	16
2.2 Potential field data	18
2.2.1 Gravity data	20
2.2.2 Magnetic data	21
2.2.3 Interpretation and modelling	22
3 Contributions to scientific journals	31
3.1 The crustal structure of Beira High, Central Mozambique – Combined investigation of wide-angle seismic and potential field data	31
3.2 Geophysical evidence for the crustal variation and distribution of magmatism along the central coast of Mozambique	32

3.3	The initial Gondwana break-up in the Africa-Antarctica Corridor – A reconstruction based on new magnetic data	33
4	The crustal structure of Beira High, Central Mozambique – Combined investigation of wide-angle seismic and potential field data	35
4.1	Introduction	36
4.2	Geological setting	38
4.3	Data acquisition and processing	42
4.4	Modelling	43
4.4.1	Wide-angle seismic study	43
4.4.2	Amplitude modelling	45
4.4.3	Gravity modelling	51
4.4.4	Uncertainty and resolution of the velocity and density model	53
4.5	Results and Interpretation	54
4.5.1	Wide-angle seismic study	54
4.5.2	Gravity modelling	61
4.6	Discussion	62
4.6.1	Sediments	62
4.6.2	Mozambique Basin	65
4.6.3	Beira High	66
4.6.4	Shelf area	71
4.6.5	Magnetic data and implications for the tectonic setting	72
4.7	Conclusion	74
5	Geophysical evidence for the crustal variation and distribution of magmatism along the central coast of Mozambique	77
5.1	Introduction	78
5.2	Data and modelling	81
5.2.1	Wide-angle seismic study	81
5.2.2	Amplitude modelling	82
5.2.3	Magnetic modelling	83
5.3	Results	87
5.3.1	Wide-angle seismic study incl. amplitude modelling	87
5.3.2	Magnetic modelling	90
5.4	Discussion	95
5.4.1	Crustal variation and extent of the HVLCB	95
5.4.2	Magnetic edge anomaly and the location of the COB	97
5.4.3	Different magnetic signature of the conjugate margins	101

5.4.4	Linking onshore and offshore volcanism	104
5.5	Conclusion	108
6	The initial Gondwana break-up in the Africa-Antarctica Corridor – A reconstruction based on new magnetic data	111
6.1	Introduction	112
6.2	Structural elements and their tectonic setting	115
6.2.1	Archean to Paleozoic	115
6.2.2	Mesozoic to Present	117
6.3	Magnetic data acquisition and processing	120
6.3.1	New magnetic data	120
6.3.2	Compilation of magnetic data in the MB	120
6.4	Results and Interpretation	122
6.4.1	Fractures in the Mozambique Basin	122
6.4.2	NE-Segment	124
6.4.3	BH-Segment	126
6.4.4	MCP-Segment	128
6.5	Discussion	130
6.5.1	Pre-rift boundaries	130
6.5.2	Initial Fit	134
6.5.3	Onset of Jurassic Rifting	136
6.5.4	The Beira High Drift	139
6.5.5	The extinct ridge in the NNV and the emplacement of the MozR	140
6.5.6	Link to the plates of Madagascar and South America	142
6.6	The new kinematic break-up model of the AAC	143
6.7	Conclusion	149
7	Conclusion	153
8	Outlook	157
	References	161
	Acknowledgements	185
	Appendix A	187
	Appendix B	191

List of Figures

1.1	The Gondwana palaeocontinent	2
1.2	General setting of a volcanic rifted margin	4
1.3	Topographic map of the research area	6
1.4	Overview of former surveys	9
2.1	Acquisition of geophysical data during the cruise SO230	14
2.2	Air guns	14
2.3	General set-up of an OBS	15
2.4	Comparison between ray tracing method and FD-modelling	17
2.5	Distribution of amplitudes of the PmP phase	19
2.6	Gravimeters used during cruise SO230	20
2.7	Sea Spy gradient magnetometer system	21
2.8	Non-uniqueness problem in modelling of potential field data	23
2.9	Characteristics of the gravity gradient	25
2.10	Gravity expression of fractures	27
2.11	Depth estimation of magnetic source bodies by 3D Euler Deconvolution	28
2.12	Comparison between average density and density gradient	29
4.1	Tectonic overview of the Mozambique Channel	37
4.2	Topographic and gravity map of the survey area	40
4.3	Seismic section, picks and modelled raypaths of OBS 21	46
4.4	Seismic section, picks and modelled raypaths of OBS 39	47
4.5	Seismic section, picks and modelled raypaths of OBS 46	48
4.6	Ray coverage of the P-wave velocity model	50
4.7	Resolution for profile AWI-20140010	52
4.8	P-wave velocity model of profile AWI-20140010	56
4.9	Results for amplitude modelling of PmP phase for station 22	58
4.10	Results for amplitude modelling of PmP phase for station 37	60
4.11	Density model for profile AWI-20140010	62
4.12	1D velocity-depth profiles	64
4.13	Comparison between Beira High and continental fragments	69

4.14	Comparison between Beira High and oceanic plateaus	69
4.15	Geological interpretation of profile AWI-20140010	72
5.1	Topographic and magnetic map of Mozambican and East Antarctic margin	79
5.2	Results for amplitude modelling of PmP phase for station 14	86
5.3	Results for amplitude modelling of PmP phase for station 6	89
5.4	Refined final P-wave velocity models	91
5.5	Magnetic models of profiles AWI-20070201 and AWI-20140010	94
5.6	Seismic reflection profiles at the Mozambican and East Antarctic margin	98
5.7	Chronology of magmatic activity at the Mozambican margin	103
5.8	Distribution and age of magmatism in SE-Africa	106
6.1	Outline and tectonic setting of the Africa-Antarctica Corridor	113
6.2	Tectonic setting of SE-Africa and the Mozambique Basin	116
6.3	Tectonic setting of Dronning Maud Land	119
6.4	Line coverage for compilation of magnetic data	121
6.5	TMI anomaly in the Mozambique Basin	123
6.6	Derivative maps of the TMI anomaly	125
6.7	Free-air gravity anomaly of SE-Africa and the Mozambique Basin	127
6.8	New magnetic anomaly picks in the Mozambique Basin	129
6.9	TMI anomaly in Dronning Maud Land	131
6.10	Free-air gravity anomaly of Dronning Maud Land	133
6.11	Comparison to synthetic magnetic profiles	134
6.12	Initial fit between Africa and Antarctica	135
6.13	Synthetic flowlines in the AAC	138
6.14	Reconstruction of the initial Gondwana break-up in the AAC	146
B.1	Seismic section and ray tracing results of OBS 11	192
B.2	Seismic section and ray tracing results of OBS 12	193
B.3	Seismic section and ray tracing results of OBS 13	194
B.4	Seismic section and ray tracing results of OBS 14	195
B.5	Seismic section and ray tracing results of OBS 15	196
B.6	Seismic section and ray tracing results of OBS 16	197
B.7	Seismic section and ray tracing results of OBS 17	198
B.8	Seismic section and ray tracing results of OBS 18	199
B.9	Seismic section and ray tracing results of OBS 19	200
B.10	Seismic section and ray tracing results of OBS 20	201
B.11	Seismic section and ray tracing results of OBS 21	202

B.12 Seismic section and ray tracing results of OBS 22	203
B.13 Seismic section and ray tracing results of OBS 23	204
B.14 Seismic section and ray tracing results of OBS 24	205
B.15 Seismic section and ray tracing results of OBS 25	206
B.16 Seismic section and ray tracing results of OBS 26	207
B.17 Seismic section and ray tracing results of OBS 27	208
B.18 Seismic section and ray tracing results of OBS 28	209
B.19 Seismic section and ray tracing results of OBS 29	210
B.20 Seismic section and ray tracing results of OBS 30	211
B.21 Seismic section and ray tracing results of OBS 31	212
B.22 Seismic section and ray tracing results of OBS 32	213
B.23 Seismic section and ray tracing results of OBS 33	214
B.24 Seismic section and ray tracing results of OBS 34	215
B.25 Seismic section and ray tracing results of OBS 35	216
B.26 Seismic section and ray tracing results of OBS 36	217
B.27 Seismic section and ray tracing results of OBS 37	218
B.28 Seismic section and ray tracing results of OBS 38	219
B.29 Seismic section and ray tracing results of OBS 39	220
B.30 Seismic section and ray tracing results of OBS 40	221
B.31 Seismic section and ray tracing results of OBS 41	222
B.32 Seismic section and ray tracing results of OBS 43	223
B.33 Seismic section and ray tracing results of OBS 44	224
B.34 Seismic section and ray tracing results of OBS 45	225
B.35 Seismic section and ray tracing results of OBS 46	226
B.36 Seismic section and ray tracing results of OBS 47	227

List of Tables

4.1	Statistics of picked phases	44
4.2	Parameters and uncertainties of modelled layers	55
5.1	Layer parameters for the magnetic modelling	84
5.2	Differences between refined and former P-wave velocity models	92
6.1	Finite rotations for the opening of the AAC and the Somali Basin	144

List of Abbreviations

AAC	Africa-Antarctica Corridor
COT	Continent-ocean transition
DML	Dronning Maud Land
DSDP	Deep Sea Drilling Project
EAAO	East African-Antarctic Orogen
GPS	Global Positioning System
HVLCB	High-velocity lower crustal body
MCP	Mozambique Coastal Plains
Moho	Mohorovičić discontinuity
MORB	Mid-ocean ridge basalt
MozR	Mozambique Ridge
NNV	Northern Natal Valley
NV	Natal Valley
SDR	Seaward dipping reflectors
SWIR	South-west Indian Ridge
TMI	Total magnetic field intensity

1 Introduction

1.1 Why is the ancient Gondwana still important?

At the moment, it is the German Science Year of the seas and oceans. It encourages us to continue the research of the seas in regard of their sustainable use and protection. A main objective is to make aware of the importance of the seas as source for food and economic space for our mankind and the ocean's influence on the climate. If we want to keep on leveraging the seas and oceans and predicting their reaction on this and future evolution, we have to understand their behaviour and development in the past.

The essential base for the formation of today's oceans is the continuous drift of the continents. This theory was heavily debated for a long time. Early studies of the continents already noticed the similarity between the coastlines of South America and Africa and found relicts of the same fossil plants at different landmasses. First in 1912, Alfred Wegener was able to present a consistent geophysical model, which accounted for most of these interdisciplinary findings. By means of his displacement theory, he was able to assemble the landmasses in a single primal continent, so-called Wegeners 'Ur-Kontinent'. Nowadays, we know that this was similar to the last Earth's super-continent Pangaea with its northern part Laurasia and its southern part being Gondwana. The main parts of Gondwana were today's landmasses of Africa, Antarctica, South America, Australia, Madagascar and India (Fig. 1.1). The dispersal of Gondwana led to the opening of the oceans and seas in the southern hemisphere. The drift of the continents changed the track of ocean currents, which had a major impact on the global climate. This influenced the life and habitat of organisms in the water and on land, which had to adapt to the new conditions. To understand and constrain these spatial and temporal changes of the processes in the past, we need precise information about the continent's position and set-up of their margins at this time.

In this regard, of special importance is the initial break-up of Gondwana. Commonly accepted is that the break-up between its eastern (Antarctica, Australia, India, Madagascar) and western part (Africa, South America) caused at first the opening of the Mozambique and Somali Basin during the Jurassic (~ 180 Ma). Evidence for the

earliest plate motions is expected at the continental margin of Central Mozambique, which represents our main research area. A consistent model of the break-up at this time is still missing. However, detailed knowledge about the initial motion and timing is fundamental for the understanding of the break-up and serves as constraint for the subsequent dispersal of Gondwana and consequently the generation of the oceans. Furthermore, insights into the driving forces of the break-up provide evidence for the current dispersal of the continents, for example as observed at the Afar-Rift.

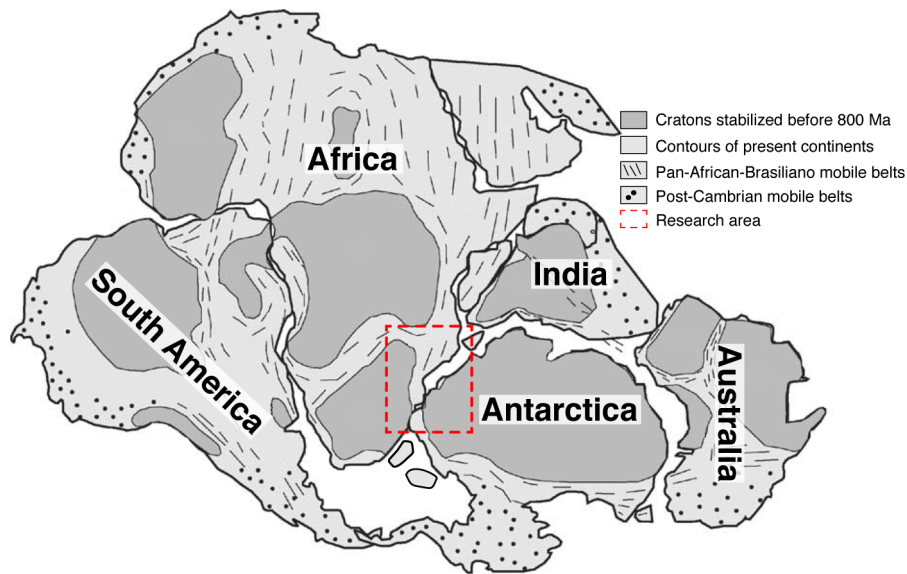


Figure 1.1: The Gondwana palaeocontinent with its cratonic blocks and Pan-African-Brasiliano mobile belts (modified from [Da Silva Schmitt et al., 2004](#)).

Additional importance of the initial break-up in the area of Central Mozambique arises by the formation of its margin at this time. Its setting has a major influence on the subsequent sedimentation, erosion, development of natural resources and habitats at the margin and consequently its purpose as source of food and raw material. In this context, exploration continues towards more complex geological areas, which requires a preceding precise estimate of the reservoir's properties. Partly, these depend on the type of the underlying crust, either being of continental or oceanic origin, which can only be assigned by detailed insights into its evolution during the initial break-up and tectonic setting. Such a crustal classification has also economical consequences. By assigning the offshore extent of distinct continental crust, and the fulfilment of further morphological and geological aspects, a country might claim an extension of its exclusive economic zone. This bears an enormous economic potential, especially for a developing country (e.g. Mozambique).

Another important fact is the dependence of the heat flux on the crustal setting along a margin. In general, oceanic crust is characterized by a higher thermal gradient than continental crust, which draws attention to the crustal classification below the huge ice sheets covering the Gondwanian continental margins of Antarctica. Here, a higher heat flux causes an additional melting at the base of the ice sheet (Kaus, 2013). In the following, the ice motion increases towards the ocean, where parts of the ice sheet separate, melt and contribute to a rising sea level. Consequently, a reliable assumption on the crustal setting allows a first regional estimate for the thermal gradients and their influence on the ice sheet dynamics.

1.2 Geological setting of a volcanic rifted margin

The driving forces for the drift of the continents is still under debate. In general, a combination of frictional drag produced by mantle convection and inter-plate forces are thought to influence the plate's motion. Accepted is that the drift of the plates leads to the periodical generation and dispersal of supercontinents, so-called the Wilson cycle. This describes the entire process beginning with the continental break-up, the subsequent onset of seafloor spreading and the development of offshore basins, towards the continuous growth of the oceans. This is followed by continent collision or subduction of sea floor, and ends in the assembly of a new supercontinent. Based on the different relative motions of the plates to each other during the cycle, three different types of margins develop, which can be classified into passive, active and transform continental margins. During the initial break-up of a continent, rifting environments dominate, which are followed by the formation of passive continental margins. In general, these are characterized by a broad transition from continental to oceanic crust, which consists of rotated continental blocks, separated by listric normal faults. Fluvial and deltaic processes drive the early sedimentation at the margin and lead to the build-up of a coastal plain and continental shelf area, which drops via the continental slope and rise towards the abyssal plain.

In this regard, Pangaea was the last known supercontinent on Earth, with its southern part being Gondwana. It is speculated whether a mantle plume or a thermal mantle anomaly caused the initial Gondwana break-up and the accompanying giant volcanism. The resultant passive continental margins were affected by a different amount of magmatism, and either show a typical setting of a magma-poor rifted margin or a volcanic rifted margin. The Central Mozambique continental margin reveals typical properties of a volcanic rifted margin (Leinweber et al., 2013), although the amount and distribution of the entire magmatism is not yet known.

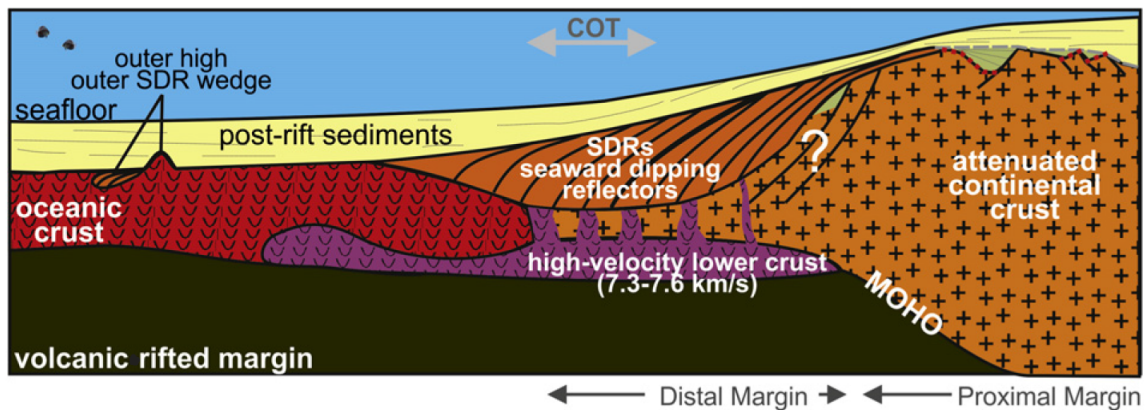


Figure 1.2: Schematic sketch of the general setting of a volcanic rifted margin (Franke, 2013). Abbreviations: COT: Continent-ocean transition, MOHO: Mohorovičić discontinuity (crust-mantle boundary), SDRs: Seaward dipping reflectors.

The majority of the world’s rifted margins are associated with excess volcanism. Well-studied examples are the volcanic rifted margins of Mid-Norway and East-Greenland and reveal the following typical features of these margins (Fig. 1.2):

LAVA FLOWS: Thick wedges of extruded lava flows are observed as seaward dipping reflectors (SDRs) in seismic reflection data (Hinz, 1981; Mutter et al., 1982) (Fig. 1.2). These consist of a mixture of volcanic flows, volcanoclastic deposits and non-volcanic sediments (Menzies et al., 2002). In the onshore area, lava flows might be as well present as widespread continental flood basalts. However, their emplacement is not synchronous with the SDRs and might predate the break-up (Hastie et al., 2014; Jourdan et al., 2008).

HIGH-VELOCITY LOWER CRUSTAL BODY (HVLCB): An up to more than 10 km thick lower crustal body with high velocities (> 7.2 km/s) underlies the continent-ocean transition (COT, Fig. 1.2) (Menzies et al., 2002). The HVLCB is believed to consist of mafic to ultramafic rocks (Mjelde et al., 2009).

INTRUSIONS: Numerous silicic intrusions and dykes are present in the rifted continental crust (Menzies et al., 2002).

NARROW TRANSITION: Usually, a comparably narrow continent-ocean transition is observed, due to a lower rate of crustal thinning (Franke, 2013). However, in a complex tectonic setting, like the presence of abandoned rifts, the transition might be significantly wider.

1.3 Geophysical investigations at the continental margin of Central Mozambique and in the Mozambique Basin

The continental margin of Central Mozambique extends from the Davie Ridge in the east towards Beira in the west (Fig. 1.3). The most prominent feature is the Zambezi delta that forms a great coastal plain and a wide shelf area in the south-western part of the margin. In contrast, a narrow shelf marks its north-eastern part. Offshore Central Mozambique, the Zambezi river transports large amounts of sediment into the abyssal plain in the Mozambique Basin. The Davie Ridge separates the Mozambique Basin from the south-western Somali Basin, which together represent the Mozambique Channel. A southern boundary of the Mozambique Basin towards the South-west Indian Ocean is not defined.

The geophysical investigation onshore Mozambique is strongly associated with the exploration of minerals and fossil resources. Mining is reported since the 13th century, whereas exploration of fossil resources began in 1904 (Salazar et al., 2013). Extensive exploration started from 1948 on, then international oil companies moved into the country (De Buyl and Flores, 1986). In the following, regional seismic and potential field surveys were conducted throughout the entire country. In the scope of the African Gravity Project (Fairhead et al., 1988), most of the acquired gravity data were merged into a continental compilation. In like manner, magnetic data were compiled in the scope of the African Magnetic Mapping Project (Barritt, 1993).

Besides bathymetric data of the sea floor, the marine geophysical investigation of the South-west Indian Ocean started with the first gravity measurements by Vening Meinesz in 1935 (Vening Meinesz, 1941). These were extended towards the Mozambique Channel in 1959 (Talwani, 1962), revealing a first rough estimate of the distribution of gravity highs and lows offshore SE-Africa. The first seismic refraction study addressing the crustal nature of the South-west Indian Ocean was conducted in 1958 and was presented by Ludwig et al. (1968). In the 1960's, single-channel seismic reflection data, further seismic refraction and gravity data, as well as the first magnetic data were recorded along transects throughout the South-west Indian Ocean and the Mozambique Channel (e.g. Green and Hales, 1966). By means of sonobuoys, the first seismic refraction data were acquired in the northern Mozambique Basin and close to the coast of Central Mozambique between 1971 and 1973 (Lort et al., 1979). The seismic signals hardly reached the basement, but depicted the presence of a huge sediment column, bearing the potential for the presence of natural resources. In the following,

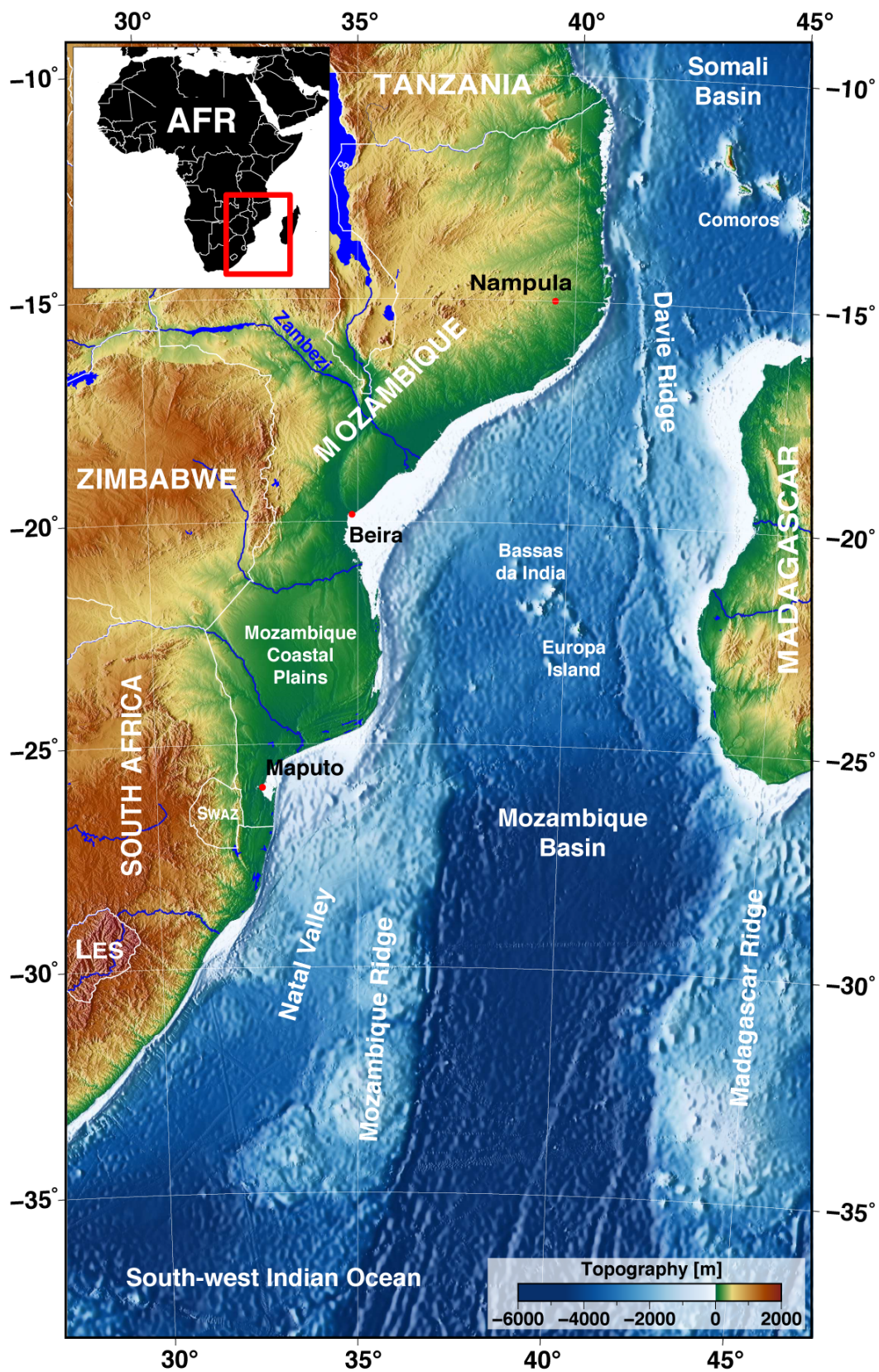


Figure 1.3: Topographic map of the research area, based on the GEBCO_2014 grid (version 20150318; Weatherall et al., 2015).

the offshore exploration along the coast of Mozambique started and French research institutions initiated several cruises in the Mozambique Basin, summarized in [Lafourcade \(1984\)](#). From the 1990's on, the offshore exploration along the shelf areas increased and nowadays the coastal areas of Mozambique are considered as a promising target for exploration companies ([Salazar et al., 2013](#)). However, based on the focus of the exploration surveys on the shelf area as well as a comparable short recording time of the seismic multichannel data, no concrete conclusions can be drawn on the crustal setting of the margin and the age of the crust offshore in the Mozambique Basin.

First distinct evidence about the crustal nature of the Mozambique Basin provided wells of the Deep Sea Drilling Project (DSDP) in 1972. In this regard, important findings were the presence of a basaltic basement of at least Coniacian age (89.8-86.3 Ma; [Gradstein et al., 2012](#)) at DSDP site 250 in the southern Mozambique Basin ([Davies et al., 1974](#)), and Valanginian to Hauterivian (139-131 Ma; [Gradstein et al., 2012](#)) sediments overlying the northern Mozambique Ridge at DSDP site 249 ([Simpson et al., 1974](#)). Further evidence on crustal ages by magnetic data revealed the investigation of magnetic spreading anomalies at the South-west Indian Ridge (SWIR) by [Bergh \(1971\)](#). Subsequently, [Bergh and Norton \(1976\)](#) extended the identifications in the southern Mozambique Basin back to the Cretaceous Magnetic Quiet Period. In agreement, [Segoufin \(1978\)](#) and [Simpson et al. \(1979\)](#) identified Mesozoic spreading anomalies in the Central Mozambique Basin up to M22 (151 Ma). First in 2005, modern systematically acquired magnetic data confirmed these results and allowed the interpretation of magnetic chrons up to M26 (157 Ma), but could not state the presence of the continent-ocean transition. Consequently, from 2005 on, additional seismic reflection, seismic refraction and potential field data were recorded close to the coast of Central Mozambique ([Reichert and Neben, 2008](#)) as well as in the Natal Valley and across the Mozambique Ridge ([Jokat, 2009](#); [Uenzelmann-Neben, 2005](#)). In main parts, our current knowledge about the crustal nature of the Central Mozambique continental margin and the Mozambique Basin is based on these studies and is briefly summarized in the following:

A narrow transition from thick continental to slightly thickened transitional crust is observed in the NE-part of the continental margin of Central Mozambique ([Leinweber et al., 2013](#)). A prominent HVLCB underlies the transitional crust and extends far into the area of distinct oceanic crust in the abyssal plain. The offshore basin is filled by an up to 10 km thick column of Jurassic sediments. Weak evidence is observed in seismic reflection data for the presence of SDRs at the continental rise ([Reichert and Neben, 2008](#)). This is accompanied by a pronounced coast-parallel magnetic low, which is in

contrary to a strong positive magnetic anomaly observed at its conjugate margin in the Riiser-Larsen Sea in Antarctica (Golynsky et al., 2007). Jurassic magnetic spreading anomalies can be confidently identified up to chron M33n (161 Ma) (Leinweber et al., 2013). The COT is expected to be even closer to the coast and might be marked by the presence of the hypothetical identification of M41n (168 Ma) (Leinweber et al., 2013).

Towards the south-west, about 80 km off the coast of Central Mozambique, a prominent gravity low characterizes nearly half of the entire margin. Its position coincides with a known basement high, the Beira High. The crustal nature of Beira High is still under debate. Gravity modelling of Watts (2001) suggests an oceanic origin. In contrast, seismic reflection data revealed the presence of half-grabens and listric normal faults at Beira High, pointing towards a continental origin (Mahanjane, 2012). Lava flows are observed in the depression between Beira High and the coast of Mozambique.

Further south-west, a thick layer of Upper Cretaceous and Tertiary sediments covers the area onshore the Mozambique Coastal Plains (MCP) (De Buyl and Flores, 1986; Flores, 1973). Several exploration wells at the MCP terminated in the underlying volcanic rocks of the Stormberg series of Middle to Upper Jurassic age (Du Toit et al., 1997). It is unknown if these volcanics represent the basement, or if the MCP are underlain by continental or transitional crust. In a similar manner, the crustal origin of the Natal Valley and Mozambique Ridge are still enigmatic. In the last 50 years, several competitive opinions arose, ranging from continental (Eagles and König, 2008; Tucholke et al., 1981), to partly continental (e.g. Ben-Avraham et al., 1995; Mougnot et al., 1991; Tikku et al., 2002), to oceanic crust (König and Jokat, 2010; Leinweber and Jokat, 2011). However, a first modern seismic refraction study across the southwestern part of the Mozambique Ridge revealed a typical velocity structure of an oceanic plateau with an up to 14 km thick HVLCB (Gohl et al., 2011). This puts at least a partly oceanic nature of the Mozambique Ridge in favour. Based on the different ideas about the crustal origin of main tectonic features in the Mozambique Basin, even more controversial reconstructions of the Mesozoic Gondwana break-up exist. Recent reconstructions share the idea of a tight Gondwana fit, with an Antarctic plate overlapping the MCP (e.g. Kristoffersen et al., 2014; Leinweber and Jokat, 2012; Nguyen et al., 2016). However, the ‘fit’ itself reveals a great variety of solutions.

Therefore, at the beginning of year 2014, new seismic refraction and potential field data were acquired in the northern Mozambique Basin during cruise SO230 and serve as database for this thesis (Fig. 1.4). The thesis has been prepared in the scope of the MOCOM project. This is a cooperation between the AWI (Alfred Wegener Institute, Helmholtz Centre for Polar and Marine Research, Germany) and the BGR

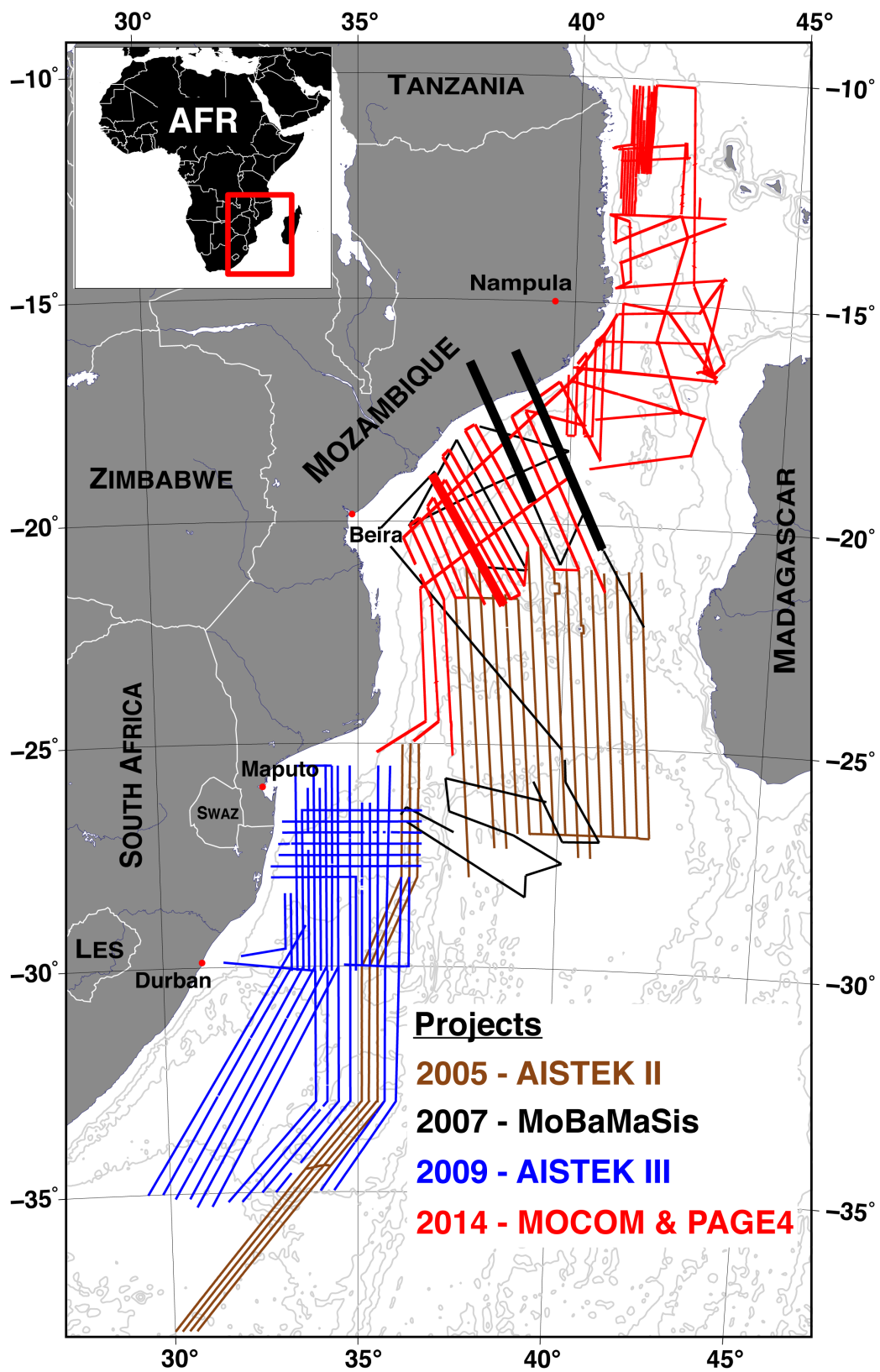


Figure 1.4: Overview of former surveys with AWI participation and the current MOCOM project in the Mozambique Basin. Bold red and black lines mark the position of the seismic refraction profiles investigated in the scope of this thesis.

(Federal Institute for Geosciences and Natural Resources, Germany), and is funded by the German Federal Ministry of Education and Research (BMBF, 03G0230A) as well as AWI internal funding.

In general, in the southern hemisphere, the research at AWI focuses on the investigation of the formation and current change of the Antarctic continent and its surrounding oceans. Regarding the geological history of Antarctica and the characterization of its offshore basins, special focus is set on the margin of Dronning Maud Land (DML) in East Antarctica. This was part of the former suture between East and West Gondwana and was affected by the initial break-up in the Jurassic. However, a several hundred meter thick ice sheet covers even the shelf areas of the margin and hinders its investigation. The still on-going identification of major large-scale tectonic units of DML is restricted to onshore geological investigations at exposed mountain peaks and demanding aero-geophysical surveys. Further evidence about the tectonic evolution of DML is expected by studying the conjugate margin of Mozambique and the offshore Mozambique Basin. In this regard, the MOCOM project represents the continuation of previous successful investigations of AWI and BGR in the Mozambique Basin (e.g. [Jokat, 2005, 2009](#); [Reichert and Neben, 2008](#)) and aims to supplement this data and to advance the interpretations.

1.4 Research questions of this thesis

The main research questions of this thesis focus on the Mozambican margin, but address the tectonic evolution of both conjugate margins and the initial Gondwana break-up, which caused their separation.

Crustal structure along the continental margin of Central Mozambique

A first modern seismic refraction study ([Leinweber et al., 2013](#)) across the north-eastern part of the margin revealed a narrow COT close to the coast, which is underlain by a pronounced HVLCB. So far it is unclear, if this crustal structure is also present in the south-western part of the margin. Here, a prominent gravity low makes up half the offshore part of the continental margin of Central Mozambique and marks the position of Beira High, whose origin is still unknown. Its classification has a major impact on the crustal setting at both conjugate margins and the development of the early Gondwana break-up in the Africa-Antarctica Corridor (AAC). Main questions are:

1. What is the origin of Beira High?
2. What is the extent of the HVLCB along the margin?

3. Are there crustal similarities between the south-west and the north-east part of the margin?
4. Where is the COT?

Distribution and age of the break-up related magmatism along the continental margin of Central Mozambique

The Karoo and Ferrar flood basalts and huge dyke swarms onshore SE-Africa and Antarctica as well as voluminous SDR wedges at the Explora Escarpment in the Lazarev and Wedell Sea testify to the large-scale volcanism connected to the dispersal of Gondwana. However, a time gap of about 20 Ma exists between the main emplacement of the flood basalts at 184-180 Ma (Jourdan et al., 2008) and the onset of the first confidently identified oceanic crust at M33n (161 Ma; Ogg, 2012) (Leinweber and Jokat, 2012). Further evidence about a possible continuation of the magmatism along the coast of Central Mozambique and about the crustal nature of the MCP, Natal Valley (NV) and Mozambique Ridge (MozR) might narrow this time gap. A detailed knowledge about the timing and distribution of break-up related magmatism is crucial for the understanding of the driving forces of the dispersal (plume or non-plume). Main questions are:

1. Is there further evidence for volcanics in Central Mozambique? If so, when were these emplaced?
2. Did continuous magmatism accompany the initial break-up?
3. Is there a difference to the observed magmatic features at the Antarctic margin?
4. Do volcanics contribute to the difference in magnetic signature of the conjugate margins?
5. What conclusions can be drawn on the Karoo Large Igneous Province (Karoo LIP) and its magmatic source?

Initial Gondwana break-up in the Africa-Antarctica Corridor

So far, reconstructions of the Gondwana break-up show clear differences in their pre-rift fit. Mostly these suffer from missing information about the exact timing of the Jurassic plate motions and the reliable tracing of fractures close to the margins. The new magnetic data might reveal important information about this. Furthermore, the origin of the different plateaus and ridges in the AAC has to be investigated, as well as the existence of possible rift jumps and/or extinct ridges, which might have contributed to their emplacement. To validate these results and the findings of this thesis, a new

kinematic break-up model of the AAC is required, which consistently explains the evolution of the conjugate margins, without contradicting the motion of the adjacent plates. Main questions are:

1. What is the origin of the Mozambique Ridge, the Natal Valley and the Mozambique Coastal Plains?
2. Were additional plates involved in the break-up of the AAC?
3. How were the plates arranged prior rifting?
4. Can Beira High be restored between the African and Antarctic plate?
5. Did the break-up proceed along former zones of weakness?
6. What conclusions can be drawn on the tectonic setting of Antarctica?
7. What are the consequences for the simultaneous opening of the Somali Basin?

2 Data acquisition, processing and modelling

During cruise SO230, the acquisition of the new geophysical dataset comprised one wide-angle seismic profile across Beira High, as well as the continuous record of magnetic, gravity and bathymetry data throughout the northern Mozambique Basin (Fig. 1.4, MOCOM project). Due to logistical reasons, additional data were acquired along the northern coast of Mozambique in the scope of the PAGE4 project (Franke, 2014). Potential field data of this project were also subject of this thesis. I participated in cruise SO230 and was involved in the acquisition and the on-board processing of the data. Subsequently, I continued the processing of the data and prepared velocity, amplitude, gravity and magnetic models as well as a magnetic compilation. These serve as base for the interpretation of the data, whose results are incorporated in the set-up of a new kinematic break-up model of the AAC and the discussion of the main research questions. In the following, the acquisition of the new dataset, its processing and modelling are briefly described.

2.1 Seismic refraction data

In general, seismic refraction studies provide information about the velocity distribution and the layering of the subsoil. Known common velocity ranges allow a subsequent interpretation of the layers and the set-up of a geological model.

For acquisition, a source emits waves of seismic energy into the subsoil (Fig. 2.1). Depending on their angle of incidence, the waves get reflected, refracted and partly converted at boundaries with an impedance contrast. A critically (critical angle of incidence) refracted wave, often called head wave, travels along the interface and permanently emits energy back to the overlying layers. In case of a constant velocity gradient, waves can even turn in a layer without strong impedance contrasts, and are called diving waves. Receivers record the arrival of the waves at the sea floor.

Seismic refraction studies can be applied to small-scale engineering geological surveys up to large-scale investigations of the earth's lithosphere. In the scope of this study, we

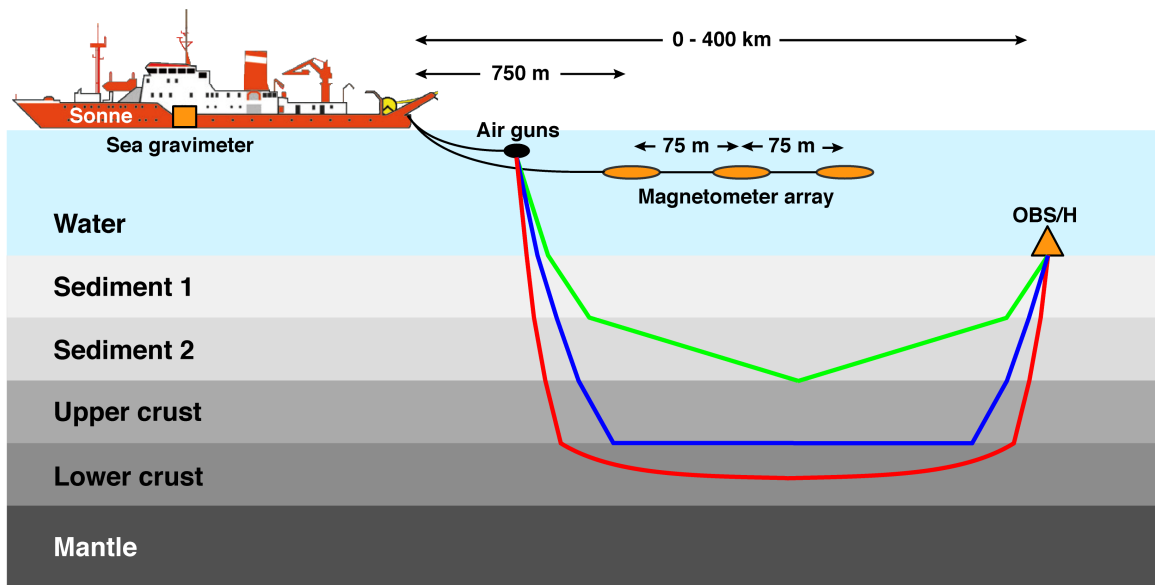


Figure 2.1: Acquisition of geophysical data during cruise SO230. The drawing is schematic, simplified and not to scale. The travel time paths of the seismic waves are coloured as follows: green – reflected wave, blue – head wave, red – refracted, diving wave.

are interested in the record of signals from the crust and the upper mantle. Therefore, a long offset configuration of a seismic transect is required to receive refractions and wide-angle reflections of the deeper layers.

2.1.1 Acquisition and processing

During cruise SO230, a cluster of 2x4 G-Guns (Fig. 2.2) with a total volume of 68 l was towed behind the ship in 10 m water depth and generated the seismic energy (Fig. 2.1). Therefore, highly pressurized air (210 bar) was released into the water once per minute. During acquisition, the ship's speed was reduced to 5 kn, resulting in a shot spacing of ~ 150 m.

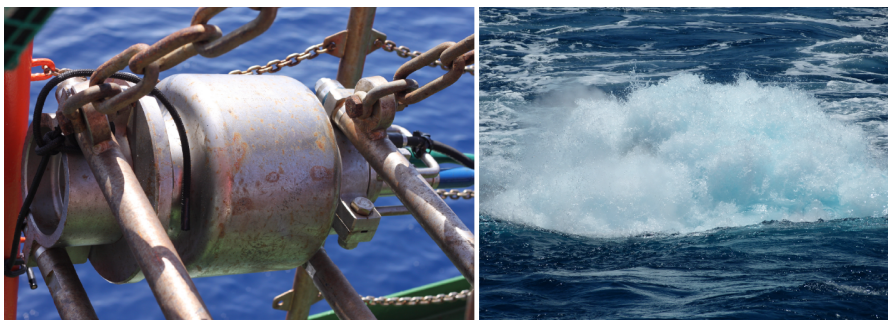


Figure 2.2: Air guns were used for the generation of the seismic signal. Left image shows a single air gun during the cruise SO230. Right image illustrates a shot (release of highly pressurized air into the water for generation of the seismic energy) as observed at the surface.

For record of the wide-angle seismic data, 33 OBS (Ocean Bottom Seismometer) of different types and 4 OBH (Ocean Bottom Hydrophone) were deployed with a 9 km spacing along the profile (Fig. 2.1). Their principle set-up is shown in Figure 2.3. In general, an OBS/H consists of a frame where the main units as a floating body, a pressure cylinder, which contains a recording unit and batteries for an autonomous work at the sea floor, as well as additional technical equipment are attached.

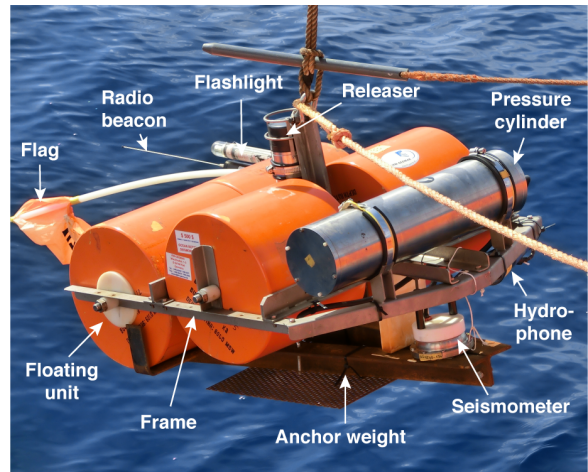


Figure 2.3: General set-up of an OBS prior deployment during the cruise SO230. The pressure cylinder contains the data recorder and batteries.

After launching the OBS/H into the water, it sunk to the sea floor, due to a mounted anchor weight. To record the seismic energy at the sea floor, all OBS/H were equipped with a hydrophone and each OBS with an additional 3-component broadband seismometer. Either a MBS (Marine Broadband Seismometer) or a MLS/MTS (Marine Longtime Recorder/Marine Tsunameter Seismocoder) recorder was securely stored in the pressure cylinder, which logged the recorded data at a sampling rate of 250 Hz or 200 Hz, respectively. By the end of the profile, a signal was sent to the release unit of the nearest OBS/H, resulting in the decoupling of the anchor weight. In the following, the OBS/H rose upwards, due to its floating body. Once at the sea surface, the signal of the radio beacon, flash light and flag helped to locate the OBS/H. After its recovery, the internal clock of the recorder was synchronized with a GPS signal and the data was downloaded for the subsequent processing.

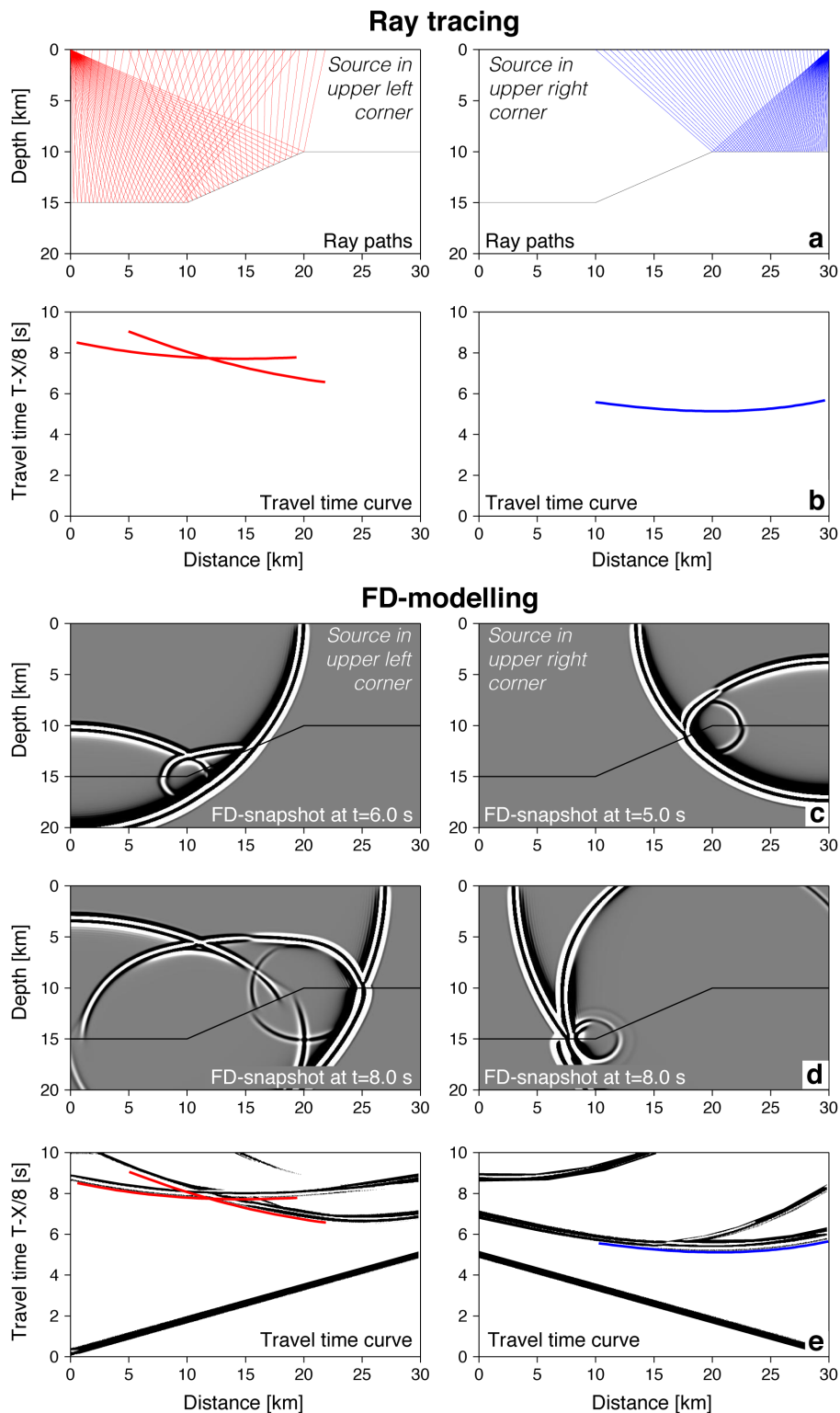
Herein, the data were corrected for the shift of the internal clock, demultiplexed, reduced to the time of acquisition and cut into time segments of one minute, due to a 60 s shot interval. In the following, the data of the hydrophone and of each of the three seismometer components were stored in separate SEG-Y files. The navigational data was used to calculate the offset of each trace to the OBS/H position and was written to the trace header. By now, the data were plotted as seismogram, with the travel time of the seismic signal over the distance of the shot to the receiving OBS/H. However, ocean currents cause the drift of the OBS/H during its descent to the sea floor, which leads to a different position as noted at its deployment. For this purpose, each trace is shifted by a constant distance to fit the trace of the first arrival of the direct water wave to zero offset. Afterwards, an AGC (automatic gain control) with an 1 s time window and a velocity reduction of 8 km/s were applied to the data. A bandpass filter

of 4-30 Hz was chosen for picking the P-waves of the sediment layers and 4-13.5 Hz for the long wavelength arrivals of the crustal phases.

2.1.2 Ray tracing vs. FD-amplitude modelling

At first, refractions and reflections of the sediment and crustal layers as well as the mantle were picked at all OBS/H stations with the software ZP (Zelt, 2004). Information from a congruent seismic reflection profile (Castelino et al., 2015) and bathymetry data served as constraint for the subsequent set-up of a starting model. Based on the ray tracing method, a velocity model was prepared with the software RAYINVR (Zelt and Smith, 1992) and the graphical user interface PRay (Fromm, 2016). The procedure of this modelling is described in detail in section 4.4.1. The inspection of the resolution of the velocity model along the seismic transect revealed only a small number of diving waves constraining the velocity gradient in the lower crust at the main research subject, the Beira High. On one hand, the survey set-up, a thick sediment coverage and the great depth suppress the record of strong signals of refractions from the lower crust. On the other hand, a pronounced topography of the basement and the crust-mantle boundary (Moho) partly hinder a modelling of the refractions of the lower crust with the ray tracing method. In contrast, a large number of reflections constrain the Moho topography at Beira High. However, the investigation of the move out of the reflections did not allow a definite assignment of a velocity gradient. Due to the importance of the characterization of Beira High for a study of the tectonic evolution of the conjugate margins, I conducted an additional amplitude modelling of the Moho reflections. At first, based on the FD (finite difference) method, synthetic seismograms were generated with the software SOFI2D (Bohlen et al., 2015a) for different models of the lower crust. Subsequently, in each synthetic seismogram the PmP phase was picked and their amplitudes exported and compared to the recorded data. The generation of the synthetic seismograms and the modelling approach are described in more detail in section 4.4.2. The compiled FD-software itself, as well as scripts and documentations of the amplitude modelling prepared in the scope of this thesis are stored at an AWI internal server and are available for further projects. In the following, the advantages of a FD-amplitude modelling as supplementary study to a ray tracing model are highlighted.

The ray tracing method is based on a high-frequency approximation of the wave equation. This allows the calculation and modelling of waves as seismic rays. However, at pronounced topography or edges, when the wavelength of the propagating wave is not significantly smaller than the wavelength of the change of the velocity model at this point, the ray tracing method fails to calculate propagating waves or accord-



ingly rays (Fig. 2.4a). Consequently, the calculated travel time curves, which are used for the comparison to the recorded OBS data, end abruptly (Fig. 2.4b) and do not allow a modelling of the reflection at this station beyond this point. In contrast, a grid-based method, as the FD-method, uses a discretised model, where differential operators approximate the partial spatial derivatives of the wave equation (Bohlen, 1998; Schmidt-Aursch, 2003). As a consequence, propagating wave fronts can be calculated at edges and at pronounced topography, too. The resulting diffracted phases and their travel time curves can be observed across the edges (Fig. 2.4c, d, e). Compared to the ray tracing method, additional later arrivals and converted phases can be observed as well (Fig. 2.4c, d, e), which allow an improved phase identification in the recorded OBS data. Furthermore, the calculated travel time curves give evidence about required adjustments of the layer's topography or velocity gradient, which otherwise might be erroneously changed during the ray tracing. For the calculation of the wave front's amplitude, the acoustic impedance is calculated and damping is applied, which allows the comparison between the amplitudes in the synthetic seismograms and the one in the recorded OBS data. Regarding the PmP reflection, calculated models with different velocity contrasts at the Moho depict a shift of the maximum amplitude towards greater offsets for higher basal velocities (Fig. 2.5). This is caused by the lower velocity contrast, which results in an interference of the Moho reflection with refractions of the crust at greater offsets. The velocity contrast, which reveals the best fit between the amplitude of the observed and synthetic data, is considered to depict the most likely basal velocity of the lower crust. Criteria for the identification of the best fit are the locations of the maxima and minima as well as the general decay of the amplitudes.

2.2 Potential field data

A reasonable investigation of the entire continental margin of Central Mozambique is not only possible by means of velocity information and stratification. Therefore, new gravity and magnetic data were acquired in the scope of this project. In contrast to seismic refraction data, these are sensitive to vertical and horizontal density and susceptibility contrasts in the subsoil, respectively.

Satellite missions already provided global potential field data (e.g. GOCE, SWARM). These were used for tracing main tectonic features and fracture zones, which reveal important information for the reconstruction of the initial break-up. However, for detailed studies and the supplement of seismic surveys, the record of high-resolution data is required. Shipborne gravity data was used for the set-up of a density model along the seismic refraction profile, to confirm the velocity model and identify problematic areas.

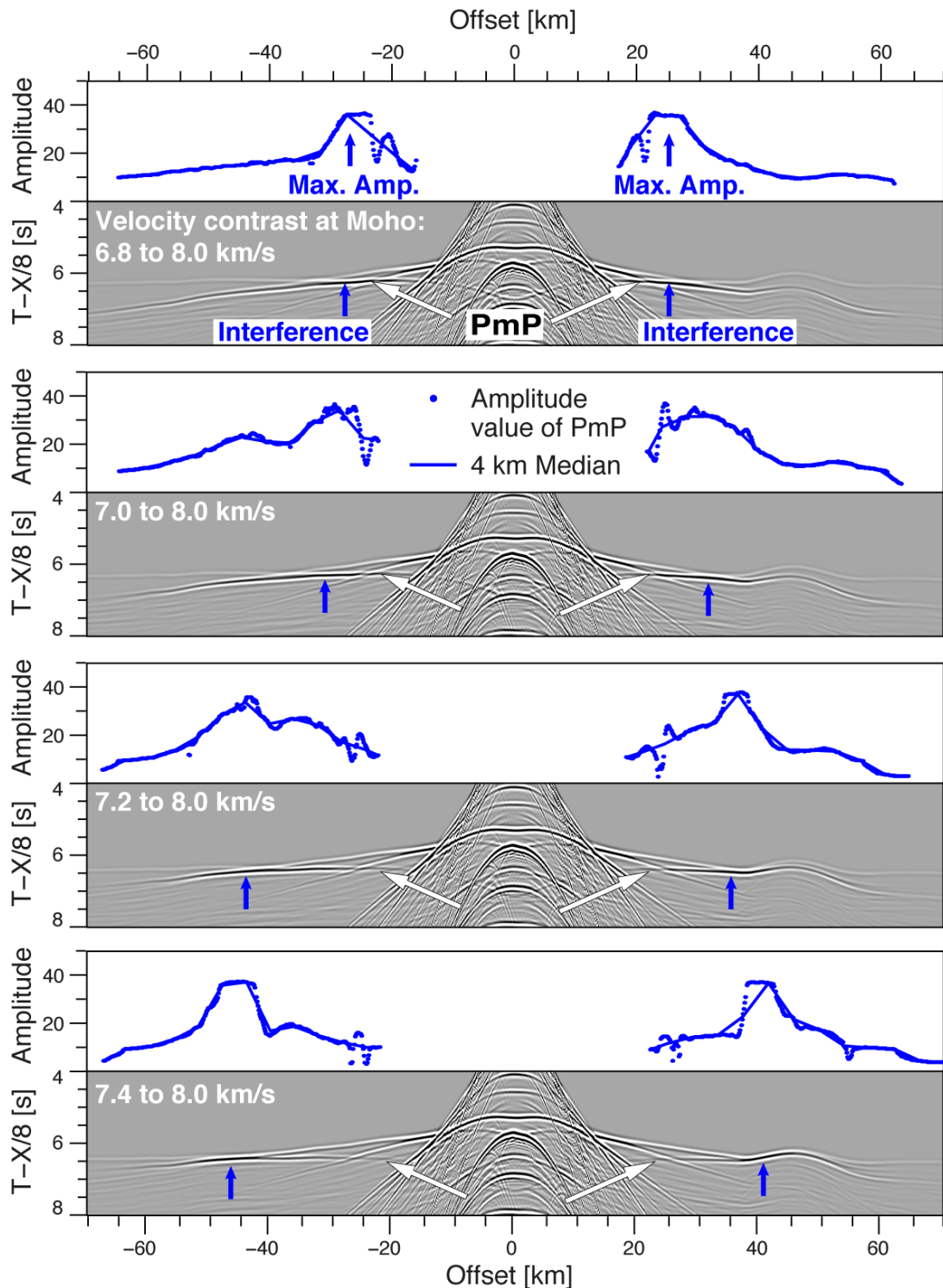


Figure 2.5: Distribution of amplitudes of the PmP phase for models with a different velocity contrast at the Moho. The upper panel shows the respective amplitude (blue circles) for each pick as well as the calculated median with a 4 km window length. In the lower panel, the onset of the PmP phase is indicated by white arrows and not entirely marked for a better visibility of areas of interfering arrivals. Note the shift of the location of interference (blue arrows) to greater offsets for models with a lower velocity contrast at the Moho. In accordance, this is well expressed by the location of the maximum amplitudes.

The magnetic data was essential for the magnetic modelling, aiming on the extraction of properties of magmatic structures, which give evidence about their origin and consequently the history of the continental margin. Furthermore, magnetic data was the only available method to obtain an age control on the break-up, by identifying magnetic spreading anomalies. In the following, the acquisition, processing and interpretation of the potential field data are described.

2.2.1 Gravity data

The Bodenseewerke marine gravimeter system KSS32M (S/N 22) (Fig. 2.6) was used for the continuous record of gravity data with a sampling rate of 1 Hz throughout the entire cruise (Fig. 2.1). During the on-board processing, in a first step the measured output voltage of the electromagnetic feedback system of the gravimeter was converted from mV to mGal. A time shift of 76 s was applied to the data, due to the overcritical damping of the sensor (Jokat, 2014). An offset of 11 m between the location of the gravimeter and the GPS antenna was accounted for to represent the data at its correct recording position. Subsequently, data outliers were removed and a 300 s long median filter was used to suppress short wavelength oscillations, caused by rough sea. After the cruise, the measured relative gravity values were tied to the IGSN71 (International Gravity Standardization Net 1971). In this regard, additional gravity measurements were conducted with a LaCoste & Romberg G480 (Fig. 2.6) in Durban and at the pier, before and after the cruise. These readings depicted a small instrumental drift of the gravimeter of -0.02 mGal, which is used for the drift correction. Therefore, the drift was linearly interpolated over time and applied to the data. However, further corrections are necessary for its subsequent use for modelling:



Figure 2.6: Gravimeters used during the cruise SO230. Left image shows the LaCoste & Romberg land gravimeter G480 for tie measurements in the harbour of Durban, RSA. Right image shows the Bodenseewerke marine gravimeter system KSS32M (S/N 22) in the gravimeter room of RV Sonne.

- **EÖTVÖS CORRECTION:** On a ship, its relative motion to the Coriolis force causes the measurement of an additional vertical component of the centrifugal acceleration. To account for the Eötvös effect, precise navigation data are required to

calculate the correction at latitude φ with the ship's velocity v in knots and its heading H :

$$g_{etv} = 7.487 * v * \cos(\varphi) * \sin(H) + 0.00415 * v^2 \quad [mGal].$$

- **LATITUDE CORRECTION:** Global variations in the centrifugal force, caused by the earth's radius and polar flattening due to its elliptical shape, result in a varying mean gravity with latitude. For correction, the theoretical gravity at a measuring point is subtracted from the observed value. The International Gravity Formula for the GRS80 (Geodetic Reference System 1980) was used for the calculation of the so-called 'normal' gravity at latitude φ :

$$g_n = 978032.7 * \left(1 + 0.0053024 * \sin^2(\varphi) - 0.0000058 * \sin^2(2 * \varphi)\right) \quad [mGal].$$

No free-air correction was necessary, due to the gravimeter's position at sea level. Consequently, these corrections already result in the free-air gravity anomaly, which is commonly used in marine gravity studies.

2.2.2 Magnetic data

Magnetic data were continuously acquired with a SeaSpy gradient magnetometer system (Fig. 2.7). The array consists of two scalar Overhauser sensors at the front and rear end, as well as a Magson vector magnetometer sensor in the centre (Fig. 2.1). The latter one contains a 3-axis fluxgate magnetometer, which could provide additional information



Figure 2.7: Two sensors of the Sea Spy gradient magnetometer system, prepared for operation during the cruise SO230.

about the horizontal and vertical components of the local earth's magnetic field. However, no reliable interpretation of the recorded vector magnetometer data was possible, due to unknown azimuthal orientations of the tow fish. This might bear distinct variations to the heading of the ship, which could not be accounted for in the processing.

The array was towed 750 m astern of the ship, with 150 m spacing between the two Overhauser sensors (Fig. 2.1). Each of them contains a proton precision magnetometer, which utilizes the quantum mechanical Overhauser effect and measures the total magnetic field intensity (TMI) (Jokat, 2014). Assuming, that the temporal variation of the earth's magnetic field over the two sensors is homogenous, the integration of the

gradient, between the two sensors, over the distance of the ship track, results in the almost variation-free total intensity. Consequently, no diurnal corrections had to be applied during processing.

Herein, the navigation data were used to transfer the magnetic data to their correct recording position, which accounts for the shift due to the cable length and 20 m offset between the cable winch and the GPS antenna. The array was towed in a water depth of 20-60 m, with an average of 30 m. In the subsequent correction of the data for the main earth's magnetic field, the IGRF-12 was calculated for the date of acquisition of each value and the average water depth. Afterwards, the magnetic anomaly data were upward continued to the sea level, which simultaneously served as de-spiking. Fitting mis-ties by a static shift and tensioned B-splines were used for levelling of the data.

For the preparation of the compilation of all available magnetic data in the Mozambique Basin, it was not possible to assign measurement lines and tie lines, due to the irregular distribution of the magnetic profiles. Therefore, the 'random line levelling' technique of [Mieth \(2014\)](#) was used. This is an adoption of the median levelling technique of [Mauring et al. \(2002\)](#) and is described in detail in [Mieth \(2014\)](#). The main steps comprise a zero-network levelling and the use of filtered tensioned splines to reduce the cross-point errors. Finally, the data were upward continued to 350 m to suppress small high-frequency anomalies and to allow a direct comparison with a magnetic compilation at the conjugate margin of DML ([Mieth, 2014](#)).

2.2.3 Interpretation and modelling

In general, the interpretation of potential field data aims on the anomaly characterization and the estimation of source parameters. However, their interpretation is mathematically non-unique, since several theoretical solutions are always possible ([Saltus and Blakely, 2011](#)). Concrete, source bodies of different size, density/susceptibility and depth can cause the same anomaly (Fig. 2.8). Furthermore, by just changing the sign of the density contrast of one anomaly body might cancel out the anomalous effect of another one.

To obtain a first idea about possible source characteristics and to limit the number of solutions, all information of previous geological and geophysical studies should be considered prior interpretation. As a consequence, the investigation is constrained by independent information and has to simultaneously satisfy several geophysical and geological observations, like seismic, gravity, magnetics and tectonics at the same time. However, an appropriate interpretation of the potential field data is still required to minimize the amount of possible solutions.

Therefore, qualitative and quantitative interpretation methods are suited. Qualitative methods are used for the identification of anomaly properties like amplitude, shape, lineaments or wavelength content. Based on these, first conclusions can be drawn on the characteristics of the source body, e.g. low/high density/susceptibility, possible strike and dip directions and depth range (Marello, 2012). For extraction of this information, several different methods are available, which can be applied to the data in the time or frequency domain. In the following, the ones used in this thesis are briefly described. All of them were calculated within the Geosoft Oasis Montaj software.

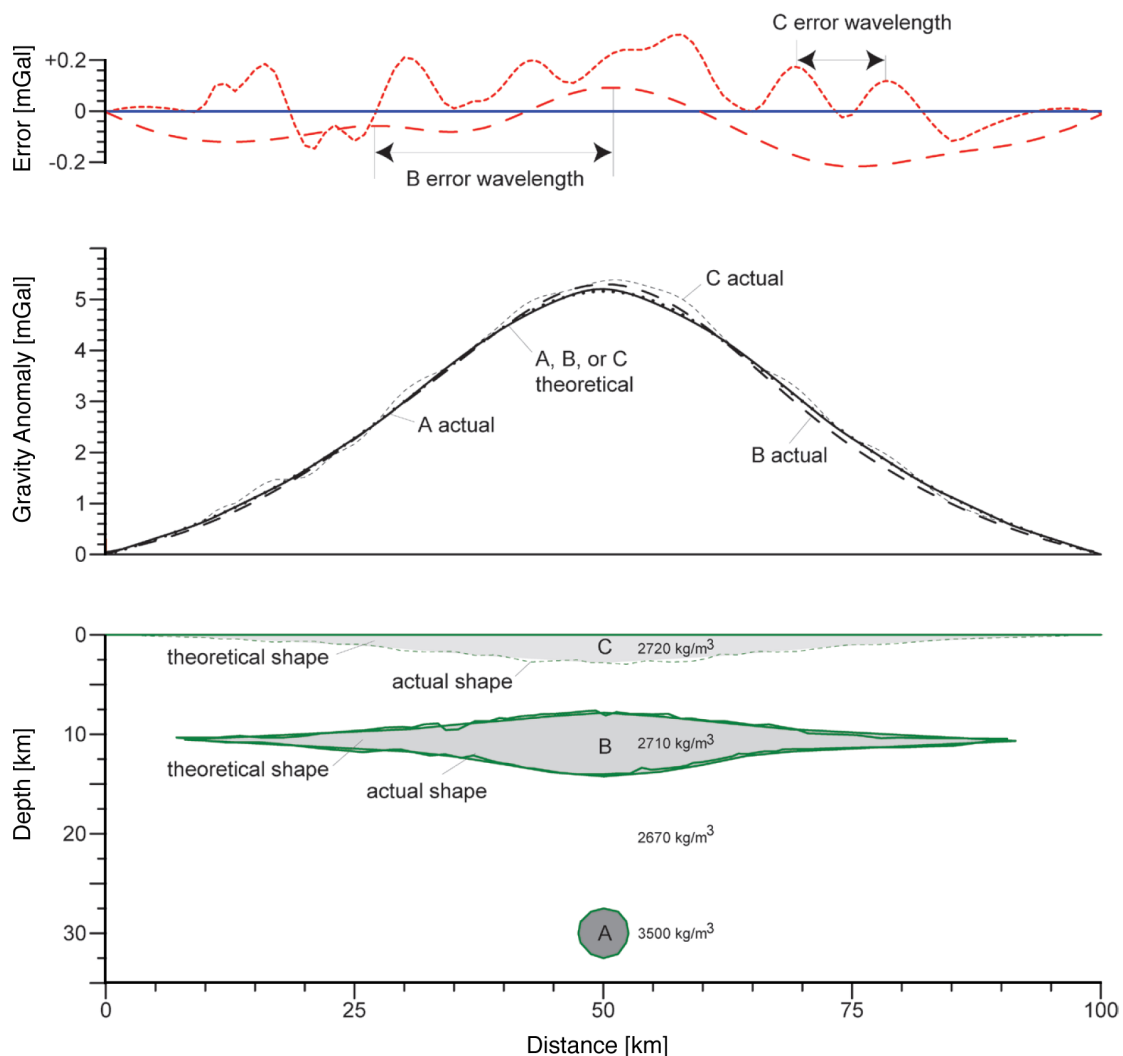


Figure 2.8: Non-uniqueness problem in modelling potential field data and the use of the error wavelength (modified from Saltus and Blakely, 2011). In general, the calculated gravity anomaly (solid black line) of the theoretical smooth-shaped source bodies (grey areas of A, B, C) cause the same anomaly. However, surface irregularities of the source bodies are expected in the real world (actual shape of A, B, C). The corresponding misfit in the calculated gravity anomaly to the observed one, depict different error wavelengths.

FILTERING: In general, filtering is used for the separation of different frequency components in the data. It was applied for emphasizing signals of anomaly bodies in a certain depth range and elimination of noise, by simultaneously avoiding ringing in the data.

UPWARD / DOWNWARD CONTINUATION: Potential field continuations are used to represent the data as observed at a different elevation, thus emphasizing or attenuating certain signals, too. In the scope of this thesis, small upward continuations were used for the suppression of short wavelength anomalies, ever caused by near-surface structures or noise. Grids showing the regional components of the data were generated by continuations up to 30 km and more. In contrast, downward continuation was sparsely and cautious used for the transfer of satellite data to the same reference level as processed shipborne data.

REDUCTION TO THE POLE (RTP): The reduction to the pole method represents the anomaly as observed at the magnetic pole, where the field is vertical (90°). Hence, a dipolar shaped magnetic anomaly observed at low magnetic latitudes, will be transformed by the RTP into a monopolar anomaly, which is centred over its causative body. Beside its correct location, these anomaly shapes allow a simplified interpretation of the source bodies. I have applied the differential reduction to pole technique ([Arkani-Hamed, 1988](#)) to the magnetic compilation. In contrast to the standard RTP, which uses a mean value of the inclination and declination of a defined area, this approach incorporates the correct declination and inclination values at each point of the grid. This allows a direct comparison of the location of magnetic features to the gravity data.

DERIVATIVES: In general, derivatives are used to emphasize high-frequent variations in potential field data, caused by sources extending towards the surface or resting close to it. On one hand, I used the resulting gradients for tracing fractures, which provide evidence about the plate motion in the past. On the other hand, the gradients were used for locating outlines of tectonic structures, domains and linear shaped features. As an example for the characteristics of gradients, [Figure 2.9a](#) shows the relation between the gravity and its derivatives observed at a fracture zone. Here, the vertical gravity (G_z) shows a broad minimum over the fracture zone and the fault core. The vertical gravity gradient (G_{zz}) depicts a distinct narrower minimum over the fault core. Combined with the horizontal gradient (G_{zx}), which reveals the maximum of its slope centred over the fault core, this allows a more precise localisation of it. The anomaly of the gradient (as well as of the TMI) decreases with depth by $1/x^3$. Accordingly,

the at the surface observed anomaly of a source body in about 9 km depth is only 0.1 %, as it would be observed by the same body located at the surface (Fig. 2.9b). In contrast, the amplitude of G_z decreases with depth by $1/x^2$, resulting in a 10 times higher signal, but a broader anomaly. This underscores the use of the vertical gravity for the interpretation (and modelling) of deep-seated structures and the contribution of their gradients to the investigation of shallow structures. However, even in small depths, the gradient's anomaly has clearly decreased, hence different combinations of the gradients are used to sharpen the signal. The following ones were used in the scope of this thesis:

- ANALYTIC SIGNAL (AS): The analytic signal is mathematically expressed as:

$$AS = \sqrt{\left(\frac{\partial F}{\partial x}\right)^2 + \left(\frac{\partial F}{\partial y}\right)^2 + \left(\frac{\partial F}{\partial z}\right)^2},$$

with F being the observed field at the position x , y and z . The results are independent of the direction of the field and the direction of magnetization, resulting in anomalies located directly above its source. Consequently, the AS was used for the localization of the edges of remanently magnetized bodies.

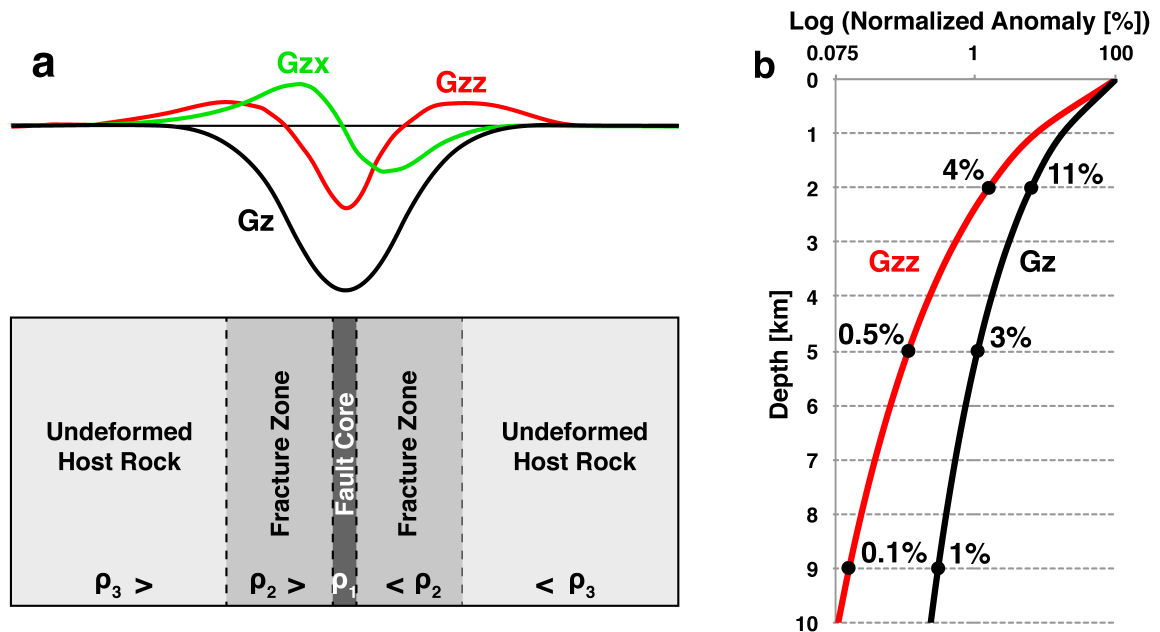


Figure 2.9: Characteristics of the gravity gradient. a) Gravity signature of a fracture zone. Densities decrease towards the fault core, due to increase in porosity and fracturing. The vertical gravity (G_z) shows a wider anomaly than their derivatives. b) Decay of the anomaly signal with depth. The signal decreases with $1/x^2$ for G_z and with $1/x^3$ for G_{zz} (as well as for the TMI).

- ENHANCED HORIZONTAL DERIVATIVE (EHD): The enhanced horizontal derivative is defined by [Fedi and Florio \(2001\)](#) as the horizontal derivative (HDR):

$$HDR = \sqrt{\left(\frac{\partial F}{\partial x}\right)^2 + \left(\frac{\partial F}{\partial y}\right)^2},$$

with F being the observed field at the position x and y, for a sum of vertical derivatives (VDR):

$$VDR = \sqrt{\left(\frac{\partial F}{\partial z}\right)^2}$$

of increasing order. In general, it emphasizes horizontal variations in different depths in the potential field data, depending on the degree of the vertical derivatives, and was used for detecting the outline of source bodies and boundaries between different geological units, based on the reduced to the pole data.

- TILT DERIVATIVE (TDR): The tilt derivative is mathematically described as:

$$TDR = \tan^{-1}\left(\frac{VDR}{HDR}\right).$$

The TDR is capable in pronouncing shallow basement structures. Here, it is especially used for an enhanced expression of fractures ([Fig. 2.10](#)).

A quantitative interpretation of the potential field data aims on the extraction of characteristics of the source bodies, e.g. quantifying their depth, size and shape. To obtain a first estimate about the depth of the anomalies, so-called depth-to-source techniques can be applied. Based on the availability of the gridded magnetic compilation of this study and a-priori information on possible source geometries in the survey area, a 3D Euler Deconvolution was used to estimate the location and depth to magnetic sources ([Fig. 2.11](#)). A main advantage in applying the Euler Deconvolution is that it is insensitive to the magnetic inclination, declination and remanence, due to the consideration of the derivatives of the magnetic field in all dimensions for calculation. The results served as evidence for the subsequent magnetic modelling.

Modelling of the potential field data can be used for a more complete estimation of the source parameters. Therefore, anomaly bodies are either assumed as simple structures or embedded in a complete geological model, which requires the division of their complex structure in several elementary bodies, like cuboids or prisms. In the scope of this thesis, gravity and magnetic modelling was conducted with the software IGMAS+ ([Götze and Lahmeyer, 1988](#); [Schmidt et al., 2007](#)). This allows the modelling along a

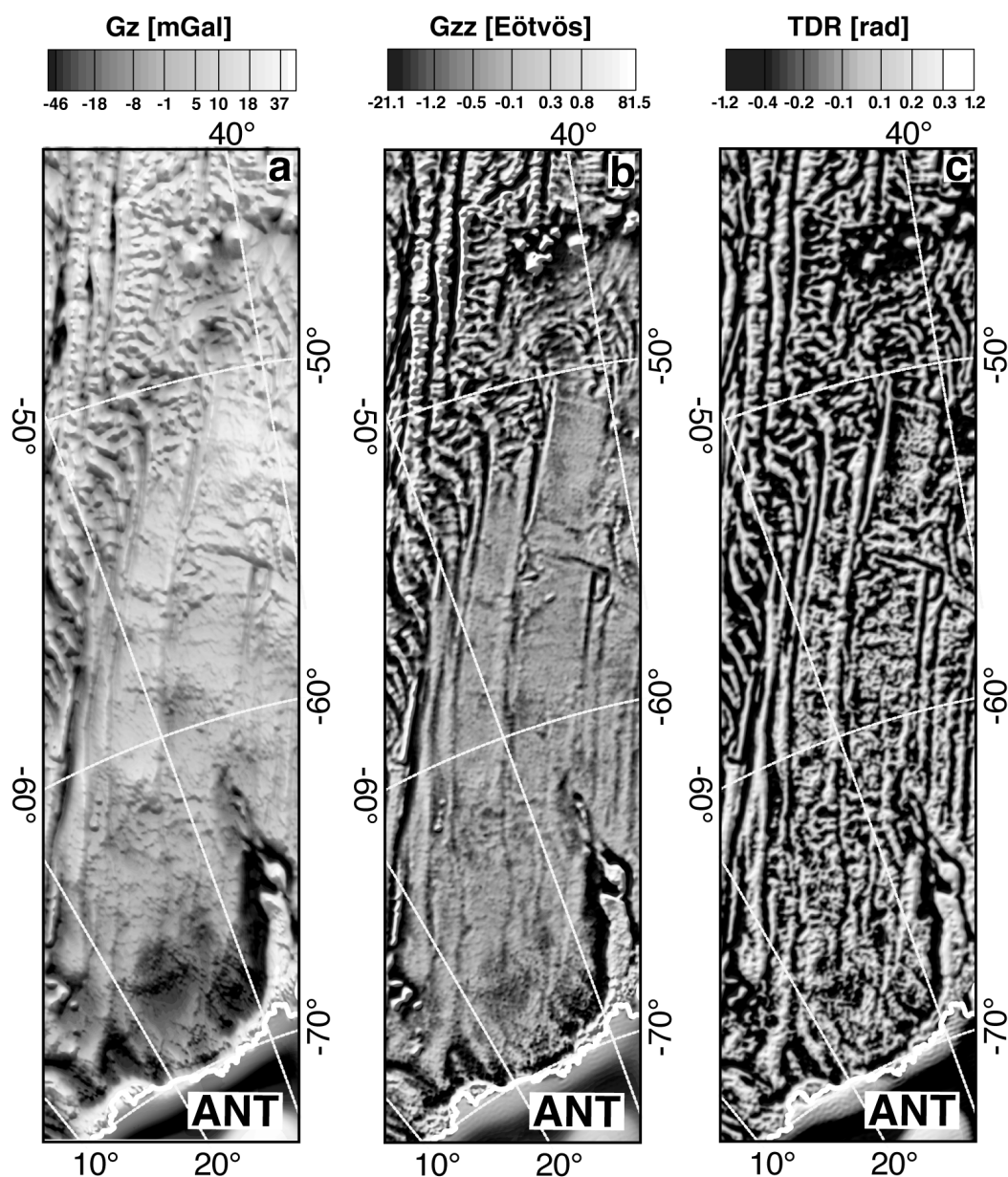


Figure 2.10: Gravity expression of fractures in the Riiser-Larsen Sea and example for the use of gradients for fracture tracing. a) In the free-air gravity anomaly data (v24.1; [Sandwell et al., 2014](#)), fractures are partly observed, but not well expressed. b) Its vertical derivative (G_{zz}) emphasizes the gravity expression of the fractures. However, tracing them in the coastal basin close to Antarctica (ANT) does not allow a distinct identification. c) The tilt derivative of the G_{zz} , clearly depicts the complete track of the fractures even closest to the ice shelf at the Antarctic margin.

series of parallel 2D-sections, which are connected by triangulation and calculates the gravitational response of generated polyhedrons. All available information from the velocity modelling and geological studies were incorporated in the respective starting model. In the following, slight adjustments of the assigned densities or susceptibilities

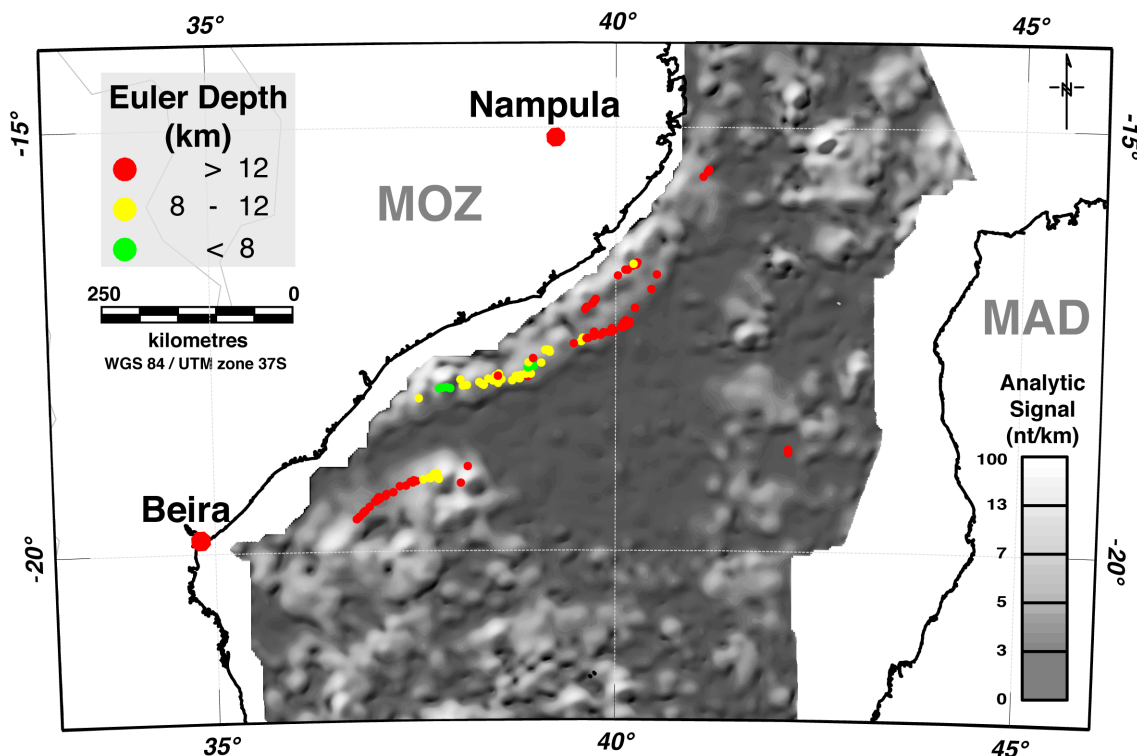


Figure 2.11: Depth estimation of magnetic source bodies by 3D Euler Deconvolution. Since the boundary between weak magnetized continental crust to strong magnetized oceanic crust is expected close to the margin of Central Mozambique (SI=0, magnetic contact), as well as the continuation of a dyke swarm and the presence of sills (SI=1, sills and dykes) are likely in this area, an intermediate structural index of 0.5 was chosen. The window size was set to 50 km and the maximal depth tolerance of the solutions to 10 %.

were necessary to reduce the mis-fit between the observed and calculated anomaly. Further details about the model set-up and the modelling process are described in section 4.4.3 for gravity data and in section 5.2.3 for magnetic data.

Additionally to the standard gravity modelling with average densities for each layer, I incorporated density gradients in the model. Based on the principle that compaction of the subsoil increases with depth, due to the increasing pressure of the overburden, results in the increase of velocity and density with depth. The seismic refraction study depicted distinct velocity gradients for most of the layers. This implies that density gradients are also present. For their incorporation, IGMAS+ voxelizes the model and allows the assignment of density functions for each layer. The corresponding gravity effect of each voxel of a layer is calculated for a sphere with the same volume as the voxel (mass point algorithm), due to its simpler computation, and is added to the normal average density of the layer. The difference between the gravity effect of an anomaly body calculated with an average density compared to the use of a corresponding density gradient is shown in Figure 2.12. This simple model depicts a greater negative anomaly

with the use of a density gradient. A density of 2.4 g/cm^3 at the upper boundary of the anomaly body causes a gravity effect, which is not entirely compensated by the higher density of 2.6 g/cm^3 at its lower boundary. This is based on the principle that a caused anomaly amplitude partly depends on the depth of the anomaly body, leading to a greater contribution of the density of 2.4 g/cm^3 at the top of the anomaly body to the calculated anomaly.

The application of density gradients to gravity modelling across a continental margin reveals an additional effect. A typical structural setting of a continental margin consists on one side of thick continental crust (and sediments), lying close to the surface, as well as of comparably light sediments (and water) down-slope the margin, which overly a thinned crust. Irrespective of the use of free-air or bouguer anomaly data, this scenario results in a lower gravity anomaly at the continental side of the margin when using density gradients instead of an average density. Consequently, the gravity contrast between the continental and oceanic side of the margin is less pronounced in case of incorporated density gradients. This results in the reverse effect of a higher gravity anomaly at its oceanic side as compared to the use of an average

density. This relation is clearly illustrated in the gravity model in Fig. 4.11. Here, a difference of up to 30 mGal is observed between the calculated anomaly with density gradients to one with an average density at Beira High. This difference exceeds the general uncertainty of the gravity modelling method of $\pm 10 \text{ mGal}$ (Ljones et al., 2004). However, for the great majority of published density models, the effect of density gradients is not considered at all. Especially seismic refraction studies provide great evidence for velocity gradients and consequently the presence of density gradients. To take the full advantage from these investigations and to prepare density models, which are able to reliably support the velocity models, the incorporation of density gradients might be considered for upcoming refraction studies and gravity models.

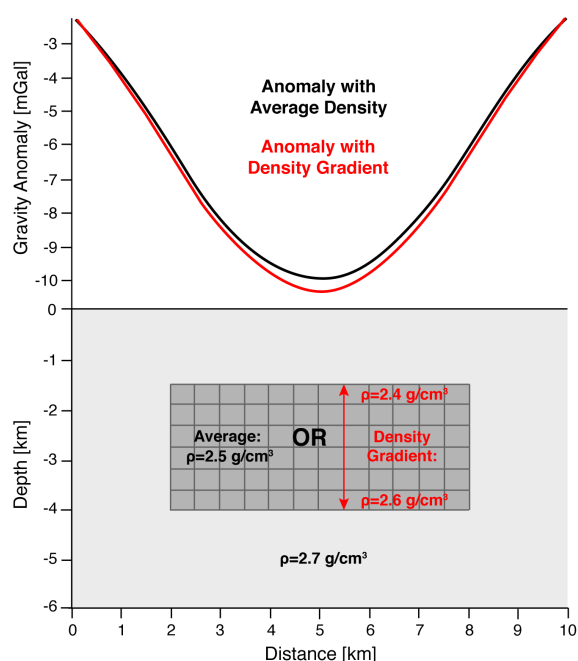


Figure 2.12: Gravity effect of an anomaly body calculated with an assigned density gradient compared to the use of an average density.

3 Contributions to scientific journals

In the scope of this dissertation, I prepared three scientific articles. This chapter summarizes the author's and co-author's contributions, main topic and current status of the manuscripts, which are presented in chapters 4, 5 and 6.

3.1 The crustal structure of Beira High, Central Mozambique – Combined investigation of wide-angle seismic and potential field data

Authors: Christian Olaf Mueller¹, Wilfried Jokat^{1,2}, Bernd Schreckenberger³

Affiliations: ¹ Alfred Wegener Institute, Bremerhaven, Germany

² University of Bremen, Bremen, Germany

³ Federal Institute for Geosciences and Natural Resources, Hanover, Germany

Journal: Tectonophysics

Status: Published on 21th June 2016, doi: [10.1016/j.tecto.2016.06.028](https://doi.org/10.1016/j.tecto.2016.06.028)

Newly acquired seismic refraction and potential field data allowed for the first time the investigation of the so far unknown origin of Beira High. A velocity, amplitude and density model with incorporated gradients were prepared along the seismic transect across Beira High. The results were compared to other continental fragments and oceanic plateaus. The identification of the major differences between these structures reveals Beira High as continental fragment, consisting of stretched, but highly intruded continental crust. Distinct differences arise to the Mozambique and Astrid Ridge, leading to the unlikely scenario of a combined emplacement history. Furthermore, a pronounced HVLCB underlies thin crust in the Zambezi Delta Depression, which points to an extension of the COT below onshore Mozambique.

I participated in the cruise and was involved in the acquisition and on-board processing of the new dataset. In the following, I processed the wide-angle seismic data and the relevant gravity and magnetic profiles. The compiling of required software, all modelling, interpretation and figures were prepared by me. Wilfried Jokat supervised the research. All co-authors revised the manuscript.

3.2 Geophysical evidence for the crustal variation and distribution of magmatism along the central coast of Mozambique

Authors: Christian Olaf Mueller¹, Wilfried Jokat^{1,2}

Affiliations: ¹ Alfred Wegener Institute, Bremerhaven, Germany

² University of Bremen, Bremen, Germany

Journal: Tectonophysics

Status: In review since 18th January 2017

For the investigation of the crustal variation along the continental margin of Central Mozambique, two former seismic refraction profiles are revised by amplitude modelling. A different stretching of the crust along the margin indicates an asymmetric set-up, as supposed for its conjugate in the Riiser-Larsen Sea. The observed HVLCB shows a spatial equal extent. Magnetic models reveal a contribution of reverse polarized SDRs to the prominent negative magnetic anomaly in the NE-part of the margin, as well as late-stage magmatism, causing the contrarious strong positive magnetic anomaly in the Riiser-Larsen Sea. The distribution of magmatism along the central coast of Mozambique depicts a continuation of the north-eastern branch of the Karoo LIP towards the far east of Mozambique, emplaced between 177-157 Ma. This indicates a later, but continuous magmatism along the Central Mozambique continental margin, which allows conclusions about the driving forces of the break-up.

In general, the seismic refraction models were previously published by [Leinweber et al. \(2013\)](#). For this study, I re-picked the crustal phases at all stations and conducted a velocity modelling by ray tracing and amplitude modelling. I prepared all magnetic models, figures and interpretations. Wilfried Jokat supervised the research and revised the manuscript.

3.3 The initial Gondwana break-up in the Africa-Antarctica Corridor – A reconstruction based on new magnetic data

Authors: Christian Olaf Mueller¹, Wilfried Jokat^{1,2}, Bernd Schreckenberger³

Affiliations: ¹ Alfred Wegener Institute, Bremerhaven, Germany

² University of Bremen, Bremen, Germany

³ Federal Institute for Geosciences and Natural Resources, Hanover, Germany

Journal: To be submitted to Gondwana Research

Status: With co-authors

Based on newly and previously acquired magnetic datasets of AWI, as well as industrial data and older shipborne magnetic data, a magnetic compilation of the Mozambique Basin was prepared. Magnetic spreading anomalies were identified in the Mozambique Basin, and tentative picks in the adjacent Natal Valley, across Mozambique Ridge and at the southern part of the Mozambique Coastal Plains, which might imply their oceanic origin. Fractures were traced throughout the entire AAC and close to the margins of Antarctica and Africa. Based on the results of the first and second manuscript as well as of further geological and geophysical constraints, assumed pre-rift and continent-ocean boundaries were assigned at both margins. This allowed the set-up of a consistent break-up model of the AAC and the adjacent Somali Basin by a single set of rotations. The pre-rift fit between Africa and Antarctica, reveals several continuations of magnetic lineations across both plates, and the link between geological structures of SE-Africa and DML.

I participated in the cruise and was involved in the acquisition and on-board processing of the new magnetic data. To enhance the coverage of our magnetic dataset towards the MCP and onshore areas, on my own initiative I approached exploration companies and organized the meetings and magnetic data exchange. I did the subsequent processing of the new magnetic data and set-up of the compilation. Furthermore, I picked all magnetic spreading anomalies and calculated the spreading models and rotation parameters. Finally, I prepared the reconstruction, figures and interpretations. Wilfried Jokat supervised the research. Graeme Eagles (AWI) revised the manuscript.

4 The crustal structure of Beira High, Central Mozambique – Combined investigation of wide-angle seismic and potential field data

Christian Olaf Mueller¹, Wilfried Jokat^{1,2}, Bernd Schreckenberger³

¹ *Alfred Wegener Institute, Bremerhaven, Germany*

² *University of Bremen, Bremen, Germany*

³ *Federal Institute for Geosciences and Natural Resources, Hanover, Germany*

Abstract

The timing and geometry of the initial Gondwana break-up between Africa and East Antarctica is still poorly known due to missing information about the continent-ocean boundaries along the rifted margins. In this context, the Beira High off Central Mozambique forms a critical geological feature of uncertain crustal fabric. Based on new wide-angle seismic and potential field data across Beira High a P-wave velocity model, supported by amplitude and gravity modelling, provides constraints on the crustal composition of this area. In the Mozambique Basin mainly normal oceanic crust of 5.5-7 km thickness with velocities of 6.5-7.0 km/s in the lower crust is present. A sharp transition towards Beira High marks the continent-ocean boundary. Here the crust thickens to 23 km at maximum. A small velocity-depth gradient and a constant increase in velocity with basal velocities of maximum 7.0 km/s are in good agreement with typical velocities of continental crust and continental fragments. The density model indicates the existence of felsic material in greater depths and supports a fabric of stretched, but highly intruded continental crust below Beira High. A gradual de-

crease in crustal thickness characterizes the transition towards the Mozambican shelf area. Here, in the Zambezi Delta Depression 12 km of sediments cover the underlying 7 km thick crust. The presence of a high-velocity lower crustal body with velocities of 7.1-7.4 km/s indicates underplated, magmatic material in this part of the profile. However, the velocity structure in the shelf area allows no definite interpretation because of the experimental set-up. Thus, the crustal nature below the Zambezi Delta and consequently the landward position of the continent-ocean boundary remains unknown. The difference in stretching below the margins of Beira High suggests the presence of different thinning directions and a rift jump during the early rifting stage.

4.1 Introduction

The supercontinent Gondwana was an assembly of several landmasses consisting of a western (Africa and South America) and an eastern part (Antarctica, Madagascar, India, Sri Lanka, Australia and New Zealand). In the Early Jurassic rifting between the two parts initiated the dispersal of Gondwana (Cox, 1992; Eagles and König, 2008; Ghidella et al., 2007; Jokat et al., 2003). This process led to the formation of the first ocean basins between eastern Africa and Antarctica, the Mozambique and Somali Basin.

The reconstruction of the initial break-up was subject of numerous publications (Cox, 1992; Eagles and König, 2008; Jokat et al., 2003; Lawver et al., 1998; Leinweber and Jokat, 2012; Martin and Hartnady, 1986; Norton and Sclater, 1979; Reeves, 2014). For a consistent reconstruction it is essential to know the crustal types of the area and their present day location. In the Mozambique Basin, the reconstructions are well constrained for Late Cretaceous and Cenozoic times. However, for Early Cretaceous and Jurassic times seismic and magnetic constraints on the crustal fabric of the area are still sparse. Former deep seismic sounding surveys were limited to the use of sonobuoys, which provided only little crustal information. These wide-angle seismic data are difficult to interpret and are unsuitable for a reliable interpretation of the crustal composition. Thus, concrete evidence of the geometry and position of the continent-ocean boundary (COB) off Mozambique is lacking (Raillard, 1990; Watts, 2001). In this context, the Beira High is a critical geological feature to understand. The modelling of the geological boundaries with the help of gravity data (Watts, 2001) was a first attempt to constrain the deeper structure of this feature. Either Beira High is of oceanic origin and presents a magmatic structure, similar to Mozambique Ridge situated more to the south, or it is simply thickened oceanic crust (Watts, 2001). Conceivable is as well a continental fragment, which rifted away from the mainland

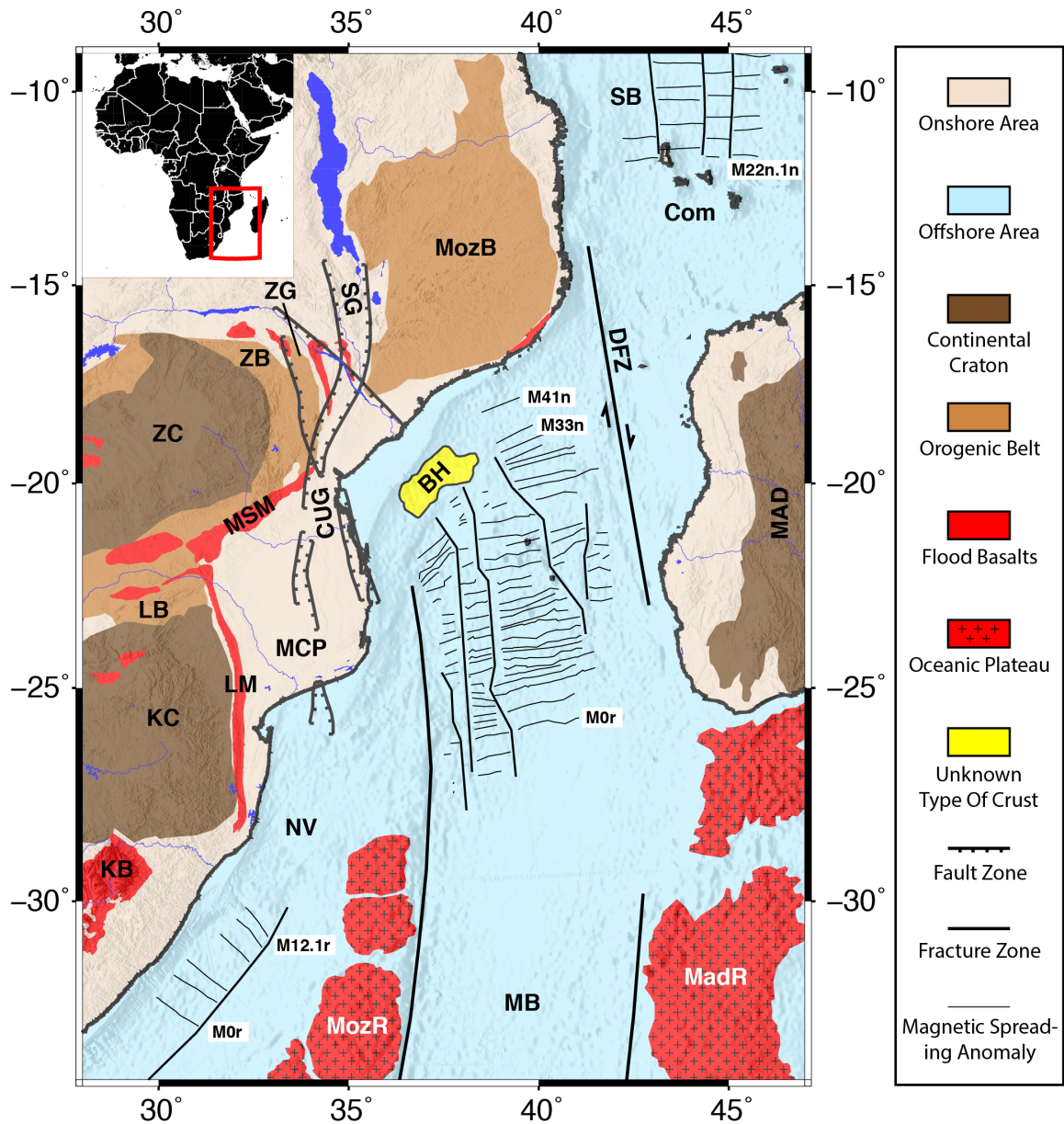


Figure 4.1: Tectonic overview of the Mozambique Channel. The major tectonic provinces and identified magnetic spreading anomalies are labelled. Abbreviations: BH: Beira High, Com: Comoros, CUG: Chissenga-Urema Graben System, DFZ: Davie Fracture Zone, KB: Karoo Basalts, KC: Kaapvaal Craton, LB: Limpopo Belt, LM: Lebombo Monocline, MAD: Madagascar, MadR: Madagascar Ridge, MB: Mozambique Basin, MCP: Mozambique Coastal Plains, MozB: Mozambique Belt, MozR: Mozambique Ridge, MSM: Mateke-Sabi Monocline, NV: Natal Valley, SB: Somali Basin, SG: Shire Graben, ZB: Zambezi Belt, ZC: Zimbabwe Craton, ZG: Zambezi Graben. Onshore the terrenes are digitized after [Leinweber et al. \(2013\)](#) and the fault systems after [De Buyl and Flores \(1986\)](#). The outline of Beira High is taken from [Mahanjane \(2012\)](#). For large igneous provinces the outline follows the 2500 m isoline of the bathymetry of the GEBCO_2014 grid (version 20150318; [Weatherall et al., 2015](#)). The locations of the magnetic spreading anomalies in the Somali Basin are taken from [Cochran \(1988\)](#), in the Mozambique Basin and northern Natal Valley from [Leinweber and Jokat \(2012\)](#), and in the southern Natal Valley from [Goodlad et al. \(1982\)](#).

along an extinct spreading centre (Mahanjane, 2012; Reeves, 2014). Furthermore, for a fundamental understanding of the driving forces of the break-up it is essential to know details on the exact timing for the first accretion of oceanic crust and the amount of volcanism related to the break-up.

Therefore, in 2014 the MOCOM-Cruise SO230 acquired first seismic refraction data across Beira High off Mozambique (Jokat, 2014). In this study, we present the results of the deep seismic experiment, supported by an amplitude modelling and a 2.5D gravity model. The main objectives are to examine the crustal structure and origin of Beira High and the adjacent shelf area. Additionally, the location of the COB and the existence of magmatic material along the margin are investigated. Implications for the tectonic evolution of the Mozambique Basin are discussed in combination with published magnetic data.

4.2 Geological setting

Today, SE-Africa and Madagascar are separated by the Mozambique Channel (Fig. 4.1). In its central area the Davie Fracture Zone divides the channel in two parts. The northern part extends to the Comoros and joins the Somali Basin. The southern part comprises the continental margin of Northern and Central Mozambique as well as Western Madagascar. The Mozambique Basin represents the southern border. Large coastal plains and broad shelf areas characterize most of these margins. In the southwestern part of the continental margin of Central Mozambique the Zambezi Delta serves as the estuary of the Zambezi River and forms the shelf area of the Zambezi Coast. Here, large sediment deposits accumulated in the Zambezi Delta Depression (ZDD). About 80 km off the coast, a distinct basement high, the Beira High, borders the ZDD to the south. It makes up half of the offshore part of the continental margin of Central Mozambique and forms a prominent gravity low (Fig. 4.2c, d).

The main tectonic units onshore SE-Africa consist of Archaean crust of the Kaapvaal Craton in the south-west and the Zimbabwe (Rhodesian) Craton in the west (Fig. 4.1). Around 2.6 Ga the collision of these two cratons caused the formation of the Limpopo Belt (Kröner, 1977). In the north-eastern part of Mozambique, the Lurio Belt is the result of the Kibaran Orogeny (assembly of Rodinia in the Mesoproterozoic) (Grantham et al., 2003). Today it acts as a prominent north-east to south-west trending boundary dividing the basement of northern Mozambique in two parts, which were affected by different metamorphic events in the Neoproterozoic (Ueda et al., 2012). Around 800-500 Ma the Pan-African Orogeny (assembly of Gondwana) led to the emplacement of the Zambezi Belt in the west and the Mozambique Belt in the north (Grantham

et al., 2003). Both belts are composed of Archaean material, reworked in Meso- to Neoproterozoic ages (Kröner, 1977).

At the initial stage of the Gondwana break-up massive magmatism accompanied the rifting and emplaced the Karoo flood basalts onshore southern Africa and the Ferrar flood basalts onshore East Antarctica (Cox, 1992; Encarnación et al., 1996; Jourdan et al., 2005). Along the southern margin of East Africa the Lebombo and Mateke-Sabi monoclines are the most prominent parts of this flood basalt province. They border the Mozambique Coastal Plains (MCP) to the west and north and were emplaced between 184 and 179 Ma (Duncan et al., 1997; Jourdan et al., 2005; Segev, 2001). In contrast, samples of the Ferrar flood basalts in East Antarctica are quite sparse. Nonetheless a similar age of 183 ± 1 Ma was identified (Duncan et al., 1997; Encarnación et al., 1996). This supports the idea of a combined history of both margins and the emplacement of the basalts caused by the same geological event (Duncan et al., 1997; Segev, 2001).

Since the Cretaceous two major fault systems developed onshore Central Mozambique (Flores, 1973). As part of the Zambezi Tectonic System (ZTS) the Zambezi Graben (Fig. 4.1, ZG) extends north-west to south-east and consists mainly of border faults (Flores, 1973; Fonseca et al., 2014; Salman and Abdula, 1995). The younger Inhaminga Tectonic System (ITS) comprises the north-south Shire Graben (Fig. 4.1, SG) and the north-east to south-west running Urema Graben, which crosscuts the ZTS. Afterwards the ITS turns north-south, joins the Chissenga Graben (Fig. 4.1, CUG) and becomes the southward expression of the East African Rift System (Flores, 1973; Fonseca et al., 2014; Mahanjane, 2012).

The offshore geophysical investigation of the Mozambique Channel started in the 70's with seismic and magnetic surveys by French expeditions (De Buyl and Flores, 1986; Flores, 1973; Heirtzler and Burroughs, 1971; Lafourcade, 1984; Lort et al., 1979; Mougenot et al., 1986; Virlogeux, 1987). A first compilation of the US and South African magnetic surveys was published by Simpson et al. (1979). Independently, Segoufin (1978) and Simpson et al. (1979) dated the earliest east-west trending spreading anomaly in the Mozambique Basin to chron M22. Based on these data a north-south oriented spreading between Africa and Antarctica was proposed. This data set was supplemented only in 2005 (AISTEK II-Cruise, RV Sonne; Jokat, 2005) where new scientific ship-towed magnetic and marine gravity data were systematically acquired in this region. The analysis of the new data (König and Jokat, 2010), in general, confirmed the existing model. However, the new data allowed the identification of magnetic spreading anomalies up to chron M26 in the northernmost survey area in the Mozambique Basin. Furthermore, evidence was found that the COB might be located much closer to the coastline than previously published. Thus, in 2007 the

4.2. GEOLOGICAL SETTING

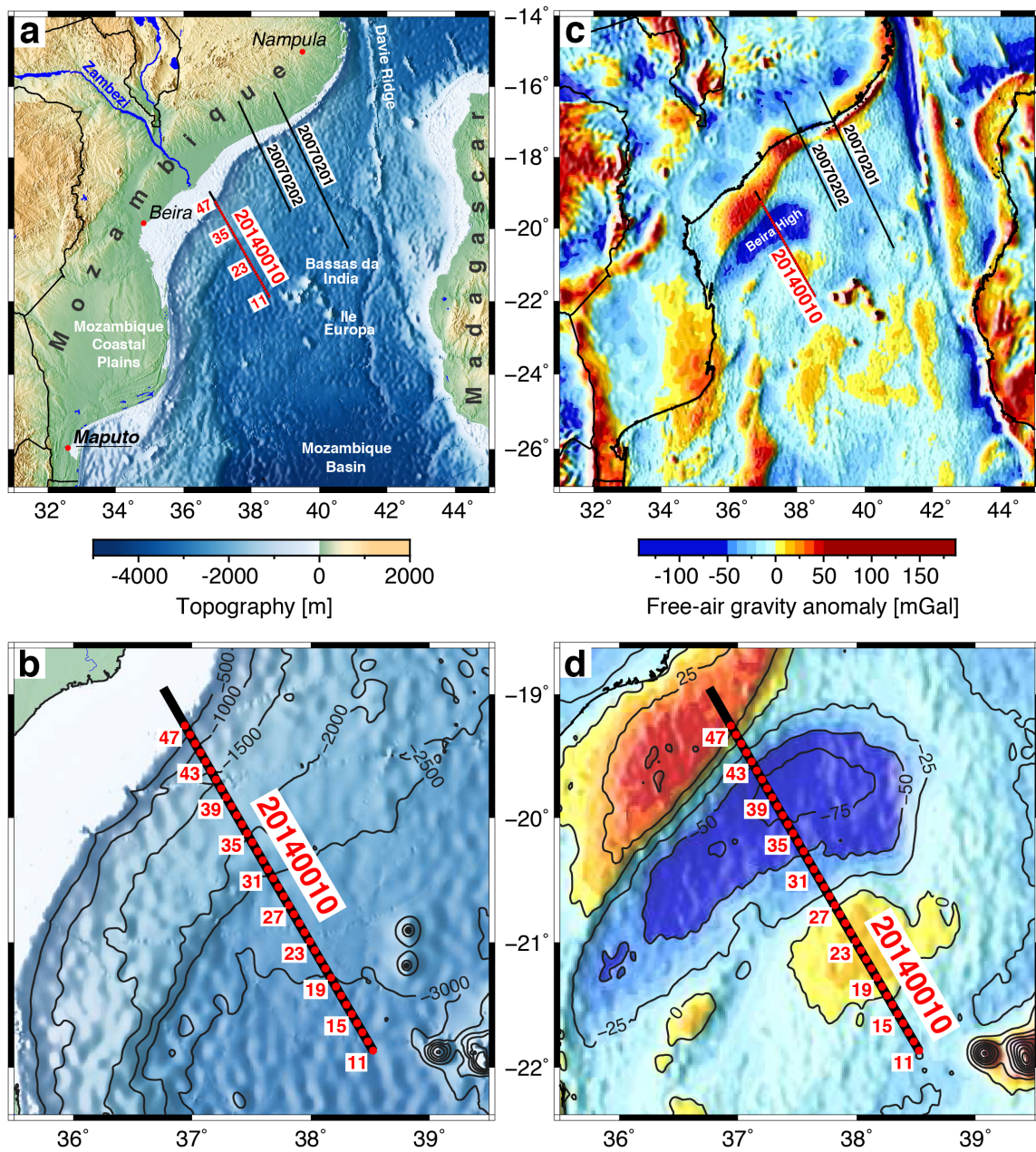


Figure 4.2: a) Bathymetric and topographic map of the survey area, based on GEBCO_2014 grid (version 20150318; [Weatherall et al., 2015](#)). Black lines show the locations of the seismic refraction profiles of the MOCOM-Cruise (profile 20140010) and the former MoBaMaSis-Cruise (profiles 20070201 and 20070202). Red dots represent the positions of the OBS/H stations used for this study. The red numbers indicate the numbering of the OBS/H stations along the profile. b) Enlargement of Figure 2a. c) Free-air gravity anomaly map of the survey area, based on [Sandwell et al. \(2014\)](#). d) Enlargement of Figure 2c.

MoBaMaSis expedition ([Reichert and Neben, 2008](#)) acquired new seismic reflection, seismic refraction and potential field data between the deep-sea abyssal plains and the Central Mozambican shelf. In the north-west, deep sounding seismic P-wave velocity

models revealed mainly normal to slightly thickened oceanic crust bordering close to the coast on continental crust (Leinweber et al., 2013). A high-velocity lower crustal body (HVLCB) underlying the lower crust extends from the coast at least 250 km southwards into the Mozambique Basin. The magnetic data showed that the oceanic crust was mainly formed during the Jurassic Quiet Period, which is almost void of any pronounced spreading anomalies. By means of extrapolating the modelled spreading velocities from the southern part of the survey, Leinweber and Jokat (2012) proposed chron M41n (166 Ma; Gradstein and Ogg, 2004) to be the oldest magnetic spreading anomaly close to the north-western Mozambican margin. For the south-western part the spreading anomalies have been interpreted to the south-eastern flank of Beira High and dated to chron M33n (Leinweber and Jokat, 2012). In agreement with other investigations (Cox, 1992; Mahanjane, 2012) the preferred break-up model by Leinweber and Jokat (2012) consists of two stages. During the first stage an anticlockwise rotation of Antarctica with respect to Africa occurred. The second stage began around M33n (159 Ma). Here, the spreading regime changed and Antarctica started to move southwards with respect to Africa (Leinweber and Jokat, 2012). However, Leinweber and Jokat (2012) disclose that the new age model might have deficits especially for the south-western part of the continental margin because of problems in the reconstruction.

Geophysical experiments targeting the deeper structure of Beira High are sparse. Most of the seismic data across Beira High are restricted to the sedimentary column in the region (De Buyl and Flores, 1986; Lort et al., 1979; Mahanjane, 2012; Nairn et al., 1991; Salazar et al., 2013). Since the Jurassic, Beira High seems to act as a barrier for sediment deposition and hydrocarbon traps in the ZDD and on Beira High are likely (Salazar et al., 2013). The structural grain of Beira High has a north-east to south-west orientation, more or less parallel to the continental margin of Central Mozambique. Based on seismic reflection data Mahanjane (2012) identified rift-grabens with an asymmetric half graben morphology on top of the south-eastern edge of Beira High. These are filled by layered successions below an identified break-up unconformity and, therefore, are interpreted as syn- and pre-rift units, leading to the assumption of a continental origin of Beira High (Mahanjane, 2012). Furthermore in the deepest part of the offshore ZDD high-amplitude and low-frequency reflectors were observed below the break-up unconformity and interpreted to present lava flows. Along one profile, Watts (2001) investigated by means of a 2D flexural backstripping and gravity modelling the crustal fabric from the continental margin across the Zambezi Coast and Beira High. The gravity high between Beira High and Mozambique (Fig. 4.2b) is interpreted to be the result of an edge effect caused by the juxtaposition of the thick, less dense continental and thin, denser oceanic crust (Watts, 2001). Therefore, the COB

is supposed to be located below the present-day coast and the Zambezi Delta is partly underlain by oceanic crust (Watts, 2001). Furthermore, Watts (2001) proposed that the oceanic crust extends further south below Beira High and that dense, magmatic material underplated the northern edge of Beira High.

4.3 Data acquisition and processing

From December 2013 to February 2014 the geophysical data were acquired during the cruise SO230 with the research vessel Sonne (Jokat, 2014). The investigations were performed in the scope of the MOCOM project (MOZambique COntinental Margin project) as cooperation between the AWI (Alfred Wegener Institute, Helmholtz Centre for Polar and Marine Research, Germany) and the BGR (Federal Institute for Geosciences and Natural Resources, Germany). During the cruise geophysical data were acquired along the central and northern Mozambican coast. In this study we will focus on deep seismic sounding and potential field data acquired across Beira High off the central coast of Mozambique (Fig. 4.2a).

The deep seismic sounding experiment was conducted along a seismic reflection profile (Castelino et al., 2015) acquired during the MoBaMaSis project in 2007 (Reichert and Neben, 2008). In total 37 seismic recording stations were deployed along the profile (20140010), consisting of 33 OBS (Ocean Bottom Seismometer, each equipped with a 3-component seismometer and a hydrophone) and 4 OBH (Ocean Bottom Hydrophones) with a spacing of approximately 9 km (Fig. 4.2b). The sampling rate of the data loggers was set to 250 Hz for MBS recorders (Marine Broadband Seismic Recorder) and 200 Hz for MLS/MTS recorders (Marine Longtime Recorder/Marine Tsunami Seismocoder). As seismic source 8 G-Guns with a total volume of 68 l ($\sim 4150 \text{ in}^3$) were towed in a 2×4 cluster at 10 m water depth. They were fired at 210 bar every full minute at a constant ship's speed of 5 kn, resulting in a shot spacing of $\sim 150 \text{ m}$.

All instruments were recovered. However, one OBS failed to record usable data. In general, the data quality is mainly good to excellent, whereas usually the hydrophone channel provided the best quality.

After data acquisition the raw data were converted to the SEG-Y format and corrected for the drift of the internal clock. To take account of the spatial drift of the instrument during its travel through the water column a relocalization was applied using direct arrivals for estimating the amount of drift.

Gravity data were continuously acquired throughout the entire cruise SO230 with a Bodenseewerke marine gravity meter KSS32M (S/N 22). Immediately before and after the cruise gravity measurements on land were carried out to tie the ship data

to the global reference system IGSN71 (International Gravity Standardization Net). The instrumental drift was quite low with 4×10^{-4} mGal per day. For calculating the free-air gravity anomaly, the Eötvös correction and instrumental drift correction were applied and, finally, the normal gravity (GRS 80) was subtracted (Jokat, 2014).

Magnetic data were continuously acquired with a SeaSpy gradient magnetometer array, consisting of two scalar Overhauser sensors and a vector magnetometer sensor (Magson). This longitudinal array was towed 750 m behind the ship, with 150 m spacing between the two Overhauser sensors and the Magson vector magnetometer in between. In general, a depth range of 20 to 60 m was used for towing the sensors. On-board processing of the magnetic data provided immediate quality control (Jokat, 2014).

4.4 Modelling

4.4.1 Wide-angle seismic study

To obtain a P-wave velocity model along the seismic refraction profile a forward modelling approach was used, utilizing the 2D ray tracing software RAYINVR (Zelt and Smith, 1992) with the graphical user interface PRay (Fromm, 2016). For set-up of the model geometry the locations of the relocated OBS were projected onto a straight model line. The starting and end point coincide with the position of the first and last shot point, respectively.

For picking of the P-waves the software ZP (Zelt, 2004) was used. In general, an automatic gain control (AGC) with an 1 s time window was applied to the data. A bandpass filter of 4-30 Hz was used for picking the arrivals of the sediment phases. In contrast, the arrivals of the crustal phases have lower frequencies. To account for these longer wavelengths and to avoid time errors a filter of 4-13.5 Hz was applied to pick the crustal arrivals. Because of its mostly excellent quality, the hydrophone channels were used for picking P-waves. Exceptions were only OBS stations 38, 39 and 44. Here, the vertical component of the seismometer was used. Depending on the signal to noise ratio a picking error ranging between 55 to 200 ms was assumed. Subsequently the picked phases were assigned to different structural layers, comprising water, sediment and crustal layers as well as the upper mantle (Table 4.1).

As a priori information the multibeam bathymetry data along the refraction profile were used to define the depth of the sea floor. In addition, the interpretation of the seismic reflection data (Castelino et al., 2015) was incorporated. These served as constraints for the depth of the sediment layers, basement and areas with low ray coverage

Layer	Phase	n of stations	n of picks	t_{as} [s]	t_{rms} [s]	χ^2
Refl. on sea floor	Pw	35	8040	0.126	0.139	1.997
Refr. in sed. layer 1	Ps1	10	194	0.113	0.061	0.364
Refl. at base of sed. layer 1	Ps1P	8	260	0.200	0.268	1.800
Refr. in sed. layer 2	Ps2	24	799	0.117	0.047	0.199
Refl. at base of sed. layer 2	Ps2P	25	819	0.196	0.182	0.942
Refr. in sed. layer 3	Ps3	34	3559	0.128	0.050	0.205
Refl. at base of sed. layer 3	Ps3P	33	2553	0.181	0.120	0.588
Refr. in sed. layer 4	Ps4	26	1073	0.150	0.076	0.484
Refl. at base of sed. layer 4	Ps4P	31	3039	0.181	0.144	0.771
Refr. in sed. layer 5	Ps5	32	2164	0.143	0.068	0.302
Refl. at base of sed. layer 5	Ps5P	31	3664	0.181	0.072	0.174
Refr. in sed. layer 6	Ps6	5	245	0.122	0.080	0.710
Refl. at base of sed. layer 6	Ps6P	5	400	0.168	0.135	0.679
Refr. in upper crust	Pc1	31	2314	0.131	0.066	0.283
Refl. at base of upper crust	Pc1P	29	1281	0.180	0.091	0.298
Refr. in middle crust at BH and trans. part	Pc2	18	8445	0.162	0.127	0.697
Refl. at base of middle crust at BH and trans. part	Pc2P	11	1041	0.182	0.226	1.742
Refr. in lower crust of oceanic part	Pc2oc	17	4315	0.148	0.078	0.334
Refr. in lower crust BH	Pc3	4	69	0.182	0.217	1.546
Refr. in high-velocity body	PcHVB	9	743	0.156	0.141	0.820
Refl. at the Moho	PmP	34	9845	0.168	0.186	1.431
Refr. in upper mantle	Pn	18	1445	0.167	0.187	1.379
Total	All	35	56297	0.156	0.135	0.961

Table 4.1: Statistics of picked phases. The columns contain the labels of the picked phases, the number of stations, for which the according phase was identified (n of stations), the number of observations (n of picks), the assigned average pick uncertainty (t_{as}), the root mean square of the travel time residual (t_{rms}) and the normalized chi-squared value (χ^2).

in the shallow part of the model. Therefore, the RMS-velocities of the sediment layers, derived from the seismic reflection data analysis (Castelino et al., 2015), were converted to interval velocities. A comparison with the velocities obtained by the refracted arrivals shows a good agreement. Consequently, the interval velocities were used for the time-depth conversion of the seismic reflection data. During the following P-wave velocity modelling for crustal phases across Beira High and the adjacent abyssal plains, the calculated depths of the sediment layers were only slightly changed. Because of the great depth of the lowermost sediment layers in the ZDD, no reliable velocity and depth information were available from the seismic reflection data and couldn't be used

as constraints for the geometry of the deeper sediment layers.

Following a modelling strategy for passive margins (Zelt, 1999) a layer-stripping approach was used for modelling the sediment layers. Afterwards, by a simultaneous adjustment of depth and velocities the crustal layers and the upper mantle were modelled (Zelt, 1999). To achieve the final velocity model the inversion method of Zelt and Smith (1992) was used to derive the best fitting velocity and depth values of each layer. Figs. 4.3 to 4.5 show data examples of the OBS stations 21, 39 and 46 with the phase identification and traced rays. The direct wave, representing the reflection at the sea floor is marked as Pw. The refractions in the sediment layers are labelled as Ps#, e.g. Ps1 is the refracted phase in sediment layer 1. Consequently the reflections at the base of the respective sediment layer are labelled as Ps#P. Waves that are refracted in the crustal layers are marked as Pc#. Pc#P represents the corresponding reflections at their base. The refracted waves to model the lower crust in the oceanic domain are marked as Pc2oc. Pc3 represents the refracted phase in the lower crust at Beira High and in the shelf area. PcHVB is the refracted wave for an identified HVLCB in the transitional domain. The abbreviation PmP marks the Moho reflection. Refracted waves penetrating the upper mantle are labelled as Pn.

In general, almost no S-wave energy is observed in the presented OBS/H data, which could be used to calculate the v_p/v_s ratio. Usually at hard reflectors as the sediment-crust boundary a partly conversion of the P-wave energy to recordable S-waves is likely. The absence of S-waves in our data might be a consequence of the high velocities of the lowermost sediments just above the acoustic basement, which cause a smaller impedance contrast to the underlying upper crust. Consequently, the transmitted and reflected S-waves are characterized by low amplitudes and are masked by the P-waves.

4.4.2 Amplitude modelling

Because of a low ray coverage with diving waves in the lower crust of Beira High (Figs. 4.6 and 4.7), the velocity-depth model is poorly constrained in this area. Thus, we conducted an amplitude modelling using Moho reflections to adjust the velocity gradients for the lower crust.

The applied ray tracing method is a high-frequency approximation of the wave equation (Zelt and Smith, 1992; Jokat and Schmidt-Aursch, 2007). However, in areas with pronounced changes in topography (e.g. at edges) no rays can be traced. Here, the usage of the finite difference (FD) method is favourable. This uses a discretised model, where the wave equation gets numerically approximated by differential operators (Bohlen, 1998; Schmidt-Aursch, 2003). As a consequence, at edges evolving

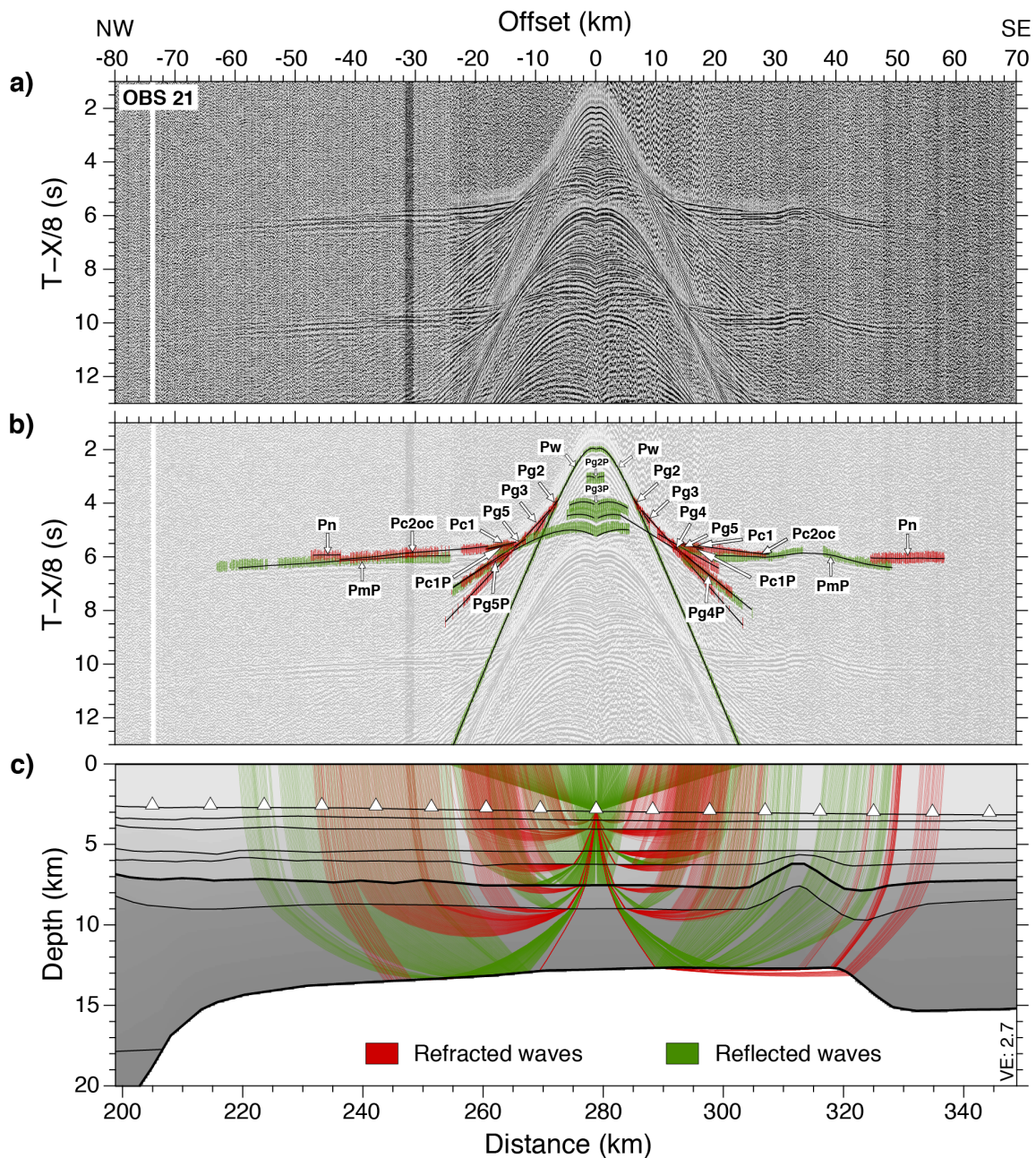


Figure 4.3: Data example of station 21. a) Seismic section of OBS 21 (hydrophone channel) with a bandpass filter of 4-13.5 Hz. A reduction velocity of 8 km/s is applied to the travel time. b) Picked phases are shown as error bars and labelled with corresponding identification number. Refracted arrivals are plotted in red, reflected arrivals in green. Modelled arrivals are displayed as black lines. c) Modelled ray paths for picks shown in b).

diffracted phases can be calculated and displayed. Therefore, synthetic seismograms based on a FD code were calculated for a few selected stations.

For calculating the synthetic seismograms the FD program SOFI2D (Bohlen et al., 2015a) was used, which is able to calculate the propagation of P- and SV-waves in an

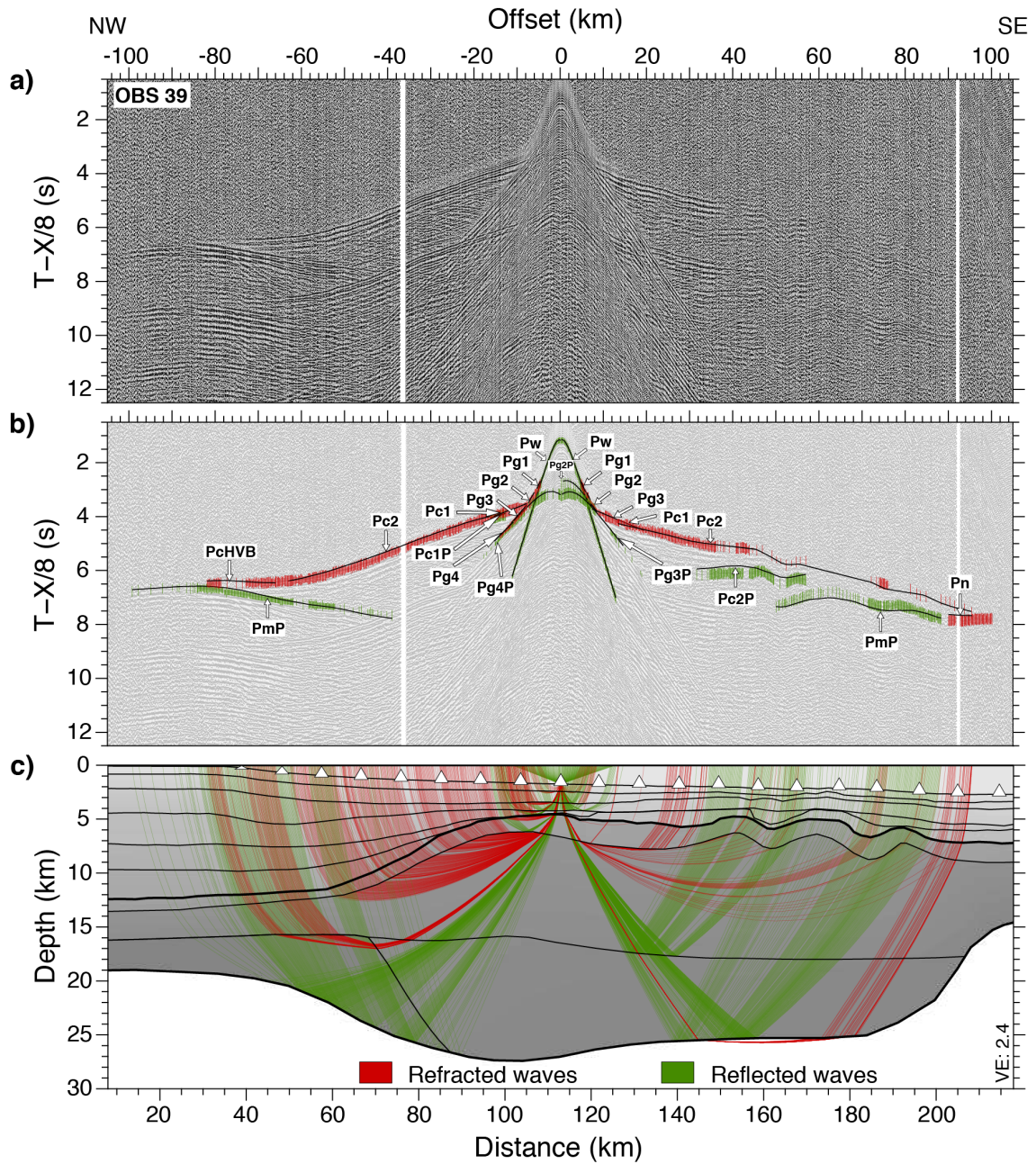


Figure 4.4: Data example of station 39. a) Seismic section of OBS 39 (vertical seismometer component) with a bandpass filter of 4-13.5 Hz. A reduction velocity of 8 km/s is applied to the travel time. b) Picked phases are shown as error bars and labelled with corresponding identification number. Refracted arrivals are plotted in red, reflected arrivals in green. Modelled arrivals are displayed as black lines. c) Modelled ray paths for picks shown in b).

inhomogeneous viscoelastic 2D medium. Additionally, at each boundary the acoustic impedance is calculated by incorporating velocity and density contrasts. Furthermore, the calculation of the whole synthetic wave field allows an improved phase identification by comparing it to the observed data. To obtain stable results with an accept-

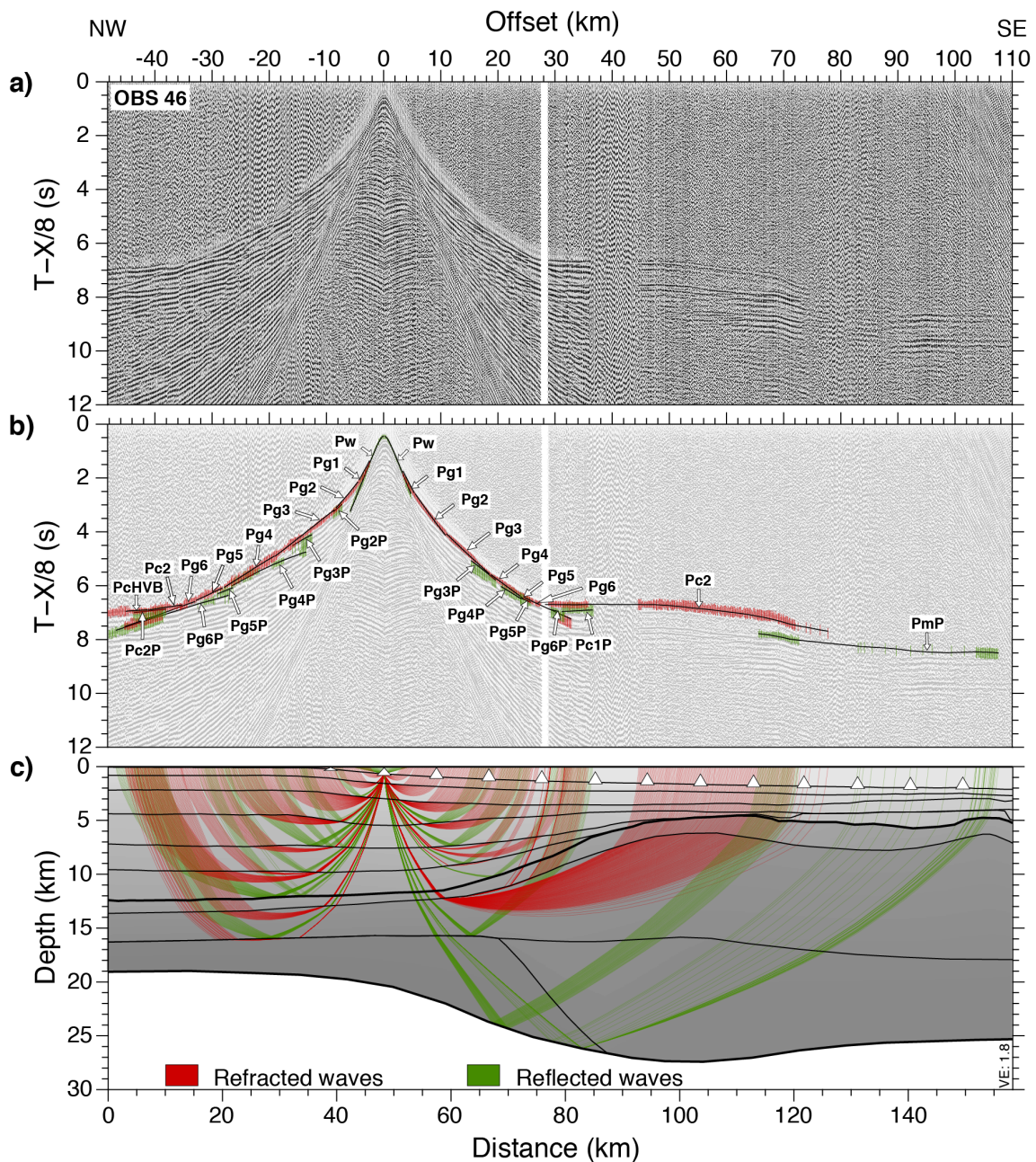


Figure 4.5: Data example of station 46. a) Seismic section of OBS 46 (hydrophone channel) with a bandpass filter of 4-13.5 Hz. A reduction velocity of 8 km/s is applied to the travel time. b) Picked phases are shown as error bars and labelled with corresponding identification number. Refracted arrivals are plotted in red, reflected arrivals in green. Modelled arrivals are displayed as black lines. c) Modelled ray paths for picks shown in b).

able computing time the method of a Standard Staggered Grid (SSG) is incorporated. Therefore, the FD operators are shifted by half the size of a cell, which allows a coarser sampling of the model (Bohlen, 1998). By grid decomposition and parallelization of calculations (MPI) the computing time is reduced (Bohlen, 2002).

For this study the model (Fig. 4.8) was sampled with a grid cell size of 25 m totalling to a grid size of 15000 x 1400 cells. The seismograms were calculated for 30 s travel time. Receivers were equally spaced every 150 m and a 4th order FD operator was used. To ensure the stability of the FD code a sampling interval of 1 ms was necessary. Basically the P-wave velocity model of the ray tracing model served as input data. A constant division of the P-wave velocity with $\sqrt{3}$ was used to calculate the S-wave velocities. The simple conversion of P-wave velocities to densities according to Barton's rule (Barton, 1986) was used to determine the densities for the calculation of the impedance contrast. The intrinsic attenuation (quality factors for P- and S-waves) needed for a viscoelastic modelling were calculated according to Brocher (2008). As upper boundary conditions a plane stress free surface was applied at the top of the model. A convolutional perfectly matched layer (CPML) terminates the model to reduce reflections from the outer boundaries (Bohlen et al., 2015b). As source signal a Ricker wavelet with a centre frequency of 5 Hz was used, which represents a reasonable compromise between resolution and computing time. In general, for the comparison between the synthetic and observed data the hydrophone component was examined. The synthetic seismograms were laterally filtered, scaled and afterwards normalized to their maximum amplitude. For displaying, to suppress reverberations in the seismogram the zero crossing was slightly shifted to negative values and the clip was adjusted.

Bohlen (1998) has shown that for a viscoelastic modelling after lateral filtering, scaling and normalization wave fields generated by a 2D line source are similar to wave fields with a 3D point source. Therefore, the trend of their maximum amplitudes is as well similar. Based on this fact as well as restricted computing time and only 2D information about the P-wave velocities a 2D FD modelling was considered as sufficient.

Mainly the Moho reflection (PmP) was used for comparison. For most of the stations this phase can be identified for large offsets and shows variations in the recorded maximum amplitudes. Additionally, for Beira High the base of the middle crust (Pc2P) was investigated. Prior to amplitude modelling, the first calculated synthetic seismograms provided additional support for the phase identification of the Moho reflection. This resulted in an adjustment of the respective picks and allowed us to better constrain the Moho topography. Subsequently, the improved model was used for the following amplitude modelling.

Different velocity gradients for the lower crust were tested. For all models the velocity at the upper boundary of the lower crust is the same, but they differ in their velocities at the Moho. To ensure that all tested models still explain the picks, the Moho depth was adjusted. However, the topography of the Moho was kept fixed. According to

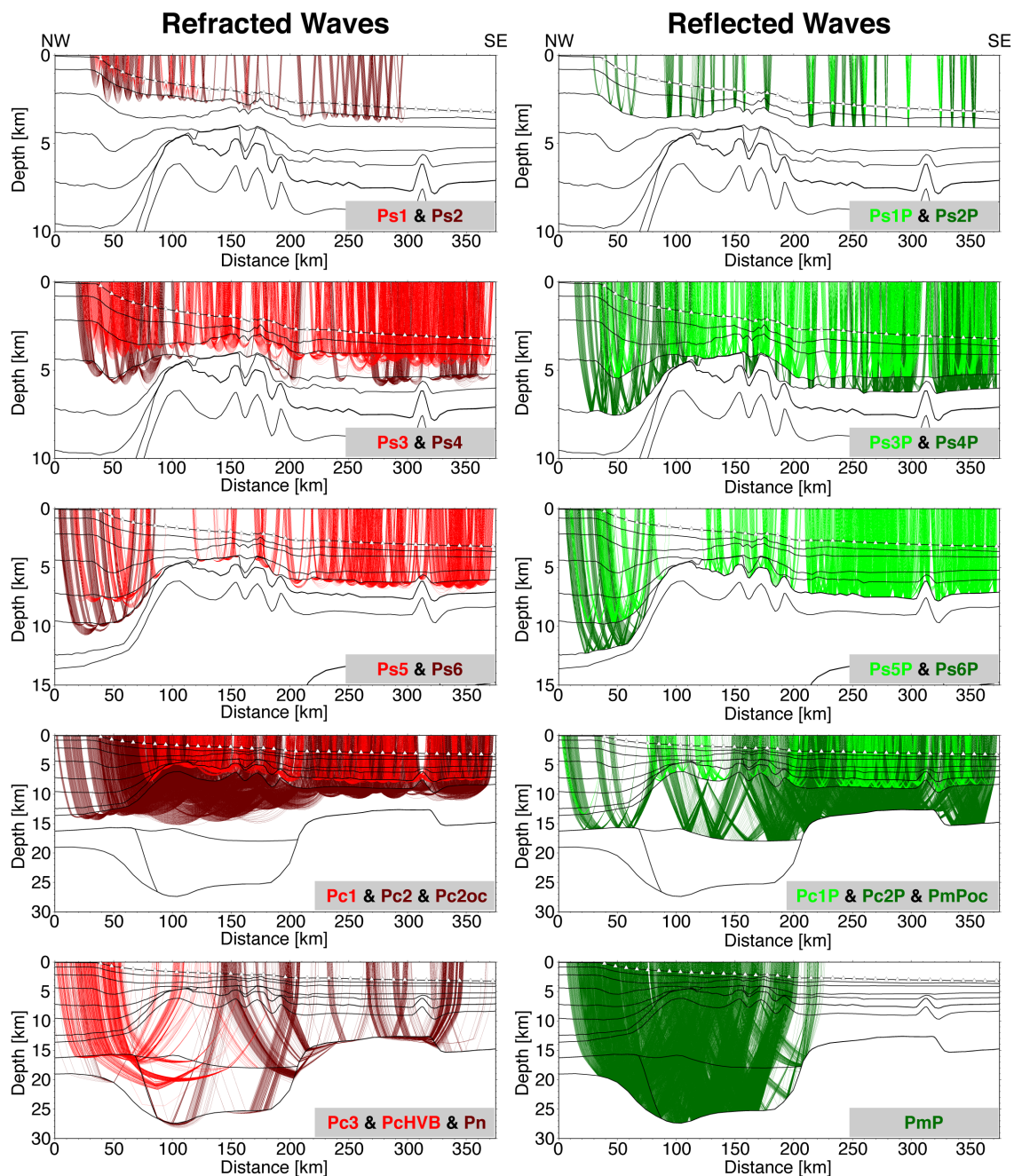


Figure 4.6: Ray coverage of the P-wave velocity model by refracted and reflected waves for each layer.

their respective conversion rule, the other parameters (S-wave velocity, density, quality factors for P- and S-waves) were adjusted as well. Additionally, a model with a separate HVLCB below Beira High and models with different basal velocities for the HVLCB in the shelf area were tested. To compare the trends of the amplitudes at first the maximum of a specific phase (e.g. PmP) was picked in the observed data and for each model in the synthetic data. Difficulties partly occurred in the observed data

in case of a poor signal to noise ratio. For picking the synthetic data, areas with many crossing phases were challenging. Subsequently, the amplitudes were exported and plotted versus the offset. The amplitudes are calculated as the envelope of the first arrival for a certain time window. However, the selected Ricker wavelet and a centre frequency of 5 Hz for the calculation of the synthetic seismograms represent only an approximation to the signal of the observed data. Minor differences are visible in the shape of the signals. Therefore, a short time window of 20 ms across the picked maximum of the first arrival was used for the calculation of the envelope. This ensures the comparability between the amplitudes of the observed and synthetic data, but results in a higher scattering of the amplitudes of the observed data. Mostly this scattering is caused by noise. Therefore, the median of the maximal amplitudes was calculated and plotted. As a result of missing noise in the synthetic data and a different power of the synthetic source the amplitudes are lower compared to the observed data. To allow an easier comparison the amplitudes of the synthetic data were multiplied by a constant value. The locations of the maxima and minima as well as the general decay of the amplitudes (Fig. 4.9d) were used as criteria for the comparison of the trends. Maxima and minima in the synthetic data are caused either by topography or by crossing and joining arrivals of other phases. For the observed data strong noise can cause local maxima, too. Clearly visible is a shift of the maxima for the different models in the synthetic data (Fig. 4.9d). This is caused by the different velocity gradients in the lower crust, resulting in a different moveout of the PmP phase and, consequently, a different offset for crossing and joining phases.

As last step the final density model derived from gravity modelling was used as input density model for the calculation of the synthetic seismograms to verify the results of the amplitude modelling.

4.4.3 Gravity modelling

A 2.5D gravity modelling was performed to confirm the velocity model and identify problematic areas. The interactive gravity and magnetic modelling software IGMAS+ (Götze, 2007; Götze and Lahmeyer, 1988; Schmidt et al., 2007) was used to calculate a density model. The starting model was defined on a series of parallel vertical cross sections, which got connected by triangulation. Subsequently the gravitational response of the generated polyhedrons was calculated.

Within the continent-ocean transition zone with pronounced topographical changes, strong variations in water depths, sediment coverage as well as layer thicknesses, the vertical density changes cannot be sufficiently modelled by a single density value for

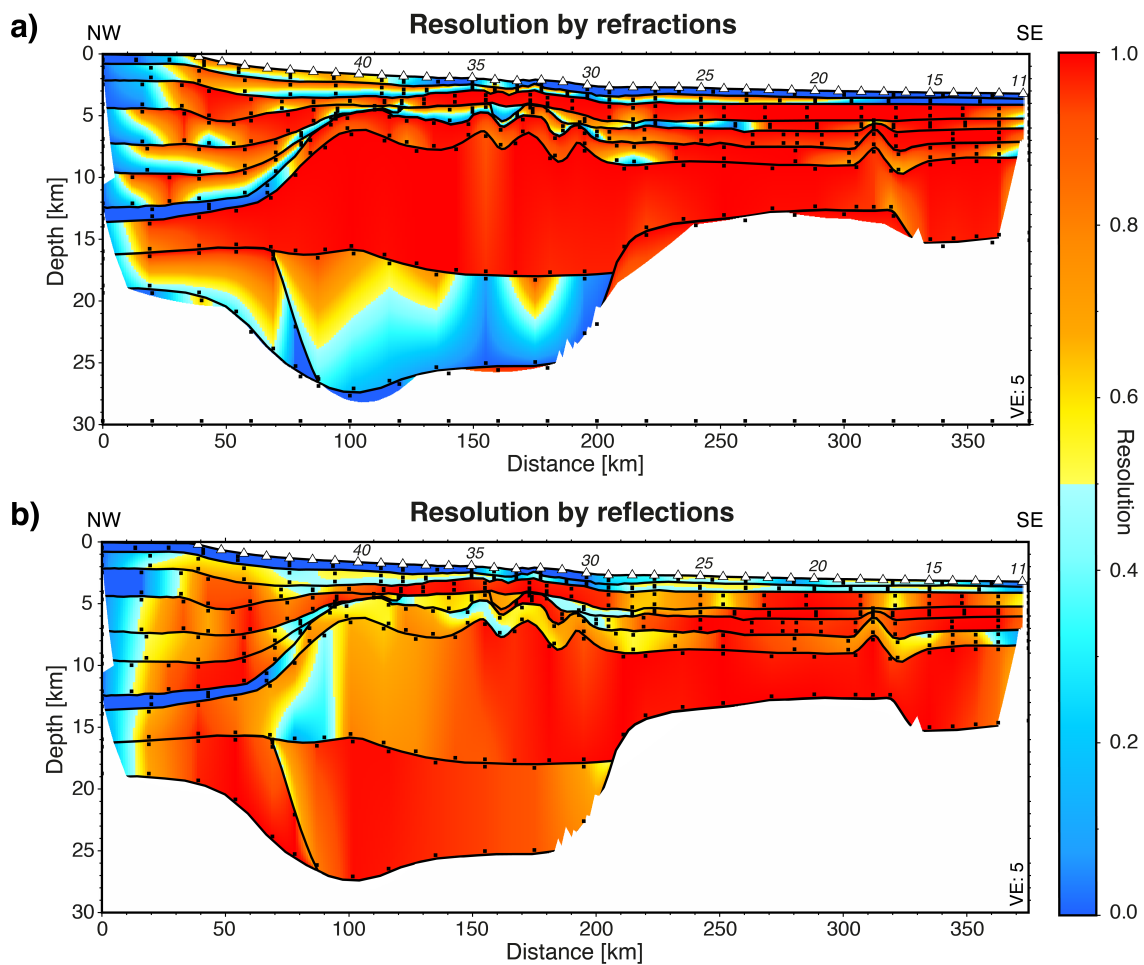


Figure 4.7: Resolution for profile AWI-20140010, represented by the diagonal elements of the resolution matrix. a) Resolution of velocity nodes by refracted waves. Black dots mark the positions of the nodes, which were used for the calculation of the resolution. b) Resolution of the depth nodes by reflected waves.

certain blocks. To account for vertical density gradients within a layer, IGMAS+ provides the possibility to voxelize the model in all dimensions and add a density function to the voxels. This allows the use of density gradients for each layer. Based on the point mass algorithm, the gravitational effect of each voxel is approximated by a sphere with the identical volume to the voxels volume. The resulting gravitational response is added to the model response.

The identified layer boundaries of the wide-angle seismic model served as input for the gravity model. For sediments the velocities were converted into densities according to Gardner (1974). Crustal velocities were converted according to Christensen and Mooney (1995). To calculate the vertical density gradients for each velocity layer, the density model was gridded in x- and y-direction in 500 m steps and in z-direction in 250 m steps. To account for lateral velocity variations and gradients in a single layer,

some areas were divided into separate parts to enable a more realistic gravity modelling. The lateral boundaries of the model were extended in SW-NE direction by 1000 km to avoid edge effects. For 200 km of these, the approximate shape and extent of Beira High and the surrounding layers were defined to account for the long wavelength gravitational effect of Beira High in its strike direction. Furthermore, to account for the gravitational effect of the continental crust below the Mozambican mainland, the modelling was extended in NW-SE direction by about 150 km. Therefore, available onshore geological information like sediment coverage and crustal thickness were incorporated for a reasonable extrapolation of our model (Leinweber et al., 2013; Nairn et al., 1991; Salman and Abdula, 1995; van der Meijde et al., 2015; Watts, 2001). The additional free-air gravity data were extracted from the satellite derived free-air gravity anomaly map of Sandwell et al. (2014). After some slight adjustments they were merged with the shipborne data. Subsequently a sufficient correlation between observed and calculated free-air gravity anomaly was achieved by a slight adjustment of the assigned densities. As last possibility the layer boundaries were adjusted. To derive the final density model the inversion method (Sæther, 1997) provided by IGMAS+ was used to achieve the best fitting densities of each layer.

4.4.4 Uncertainty and resolution of the velocity and density model

In total, 56297 picks were used for modelling the entire line (Table 4.1). To evaluate the quality of the final P-wave velocity model the χ^2 -errors were calculated (Zelt and Smith, 1992). For most identified phases of this study the assigned pick uncertainty (t_{as}) is slightly greater than the travel time residual (t_{rms}), resulting in χ^2 values < 1 , indicating a partly overestimation of the assigned pick uncertainties. However, for the entire model t_{rms} is 0.135 s and t_{as} is 0.156 s. This results in a $\chi^2=0.96$ that is close to the optimal value of 1 and shows that the measured travel times are well reproduced by the modelled ones.

The estimation of velocity and depth uncertainties of the model follows the method described by Schlindwein and Jokat (1999). Therefore, single velocity and boundary knots were perturbed until the calculated travel times are not anymore within the assigned uncertainty range of the observed data. The velocity uncertainties in the sediment layers range from ± 0.05 km/s for the uppermost ones to ± 0.2 km/s for the lowermost sediment layer (Table 4.2). In general, the velocities in the crustal layers have an uncertainty of ± 0.1 km/s. Because of the sparse number of diving waves in the lower crust of Beira High (Fig. 4.6) velocities vary here up to ± 0.2 km/s. The

depth uncertainties range from ± 0.1 to ± 0.3 km for the sediment layers. For most of the crustal layers the boundaries can be varied by ± 0.3 km. At Beira High the base of the middle crust has an uncertainty of ± 0.5 to ± 1.0 km because of a low impedance contrast. The Moho depth in the Mozambique Basin can be varied by ± 0.5 km and at Beira High and in the shelf area by ± 1.0 km.

The inversion method of [Zelt and Smith \(1992\)](#) was used to calculate the resolution of the final P-wave velocity model. [Fig. 4.7](#) shows the diagonal elements of the resolution matrix for refracted and reflected waves and illustrates how well the velocities and boundaries nodes in our model are resolved. While refracted phases are used for calculating the velocity structure of the model, their resolution is plotted separately. About every 20 km, the resolution of the velocity nodes ([Fig. 4.7a](#)) was calculated for each layer separately. Reflected arrivals provide good constraints on the topography of the layer boundaries. Their resolution was calculated for depth nodes at the same positions as the velocity nodes ([Fig. 4.7b](#)). An optimal resolution is achieved in case of a resolution matrix value of 1, however a value greater than 0.5 depicts a sufficient resolution of the respective model parameter ([Zelt, 1999](#)). Based on a good ray coverage ([Fig. 4.6](#)), the model has a good resolution. The two uppermost sediment layers are less well resolved due to partly missing or unclear arrivals. In these areas especially the incorporation of the seismic reflection data served as a good constraint. To overcome the low resolution of the velocities in the lower crust of Beira High, the amplitude modelling revealed important information.

In general, the density model is consistent with the P-wave velocity model. Furthermore, there is a good agreement between calculated and observed free-air gravity anomaly. The standard deviation of 4 mGal is still within the uncertainty of the gravity modelling method (± 10 mGal, [Ljones et al., 2004](#)). There is a maximal deviation of 7 mGal at km 105. This residual can be attributed to the 3D effect of the Beira High and the HVLCB.

4.5 Results and Interpretation

4.5.1 Wide-angle seismic study

The final P-wave velocity model of the refraction profile AWI-20140010 is shown in [Fig. 4.8](#). For the following description and interpretation of the results, the model is divided into three parts, based on the varying P-wave velocity structure and crustal thickness along the profile. Subsequently, these parts are referred to as the Mozambique Basin, the Beira High, and the Shelf area.

4. THE CRUSTAL STRUCTURE OF BEIRA HIGH

Layer	Type	P-wave velocity [km/s]	Density range [g/cm ³]	Upper bound. uncert. [km]	Velocity uncertainty [km/s]
Water Layer	Water	1.5	1.03	±0.0	±0.01
SEDIMENT 1	Sed.				
All		1.7 - 2.1	2.02 - 2.09	±0.1	±0.05
SEDIMENT 2	Sed.				
Shelf area		2.4 - 2.8	2.17 - 2.26	±0.2	±0.1
Beira High		2.35 - 2.6	2.14 - 2.19	±0.2	±0.1
Moz. Basin		2.15 - 2.35	2.12 - 2.14	±0.2	±0.1
SEDIMENT 3	Sed.				
Shelf area		3.1 - 3.55	2.30 - 2.40	±0.15	±0.1
Beira High		2.7 - 3.2	2.23 - 2.30	±0.15	±0.1
Moz. Basin		2.4 - 2.75	2.17 - 2.23	±0.15	±0.1
SEDIMENT 4	Sed.				
Shelf area		3.5 - 4.0	2.35 - 2.48	±0.15	±0.1
Beira High		3.2 - 3.4	2.30 - 2.35	±0.15	±0.1
Moz. Basin		3.15 - 3.3	2.30 - 2.33	±0.15	±0.1
SEDIMENT 5	Sed.				
Shelf area		4.3 - 4.6	2.52 - 2.56	±0.2	±0.1
Beira High		3.45 - 3.6	2.40 - 2.43	±0.2	±0.1
Moz. Basin		3.6 - 4.1	2.43 - 2.49	±0.2	±0.1
SEDIMENT 6	Sed.				
Shelf area		4.8 - 5.1	2.63 - 2.67	±0.3	±0.2
Beira High		3.5 - 3.6	2.40 - 2.43	±0.2	±0.1
UPPER CRUST					
Shelf area	Trans.?	5.5 - 5.7	2.67 - 2.72	±0.3	±0.3
Beira High	Cont.	5.4 - 5.8	2.64 - 2.67	±0.2	±0.1
Moz. Basin	Oc.	5.6 - 5.8	2.66 - 2.70	±0.2	±0.1
MIDDLE CRUST					
BH NW-part	Cont.	6.3 - 6.7	2.76 - 2.85	±0.3	±0.1
BH SE-part	Cont.	6.3 - 6.8	2.83 - 2.96	±0.3	±0.1
LOWER CRUST					
Shelf area	Trans.?	6.3 - 6.7	2.86 - 2.94	±0.5	±0.1
BH NW-part	Cont.	6.8 - 6.9	2.88 - 2.94	±1.0	±0.2
BH SE-part	Cont.	6.9 - 7.0	2.98 - 3.04	±0.5	±0.2
Moz. Basin	Oc.	6.5 - 7.0	2.89 - 3.00	±0.3	±0.1
HVLCB	Und./serp.	7.1 - 7.4	3.10 - 3.16	±0.5	±0.1
MANTLE	Mantle				
Shelf area		8.1 - 8.3	3.36 - 3.40	±1.0	±0.2
Beira High		8.0 - 8.2	3.33 - 3.38	±1.0	±0.2
Moz. Basin		7.9 - 8.1	3.33 - 3.38	±0.5	±0.2

Table 4.2: Layer parameters and according uncertainties. P-wave velocities and densities partly vary within one respective layer due to differences in geological setting and burial.

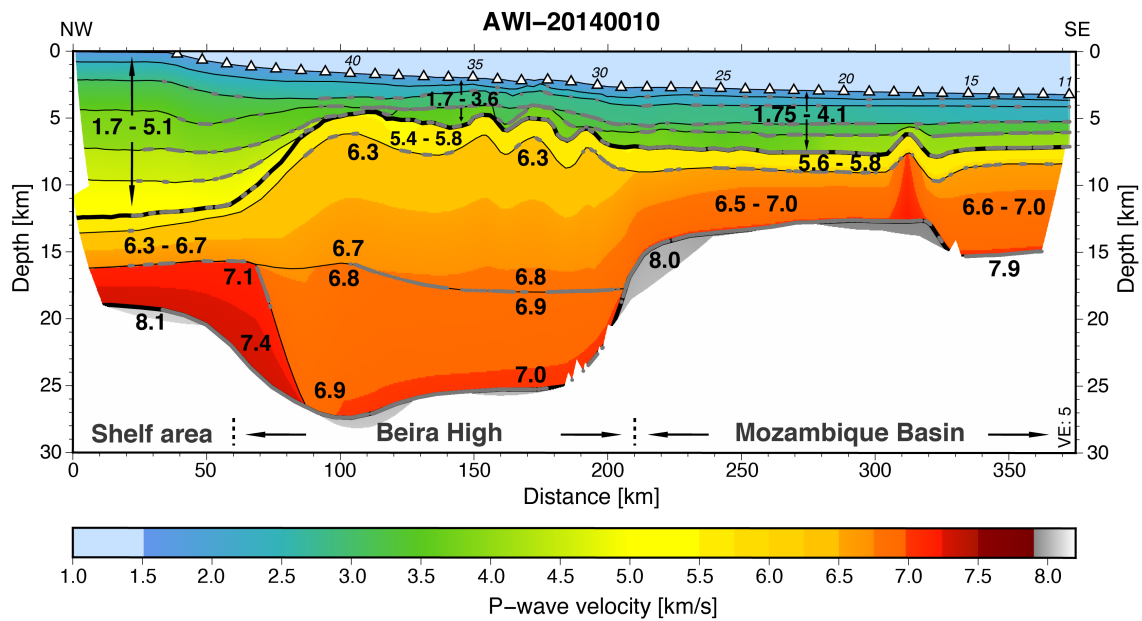


Figure 4.8: P-wave velocity model of AWI-20140010. Model is only plotted for areas covered by ray paths. Parts of layer boundaries constrained by wide-angle reflections are marked as thick grey line. The numbers indicate P-wave velocities in km/s (see Table 4.2 for details).

Mozambique Basin (km 210 – 375)

This part of the profile is covered by 4 km of sediments consisting of five layers with varying velocities (Fig. 4.8, 1.75-4.1 km/s). In the deepest sediment layer the velocities laterally decrease from the SE with velocities of 3.9-4.1 km/s towards the Beira High (km 210-270) with velocities of 3.6-3.8 km/s. At a depth of 7 km a strong reflection marks the top of the acoustic basement. In general, the basement topography is very smooth. The mean crustal thickness is about 6-7 km. The crust can be divided in a 1.5 km thick upper crust with velocities of 5.6-5.8 km/s and a lower crust with a thickness of 4.5-6 km and velocities of 6.5-7.0 km/s.

To confirm these lower crustal velocities an amplitude modelling was applied for selected stations. Fig. 4.9 shows the results for station 22. In this area the Moho is quite flat (Fig. 4.9a). Hence, there are only minor topographic effects, which could influence variations of the seismic amplitudes. Reflections from the Moho as well as refractions from the upper mantle have an excellent signal to noise ratio. The upper mantle velocity in this part of the model is 8.0 km/s. In the observed data the PmP reflection is visible about 40 km to both sides of the station (Fig. 4.9b). The median of the maximal amplitudes clearly shows varying amplitudes with local maxima at -25 to -35 km and 25 to 40 km (Fig. 4.9d). For negative offsets a good correlation between observed and synthetic data (Fig. 4.9c) is visible for the 6.8- and 7.0-model. Here the

location of the maximum at -27 km and the trend for greater offsets coincide quite well. The 7.2- and 7.4-model show a different trend and offset for the maximum. For positive offsets the location of the local maximum fit best for the 7.0- and 7.2-models. However, the slopes of the maximum show the best correlation for the 7.0-model. The 6.8-model shows a very similar trend, but the maximum is clearly off. For the 7.4-model neither the general trend nor the location of the maximum fits. Based on these results a velocity contrast of 7.0 to 8.0 km/s at the Moho is likely (Fig. 4.9d).

A buried seamount is located at km 310. Further south-east, in close vicinity to the volcanic area of Bassas da India, the crust thickens to 8 km. For this area, the amplitude modelling revealed as well the best fit for the 7.0-model.

Beira High (km 60 – 210)

Across the Beira High the sediments are 2.5-4 km thick and their velocities range between 1.7-3.6 km/s. A pronounced basement topography with deep half-graben structures led to a partly challenging phase identification for the lower sediment units and the upper crust. To overcome difficulties in the assignment of refracted and reflected arrivals of the sediment layers, the incorporation of the layer boundaries based on the reflection seismic data served as a good constraint. In comparison to the profile section in the Mozambique Basin the basement at Beira High is elevated and located in a depth range of 4.5-6.5 km. The crust has a thickness of 20-23 km and consists of 3 different layers. In plane sections the upper crust is about 2 km thick and in half-grabens up to 3.5 km. The velocities range between 5.4 to 5.8 km/s. Based on a good ray coverage of refractions (Fig. 4.6) the middle crust velocities were fixed to 6.3-6.7 km/s in the NW-part. Slightly higher velocities of 6.3-6.8 km/s were modelled in the SE-part. Here, the maximum thickness of the middle crust is about 12 km. The boundary to the lower crust is constrained by a low amplitude reflection, suggesting a small velocity and density contrast.

Because of the low ray coverage with diving waves in the lower crust its velocity gradients are not well constrained (Fig. 4.6). However, the Moho topography is based on several reflections and the mantle velocity on a sparse number of refractions. This allows the application of the amplitude modelling to several stations. The results for station 37 are shown in Fig. 4.10. The station is located at the centre of Beira High and provides information for a wide area of the lower crust (Fig. 4.10a). PmP reflections are visible for -30 to -120 km and 35 to 70 km offset (Fig. 4.10b). Additionally, a second reflection of the PmP is visible in the observed and even better in the synthetic data joining the first PmP reflection at -95 km offset (Fig. 4.10c). For offsets -30 to -85 km a good correlation to the observed data is visible in the 6.8-, 6.9- and 7.1-models

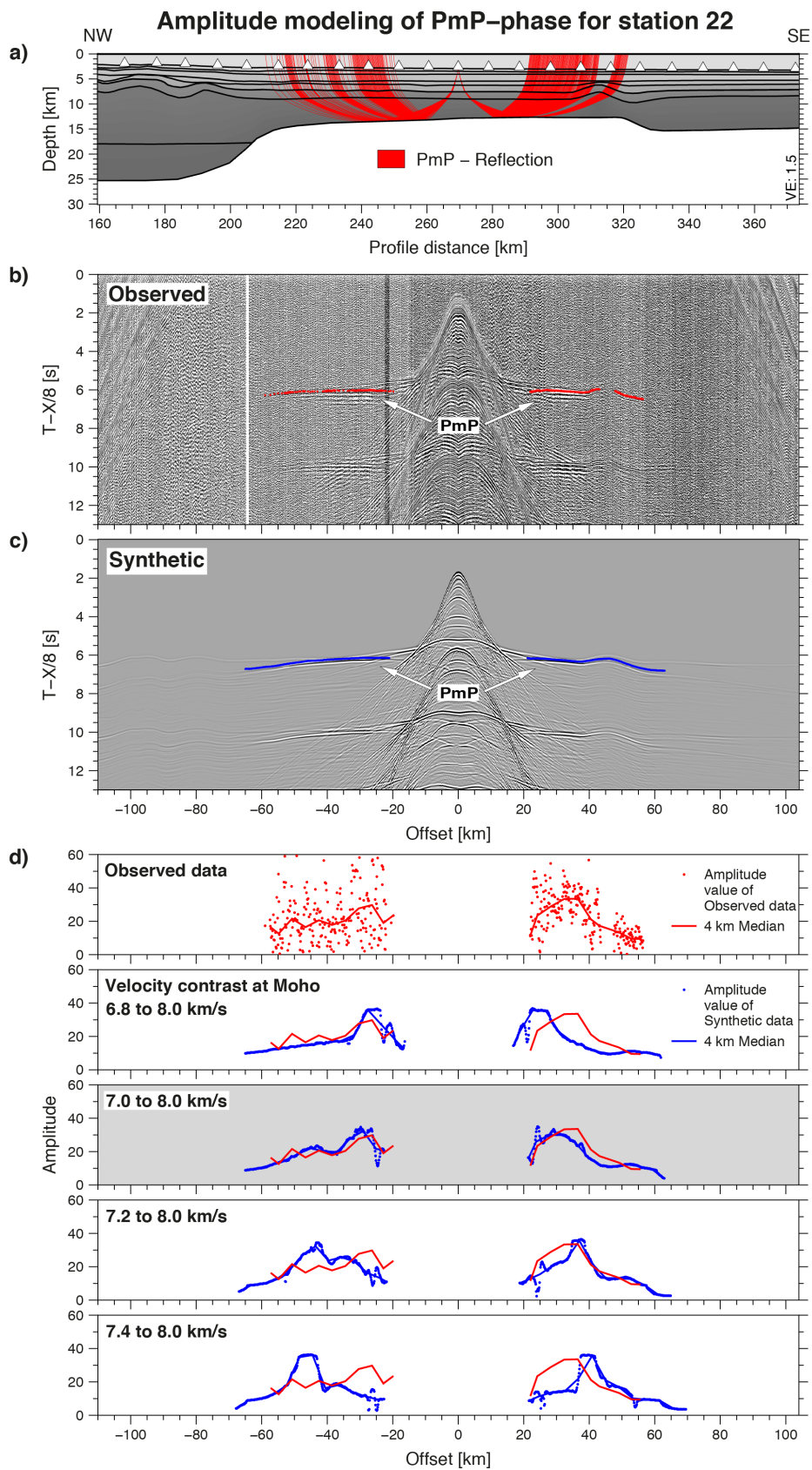


Figure 4.9: Results for amplitude modelling of PmP phase for station 22. Continues ...

(Fig. 4.10d). However, for the 7.1-model the local maxima and corresponding slopes are slightly shifted. For larger, negative offsets the amplitudes of the observed data clearly decrease. The 6.8- and 6.9-models show the best fit, whereas for models with higher basal velocities the amplitudes decrease at larger offsets or show a maximum. For positive offsets a similar trend is visible for velocity contrasts of 7.0 and 7.2 to 8.0 km/s at the Moho. The location of the local maximum fits best for the 7.0-model and is shifted for the other ones.

A tested model with a separate HVLCB below Beira High couldn't fit the amplitudes of the observed data at all. In this case the amplitudes are much lower and show a different trend. More synthetic seismograms were calculated for stations 31, 33 and 35. These stations show as well a tendency to slightly lower velocities than 7.0 km/s for the north-western part of Beira High and velocities around 7.0 and 7.1 km/s for the south-eastern part. Therefore, a velocity contrast of 6.9 to 8.0 km/s at the Moho is applied for the north-western part and 7.0 to 8.0 km/s for the south-eastern part.

Shelf area (km 0 – 60)

A 12 km thick pile of sediments is visible in the ZDD, with velocities of up to 5.1 km/s. Because of shallow water depths the early arrival of the multiple, and the pronounced topography of the crust at the transition from Beira High towards the shelf area made the phase identification in this area challenging. Here, the crust has a thickness of about 7 km, and is, thus, significantly thinner than below the Beira High. A sparse number of identified phases constrain the topography and velocities of the upper crust. Below, the lower crust shows velocities of 6.3-6.7 km/s. The top of an underlying HVLCB is constrained by weak reflections. In contrast, strong reflections are visible at the Moho, indicating a gentle slope from Beira High towards the shelf and a smooth topography below the shelf. Only in the uppermost part of the HVLCB refractions constrain the depicted velocities of 7.1 km/s. For the stations closest to the shelf only short first arrivals of the PmP phase are visible and aren't suited for an amplitude modelling. A longer first arrival of the PmP reflection with varying amplitudes was identified for station 39, which was used to obtain evidence about the velocity gradient of the HVLCB. The PmP reflections north of station 39 were all reflected at the slope

Figure 4.9 (cont.): a) Calculated rays of PmP reflection obtained by ray tracing for 7.0-model. b) Seismogram of observed data. Picks of PmP phase are shown as red dots. c) Synthetic seismogram of 7.0-model. Picks of PmP phase are shown as blue dots. d) Maximal amplitude values of PmP phase for observed and synthetic data. For median calculation a window length of 4 km was used. The preferred model is shaded in grey.

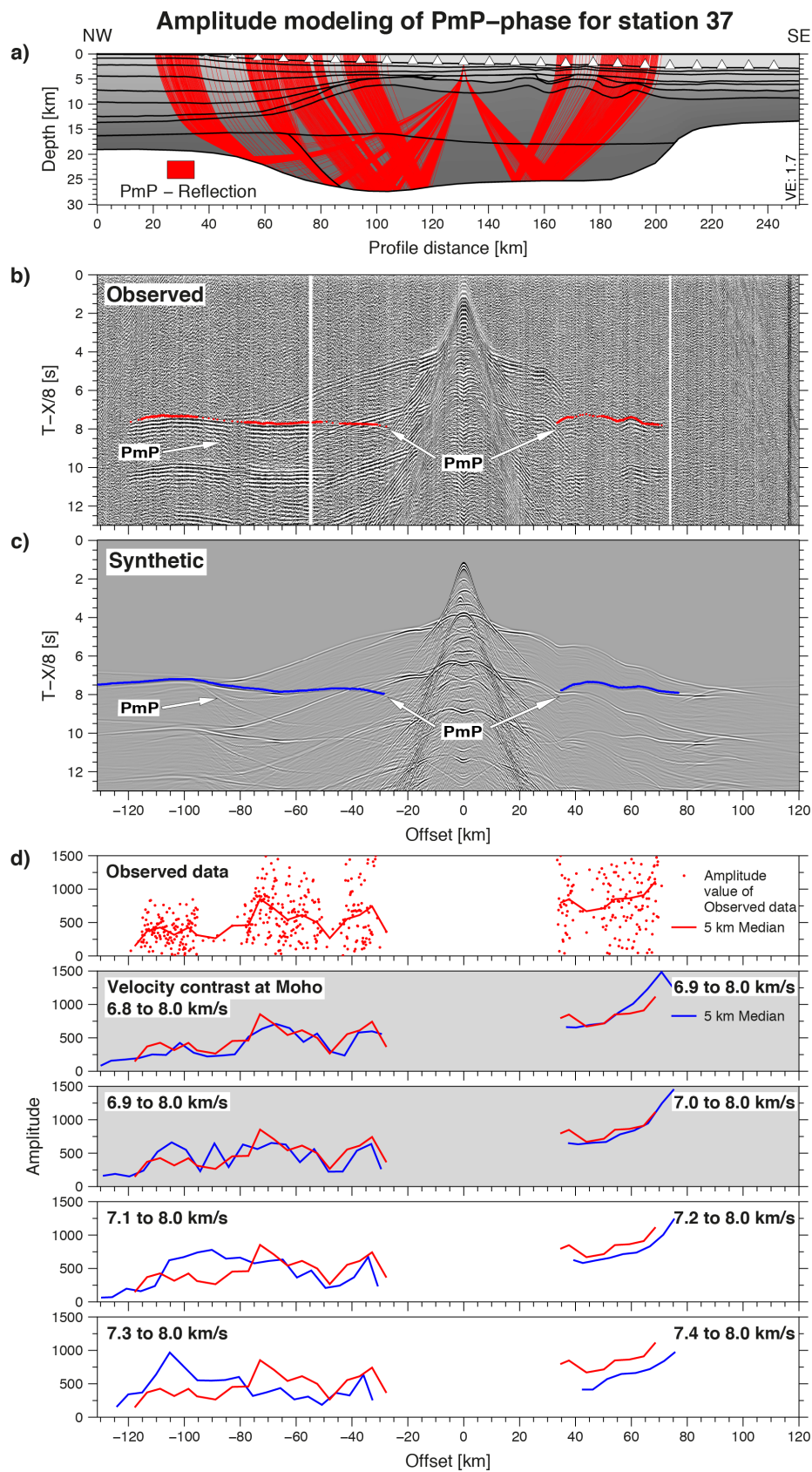


Figure 4.10: Results for amplitude modelling of PmP phase for station 37. Continues ...

of the Moho (Fig. 4.4). The best correlation for the location of the local maximum was achieved for a velocity contrast of 7.4 to 8.1 km/s at the Moho.

4.5.2 Gravity modelling

The free-air gravity anomaly varies between -80 mGal and +40 mGal along the profile. The starting model revealed already a very good correlation between the calculated and observed free-air anomaly, except the minimum values at Beira High. Here, the calculated free-air anomaly was larger than the observed one.

The final density model (Fig. 4.11b) shows densities of 2.02-2.49 g/cm³ and 2.02-2.43 g/cm³ for the sediment layers in the Mozambique Basin and on top of Beira High. In the shelf area in the deep sediment basin of the ZDD densities up to 2.67 g/cm³ were identified. Along the entire profile the upper crust shows similar densities of 2.64-2.72 g/cm³. In the Mozambique Basin and in the shelf area densities of 2.89-3.00 g/cm³ and 2.86-2.94 g/cm³ characterize the lower crust, respectively. Across Beira High the free-air gravity anomaly shows two local minima: a minimum of -40 mGal at km 170-205 and a second minimum of up to -80 mGal at km 70-170. To model this anomaly the middle and lower crust of Beira High is divided in a north-western and a south-eastern part. From the seismic data it is known that the SE-part of Beira High has slightly higher velocities than the NW-part. Thus, we used slightly different densities for both areas. In the SE-part no density changes were necessary for the middle crust (2.83-2.96 g/cm³) and for the lower crust (2.98-3.04 g/cm³). However, for the NW-part the densities had to be adjusted by up to -0.1 g/cm³, resulting in densities of 2.76-2.85 g/cm³ for the middle crust and 2.88-2.94 g/cm³ for the lower crust. The HVLCB depicted higher densities of 3.10-3.16 g/cm³. Finally, the mantle was modelled with a density of 3.33 g/cm³ in the Mozambique Basin and below Beira High and 3.36 g/cm³ below the shelf area. Only at km 80-110 the boundary between middle and lower crust was lowered by 0.5 km. This isn't in contradiction to the P-wave velocity model, due to missing constraints by reflections in this area. Consequently, this change was applied to the final velocity model (Fig. 4.8).

In addition, the calculated free-air gravity anomaly without the usage of density gradients is plotted in Fig. 4.11a. Here, the mean value between the upper and lower

Figure 4.10 (cont.): a) Calculated rays of PmP reflection obtained by ray tracing for 7.0-model. b) Seismogram of observed data. Picks of PmP phase are shown as red dots. c) Synthetic seismogram of 7.0-model. Picks of PmP phase are shown as blue dots. d) Maximal amplitude values of PmP phase for observed and synthetic data. For median calculation a window length of 5 km was used. The preferred models are shaded in grey.

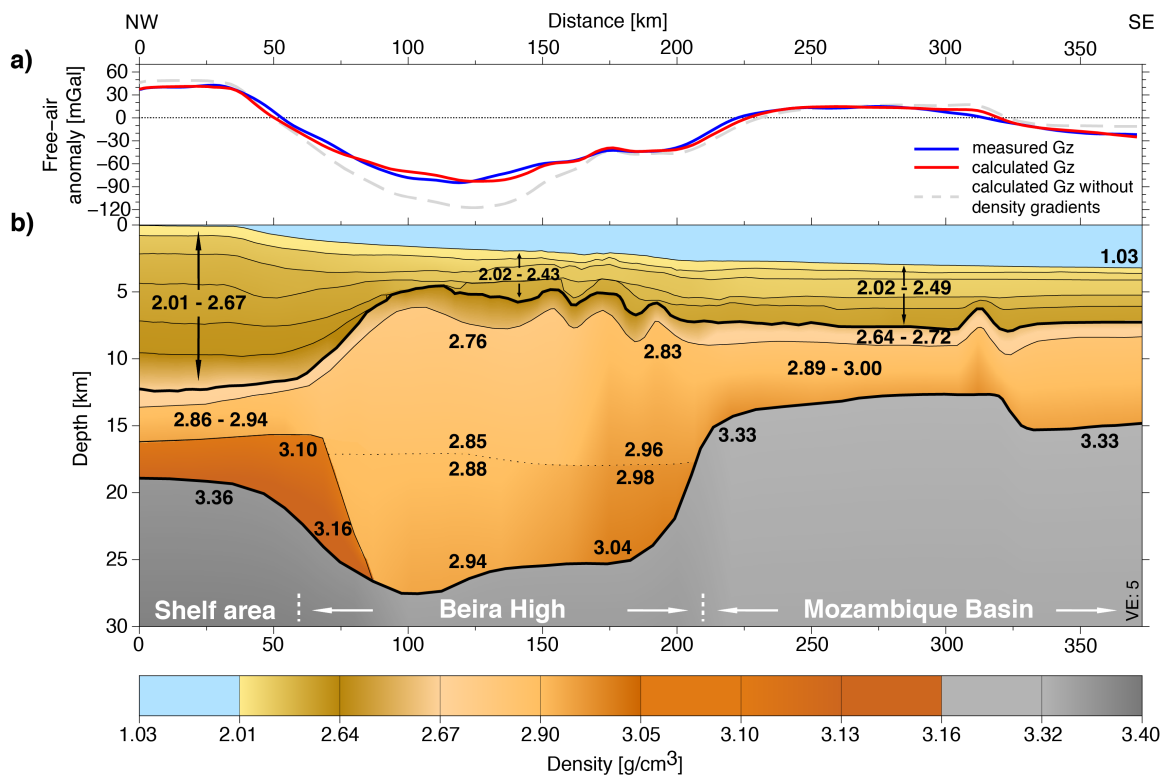


Figure 4.11: Density model for profile AWI-20140010. a) Measured and calculated free-air gravity anomaly. Additionally, the calculated anomaly without the usage of density gradients is plotted. b) Density model with incorporated density gradients. The numbers indicate the assigned densities (in g/cm^3) at the upper and lower boundaries (detailed values in Table 4.2).

layer boundary was used for calculation. The main difference of -30 mGal compared to the model with density gradients is visible in the area of Beira High and corresponds to the thickest crustal part. To achieve a good fit for the density model without density gradients, the densities of the middle and lower crust in the NW-part have to be increased by $+0.05$ g/cm^3 . This suggests clearly the advantage in incorporating density gradients to the gravity modelling for areas with a pronounced topography and presents the logical link to account for the velocity gradients known from the seismic refraction data.

4.6 Discussion

4.6.1 Sediments

The thickness of the sedimentary unit varies between 3 km on top of Beira High and 12 km in the ZDD. Along our profile, maximum velocities of 4.1 km/s in the Mozambique

Basin along this profile are lower than velocities of 5.0 km/s in the north-eastern part of the central coast of Mozambique (Leinweber et al., 2013). This is attributed to an elevated basement depth of 7 km instead of 10 km. In contrast, the thick pile of sediments in the ZDD depicts velocities up to 5.1 km/s and densities up to 2.67 g/cm³ in 12 km depth, representing already typical density values for the upper crust. Mahanjane (2012) interpreted reflections with a high-amplitude and low-frequency characteristic in the deepest part of the ZDD as lava flows. Such dense volcanic material accumulated and interbedded in thick sections in this deepest sediment layer explains the higher layer densities. This lowermost sediment layer probably belongs to the Karoo Group section, bearing terrigenous material covered by basalt and rhyolitic tuff of the Stormberg series (Salman and Abdula, 1995). The Middle to Late Jurassic age of the volcanic material implies its emplacement during the initial phase of rifting (De Buyl and Flores, 1986; Nairn et al., 1991; Salman and Abdula, 1995). Based on the interpretation of seismic reflection data the presence of pre-rift units are suggested on top of Beira High as well (Mahanjane, 2012). For km 120-160 (Fig. 4.8), directly below an identified break-up unconformity (Mahanjane, 2012), the hummocky reflection pattern at 4.5 s TWT shows again high amplitudes and low frequencies. Beneath, the seismic energy is diminished and the underlying sediments show low to moderate reflector amplitudes. This implies a scattering of the seismic energy at the upper interface of the high-amplitude reflections, which is a typical feature of basaltic surfaces. The OBS data provide a layer thickness of 0.5-1.5 km and a seismic velocity of 3.5-3.6 km/s. This is within the typical velocity range of lava flows interbedded in sediments in this depth (Sigurdsson et al., 2015). Similarly, time-depth converted seismic reflection data depict an equal depth for the upper interface of the Karoo unit of 4.5 km at this profile section (De Buyl and Flores, 1986). These evidence might support the idea of a thin layer of preserved terrigenous sediments of the Karoo Group section, covered by Middle to Late Jurassic volcanics of the Stormberg series on top of Beira High.

Especially in the south-eastern part of Beira High an asymmetric half-graben morphology characterized by listric normal faults is visible in the seismic reflection data. The infill consists of syn- and pre-rift successions, separated again by high-amplitude reflections of the rift-onset unconformity (Mahanjane, 2012). Because of the pronounced topography of the basement and the sediment structures in this area maximum velocities of 3.6 km/s for the deepest part of these grabens are only little constrained by the seismic refraction data.

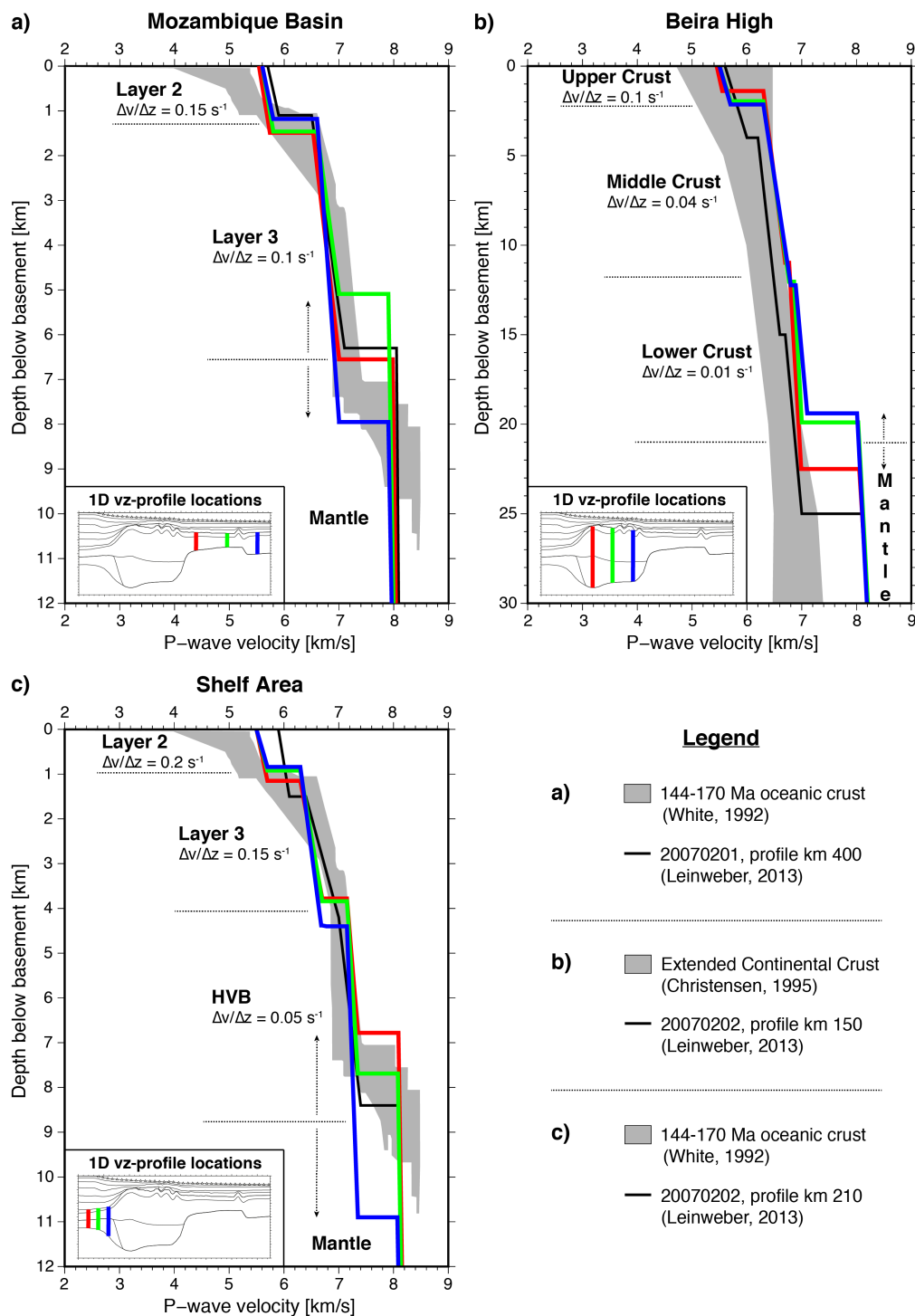


Figure 4.12: 1D velocity-depth profiles for each part of the seismic refraction profile. a) oceanic and c) transitional crust are compared to 144-170 Ma old oceanic crust from the NW-Atlantic (White et al., 1992). b) Beira High is compared to the velocity structure of extended continental crust of western Europe and the western United States (Christensen and Mooney, 1995). The black line indicates the velocity-depth structure of a comparable crustal section from the north-eastern part of the continental margin of Central Mozambique (Leinweber et al., 2013). Dotted lines separate different crustal units and the arrows depict a variable depth range of the Moho. The velocity-depth gradients are labelled with $\Delta v/\Delta z$ [1/s].

4.6.2 Mozambique Basin

Based on the modelled velocity structure, crustal thickness and the published magnetic spreading anomalies in this area (König and Jokat, 2010; Leinweber and Jokat, 2012), we interpret that km 210-375 of the profile (Fig. 4.8) are underlain by oceanic crust.

Subsequently, the crustal composition is compared to normal oceanic crust of similar age (White et al., 1992) and to the crust in the north-eastern part of the margin (Fig. 4.12a). A comparison to layer 2 of normal oceanic crust depicts quite high velocities for layer 2 along our profile (5.6-5.8 km/s), but a smaller velocity depth gradient (about 0.15 s^{-1}) and a similar thickness. However, compared to oceanic layer 2 in the north-eastern part of the margin (Leinweber et al., 2013) the velocities along our profile are slightly lower (Fig. 4.12a). The different basement depth between the survey areas might explain these differences.

The depicted velocities of 6.5-7.0 km/s for oceanic layer 3 and a velocity gradient of about 0.1 s^{-1} are in good agreement to normal oceanic crust and fit as well to layer 3 of the more distal oceanic crust in the north-eastern part of the margin (which is not affected by the HVLCB). In accordance, the gravity modelling revealed densities ranging between 2.89-3.00 g/cm³ for oceanic layer 3. These densities represent typical values for oceanic crust in 10-15 km depth (Carlson and Raskin, 1984) consisting of metagabbros and gabbros. The total thickness of the oceanic crust varies along the profile, due to a variable thickness of oceanic layer 3. South-east of km 330, a possible connection to the adjacent volcanic area of Bassas da India might cause a thickening of the crust of up to 8 km. Bassas da India is composed of a series of buried seamounts and volcanoes, emplaced during younger magmatic activity in this area (Raillard, 1990). Here, conceivable is an accumulation of magmatic material to both sides of a major fracture zone, identified in the magnetic and free-air gravity anomaly data, causing the rise of a seamount on one side and a thickening of the crust at the other side.

The amplitude modelling of the PmP phase did not support the presence of seismic velocities higher than 7.0 km/s in this part of the profile. Therefore, no information point to an underlying HVLCB in this area. Evidence for a HVLCB were only identified in the shelf area, where the HVLCB extends maximum 130 km away from the coast. This is in clear contrast to the oceanic crust in the north-eastern part of the margin, where Leinweber et al. (2013) modelled a HVLCB stretching up to 300 km away from the coast. This could be attributed to a different magmatic activity in both regions. However, potential field data provide only little evidence for the existence of a major fracture zone that could prevent an interaction between the south-western and north-eastern part of the margin. Another possibility is that the marginal areas developed at

different times, which were characterized by a different amount of magmatism. This would support a more complex opening history of the area with different rift stages (Cox, 1992; Mahanjane, 2012).

4.6.3 Beira High

At first the extracted 1D velocity-depth profiles of Beira High (Fig. 4.12b) are compared to the average velocity structure of extended continental crust (Christensen and Mooney, 1995) and to extended continental crust onshore Mozambique (profile 20070202, km 150; Leinweber et al., 2013).

A thickness of about 2-3.5 km and velocities of 5.4-5.8 km/s characterize the upper crust at Beira High. For the continental crust onshore Mozambique in the north-eastern part of the margin, Leinweber et al. (2013) depicted a slightly thicker upper crust with minimum velocities of 5.6-6.0 km/s and the same high velocity gradient of 0.1 s^{-1} . In agreement to a global study of Christensen and Mooney (1995), calculated average values of extended continental crust range in 5 km depth about 5.59 ± 0.88 km/s. Additionally, a consideration of smaller continental fragments (total thickness ≤ 25 km, Fig. 4.13) reveals a similar thickness of 2-3 km for the upper crust and variable velocities of 5.0-5.9 km/s. However, the typical velocities of 5.9-6.2 km/s (Christensen and Mooney, 1995) for granitic gneisses of the normal upper continental crust are missing. An intense faulting and stretching of the upper brittle crust during rift-related extension or interbedded metasedimentary or carbonate rocks of pre-rift times might explain these lower velocities (Chian et al., 2001).

For the middle and lower crust at Beira High the velocity modelling revealed a slightly different characteristic for the north-western and south-eastern part. However, both parts show normal velocities expected at the Moho in continental crust (up to 7.1 km/s; Christensen and Mooney, 1995). The consideration of the velocity-depth gradients reveals a similar result. Here, the combined velocity-depth gradient for middle and lower crust in the NW-part of 0.025 s^{-1} is only slightly greater than for 40 km thick normal continental crust (0.01 - 0.02 s^{-1} ; Mooney et al., 2002). A velocity-depth gradient of 0.035 s^{-1} for the SE-part is in agreement to the averaged velocity structure of extended continental crust (Fig. 4.12b) and to the velocity structure onshore the north-eastern part of the margin (Leinweber et al., 2013). The general velocity distribution of Beira High, compared to extended continental crust (Fig. 4.12b), increases at the upper limit towards higher velocities. The differences might be attributed to the higher rate of rift-related stretching and to the influence of an intensive rift-magmatism, resulting in partly intruded crust.

The densities at Beira High are in good agreement to density values of crystalline rocks suggested by [Christensen and Mooney \(1995\)](#) for continental crust. However, the density model depicts a clear difference of 0.1 g/cm^3 between the two parts of Beira High. Based on studies of [Christensen and Mooney \(1995\)](#) and [Rudnick and Fountain \(1995\)](#) the middle continental crust consists most likely of rocks of the amphibolite facies and gneisses and the lower crust of granulite up to mafic granulite. Therefore, in accordance to the study of [Rudnick and Fountain \(1995\)](#) the lower densities in the NW-part of Beira High may indicate the existence of large amounts of granitic and tonalitic gneisses in the middle crust and felsic to intermediate granulites in the deeper parts of the lower crust. In contrast the densities of the middle and lower crust in the SE-part indicate the presence of intruded continental crust, which got affected by a partly greater magmatic activity, maybe connected to the nearby onset of oceanic crust. Furthermore, it is remarkable that the middle crust in the SE-part of Beira High and the adjacent oceanic crust show similar densities. This might give rise to the possibility of incorporated gabbroic material, emplaced during a phase of rifting, contributing to the higher densities in this part of the profile.

The investigation of a possible oceanic origin of the whole Beira High reveals at first similar minimum and maximum velocities for Beira High and the adjacent oceanic crust. The upper crust of Beira High shows velocities in the same range as oceanic layer 2, but is slightly thicker and has a smaller velocity gradient. The subsequent velocities of 6.3 km/s at the upper boundary of the middle crust are unlikely for oceanic layer 3 and do not correlate to observed velocities of 6.5 and 6.6 km/s in the Mozambique Basin (upper boundary of oceanic layer 3). The main part of oceanic layer 3 consists usually of gabbro, which shows upper velocities of at least 6.5 km/s ([Christensen and Mooney, 1995](#)). A lowering of these upper velocities could suggest a broader extension in depth for the transitional area from layer 2 to layer 3, caused by a mix of basalt, metagabbro and gabbro in the upper part of layer 3. However, the clear increase in velocity at the boundary between upper to middle crust of partly 5.7 to 6.3 km/s doesn't indicate a gradual change in rock composition.

Even more noticeable is the clear difference of the velocity-depth gradients of 0.025 s^{-1} for the middle and lower crust in the NW-part of Beira High in comparison to 0.1 s^{-1} for oceanic layer 3 in the Mozambique Basin. This represents a four times smaller increase of velocity with depth for Beira High. Such small velocity-depth gradients are not known for oceanic crust, including oceanic plateaus.

Comparing the densities reveals similar results. Gabbro, as main part of the oceanic layer 3, shows in about 5 km depth a mean minimum density of 2.86 g/cm^3 (2.93 ± 0.07

g/cm³) and for metagabbro of minimum 2.83 g/cm³ (2.90±0.07 g/cm³) (pressure of 100 MPa; Carlson and Raskin, 1984). Velocity-density conversions for magmatic material (Brocher, 2005; Godfrey et al., 1997) reveal for a P-wave velocity of 6.3 km/s a similar high density value of 2.91 g/cm³. In contrast, depicted densities of 2.76 g/cm³ for the upper boundary of the middle crust in about 7-9 km depth at Beira High show that even the lowest mean density values of gabbroic material of oceanic layer 3 are still too high. As long as no excessively vertical extended transitional area between the oceanic layers 2 and 3 and great portions of diabase and basalts are present, rocks of oceanic layer 3 cannot be characterized by these densities. Although the increase in density with depth is for gabbroic material quite small, still densities at 20 km depth are in the range of 2.98±0.03 g/cm³ (Christensen and Mooney, 1995). Especially in the NW-part the identified densities in the middle crust at Beira High are up to 0.1 g/cm³ lower compared to a normal rock composition of oceanic layer 3. A consideration of the lower continental crust and oceanic layer 3 depicts only minor differences in densities due to partial similarities in rock composition. However, maximum densities of 2.94 g/cm³ at about 28 km depth in the NW-part are clearly lower than 3.00±0.03 g/cm³ in 30 km depth for gabbro (Christensen and Mooney, 1995). At least a slight decrease of the densities of oceanic layer 3 in this depth could be connected to high proportions of plagioclase in the gabbroic material (Nicolas and Boudier, 2000). Nevertheless over-thickened oceanic crust is always characterized by an underlying thick HVLCB (Fig. 4.14), which consists of dense ultramafic material with densities greater than 3.1 g/cm³. These values exceed the depicted densities at Beira High up to 0.2 g/cm³.

Due to the geographical position and tectonic events, which affected the crustal structure of Beira High, a comparison to extended continental crust and standard oceanic crust does not reveal definite hints about its origin. More evidence are obtained by taking continental fragments (CFs) and oceanic plateaus (OPs) into account (Figs. 4.13 and 4.14). Carlson et al. (1980) already identified the major differences between these crustal features. Subsequently, the findings are supplemented and applied to Beira High:

1. *OPs and CFs show similar velocities of 6.7-7.0 km/s for oceanic layer 3 (OP) and the lower continental crust (CF), respectively. However for CFs these velocities tend to occur at deeper levels.*

At Beira High velocities greater than 6.6 km/s are observed at depths greater than 10 km (Fig. 4.8). A similar depth range (and even deeper) is visible for CFs (Fig. 4.13). In contrast, OPs reveal the top of oceanic layer 3 at 5-9 km depth. Furthermore at some OPs velocities exceed already 7.0 km/s at the 10 km depth level (Fig. 4.14).

4. THE CRUSTAL STRUCTURE OF BEIRA HIGH

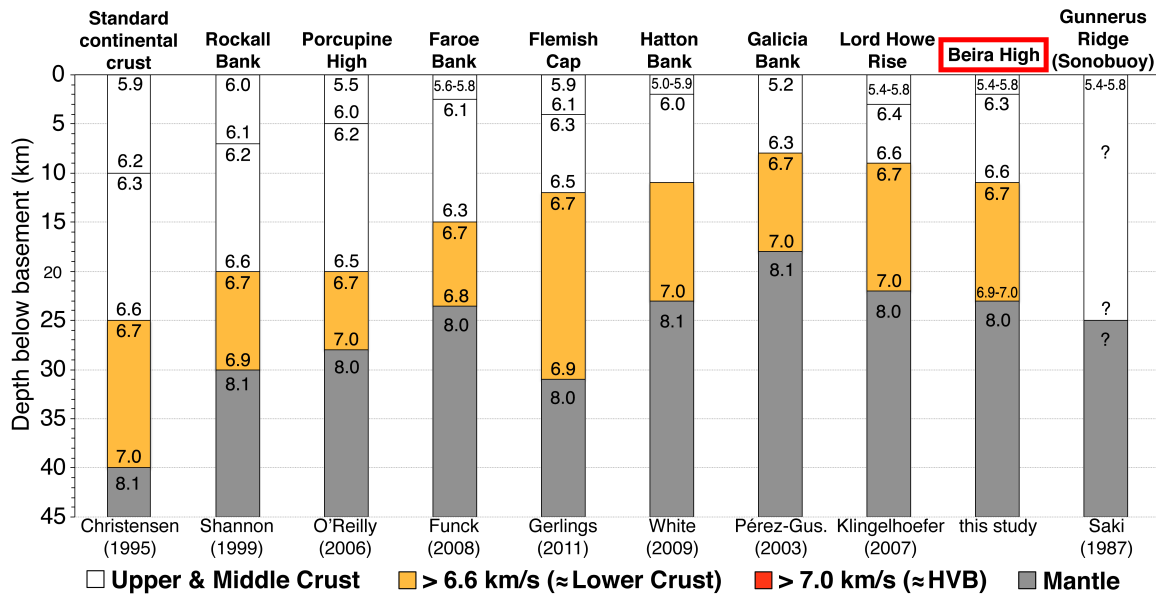


Figure 4.13: Comparison of the crustal structure of Beira High and continental fragments. 1D velocity-depth structures of the crust are extracted from the main part of the respective structure. The numbers present P-wave velocities in km/s (based on the studies of Christensen and Mooney, 1995; Funck et al., 2008; Gerlings et al., 2011; Klingelhofer et al., 2007; O’Reilly et al., 2006; Pérez-Gussinyé et al., 2003; Saki et al., 1987; Shannon et al., 1999; White and Smith, 2009).

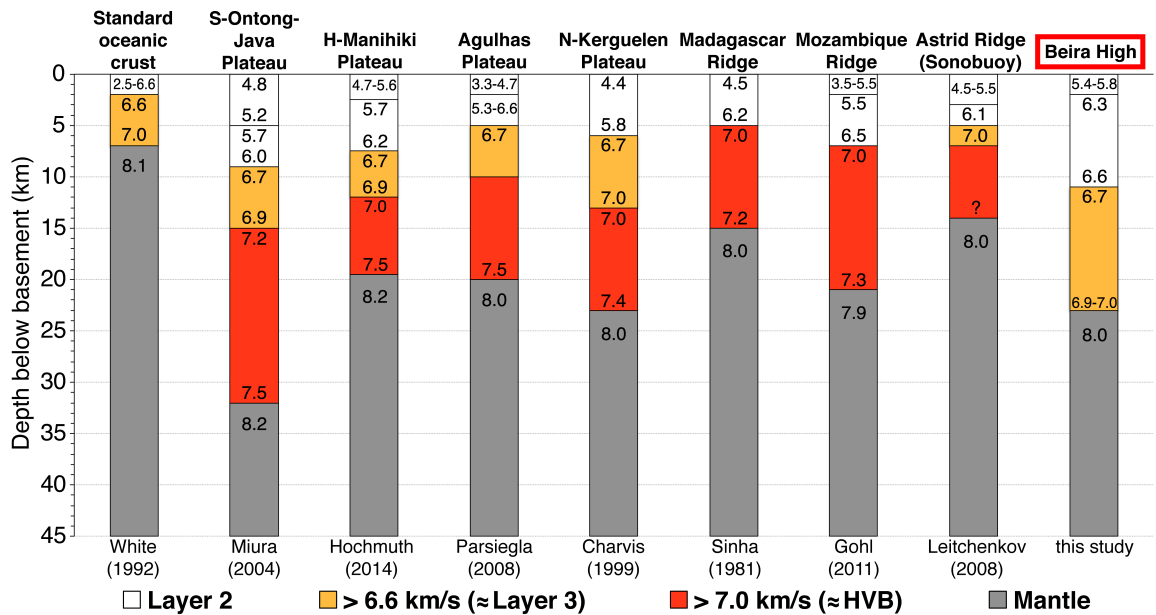


Figure 4.14: Comparison of the crustal structure of Beira High and oceanic plateaus. 1D velocity-depth structures of the crust are extracted from the main part of the respective structure. The numbers present P-wave velocities in km/s (based on the studies of Charvis and Operto, 1999; Gohl et al., 2011; Hochmuth et al., 2014; Leitchenkov et al., 2008; Miura et al., 2004; Parsiegla et al., 2008; Sinha et al., 1981; White et al., 1992).

2. *A distinct HVLCB (>7.0 km/s) is observed in the central part of OPs and not at CFs.*

Constraint by the amplitude modelling Beira High shows no evidence for the presence of a HVLCB. This is in agreement to CFs, where in general no HVLCB is observed in the central part, although their flanks are partly accompanied by HVLCBs. In contrast, typically a 6-15 km thick HVLCB with basal velocities of 7.3 -7.6 km/s underlies the central part and flanks of OPs (Fig. 4.14). Over-thickened oceanic crust of 23 km thickness without a HVLCB (velocities of 6.9-7.0 km/s at the Moho) in 28 km depth has not been observed so far.

3. *Crustal structure of CFs correlates well with the structure of continental shields, whereas OPs do not.*

For Beira High velocities of 6.3 to 7.0 km/s are observed for the middle and lower crust, which are typical for continental shields. However velocities of the upper crust are lower than standard values (explanation in upper text). OPs are characterized by a wide range of possible velocities in the upper crust, high velocities at comparable low depth levels in the middle and lower crust, and basal velocities greater than 7.0 km/s, which do not correlate to continental shields.

4. *Monotonous increase in velocity with depth is typical for the middle and lower crust of CFs, whereas OPs show clear velocity “jumps”.*

In middle to lower crust of Beira High no major “jumps” in velocities are observed (Fig. 4.8). This results in a relatively monotonous increase in velocity with depth, as known from CFs (Fig. 4.13). In contrast OPs show distinct velocity differences at the boundary between oceanic layers 2 and 3 (≥ 0.3 km/s) and in some cases at oceanic layer 3 to the HVLCB (Fig. 4.14).

5. *CFs are characterized by smaller velocity-depth gradients in the middle to lower crust than OPs.*

The velocity-depth gradients of middle to lower crust at Beira High vary between 0.025 and 0.035 s^{-1} . These are in good agreement to CFs with a maximal thickness of 25 km. Even smaller gradients are observed for greater CFs (>25 km thickness, Fig. 4.13). On the other hand, comprised velocity-depth gradients of oceanic layer 2 and 3 greater than 0.1 s^{-1} characterize OPs.

This comparison points out a distinct similarity of the crustal structure of Beira High and continental fragments. A postulated combined history of Beira High with the oceanic plateaus Mozambique Ridge and Astrid Ridge (Leinweber and Jokat, 2012; Watts, 2001) is unlikely due to distinct differences in their crustal structures (Fig. 4.14). High velocity-depth gradients and shallow, thick HVLCBs characterize both oceanic plateaus, which is in clear contrast to Beira High.

4.6.4 Shelf area

The crustal structure in the shelf area off Mozambique shows a clear thinning of the crust compared to Beira High. The crust is characterized by a thickness of 7-8 km and a slightly greater velocity-depth gradient than in the oceanic domain in the SE of the profile (Mozambique Basin), which is in good agreement to normal oceanic crust (Fig. 4.12c). Furthermore, oceanic layer 3 in the shelf area has about half the thickness than in the SE of the profile and is underlain by a HVLCB with velocities up to 7.4 km/s. The crustal structure in the NE-part of the margin depicts clear similarities. Here, [Leinweber et al. \(2013\)](#) identified close to the coast a similar crustal structure with slightly higher velocity-depth gradients and suggested a transitional or oceanic origin of this part. In contrast, the possible presence of terrigenous pre-rift sediments of the Karoo Group section in the ZDD supports the possibility of highly stretched continental crust. A consideration of the identified velocities in this area provides no reliable evidence about the origin, due to a partly similar velocity range for highly stretched continental and oceanic crust ([Shannon et al., 1999](#)). A typical characteristic of highly stretched continental crust is the presence of extensional features as rotated fault blocks ([Franke, 2013](#)). However, the thick pile of sediments in the ZDD (about 12 km) and the emplacement of break-up related volcanic rocks like lava flows in the deepest part of the basin mask the basement structure. Hence, a final classification of the crustal origin in this area by seismic and gravity data remains ambiguous.

The detected HVLCB in the shelf area represents a common feature at volcanic passive margins. The similarities in velocity and thickness as well as the close vicinity to the HVLCB in the NE-part of the margin suggest a combined emplacement history. [Leinweber et al. \(2013\)](#) favour the interpretation of magmatic underplating, caused by the interplay of active upper mantle convection accompanied by increased upper mantle potential temperatures. Along this profile distinct velocity differences at the top of the HVLCB as well as at the Moho partly cause strong reflected phases and depict an usual characteristic of magmatic underplating. Additionally detected intrusions like lava flows, seaward dipping reflectors and partly sill-like intrusions in the upper crust and lowest sediment layers document a partial melt of the overburden and support the idea of hot and dense magmatic material that was attached to the lower crust.

Generally, lower mantle velocities and the absence of Moho reflections due to a low velocity contrast indicate the presence of serpentinized mantle. The gradual process of hydration of olivine to serpentine, triggered by seawater influx through the thinned and brittle crust causes the serpentinization. Based on this study mantle velocities of 8.1 km/s were identified in the shelf area and depict no gradual velocity increase towards

the mantle. Therefore, our results do not support the presence of mostly serpentinized mantle in the area between Beira High and the Mozambican shelf.

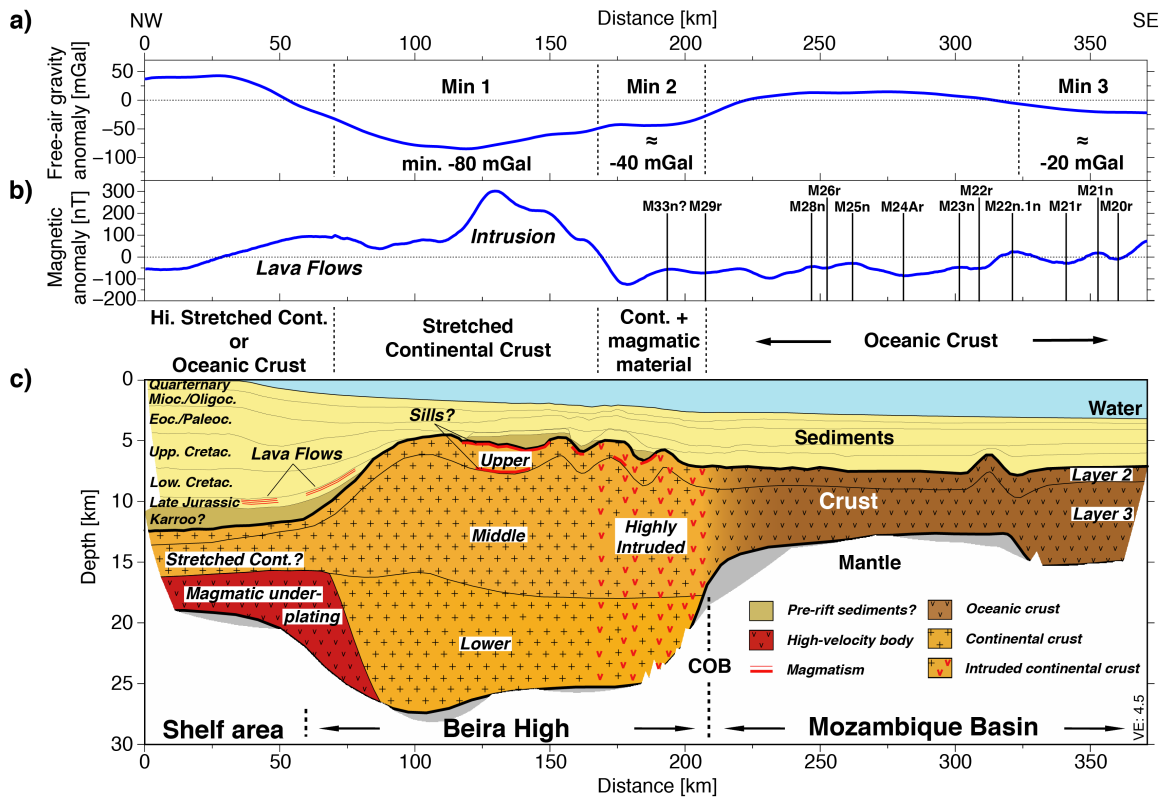


Figure 4.15: Geological interpretation of profile AWI-20140010. a) The free-air gravity anomaly and b) the magnetic anomaly along the profile are shown. Magnetic chrons are taken from [Leinweber and Jokat \(2012\)](#). c) Geological interpretation of the profile. Identification of sediment units is based on [Castelino et al. \(2015\)](#).

4.6.5 Magnetic data and implications for the tectonic setting

Magnetic spreading anomalies in the Mozambique Basin are identified by [Leinweber and Jokat \(2012\)](#) to the south-eastern termination of Beira High (Fig. 4.15b). Here, M29r (157.6Ma) is most likely the oldest magnetic spreading anomaly, coinciding with the transition from Beira High to the oceanic crust (Fig. 4.15c). At Beira High the magnetic data show long wavelength anomalies for km 160-210 (Fig. 4.15b). By means of the seismic reflection data these can be assigned to the presence of intruded magmatic material that rose along major fault zones ([Mahanjane, 2012](#)) into the upper crust. A distinct positive magnetic anomaly of up to 300 nT is visible in the main part of Beira High (km 120-160). The location coincides with two prominent intra-basement reflections of low frequency and high amplitudes. These show a typical shape of saucer-shaped sills ([Polteau et al., 2008](#)). The magmatic intrusions rest in the upper crust

and can be attributed to cause the strong magnetic anomaly. Therefore, no magnetic spreading anomalies are detected at Beira High, which supports the idea of partly highly intruded continental crust.

Conspicuous is the narrow transitional area (Fig. 4.15c, km 185-215) of about 30 km where the crust thins from 20 km thickness at Beira High to about 6 km in the Mozambique Basin. Based on the crustal structure and the magnetic data, the COB is expected to be located in this area. The narrow transition implies either a short period of extension or a strike-slip movement that affected this part of the margin. Conceivable are different thinning directions that have been active during the initial break-up in this area. As a consequence, a V-shaped basin formed in the area of the ZDD (Mahanjane, 2012; Peron-Pinvidic and Manatschal, 2010). The Jurassic southwards movement of Antarctica with respect to Africa (Jokat et al., 2003; Leinweber and Jokat, 2012) might have caused a rift jump, which originates from the north-western boundary of Beira High. This points towards a failed rift in the ZDD. Here, the crust thins in a 60 km wide transitional area from Beira High to the shelf area (km 30-90) and depicts in this part a longer period of rifting. Failed rifts are already known from other case studies of continental fragments (Chian et al., 2001; Radhakrishna et al., 2012). In general, the nature of crust in the area of failed rifts depends on the stage of the aborted rift as well as the input of magma and depicts various possibilities, e.g. hyper extended continental crust, exhumed mantle or proto-oceanic crust (Peron-Pinvidic and Manatschal, 2010). However, based on the seismic velocities in the ZDD the crustal nature remains unclear. For the same area the magnetic data show increased values of up to 120 nT at km 30-80 (Fig. 4.15b), most likely caused by lava flows. These extend along the entire north-western boundary of Beira High and were emplaced during the initial break-up (Mahanjane, 2012). The volcanic flows mask possible magnetic spreading anomalies in the ZDD and suppress a clear classification of the crustal nature and potential COB in this area.

From the tectonic point of view, the existence of a continental fragment at the margin of Central Mozambique has important implications for Jurassic plate kinematic reconstructions in our research area. A more complex scenario for the early opening of the Mozambique Basin than proposed by Leinweber and Jokat (2012) is likely. However, including a revised kinematic model is beyond the scope of this contribution and will be introduced in a separate contribution. In general, the classification of Beira High as a former part of Africa or Antarctica mainly depends on the crustal nature below the ZDD, which is still unknown. Successful emplaced oceanic crust in the ZDD would indicate that Beira High is a part of Antarctica and might be separated by a rift jump. On the other hand, in case of highly extended continental crust in the ZDD the clas-

sification remains ambiguous. Despite this, the SW-NE elongation of Beira High with its present-day position parallel to the central coast of Mozambique points towards a mainly NW-SE stress direction during the initial break-up between Africa and Antarctica. Therefore, our results support a NW-SE or anticlockwise initial opening of the Mozambique Basin. However, further investigations along the margins of Mozambique and Antarctica are required to verify the early motions (e.g. a strike-slip movement; Cox, 1992) during the initial rifting between Africa and Antarctica.

4.7 Conclusion

This study presents for the first time insights about the crustal nature of Beira High based on wide-angle seismic and potential field data.

[1] In the Mozambique Basin typical oceanic crust with 5.5-7 km thickness is present. High velocities in the upper crust of 5.6-5.8 km/s are in good agreement to the NE-part of the margin. Basal velocities of 7.0 km/s do not indicate the existence of an underlying HVLCB.

[2] There is a sharp transition from the oceanic domain towards Beira High, where the crust thickens to 20-23 km. A homogenous increase in velocity up to 7.0 km/s and a small velocity-depth gradient characterize the main part of the crust. This is in good agreement with the velocity structure of continental fragments and in clear contrast to oceanic plateaus and the oceanic crust in the Mozambique Basin. The gravity modelling depicts low densities of 2.76-2.94 g/cm³ for the main part of Beira High, which implies the presence of felsic material into greater depths. This supports the idea of stretched and partly highly intruded continental crust at Beira High.

[3] Towards the ZDD there is a gradual decrease in crustal thickness to 7-8 km. Here, the high velocity-depth gradients and densities of the crust are in good agreement with values typical for oceanic crust. However, due to possibly preserved pre-rift sediments and similar known velocities for highly extended continental crust, a continental origin cannot be rejected. Therefore, the nature of crust in the ZDD is unclear.

[4] Evidence of an increased magmatism during the early break-up comes from an underlying HVLCB in the shelf area. Clear reflections at the upper and lower boundary of the HVLCB point to a magmatic underplating as known from the north-eastern part of the margin. More volcanics are present, like lava flows, overlying the oldest

sediments in the ZDD, and sill-like intrusions at Beira High.

[5] The COB is located at the south-eastern termination of Beira High. The narrow transition implies either a short period of extension or a strike-slip movement, which affected this part. Both possibilities point to the presence of different thinning directions during the initial break-up in this area. This gives rise to a possible rift jump, originating from the north-western boundary of Beira High. The consequence is a failed rift between onshore Mozambique and Beira High.

Acknowledgements

We thank captain Detlef Korte and his crew of R/V Sonne for their support and assistance during the cruise SO230. We acknowledge the IFM-Geomar for providing the OBS/H stations. Furthermore, we like to thank Jürgen Gossler and Ingo Heyde for supporting the OBS deployment and gravity/magnetic data acquisition, respectively. For their support with the software SOFI2D we thank Thomas Bohlen and Tilman Metz. We gratefully acknowledge Tabea Altenbernd for her effort in improving the manuscript in terms of content and English. Additionally, we thank Frauke Klingelhofer and one anonymous reviewer for their comments that improved this article. Furthermore thanks go to Schlumberger Multiclient for providing insights into some regional MCS and magnetic data. This project is funded through a grant by the German Federal Ministry of Education and Research (BMBF, 03G0230A) and by AWI internal funding.

5 Geophysical evidence for the crustal variation and distribution of magmatism along the central coast of Mozambique

Christian Olaf Mueller¹, Wilfried Jokat^{1,2}

¹ *Alfred Wegener Institute, Bremerhaven, Germany*

² *University of Bremen, Bremen, Germany*

Abstract

For our understanding of the timing and geometry of the initial Gondwana break-up, still a consistent image of the crustal composition of the conjugated margins of Central Mozambique and Antarctica and the location of their continent-ocean boundaries is missing. In this regard, a main objective is the explanation for the source of the different magnetic signature of the conjugate margins. Based on a revised investigation of wide-angle seismic data of two profiles across the Mozambican margin by means of an amplitude modelling, this study presents the crustal composition along the margin of Central Mozambique. Supported by 2D magnetic modelling, the results are compared to the conjugated margin in Antarctica and allow conclusions on their joined tectonic evolution. Conspicuous is the equal spatial extent of the HVLCB along the margin of Central Mozambique of 190-220 km and its uniform maximal emplacement time until 159 Ma (M29r). Consistently, at both margins, magnetic spreading anomalies can be identified close to the present coast. The onset of oceanic crust is marked by the presence of the oldest magnetic spreading anomaly M38n.2n (164.1 Ma). Magmatic intrusions and SDRs contribute to the margin's magnetic signature, respectively. The reversed polarized SDRs at the Mozambican margin are mainly emplaced between

168.5-166.8 Ma. The supposed SDRs in the Riiser-Larsen Sea might be emplaced sometime between 168.5-164.1 Ma, but got overprinted by normal polarized intrusions of a late stage of rift volcanism. The distribution of the magmatic material along the central coast of Mozambique clearly indicates the eastern extension of the north-eastern branch of the Karoo triple rift, terminating close to Davie Ridge. The main magmatic phase affecting the margin lasted at least 12 Ma between 169-157 Ma, followed by the cease of the magmatism, possibly due to the relative southwards motion of the magmatic centre.

5.1 Introduction

In Early Jurassic times the dispersal of the supercontinent Gondwana started with the opening of the Mozambique Basin (e.g. Cox, 1992; Eagles and König, 2008; Jokat et al., 2003; Nguyen et al., 2016; Reeves et al., 2016). Commonly accepted is the oceanic nature of its main part, placing it as one of the oldest oceanic basins between Eastern Africa and Antarctica. However, the onset of oceanic crust and the crustal structure of the continental margin along the coast of Mozambique are still ambiguous. Plate kinematic reconstructions significantly differ in their pre-break-up fit and their Jurassic plate movements. To solve this problem it is critical to identify the onset of oceanic crust. Systematic offshore magnetic data are important constraints to locate this boundary. Off Central Mozambique, the continental margin is characterized by a reversed magnetic anomaly showing variable amplitudes (Fig. 5.1c). In contrast, the conjugate Antarctic margin in the Riiser-Larsen Sea shows a strong positive magnetic anomaly, but more landward than along Central Mozambique (Fig. 5.1d). The reasons for this pronounced different anomaly pattern has yet to be explained. The pronounced negative magnetic signal along the whole margin of Central Mozambique is either a simple edge effect (Nguyen et al., 2016; Reichert and Neben, 2008), caused by a narrow continental margin where different magnetised continental and oceanic crust are close together, or caused by the existence of reversed polarized seaward dipping reflectors (SDRs) (Leinweber et al., 2013). Also conceivable is the contribution of an early magnetic spreading anomaly, located close to the coast. Despite this, conclusions on the magnetic sources reveal evidence about the amount of volcanism along the margin, which contributes to our understanding of the driving forces for the break-up.

Offshore the coast of Central Mozambique, the Mozambique Basin represents the southern part of the Mozambique Channel. The Davie Fracture Zone and the island of Madagascar border it to the east (Fig. 5.1a). The Mozambique Coastal Plains (MCP) and the Natal Valley define its western boundary. In the 1970s seismic and magnetic

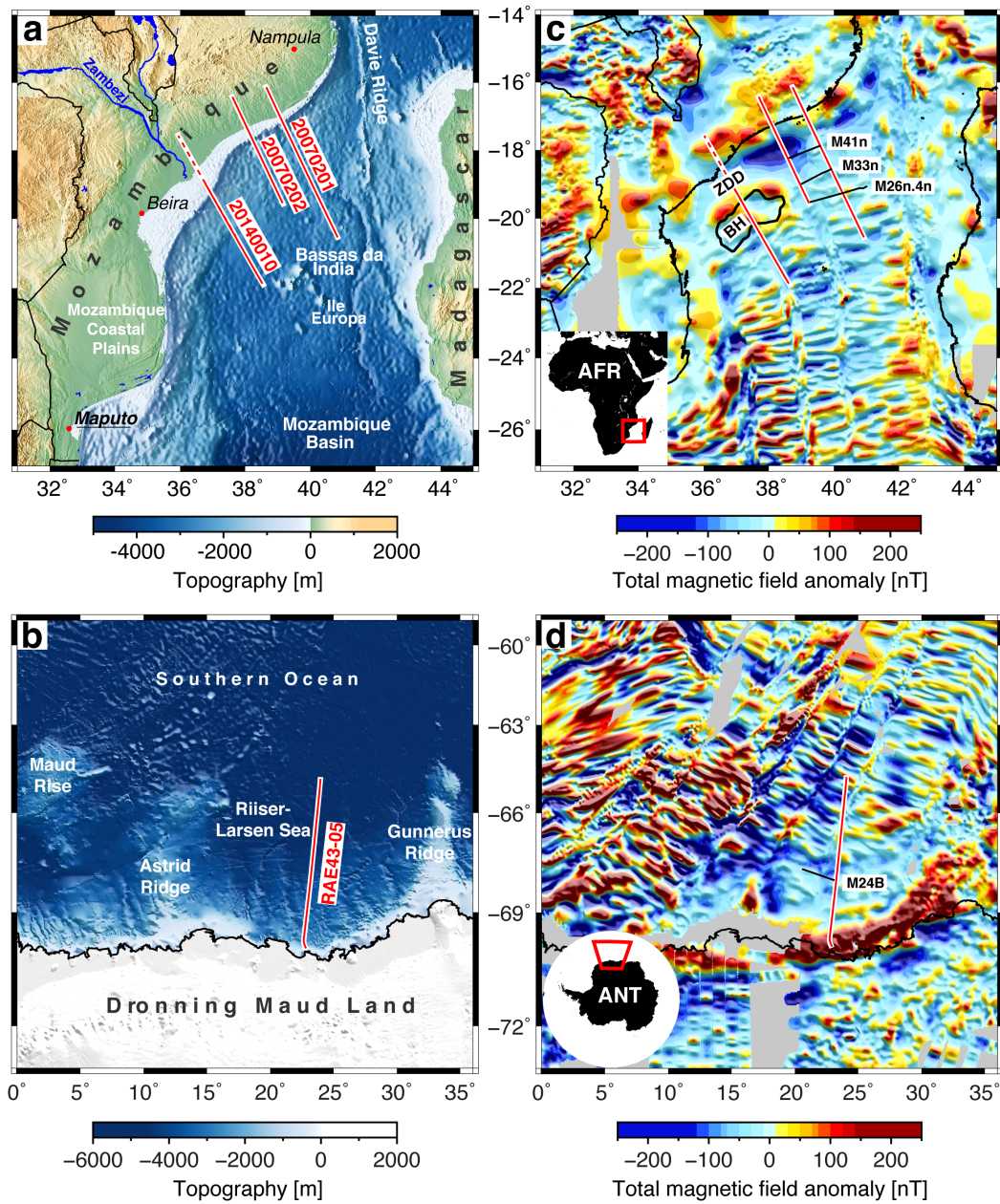


Figure 5.1: a) Bathymetric and topographic map of the Mozambique Basin and the central and southern continental margin of Mozambique, based on the GEBCO_2014 grid (version 20150318; Weatherall et al., 2015). Red lines indicate the locations of the seismic refraction profiles of the MOCOM-Cruise (profile 20140010) and the MoBaMaSis-Cruise (profile 20070201 and 20070202). The dashed red line marks the extension of profile 20140010 for the magnetic modelling. b) Bathymetric and topographic map of the conjugate Antarctic margin, based on the GEBCO_2014 grid (version 20150318; Weatherall et al., 2015). The red line marks the position of the seismic reflection profile used in this study. c) Total magnetic field anomaly map of the Mozambique Basin and the central and southern continental margin of Mozambique, based on the EMAG2 grid (version 2; Maus et al., 2009). Magnetic chrons were taken from Leinweber and Jokat (2012). d) Total magnetic field anomaly map of the conjugate Antarctic margin. The position of magnetic chron M24B according to the interpretation of Leitchenkov et al. (2008) is plotted.

surveys by French expeditions already proofed the oceanic nature of the Mozambique Basin (Segoufin, 1978; Simpson et al., 1979). First in 2005 (AISTEK II-Cruise, RV Sonne; Jokat, 2005), newly systematically acquired scientific magnetic data allowed the identification of magnetic spreading anomalies in the Mozambique Basin up to chron M26n.4n (157 Ma; Ogg (2012); Fig. 5.1c) and revealed evidence for a likely location of the continent-ocean boundary (COB) much closer to the coast than previously assumed (König and Jokat, 2010). Therefore, in 2007 the joint German/French MoBaMaSis-Cruise (Reichert and Neben, 2008) acquired new seismic and potential field data along the Central Mozambican shelf to define the geometry of the COB. The investigation along two seismic refraction profiles across the northern margin of Central Mozambique identified slightly thicker than normal oceanic crust (Fig. 5.1; line 20070202, 8.5 km thickness) close to the margin (Leinweber et al., 2013). A high-velocity lower crustal body (HVLCB) and a pronounced magnetic and gravity anomaly mark the narrow transition towards the continental crust onshore Mozambique. Magnetic spreading anomalies could not be identified north of 18.5°S (Fig. 5.1c; M33n (161 Ma); Ogg (2012)), caused by a basement depth of about 10 km and a weak magnetic field during the Jurassic Magnetic Quiet Zone (JQZ). Thus, the onset of the first fully developed oceanic crust as well as the location of the COB could not be determined, leading to a declaration as transitional crust for the area between the coast and the magnetic isochron M33n (Leinweber et al., 2013). Nevertheless, based on the similarity of the crustal structure of this transitional crust to slightly thickened oceanic crust and by extrapolating the modelled spreading velocities, Leinweber and Jokat (2012) postulated M41n (167 Ma; Ogg (2012); Fig. 5.1c) as oldest possible magnetic spreading anomaly in the Mozambique Basin. However, the great lateral extent of 350 km of the HVLCB underlying the margin is conspicuous. The great extent of the HVLCB far into the oceanic basin is very untypically for rifted continental margins, but is only sparsely constraint by diving waves in the most distal part of the P-wave velocity models of Leinweber et al. (2013). While these two seismic refraction lines provided reasonable models on the crustal structure along the north-eastern part of the margin, the nature of the south-western part remained poorly constrained.

Thus, in 2014, the MOCOM expedition (Jokat, 2014) acquired an additional seismic refraction profile in the south-western part of the margin across a prominent basement high, the Beira High. In parallel, additional potential field data were gathered along the margin to trace a possible continuation of the crustal structures in this part. The data analysis revealed a continental origin of Beira High, consisting of stretched, but partly highly intruded continental crust (Mueller et al., 2016). The adjacent area between Beira High and the coast is characterized by an 11 km thick pile of sediments filling the

Zambezi Delta Depression (ZDD) and a 7 km thick crust including a HVLCB similar to the transitional crust in the northern part of the margin. However, velocities of 6.3-6.7 km/s for the lower crust could not rule out the presence of stretched continental crust and left the location of the COB unknown (Mueller et al., 2016). Differences compared to the northern part of the margin, comprising a smaller extent of the underlying HVLCB and a slightly wider area of the pronounced negative magnetic signature, are still lacking an explanation.

In an attempt to characterize the investigated part of the Mozambican margin, we conducted a synthetic amplitude modelling along the two seismic refraction profiles of the MoBaMaSis-Cruise to make the results of the two surveys comparable. In addition, we perform a magnetic modelling along two profiles across the margin of Central Mozambique and compare the results with the conjugated margin in the Riiser-Larsen Sea to provide an explanation for the different magnetic signature. Subsequently, new findings on the amount of break-up related volcanism and implications for the tectonic evolution of the margin are discussed.

5.2 Data and modelling

5.2.1 Wide-angle seismic study

For our interpretation of the COB, the geometry and internal structure of the HVLCB along the margin is of special interest. Thus, we tried to extend the modelling for the older lines to ensure that our interpretation is based on the same principles. The starting point for a detailed analysis of the HVLCB was that Leinweber et al. (2013) reported difficulties in picking the arrivals of the refracted and reflected phases of the lower crustal layers and the mantle (Leinweber et al., 2013). These problems are caused a) by interfering arrivals with similar arrival times, and b) by the layer topography. Combined with a partly sparse number of first arrivals, this led to larger uncertainties on the extent and thickness of the lowermost layers (Leinweber et al., 2013). Therefore, in a first step, the velocity models of the two seismic refraction profiles 20070201 and 20070202 (Leinweber et al., 2013) were slightly refined, where necessary. With the subsequent amplitude modelling we intend to increase the accuracy of the model by a stepwise comparison of the refined picks with picks in synthetic seismograms calculated with a finite difference method.

In this context, for all stations the P-wave arrivals originating from the lower crust and the HVLCB were partly re-evaluated and the picks were slightly modified where necessary. The software ZP (Zelt, 2004) was utilized for picking. For the analysis,

the hydrophone channel was selected, because of its excellent quality. An automatic gain control (AGC) with an 1 s time window was applied to the data to improve the visibility of late arrivals. Additionally, a bandpass filter of 4-13.5 Hz was used, due to the focus on the identification of the long wavelength arrivals of the lower crustal phases. Assigned picking errors range between 55 to 200 ms according to the signal to noise ratio.

The partly refined arrivals entail the modification of the P-wave velocity models of [Leinweber et al. \(2013\)](#). For this, we used the 2D ray tracing software RAYINVR ([Zelt and Smith, 1992](#)) with the graphical user interface PRay ([Fromm, 2016](#)). The velocity models of [Leinweber et al. \(2013\)](#) served as starting models. Subsequently, by means of a forward modelling approach, the lower crustal layers and the upper mantle were modelled. To achieve the final velocity model, the inversion method of [Zelt and Smith \(1992\)](#) was used to calculate the best fitting velocity and depth values for each layer.

5.2.2 Amplitude modelling

Based on the partly challenging phase identification and a low ray coverage of the diving waves through the HVLCB, its extent and velocity gradient are not well constrained along the entire profile. In contrast, the Moho topography is well constrained by reflections. Therefore, an amplitude modelling (Figs. 5.2 and 5.3) of the PmP reflections is suited to adjust the velocity gradients of the HVLCB and the lower crust as well as their geometry. For this, synthetic seismograms were calculated with the finite difference (FD) program SOFI2D (version for P- and SV-waves; [Bohlen et al., 2015a](#)). Based on the FD method, the software uses a discretised depth model, where differential operators numerically approximate the wave equation. In contrast to the ray tracing method, for areas of pronounced topography, the FD-technique ensures the calculation of diffracted phases caused by abrupt changes in layer topography. Furthermore, the software's computation of the whole synthetic wave field and of the acoustic impedance allows a reliable direct comparison between the observed and synthetic amplitudes.

The subsequently described amplitude modelling follows the approach of [Mueller et al. \(2016\)](#). The models were sampled with a cell size of 25 m, resulting in a grid size of 16800 x 1400 cells for profile 20070201 and 9600 x 1200 cells for profile 20070202. The ray tracing P-wave velocity models served as input model, respectively. Additional required parameters were achieved by a simple division of the P-wave velocities by $\sqrt{3}$ for S-wave velocities, a conversion to densities by Barton's rule ([Barton, 1986](#)), as well as a conversion to quality factors (intrinsic attenuation) according to [Brocher \(2008\)](#). The seismograms were calculated for 30 s travel time and were sampled each millisecond.

A 4th order FD operator was used and the receivers were equally spaced every 150 m. To ensure an acceptable computation time as well as a sufficient resolution of the synthetic data at once, a Ricker wavelet with a centre frequency of 5 Hz was chosen as source signal. At the top of the model a plane stress free surface was applied. To reduce reflections from the outer boundaries, a convolutional perfectly matched layer (CPML; [Bohlen et al., 2015b](#)) terminated the model. After the calculation the synthetic seismograms were filtered, scaled and normalized to their maximum amplitude.

Synthetic seismograms were generated for models with a different extent of the HVLCB and with a different velocity contrast at the Moho (Figs. [5.2](#) and [5.3](#)). Throughout all models the topography of the Moho was kept fixed, but their depth was suitably adjusted to ensure that the models still explain the picks. Additionally, the converted input models (shear wave velocity, density, quality factors) were corrected. Subsequently, for a single station the PmP phase was picked in the observed data as well as in all synthetic models to compare the results. At each pick the maximum amplitude was calculated as the envelope over a time window of 20 ms. Finally, the median of the maximum amplitudes was plotted over distance. Criteria for the comparison between the observed data and the synthetic models were the location of the minima and maxima of the median as well as the general decay.

5.2.3 Magnetic modelling

A second objective of the study was to provide constraints on the opposite polarity of the magnetic edge anomalies along the conjugate margins. Thus, along the two profiles 20070201 and 20140010, a 2D magnetic modelling was performed to gain an estimate for a possible edge effect and the influence of local magnetic sources along the continental margin of Central Mozambique. The interactive gravity and magnetic modelling software IGMAS+ ([Götze, 2007](#); [Götze and Lahmeyer, 1988](#); [Schmidt et al., 2007](#)) was used to calculate the magnetic models. The layer boundaries of the respective final seismic refraction model were incorporated into a starting model along a single 2D section. The model was extended in-line by about 200 km and the section was mirrored and placed at a 200 km lateral spacing in each direction to avoid edge effects during the modelling. Subsequently, the sections were connected by triangulation and the magnetic response of the generated polyhedrons was calculated.

The high-resolution magnetic data, which were contemporaneously acquired during the acquisition of the respective seismic refraction profile ([Jokat, 2014](#); [Reichert and Neben, 2008](#)), were used as observed magnetic data (observed total magnetic field anomaly, Observed B_a). The processed magnetic data of profile 20070201 were pub-

5.2. DATA AND MODELLING

Layer	M [A/m]	κ [SI]	Q	NRM Decl. [°]	NRM Incl. [°]	Reference
Water	0	0	0	-	-	
Sediments	0.006	0.0002	0.1	-13	-53	Marello et al. 2010; Roeser et al. 2002; Schön 1983
OC. LAYER 2						Gee and Kent 2007; Harrison 1976; König and Jokat 2010;
AWI-20070201	6	0.006	40	335	-50	Schreckenberger et al. 1992
AWI-20140010	5	0.006	30	335	-50	
OC. LAYER 3						Gee and Kent 2007; Harrison 1976; Schön 1983;
AWI-20070201	2	0.006	15	335	-50	Schreckenberger et al. 1992
AWI-20140010	1	0.006	10	335	-50	
Cont. Upper Crust	0.9	0.03	0.2	-13	-53	Hemant 2003; Marello et al. 2010
Cont. Middle Crust	0.45	0.015	0.2	-13	-53	
Cont. Lower Crust	0.2	0.005	0.4	-13	-53	Arkani-Hamed 1993; Marello et al. 2010
Mantle	0.03	0.0006	0.8	-13	-53	Ferré et al. 2014; Marello et al. 2010
HVLCB	0.04	0.001	0.6	335	-50	Gee and Kent 2007; Roeser et al. 2002
INTRUSION						Aubourg et al. 2008; Jones et al. 2001; Schön 1983
AWI-20070201	7.75	0.01	30	335	-50	
AWI-20140010	6.5	0.01	25	335	-50	
SDRs	4.75	0.005	35	335	-230	Delius et al. 2003; Direen and a.J. Crawford 2003; Roeser et al. 2002
Lava Flows	5.1	0.005	40	335	-50	Delius et al. 2003; Direen and a.J. Crawford 2003; Roeser et al. 2002

Table 5.1: Layer parameters for the magnetic modelling. The columns contain the layer declaration, the total magnetization M, the assigned magnetic susceptibility κ (kappa), the assigned Königsberger ratio Q, and the assigned declination (Decl.) and inclination (Incl.) of the natural remnant magnetization (NRM).

lished by [Leinweber and Jokat \(2012\)](#), and of profile 20140010 by [Mueller et al. \(2016\)](#). Additional magnetic data were extracted from the EMAG2 grid (version 2, without directional gridding; [Maus et al., 2009](#)) for onshore Mozambique. Based on a general reference level of 4 km above the WGS84 ellipsoid for the onshore magnetic data of the EMAG2 grid, these data were downward continued to the WGS84 ellipsoid. After slight adjustments they were merged with the shipborne magnetic data.

Information on the respective layer parameters for a magnetic modelling in this area

are restricted to studies about modelled magnetic spreading anomalies and magnetic sources in the upper oceanic crust (König and Jokat, 2010; Leinweber et al., 2013; Segoufin, 1978; Simpson et al., 1979). Additionally, based on the limited drill hole depth of the exploration wells along the Mozambican shelf, information about the magnetic properties of the crustal rocks is missing, too. Therefore, most modelling parameters for the crustal fabric base on average values of global studies and published magnetic models, as well as on results of drill holes outside the study area. The applied layer parameters and their references are summarized in Table 5.1. By knowing the magnetic field intensity of the recent earth's magnetic field in the survey area (about 31000 nT), the magnetic property of the respective layer is defined by its assigned magnetic susceptibility χ (crucial for the amount of the induced magnetization), the Königsberger ratio Q and by the declination and inclination of the natural remnant magnetization (NRM). Some references state only a value for the NRM. In this case, a common Q for this layer (Marello et al., 2013; Schön, 1983) was used for the conversion to the magnetic susceptibility. For simplification, the mean present-day declination and inclination of the earth's total magnetic field in the survey area were assigned as the direction of the NRM of the sedimentary and crystalline rocks. Evidence about the declination and inclination of the total magnetic field at the time of the initial Gondwana break-up rely on investigations on break-up related emplaced dykes onshore Mozambique (Jones et al., 2001). These values were used as a rough estimation for the direction of the NRM of the magmatic rocks. For assigning a reverse layer magnetization compared to the present direction of the total magnetic field, the inclination value was simply rotated by 180° . During modelling, the main focus was on the continent-ocean transition (COT) and its adjacent areas. In contrast, for modelling the seafloor spreading magnetic anomalies in the oceanic domain along the profiles, the modelling software isn't suited and a loose fit was considered as sufficient in these areas. Concerning the Curie depth, underneath a rock temperature increases to greater than 550°C and it loses its ferromagnetic characteristics, a global study of Artemieva (2006) estimates a Curie depth of 30-35 km for the area onshore Central Mozambique. In our crustal models, this depth range coincides with the transition of the middle to the lower continental crust. Taking the very old oceanic crust (> 140 Ma) and a mean basement depth of about 8 km into account, we suggest in the oceanic domain the Curie depth inside the gabbros of oceanic layer 3.

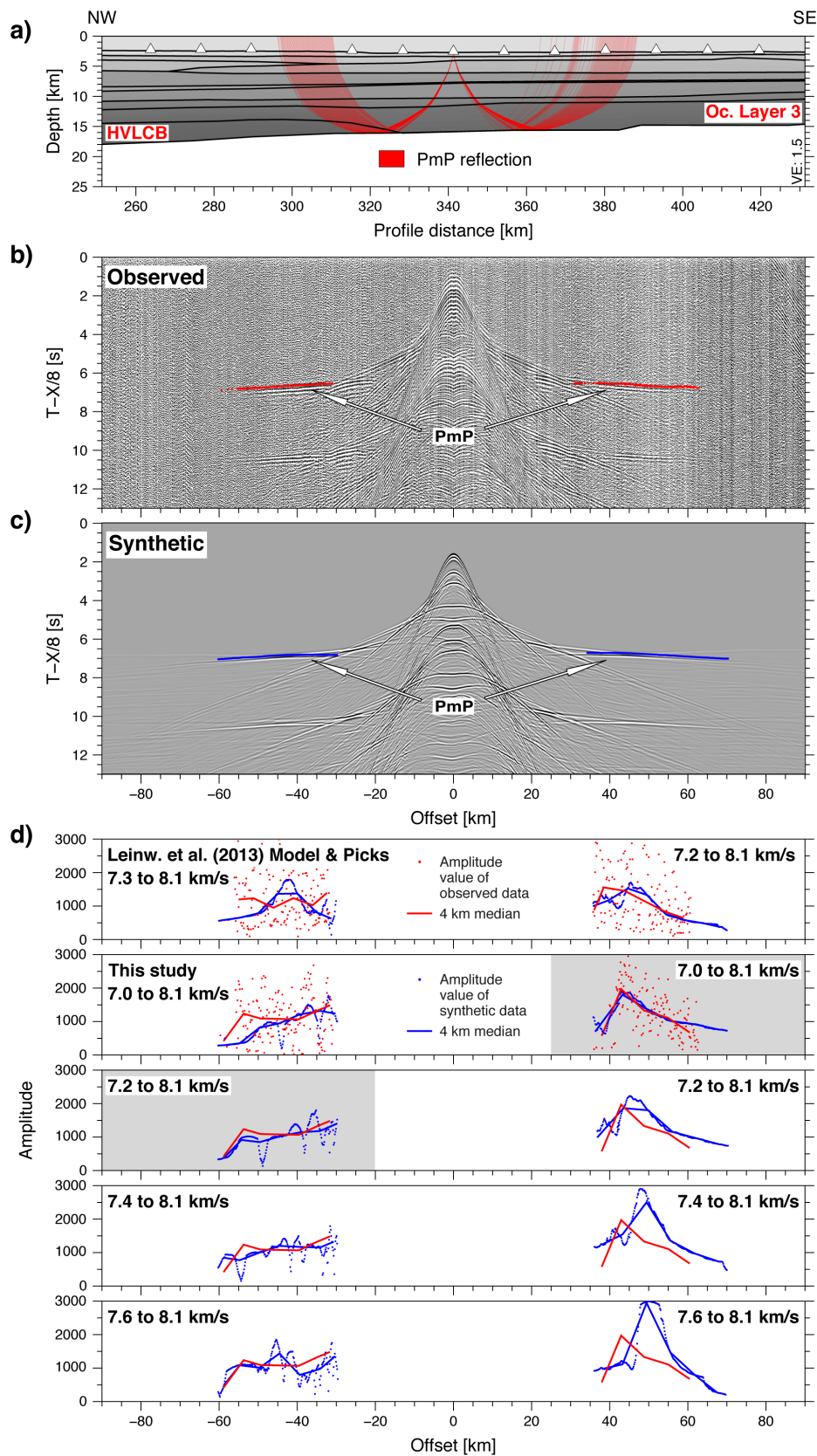


Figure 5.2: Results of the amplitude modelling of the PmP phase for station 14 of profile 20070201. Continues ...

5.3 Results

5.3.1 Wide-angle seismic study incl. amplitude modelling

Refining parts of the velocity models of [Leinweber et al. \(2013\)](#) led to changes of the characteristics of the crustal layers. The sediment layers were not changed at all. The differences between the revised models of this study to the models of [Leinweber et al. \(2013\)](#) are summarized in [Table 5.2](#). Changes of the velocities of the lower crust and HVLCB are mostly within the error range. However, changes in the layer thickness of the lower crust and the HVLCB, as well as of the Moho topography, are partly clearly beyond the error range. Based on the low ray coverage of deep penetrating diving waves in the more distal part of the HVLCB, its extent and basal velocities are not well constrained. Therefore, an amplitude modelling was applied and in the following its results ([Figs. 5.2](#) and [5.3](#)) are described.

Profile 20070201

Along profile 20070201 ([Fig. 5.4a](#)) an amplitude modelling was applied to six stations. The results for station 14 are shown in [Fig. 5.2](#). The station is located on oceanic crust, where the Moho is quite flat ([Fig. 5.2a](#)). Here, the PmP phase is clearly visible for -30 to -60 km and 35 to 65 km offset ([Fig. 5.2b](#)). For positive offsets, the amplitude modelling for the model of [Leinweber et al. \(2013\)](#) (based on their picks and model), with a velocity contrast of 7.2 km/s at the crust-mantle boundary, shows a similar decay of the median, but the local maximum of the synthetic data is shifted by about 10 km ([Fig. 5.2d](#)). However, the amplitude modelling for the refined model of this study shows for positive offsets a good fit for a velocity contrast of 7.0 to 8.1 km/s at the Moho. Models with greater velocity contrasts show a similar trend of the median, but the local maximum is as well clearly shifted to greater offsets. On the other side, at negative offsets the model of [Leinweber et al. \(2013\)](#) shows no clear correlation at all between the observed and the synthetic data. For the refined model, a velocity contrast at the Moho of 7.2 to 8.1 km/s depicts the best correlation. The other models show

Figure 5.2 (cont.): a) Calculated rays of the PmP reflection obtained by ray tracing for the favoured model. b) Seismogram of the observed data at station 14. Picks of the PmP phase are shown as red dots. c) Synthetic seismogram for station 14, based on the favoured model. Picks of the PmP phase are shown as blue dots. d) Maximal amplitude values of the PmP phase for the observed and synthetic data. For median calculation a window length of 4 km was used. The preferred models are shaded in grey.

a similar trend, too. However, for the 7.0-model, the location of the second maximum at -55 km of the synthetic data does not fit. For the 7.4 and 7.6-model, the location of the first maximum is shifted to greater offsets and the decay of the median differs slightly.

The examination of the amplitude modelling of stations 5 and 10 (located in the more distal oceanic part, Fig. 5.4a) consistently reveals the best correlation for a seismic velocity of 7.0 km/s at the Moho. In contrast, the amplitude modelling of stations 18, 22 and 28 (located closer to the COB, Fig. 5.4a) depicts the best fit for the 7.2- and 7.4-models. Consequently, we favour the interpretation that the south-eastern limitation of the HVLCB is identified by the amplitude modelling of station 14 and is located at km 325 (Fig. 5.4a) instead of at km 450 (Leinweber et al., 2013).

Profile 20070202

At profile 20070202 (Fig. 5.4b), the extent and the basal velocities of the HVLCB are as well investigated by an amplitude modelling at five stations. Fig. 5.3 presents the results for station 6, which is located close to the onset of oceanic crust. Here, the reflected phase of the Moho (PmP) is visible to both sides in a 35 km wide range (Fig. 5.3b). The amplitude modelling of the model of Leinweber et al. (2013), with a basal velocity of about 7.4 km/s, reveals only a low correlation between the observed and the synthetic data (Fig. 5.3d). In contrast, the modelling of the re-evaluated model based on this study confirms a velocity contrast of 7.4 to 8.1 km/s. This good fit is caused by the adjusted Moho topography compared to the model of Leinweber et al. (2013), which leads in general to a similar trend of the median and shows the best fit for a basal velocity of 7.4 km/s (Fig. 5.3d). In comparison, for models with lower basal velocities the first local maximum is located at smaller offsets. On the other hand, a higher velocity (7.6-model) shows a slightly different trend and a different decay of the median. The amplitude modelling of station 2, located at the transition to the distinct continental crust (Fig. 5.4b, COT), reveals the best fit for a velocity contrast of 7.4 to 8.1 km/s, too. The modelled stations 9 and 10 in the oceanic domain showed a decrease of the basal velocities to 7.2 km/s for kms 290-350 (Fig. 5.4b). Further south-east, station 11 depicts the best fit for the 7.0-model, which marks the southern termination of the HVLCB.

In summary, the re-evaluation of the picks of the crustal phases and the amplitude modelling along both lines led to changes of the extent of the HVLCB. In comparison with the velocity-depth models of Leinweber et al. (2013), its extent is shortened by 145 km along profile 20070201 (Fig. 5.4a). At profile 20070202, according to Leinweber

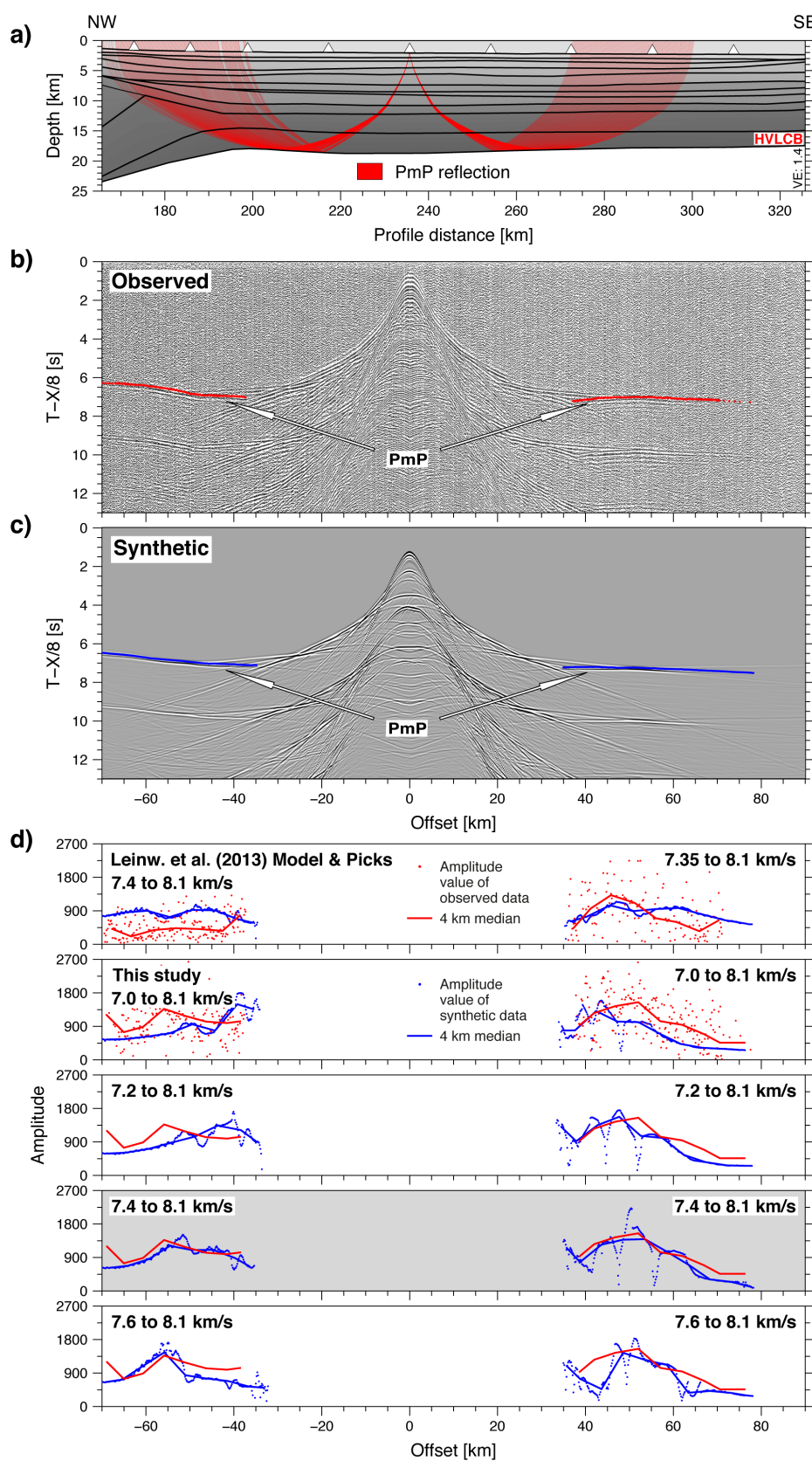


Figure 5.3: Results of the amplitude modelling of the PmP phase for station 6 of profile 20070202. Continues ...

et al. (2013), the HVLCB extends beyond the end of the profile. Thus, its extent is shortened by 60 km at minimum.

5.3.2 Magnetic modelling

Profile 20070201

The observed total magnetic field anomaly varies between +50 nT and -300 nT along profile 20070201 (Fig. 5.5a, blue line). Here, the distinct continental and oceanic areas are characterized by a similar magnetic anomaly of about 0 nT to -50 nT. A prominent minimum marks the transition from the thick continental crust to the thinner crust in the Mozambique Basin. The starting model already revealed a good correlation between the observed and modelled B_a . However, in the COT the calculated anomaly didn't fit.

In the final magnetic model, typical susceptibility values χ and Königsberger ratios Q for oceanic crust were used in the area, where clearly identified magnetic spreading anomalies (Leinweber and Jokat, 2012) already proofed the oceanic nature (Fig. 5.5a, oceanic domain). Their magnetization is dominated by a strong NRM. Hence, the oceanic layer 2 shows a magnetization of 6 A/m with a Q of 40 and layer 3 a magnetization of 2 A/m with a Q of 15. In contrast, for continental crust predominates the induced magnetization, expressed by a higher χ and a lower Q (Table 5.1). Accordingly, the upper continental crust is characterized by a χ of 0.03 and a Q of 0.2 resulting in a total magnetization of 0.9 A/m. For the deeper layers of the continental crust χ decreases and Q slightly increases. Sedimentary and mantle rocks show very low χ and Q and are treated as nearly non-magnetic, which have only minor influence on the modelled B_a . Similarly, due to a great fraction of ultramafic rocks, which contain only paramagnetic silicates and spinels (Gee and Kent, 2007), the HVLCB shows a low χ of 0.001 and a Q of 0.6. Additional magnetic sources are required in the COT to obtain a better fit between the observed and modelled B_a (Fig. 5.5a). Interpretations of seismic reflection studies in this area (Castelino et al., 2015; Mahanjane, 2012; Reichert and Neben, 2008) depict evidence for the existence of magmatic material (e.g. seaward

Figure 5.3 (cont.): a) Calculated rays of the PmP reflection obtained by ray tracing for the favoured model. b) Seismogram of the observed data at station 6. Picks of the PmP phase are shown as red dots. c) Synthetic seismogram for station 6, based on the favoured model. Picks of the PmP phase are shown as blue dots. d) Maximal amplitude values of the PmP phase for the observed and synthetic data. For median calculation a window length of 4 km was used. The preferred model is shaded in grey.

5. MAGMATISM ALONG THE CENTRAL COAST OF MOZAMBIQUE

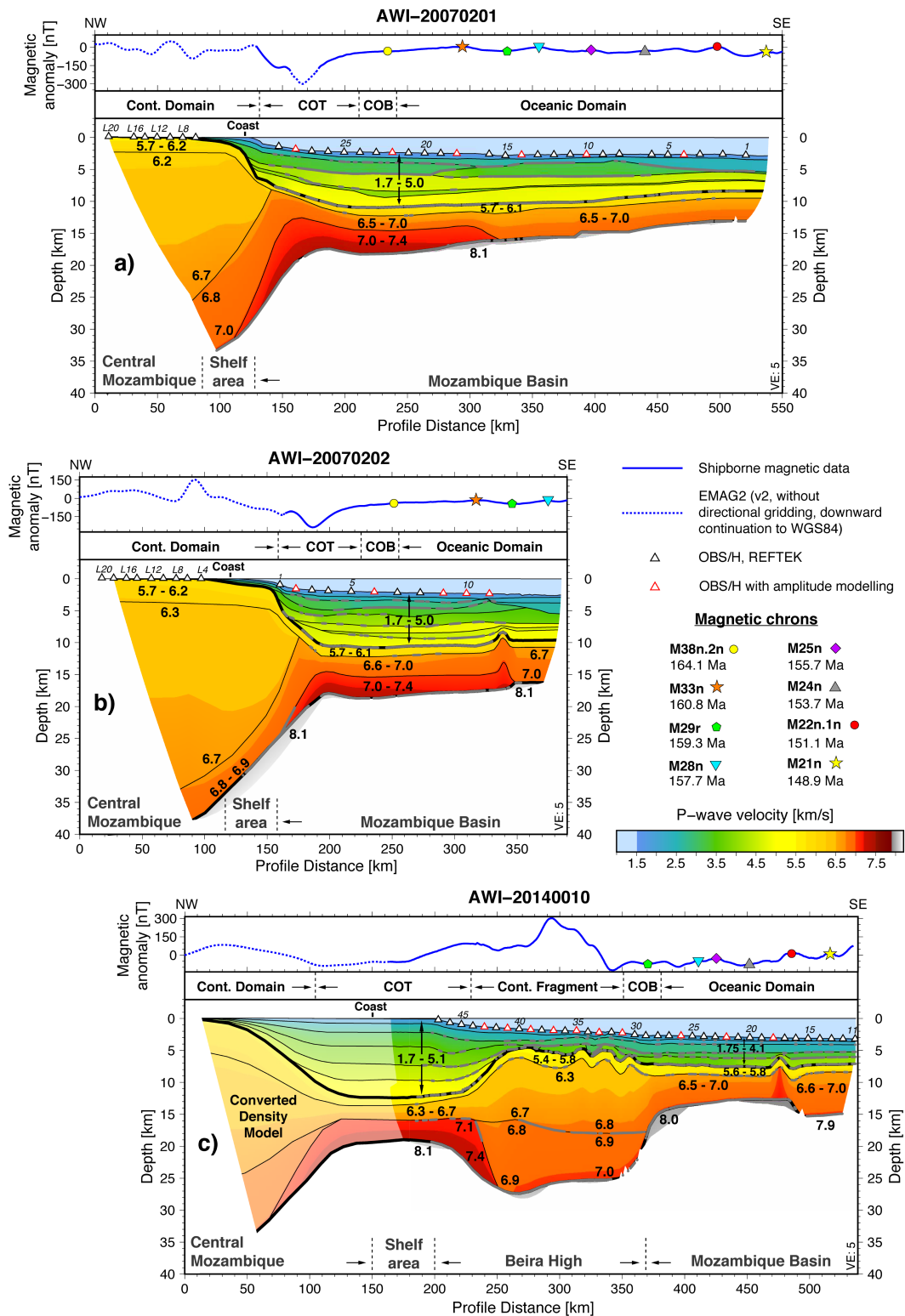


Figure 5.4: Refined final P-wave velocity models, including the results of the amplitude modelling, of profiles a) AWI-20070201, b) AWI-20070202 and c) AWI-20140010. P-wave velocity model, processed shipborne magnetic data as well as converted density model of profile AWI-20140010 were taken from [Mueller et al. \(2016\)](#). The locations of the selected magnetic chrons up to M33n are based on [Leinweber and Jokat \(2012\)](#). The position of the oldest magnetic spreading anomaly M38n.2n is based on this study.

5.3. RESULTS

a) Profile 20070201				
Investigated phases	This study		Leinweber et al. (2013)	
	t_{rms} [s]	χ^2	t_{rms} [s]	χ^2
Pc2, Pc3	0.067	0.618	0.061	0.367
Pc3P, PmP	0.072	0.572	0.057	0.247
Total	0.065	0.478	0.061	0.416
Changes in crustal composition	This study		Leinweber et al. (2013)	Error range
Velocity at upper boundary of lower crust	kms 230-530: 6.5 km/s		6.4 km/s	± 0.1 km/s
Thickness of lower crust	kms 230-530: 2.5 km		1.5-2 km	± 0.5 km
Thickness of HVLCB	3.5 km		2-5 km	± 0.5 km
Extent of HVLCB	215 km		360 km	
b) Profile 20070202				
Investigated phases	This study		Leinweber et al. (2013)	
	t_{rms} [s]	χ^2	t_{rms} [s]	χ^2
Pc2, Pc3	0.059	0.555	0.081	0.590
Pc3P, PmP	0.106	1.109	0.102	0.822
Total	0.074	0.738	0.079	0.621
Changes in crustal composition	This study		Leinweber et al. (2013)	Error range
Velocity at upper boundary of lower crust	kms 225-330: 6.6 km/s		6.4-6.7 km/s	± 0.1 km/s
Thickness of lower crust	kms 225-330: 2.5-3.5 km		2.5-3 km	± 0.5 km
	kms 330-350: 4 km		1 km	± 0.5 km
	kms 350-375: 5km		1 km	± 0.5 km
Thickness of HVLCB	kms 225-330: 2.5-3.5 km		4 km	± 0.5 km
	kms 330-350: 4 km		7 km	± 0.5 km
Moho depth changed at kms 250-350	17.5-19 km		19 km	± 1 km
Extent of HVLCB	190 km		>250 km	

Table 5.2: Differences between refined models of this study to models of [Leinweber et al. \(2013\)](#). The profile distances refer to the final P-wave velocity models of Figures 5.4a and 5.4b.

dipping reflectors) in the upper crust. Therefore, two magnetic features with an increased NRM were incorporated in the model. Based on the strong negative anomaly (Fig. 5.5a, kms 135-185), a magnetic body with a reversed polarization compared to the present direction of the earth's magnetic field with a χ of 0.005 and a Q of 35 was

defined, resulting in a magnetization of 4.75 A/m. This extends from kms 155-210, terminating slightly south-east of the position of the previously published extrapolated magnetic spreading anomaly M41n (Leinweber et al., 2013). The second anomaly mass, located at kms 125-155, depicts a polarization identical to the present direction of the earth's magnetic field with a magnetization of 7.75 A/m (χ of 0.01; Q of 30). Consequently, by means of the two additional anomaly masses in the COT, a sufficient fit between the observed and the modelled B_a is achieved (Fig. 5.5a, blue and red line). Local differences of maximum 50 nT still occur in the distinct continental and oceanic areas.

Profile 20140010

Along profile 20140010, the observed B_a varies between +300 nT and -150 nT (Fig. 5.5b, blue line). Positive anomalies are located in the area of the distinct continental crust, at Beira High and its north-western flank, as well as in the most south-eastern part of the profile close to the volcanic islands of Bassas da India and Île Europa (Fig. 5.1a). An equal anomaly of about -50 nT is visible in the shelf area and in the oceanic domain of the Mozambique Basin (Fig. 5.5b). By assigning similar magnetization values as for profile 20070201, the starting model already revealed a good correlation between the observed and modelled B_a . A sole exception is the area of Beira High, where the modelled anomaly was smaller by up to 200 nT.

The final magnetic model (Fig. 5.5b) shows a slightly lower NRM of the oceanic crust, compared to profile 20070201, resulting in a Q of 30 for the oceanic layer 2 and a Q of 10 for layer 3 (Table 5.1). Seismic reflection and refraction studies (Mahanjane, 2012; Mueller et al., 2016) indicate the existence of magmatic material at the centre and the north-western flank of Beira High, which coincides with the position of the highest positive anomalies. Therefore, an anomaly mass, located at kms 285-335, was included in the model. A χ of 0.01 and a Q of 25 are suited to fit the observed B_a at the centre of Beira High. The second anomaly mass with a high NRM (Q of 40) is placed at kms 185-240. Subsequently, minor differences between the observed and the modelled B_a remained only in the oceanic domain.

5.3. RESULTS

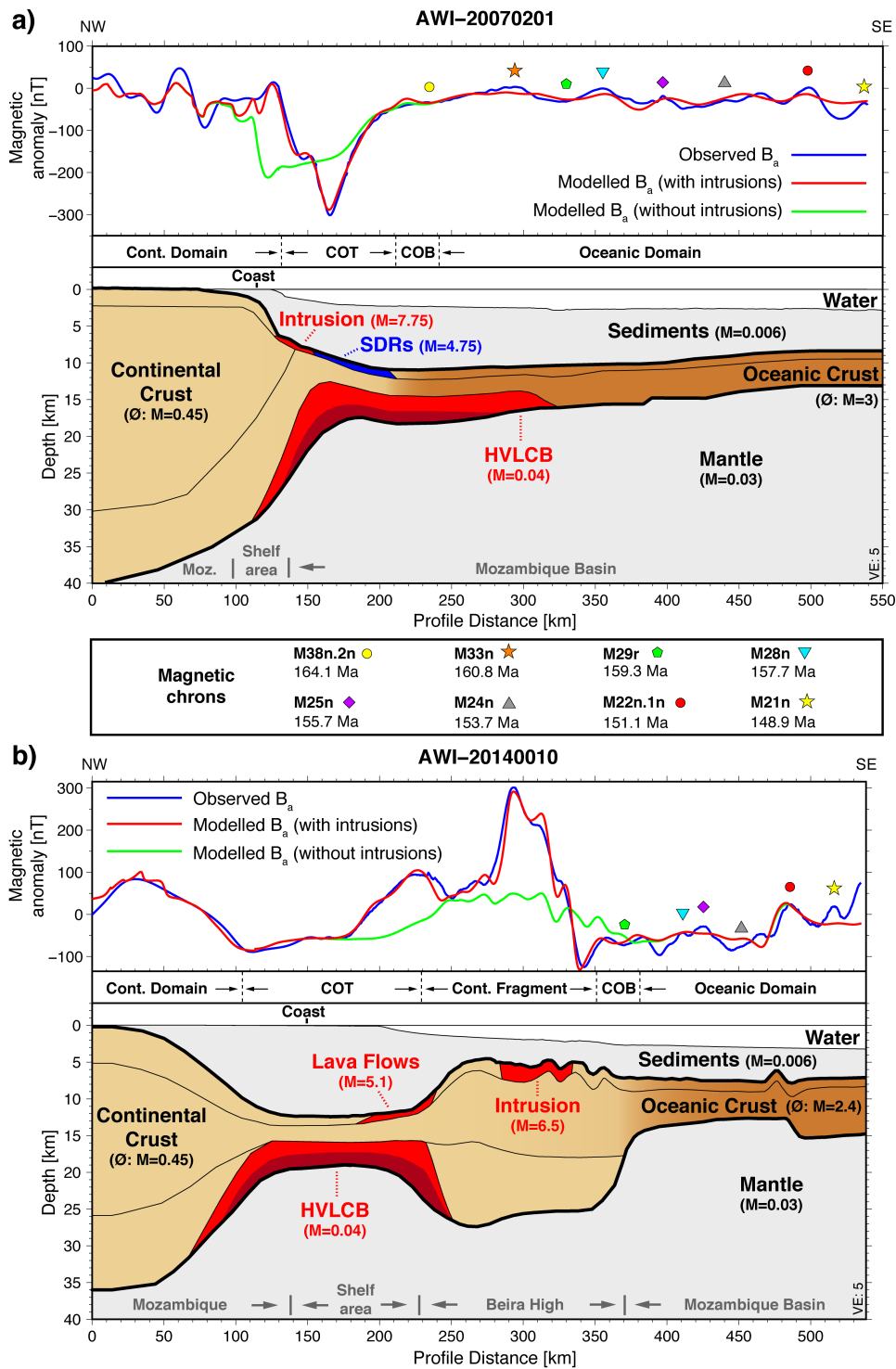


Figure 5.5: Magnetic models of profiles a) AWI-20070201 and b) AWI-20140010. The upper panels show the observed total magnetic field anomaly (Observed B_a) and the modelled ones, respectively. The modelled total magnetic field anomaly with intrusions (Modelled B_a (with intrusions)) contains additionally the magnetic response of the layers ‘intrusion’, ‘lava flows’ and ‘SDRs’. The positions of the selected magnetic chrons up to M33n are based on [Leinweber and Jokat \(2012\)](#). The position of the oldest magnetic spreading anomaly M38n.2n (Fig. 5.5a, upper panel, km 235) is based on this study. The numbers indicate the total magnetization M . For continental and oceanic crust only averaged values are shown (detailed values of all layers in Table 5.1).

5.4 Discussion

5.4.1 Crustal variation and extent of the HVLCB

The re-evaluation of the refraction profiles by means of the amplitude modelling confirmed in general the models of [Leinweber et al. \(2013\)](#). However, changes in the crustal composition, especially in the extent of the HVLCB, had to be introduced to achieve a better fit of the amplitudes. At profile 20070201, the investigation revealed normal oceanic crust ([White et al., 1992](#)) with 5.5-6 km thickness and a constant basal velocity of 7.0 km/s for the area south-east of km 325 (Fig. 5.4a, oceanic domain). Additionally, this shows a similar composition as oceanic crust of the same age identified at profile 20140010, kms 390-460 (Fig. 5.4c, oceanic domain). Only a small section (kms 350-385) of normal oceanic crust is covered by profile 20070202 (Fig. 5.4b, oceanic domain). This section is located south-east of an adjacent buried seamount, where the lower oceanic crust thickens to 5.5 km. In agreement with profile 20140010, the accumulation of magmatic material might be caused by the profile crossing a fracture zone ([Leinweber et al., 2013](#)), leading to the rise of magma on one side and to a thickening of the lower crust at the other side ([Mueller et al., 2016](#)).

Consistently, all three profiles show an area with high lower crustal velocities up to 7.4 km/s (Fig. 5.4). In this area the transition from the continental to oceanic crust is expected. For kms 200-325 at profile 20070201 (Fig. 5.4a, south-east of COB) and kms 210-330 at profile 20070202 (Fig. 5.4b, south-east of COB), a similar crustal composition of the crust overlying the HVLCB is identified, characterized by velocities of 5.7-6.1 km/s for oceanic layer 2 and 6.5/6.6-7.0 km/s for layer 3. By means of 1D velocity profiles, [Leinweber et al. \(2013\)](#) already showed their affinity to normal oceanic crust ([White et al., 1992](#)). Additionally, a clear similarity arises to the distinct oceanic crust in the south-eastern part of the profiles (Figs. 5.4a and 5.4b, oceanic domain) by comparing the layer velocities. Hence, we expect a partial continuation of the oceanic crust in the area underlain by the HVLCB.

In contrast, for the profile section close to the margin (Figs. 5.4a and 5.4b, COT), the velocity structure does not allow a clear identification of the nature of the crust. However, the likely presence of SDRs ([Reichert and Neben, 2008](#)), which are thought to be emplaced directly before the onset of oceanic crust, and a tilted basement towards the distinct continental crust in this area as well as a clear thickening of the crust, rule out the extension of normal oceanic crust far into the COT (Figs. 5.4a and 5.4b). Alternate compositions are the presence of exhumed mantle or stretched, highly intruded continental crust. The occurrence of extruded magmatic material, as well as the rise

of the top of the HVLCB in the COT might be suggestive for an exhumed mantle. However, a clear velocity contrast of 7.4 to 8.1 km/s at the Moho does not imply an exhumation of intruded mantle material. Furthermore, the existence of exhumed mantle is usually related to highly stretched margins (Franke, 2013; Thybo and Artemieva, 2013), as observed at magma-poor ones (Peron-Pinvidic et al., 2013). In contrast, our seismic refraction study reveals a narrow COT (Figs. 5.4a and 5.4b) from the distinct thick continental crust to the thinned crust in the Mozambique Basin, most likely due to a short period of rifting affecting this part of the margin (Mahanjane, 2012). This is supported by the plate kinematic reconstructions, suggesting an anticlockwise rotation of East Antarctica at its first stage (Leinweber and Jokat, 2012), which might lead to a longer lasting rifting in the west and a short termed in the north-eastern part of the margin of Central Mozambique. Therefore, the presence of stretched continental crust is suggested in the narrow COT.

In the ZDD, profile 20140010 depicts lower velocities of 6.3-6.7 km/s for the lower crust (Fig. 5.4c, kms 165-200), overlying the HVLCB (Fig. 5.4c). Mueller et al. (2016) stated no definite classification of their origin, due to a partly similar velocity range for highly stretched continental and oceanic crust. Furthermore, no clear evidence is available about the basement topography in the ZDD, because of overlying volcanic rocks and an 11 km thick sediment pile. The fact that this area is characterized by lower crustal velocities compared to the distinct oceanic crust in the south-eastern part of this profile (Fig. 5.4c, oceanic domain) and to the profiles in the north-eastern part of the margin (Figs. 5.4a and 5.4b, oceanic domain), might exclude the presence of normal oceanic crust in the ZDD. The clear velocity contrast at the upper and lower boundary of the HVLCB points towards mainly stretched continental crust. However, the occurrence of partly plane deposited lava flows in the ZDD and a probably longer phase of rifting affecting this area (Leinweber and Jokat, 2012; Mahanjane, 2012), might allow the presence of exhumed mantle, too (Mahanjane, 2012).

Conspicuous is the almost equal extent of the HVLCB of about 190-215 km along all three profiles (Fig. 5.4). A global comparison for the HVLCB of volcanic rifted margins reveals similar extents ranging between 90-225 km (Voss and Jokat, 2007). Off Mozambique, the HVLCB is about 3 km thick on average, with a maximum thickness of 7 km close to the margin. Based on the results of the amplitude modelling, profiles 20070201 and 20070202 show a lateral variation of the basal velocities for the HVLCB of 7.2-7.4 km/s (Figs. 5.4a and 5.4b). In contrast, the complete landward extent of the HVLCB along profile 20140010 was not covered by the seismic refraction study, but indicates a constant velocity of 7.4 km/s at the crust-mantle boundary (Fig. 5.4c). Regarding the origin of the HVLCB, we follow the argumentation of Leinweber et al.

(2013), which identified a highly active upper mantle convection and increased mantle potential temperatures during the break-up, suggesting the existence of a magmatic underplating in this area. The presence of intrusive and extrusive magmatic material in this area (Mahanjane, 2012), as well as clear seismic reflections at the Moho, support the idea of magmatic underplating along the margin (Mjelde et al., 2002; Thybo and Artemieva, 2013). Based on commonly known basal velocities for normal lower crust of 7.2 km/s (Thybo and Artemieva, 2013; White et al., 1992), we interpret areas with velocities of greater than 7.2 km/s (Fig. 5.5, dark red) as magmatic underplating and areas with 7.0-7.2 km/s as intruded lower crust. Consequently, magmatic material of maximum 3 km thickness underplates the continental margin of Central Mozambique. These results indicate the presence of normal oceanic crust of about 6.5 km thickness to the southern onset of the COT along profiles 20070201 and 20070202 (Figs. 5.4a and 5.4b, COB) and thin crust of about 5 km thickness in the shelf area at profile 20140010 (Fig. 5.4c, COT).

5.4.2 Magnetic edge anomaly and the location of the COB

In the area of the distinct crustal domains, differences between the magnetic models of profile 20070201 and 20140010 only occur in the oceanic domain (Fig. 5.5). Here, about 1 A/m lower values are depicted for the oceanic crust at profile 20140010. However, common magnetization values of oceanic rocks are in a similar range, comprising values of 4-6 A/m for oceanic layer 2 and 1-2 A/m for layer 3 (Gee and Kent, 2007). The variation in magnetization between the two profiles might be attributed to a slightly different age of the crust and a different magma composition and supply, caused by the position of Beira High.

The magnetic modelling for profile 20070201 without additional anomaly masses reveals a negative magnetic edge anomaly in the transitional area (Fig. 5.5a, COT), but with a different shape and only about half of the amplitude of the observed negative magnetic anomaly. Therefore, additional magnetic sources are included to model the magnetic anomaly on profile 20070201 close to the margin and on profile 20140010 at Beira High. The magnetic sources had to be modelled with a strong NRM (Q of 25-40), which points towards magmatic material. Based on their induced magnetization, these can be classified into two groups. Along both profiles at the transition towards thinner crust, the magnetic sources have a χ of 0.005 (Fig. 5.5a (kms 155-210), 5.5b (kms 185-240)). In contrast, the magnetic sources in the area of thicker continental crust are characterized by a χ of 0.01 (Fig. 5.5a (kms 125-155), 5.5b (kms 285-335)). Differences in magnetization of this scale are observed by Miltitzer and Scheibe (1981)

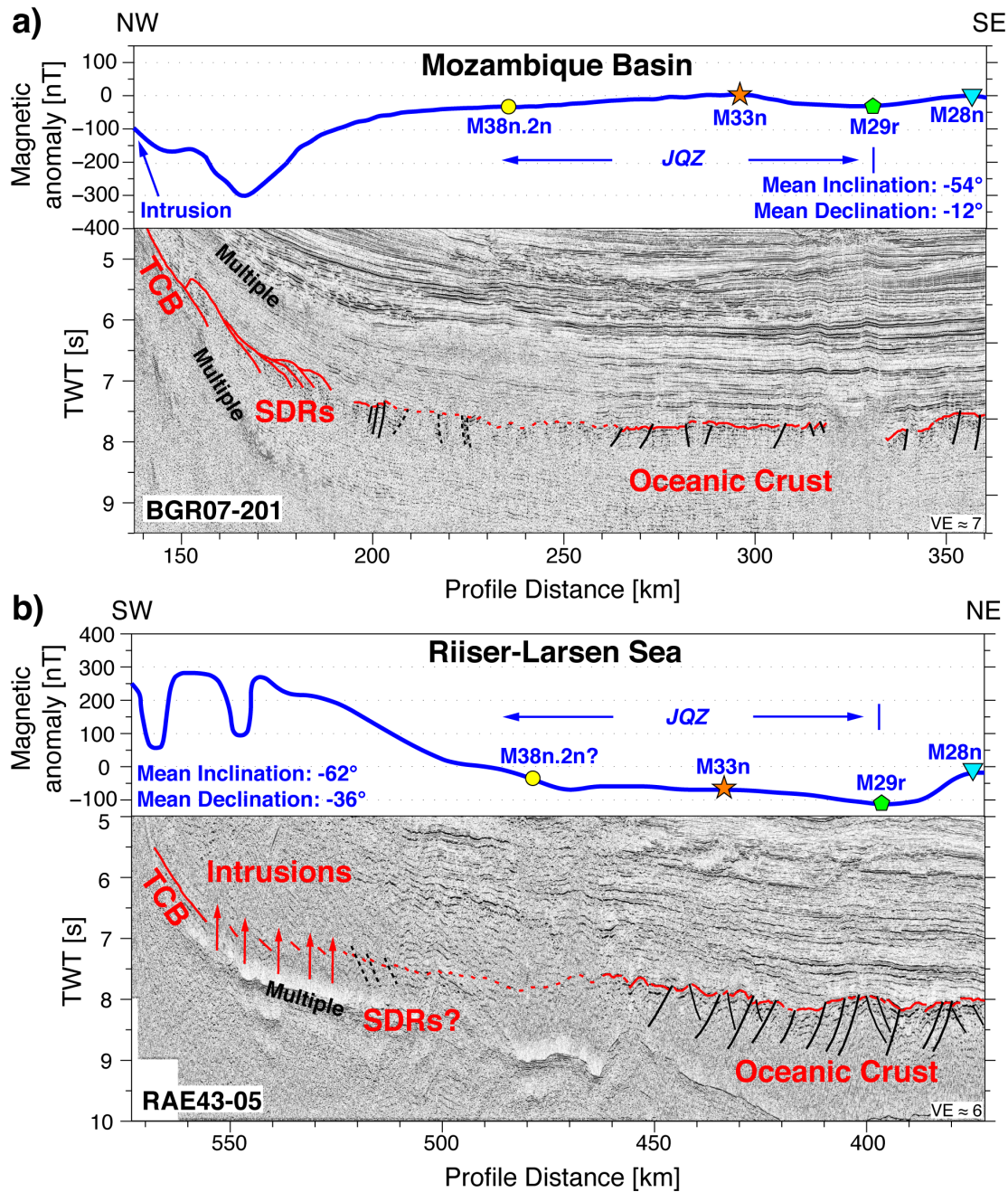


Figure 5.6: Basement and magnetic interpretation for two seismic reflection profiles of the conjugated margins. a) Seismic data of profile BGR07-201 is processed and published by [Castelino et al. \(2015\)](#). The shipborne magnetic data and the magnetic chrons up to M33n are taken from [Leinweber and Jokat \(2012\)](#). The oldest magnetic spreading anomaly M38n.2n is based on this study. Abbreviations: COB: Continent-Ocean Boundary, COT: Continent-Ocean Transition, JQZ: Jurassic Magnetic Quiet Zone, SDRs: Seaward Dipping Reflectors, TCB: Top of Continental Basement. b) Seismic data of profile RAE43-05 was acquired during the Polar Marine Geosurvey Expedition (PMGRE-98) RAE-43 and is taken from the Antarctic Seismic Data Library System (SDLS). Simultaneously acquired magnetic data is taken from [Leitchenkov et al. \(2008\)](#). New identifications of magnetic chrons in the Riiser-Larsen Sea are based on the continuation of the identifications of [Leinweber and Jokat \(2012\)](#).

between effusive and intrusive rocks. Caused by a rapid crystallisation of effusive rocks, they contain more fine-grained ferromagnetic particles as intrusive rocks, resulting in lower values of κ (Miltitzer and Scheibe, 1981). This classification is supported by the results of the seismic reflection studies along the according seismic reflection profile (Castelino et al., 2015; Mahanjane, 2012; Mueller et al., 2016; Reichert and Neben, 2008). Following the interpretation of Reichert and Neben (2008), there is evidence for SDRs (effusive rocks) at kms 150-190. A magnetic source body with a reversed polarization compared to the present earth's magnetic field and a magnetization of 4.75 A/m is sufficient to better fit the additional strong negative magnetic anomaly (Fig. 5.5a; SDRs). Similar magnetizations are already identified for drilled lava flows in the Indian Ocean (Delius et al., 2003). This magnetic source extends about 20 km further south-east than the identified SDRs in the seismic reflection data (Fig. 5.6a), terminating seaward beyond the location of the previously published magnetic spreading anomaly M41n. The seismic reflection data show a disturbed basement topography with partly low amplitude reflections in the area south-east of the SDRs at kms 190-260 (Fig. 5.6a). This also affects the overlying sedimentary layers and might be caused by hydrothermal venting in this area during its formation. The basement is slightly tilted seawards up to km 235. South-east of km 235, the basement levels out. We interpret this change in the basement geometry at km 235 as onset of the normal oceanic crust. In order to calculate the age of the oceanic crust at this location, we apply the same spreading velocity of 16 km/Ma (Leinweber et al., 2013) as for the time after M33n. This yields an age of 164.1 Ma (chron M38n.2n) for the initial formation of normal oceanic crust along this profile. A north-westwards extension of proto-oceanic crust below the SDRs cannot be ruled out by means of this magnetic study. The modelled magnetic body at kms 125-155 (Fig. 5.5a), which might significantly contribute to the margin-parallel, positive magnetic anomaly (Fig. 5.1c) is not covered by one of the seismic reflection profiles available for this study. However, Jaritz et al. (1977) identified volcanic outcrops in the area of the Moma district just landward of profile 20070201 with an age of 177 ± 3 to 157 ± 3 Ma. Furthermore, Reeves et al. (2016) mapped the coast-parallel Limpopo-Angoche dykes (Early to Mid Jurassic age) in this area, which support the possibility of intrusions in this part of the profile.

Surprisingly the conjugate margin in the Riiser Larsen Sea (Antarctica) is not bounded by a negative magnetic anomaly in the north. Instead, only a strong positive magnetic anomaly up to 400 nT is present. Figure 5.6b shows the sediment and basement geometry along the seismic reflection line RAE43-05 (Leitchenkov et al., 2008), which is almost conjugate to our refraction profile 20070201 and the reflection line BGR07-201 off Mozambique (Fig. 5.6a). Leitchenkov et al. (2008) suggest strongly stretched con-

tinental crust for the displayed part of the profile in the Riiser Larsen Sea, and propose chron M24B as the oldest magnetic spreading anomaly, which is located beyond the north-eastern termination of the displayed part of the profile. However, based on the investigation of [Leinweber and Jokat \(2012\)](#), who identified chron M25n in the western part of the Riiser-Larsen Sea, and by a clear similarity to the magnetic anomaly along profile 20070201 at the conjugated margin, we suggest conformably the existence of the magnetic spreading anomalies up to M33n in this part of the Riiser-Larsen Sea. Taking the basement faults tilted towards the continent and a rough basement topography into account (Fig. 5.6b), we favour the interpretation of oceanic crust extending south-westwards closer to the Riiser-Larsen Sea coast. The prominent positive coast-parallel magnetic anomaly characterizing the margin of the Riiser-Larsen Sea (Fig. 5.1d), is visible in the southern end of the profile (Fig. 5.6b). Here, the seismic reflection line crosses the northern edge of this magnetic anomaly and provides good evidence for the existence of intrusions pinching through the basement into the lowest sediment layer (Fig 5.6b, kms 525-555). Based on a magnetic modelling, [Leitchenkov et al. \(2008\)](#) states a magnetization of 0.35-0.7 A/m for the intruded magmatic bodies. Such a low magnetization is disproportionate to common magnetization values of intrusions of 3-25 A/m ([Aubourg et al., 2008](#); [Gee and Kent, 2007](#)) and to our findings at the conjugated margin. However, the fact that intrusions pinch through the basement, implies that a later stage of magmatism at a period of different polarization affected the margin and might caused an overprint of the magnetic signature of the previously emplaced magmatic material. This could lead to the untypical low values of magnetization for the intrusions, modelled by [Leitchenkov et al. \(2008\)](#). At kms 460-520 of profile RAE43-05 (Fig. 5.6b), the basement is hardly visible, due to a low resolution of the seismic data as well as low amplitude reflections, which might be caused by hydrothermal venting, too. This area is characterized by a continuous decrease of the amplitude of the magnetic anomaly. The observed low-angle limb is typical for SDR sequences, which exhibited polarity reversals ([Eagles et al., 2015](#)). Therefore, in agreement with our interpretation of the continental margin off Central Mozambique, the existence of SDRs at this part of the margin is suggested. Furthermore, a tilted basement topography is visible up to km 480 along this profile, too. Based on the similar characteristics of the margin compared to Central Mozambique, the oldest magnetic spreading anomaly M38n.2n is placed at km 480 (Fig. 5.6b).

Along profile 20140010, the magnetic anomaly in the upper crust of Beira High is modelled with a common magnetization typical for intrusive rocks. In agreement, [Mueller et al. \(2016\)](#) suggest the presence of partly highly intruded continental crust at Beira High, based on seismic refraction data and gravity modelling. Furthermore, a

typical reflection characteristic of saucer shaped sills is observed in this part (Mueller et al., 2016). In contrast, the location of the magnetic source at kms 185-240 coincides with identified lava flows (effusive rocks) at the north-western flank of Beira High and in the ZDD (Mahanjane, 2012; Mueller et al., 2016). At the flanks of Beira High, partly these show a similar layering like SDRs, but for clearness in the following discussion, these are referred to as lava flows. These are characterized by a similar magnetization as the SDRs at profile 20070201, but with a normal polarization. A comparison to the inferred SDRs in the Riiser-Larsen Sea reveals the same polarization and a similar limb of the magnetic anomaly, leading to a likely joint emplacement history.

At profile 20140010, no additional magnetic sources were required to model the edge anomaly in the area between Beira High and onshore Mozambique. However, volcanic material of the Stormberg series were already drilled at the north-western end of the profile (Du Toit et al., 1997). Additionally, their southern continuation has already been identified on a seismic reflection profile onshore Mozambique (Lafourcade, 1984), too. This contradiction can be attributed to the usage of the magnetic data of the global EMAG2 grid (version 2, without directional gridding; Maus et al., 2009) in this part of the model (Figs. 5.4 and 5.5, continental domain and partly COT). For this purpose the data were downward continued to our reference level. However, the resolution of the data in this area is low and represents only a general trend of the magnetic anomaly. Local anomalies are not resolved by the EMAG2 data in this part of the margin. Consequently, a reasonable fit to the observed magnetic anomaly is achieved without additional magnetic sources onshore Mozambique. However, the presence of intrusions and magmatic flows is likely (Mahanjane, 2012; Reeves et al., 2016).

5.4.3 Different magnetic signature of the conjugate margins

The extent and different polarization of the SDRs and lava flows at the conjugated margins of Mozambique and the Riiser-Larsen Sea, testifies a complex break-up history. In general, the SDRs in the north-eastern part of the Mozambican margin, the proposed SDRs in the Riiser-Larsen, and the lava flows at the north-western flank of Beira High are characterized by a similar downslope extent of about 50 km and a magnetization of about 5 A/m (Fig. 5.5). The same polarization and a similar limb of the caused magnetic anomaly depict the SDRs in the Riiser-Larsen Sea and the lava flows at Beira High. The assumption that Beira High is a continental fragment of the Antarctic continental margin, suggests that both parts are affected by the same magmatic events during the initial break-up and explains the similarities in magnetization of the intrusions and SDRs. The reversed polarization of the SDRs at the north-eastern part of

continental margin of Central Mozambique might point to an emplacement during a chronologically different magmatic event, at times of a reversed polarized earth magnetic field. On the basis of the commonly accepted assumption that SDRs represent sub-aerially lava flows, emplaced just before the onset of the first oceanic crust (Hinz, 1981; Mutter et al., 1982), an age greater than the oldest identified magnetic spreading anomaly M38n.2n (164.1 Ma; Ogg, 2012) seems likely.

Although rapid polarity changes mark the JQZ, the geomagnetic polarity time scale (Ogg, 2012) reveals a rather predominantly normal polarity for ages of 166.8-164.1 Ma (Fig. 5.7, M39-M38). In contrast, for ages of 168.5-166.8 Ma (M42-M40) three-fourths of this period are characterized by a reversed polarization, preceded by a phase of rather uniformly distributed polarizations (Fig. 5.7). Based on a spreading velocity of 16 km/Ma at the margin of Central Mozambique, identified for times after M33n (Leinweber et al., 2013), and extrapolated to the preceding phases of the initial drifting and final rifting, would require a period of 3 Ma of reversed polarization for the emplacement of the 50 km wide area of SDRs along the margin of Mozambique (Fig. 5.6a). Consequently, the main part of the reversed polarized SDRs at the margin of Central Mozambique has to be quite quickly emplaced in a shorter period from 168.5-166.8 Ma (M42-M40). In contrast, the lava flows at Beira High and the SDRs in the Riiser-Larsen Sea show a primarily normal polarization, whereas the limb of the caused magnetic anomaly reveals a typical shape for SDRs affected by polarity reversals. Therefore, by considering the geomagnetic polarity time scale, an emplacement sometime between 168.5-164 Ma (M42-M38) is supposed, which comprises the change from the phase of reversed polarization to the period of predominantly normal magnetization (Fig. 5.7). As a consequence, the SDRs in the Riiser-Larsen Sea and the lava flows at Beira High are only partly emplaced at the same time as the SDRs at the north-eastern continental margin of Central Mozambique and shortly after them, causing the difference in polarization. Such a difference in emplacement time of the SDRs, might be caused the relative southwards movement of East Gondwana with respect to West Gondwana, resulting in a longer lasting influence of the magmatic source (e.g. mantle plume) on the margin of Antarctica. As one possibility, this might imply that the SDRs at both margins got emplaced at a similar time, but the longer lasting influence of the hot mantle caused a later cooling of the extruded magmatic material (SDRs) below the Curie temperature at a different polarized magnetic period. On the other hand a late stage of rift volcanism might affected the margin of Antarctica. This is supported by the identified intrusions in the COT in the area of the referred SDRs (Fig. 5.6b), where they pinch through the basement into the lowermost sediment layer. Consequently, the normal polarization of the intrusions partly

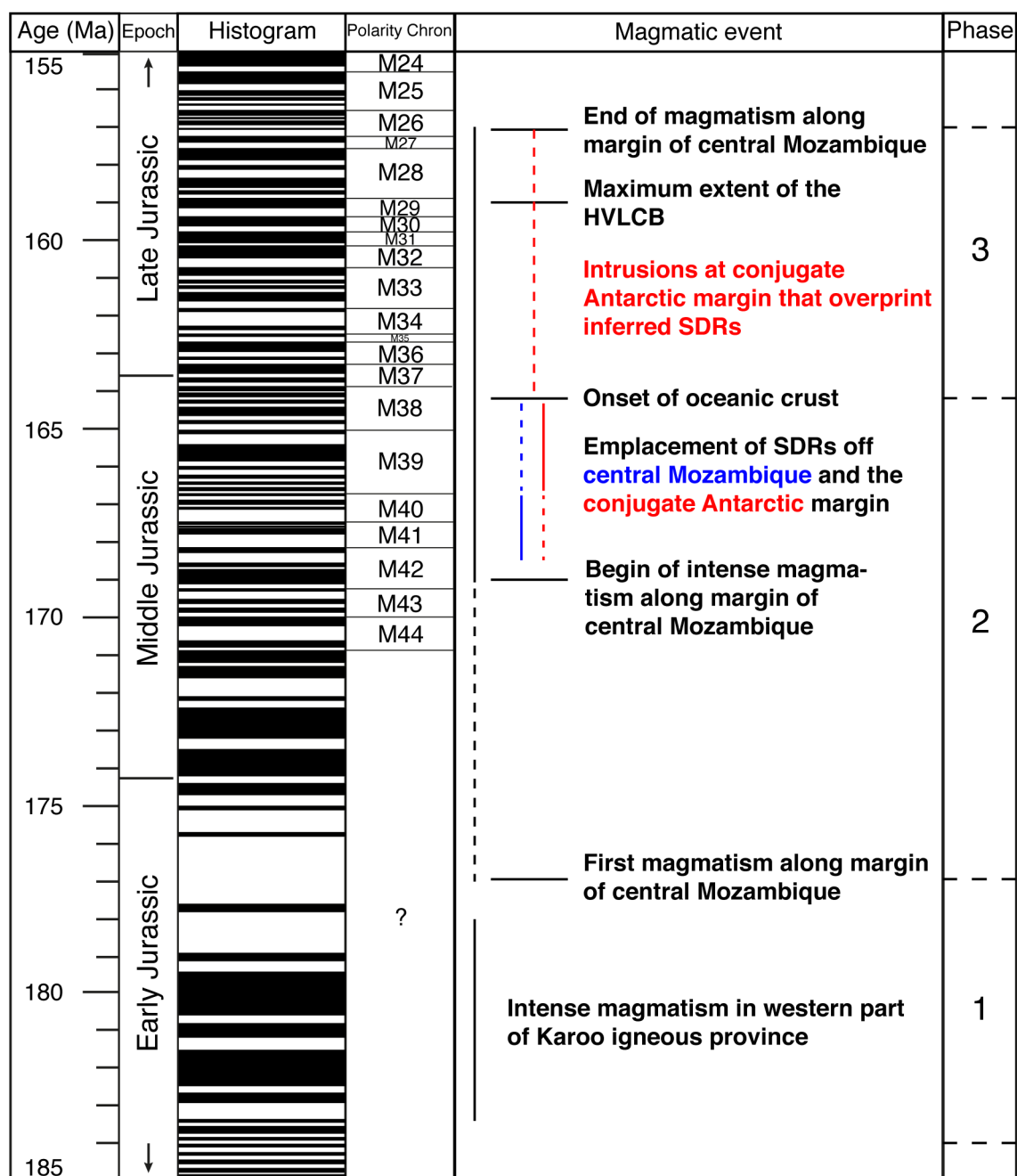


Figure 5.7: Chronology of the magmatic activity at the margin of Central Mozambique. The geomagnetic polarity timescale is based on the mid-depth deep-tow model of Ogg (2012) up to chron M44, as well as Ogg et al. (2012) for Early Jurassic times. The labelled magmatic events and phases are described in the text. Black rectangles in the histogram represent periods of normal polarization, white rectangles periods of reversed polarization.

overprints the magnetic signature of the SDRs and causes the difference in polarization between the conjugated margins. Unfortunately, there are no rock samples available in the area because the several hundred-meter thick Antarctic ice sheet covers even the shelf areas of the Riiser-Larsen Sea. An emplacement of SDRs in two distinct phases

is as well suggested for the Explora Wedge in the Lazarev Sea (Hinz et al., 2004). The Explora Wedge is thought to be emplaced during the initial break-up of East and West Gondwana in Early Jurassic times, too. Based on seismic reflection data, Hinz and Krause (1982) identified two independent zones of SDRs in the Lazarev Sea. Here, the 100 km wide wedge of inner SDRs shows a low and partly distinct negative magnetic signature (Kristoffersen et al., 2014). Adjacently, a less voluminous zone of outer SDRs is observed to the north (Hinz and Krause, 1982). On contrary, these SDRs are marked by a distinct positive anomaly in the magnetic data (Kristoffersen et al., 2014). The difference in thickness and magnetic signature implies an emplacement by at least two episodes (Hinz et al., 2004). It is likely, that the first episode of volcanism at 168.5-166.8 Ma (M42-M40), emplacing the Explora Wedge, might have affected the Riiser-Larsen Sea as well. Subsequently, the second episode of volcanism, caused the emplacement of the normal magnetized outer SDRs in the Lazarev Sea and the intrusions in the Riiser-Larsen Sea, which overprint the magnetic signature of the reverse polarized SDRs. Based on the relative southwards motion of Antarctica, the margin of Africa was not affected by this second phase.

5.4.4 Linking onshore and offshore volcanism

To put our results in the context of the break-up related magmatism of the Karoo Large Igneous Province (Karoo LIP), Fig. 5.8 shows the distribution and age of these magmatic rocks in SE-Africa. These have been subject to numerous investigations. Here, general characteristics of the Karoo LIP are discussed in the view of our findings. Clearly visible is the magmatic expression of three separate magmatic branches onshore SE-Africa (Fig. 5.8), forming the Karoo triple rift (Burke and Dewey, 1973; Hastie et al., 2014; Klausen, 2009). Its north-western and southern branch are well defined by the great extent of the flood basalts and dyke swarms (Fig. 5.8, ODS, LDS, RRDS), respectively. In contrast, its north-eastern branch is not traced east of the Mateke-Sabi monocline (Fig. 5.8, MSM). An essential contribution to the identification of its eastern continuation is the finding of the coast-parallel Limpopo-Angoche dykes (Fig. 5.8, LADS) of Early to Middle Jurassic age by Reeves et al. (2016), stretching in the same direction as the MSM and bordering in the vicinity west of Davie Ridge (Figs. 5.1a and 5.8). Encountered volcanic rocks of the Stormberg series (Du Toit et al., 1997) at the Lower Zambezi (Figs. 5.1a and 5.8) support these findings, whereas seismic reflection studies proved their extension further downslope towards the shelf area (Lafourcade, 1984; Mahanjane, 2012). Furthermore, at the western termination of the LADS, Jaritz et al. (1977) identified volcanic outcrops with an age of 177 ± 3 to

157±3 Ma in the coastal and tidal areas between Moma and Mogincual. In agreement, our magnetic modelling depicts magmatic intrusions for the tidal area of Moma, too. Consequently, this great amount of magmatic material causes the coast-parallel positive magnetic anomaly along the margin of Central Mozambique (Fig. 5.1c) and forms the eastern continuation of the north-eastern branch of the Karoo triple rift (Fig. 5.8). Offshore Central Mozambique, the identified HVLCB marks the southern extension of the north-eastern branch (Fig. 5.8). The SDRs along the north-eastern margin of Central Mozambique and the lava flows and intrusions at Beira High are as well part of this branch.

A continuation of the HVLCB towards the MCP and along the southern branch of the Karoo triple rift is likely. At the MCP, a Cretaceous and Cenozoic sediment cover prevents the finding of flood basalts at the surface east of the Lebombo monocline. However, several exploration wells at the MCP already encountered volcanics of the Stormberg series (Fig. 5.8), which are considered to be of Middle Jurassic age (Du Toit et al., 1997). The emplacement of the large igneous province of the Mozambique Ridge (Fischer et al., 2016; Gohl et al., 2011; Leinweber and Jokat, 2011) and the terrace of the northern Natal Valley are evident for the long-lasting magmatism along the southern branch of the Karoo LIP and the relative southwards movement of the magmatic centre.

Investigations onshore SE-Africa revealed a start of the main emplacement phase of the Karoo LIP at about 184 Ma (Hastie et al., 2014; Jourdan et al., 2008). In a first phase from 184-177 Ma (Fig. 5.7), mostly basaltic magmatism caused the emplacement of the great Karoo flood basalts in southern Africa (Jourdan et al., 2008). Along the north-eastern branch of the Karoo LIP, ages of 178-174 Ma at the MSM, 166±10 Ma in the Lupata area of the Lower Zambezi (Flores, 1964) as well as 177±3 for the first volcanics in the tidal areas between Moma and Mogincual (Fig. 5.8) indicate a later onset of magmatism to the east, at the end of this first phase. This implies a first impact of the thermal mantle anomaly or plume in the vicinity of the centre of the Karoo triple rift or closer to its north-western branch (Burke and Dewey, 1973; Cox, 1992). Furthermore, it shows that it took a certain time until the present coast of Central Mozambique got affected by the magmatism. A second phase of magmatism from 177-164.1 Ma was most likely accompanied by the initial Jurassic rifting between East and West Gondwana. In this period, the MORB-like Rooi Rand dykes with an age of 178-172 Ma got emplaced along the southern branch of the Karoo LIP. At the same time, the identified HVLCB along the north-eastern branch began to develop. SDRs with ages of 168.5-164.1 Ma (M42-M38) offshore Central Mozambique and Antarctica indicate the end of this second phase. The subsequent onset of fully developed oceanic

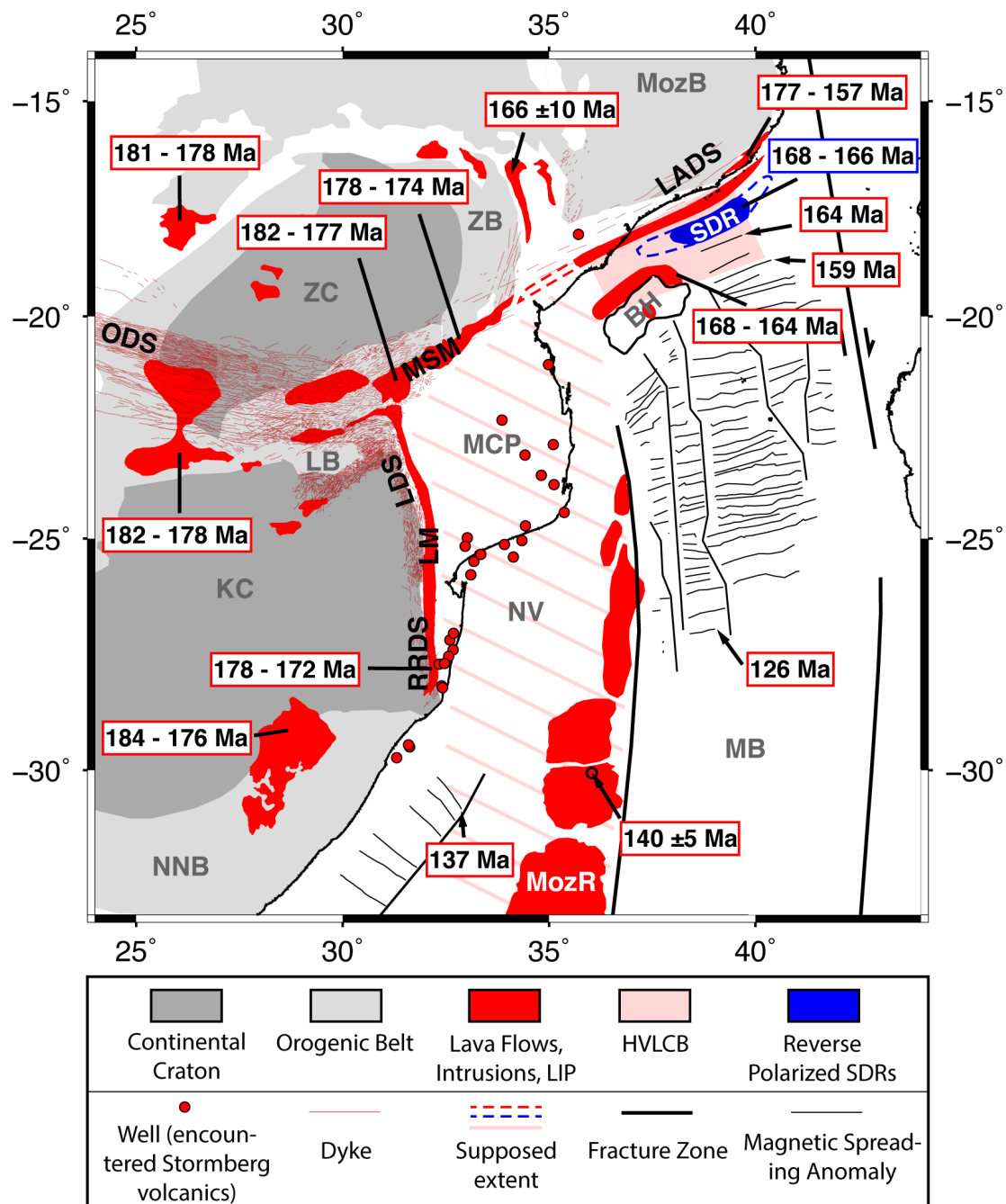


Figure 5.8: Distribution and age of the Karoo LIP in SE-Africa. The terrains are digitized after Eales et al. (1984), Nguuri et al. (2001) and Sahu (2000). The location of the dykes base on the publications of Reeves (2000) and Reeves et al. (2016). The ages of the flood basalts and dykes are taken from Flores (1964), Jaritz et al. (1977) and Jourdan et al. (2008). The stated ages represent the duration of magmatism in the respective area, based on the majority of the identified ages of lava flows, dykes, plutons and rhyolites. The location of the wells and their encountered layers are taken from Du Toit et al. (1997). The position of the magnetic spreading anomalies in the Mozambique Basin base on Leinweber and Jokat (2012) and in the southern Natal Valley on Goodlad et al. (1982). Their ages accord with the geomagnetic polarity time scale of Ogg (2012). The presented locations of the SDRs, the lava flows around Beira High, the HVLCB, and the coast-parallel intrusions base on this study. Continues ...

crust at 164.1 Ma (M38n.2n) marks the begin of a third phase. Based on our study along the north-eastern branch of the Karoo LIP, this period probably terminates at about 157 Ma. Here, conspicuous is the similar spatial extent of the identified HVLCB and the simultaneous end of its emplacement. This is detectable at profiles 20070201 and 20070202 (Figs. 5.4a and 5.4b), where the southern limit of the HVLCB consistently coincides with the magnetic spreading anomaly M29r (159 Ma; Ogg, 2012). At profile 20140010, the HVLCB is bordered in the south by the Beira High (Fig. 5.4c), which most likely got separated from Antarctica by a small rift jump at 160 Ma, which is supported by the emplacement of the oldest magnetic spreading anomaly M29r, south of Beira High. A similar age of 157 ± 3 Ma is depicted for the youngest volcanic rocks onshore in the Moma district (Jaritz et al., 1977). This might imply the cease of the high magmatic activity at about 157 Ma affecting the margin of Central Mozambique, due to the relative southwards motion of the magmatic centre.

So far, conclusions on the duration of the entire magmatic activity of the Karoo LIP are mainly restricted to investigations onshore SE-Africa. Accordingly, Jourdan et al. (2007) suggests that the whole magmatic activity of the Karoo province spans from 184-172 Ma, including the begin of oceanization processes at the end of this period. However, to obtain an idea for the entire magmatism, sound constraints about the nature of the crust underlying the MCP and about the onset of first oceanic crust in the Natal Valley are still missing. Now, based on our study, the entire magmatism along the coast of Central Mozambique was determined and might serve as indication for the duration of magmatism of the Karoo LIP. By a joint interpretation with the investigations onshore Mozambique, the magmatism at the continental margin of Central Mozambique lasted for about 20 Ma from 177-157 Ma (Fig. 5.7) at maximum. This period comprises the emplacement of the first magmatic material about 13 Ma prior to the onset of drifting at 164 Ma and the last about 7 Ma after it (Fig. 5.7). However, the start of magmatic activity in this area at 177 ± 3 Ma is only based on a single sample (Jaritz et al., 1977). The majority of the sampled rhyolites and tholeiites are emplaced between 169 ± 3 to 157 ± 3 Ma (Jaritz et al., 1977). This might narrow the phase of intense magmatic activity to about 12 Ma, with a preceding emplacement of

Figure 5.8 (cont.): Abbreviations: BH: Beira High, KC: Kaapvaal Craton, LADS: Limpopo-Angoche Dyke Swarm, LB: Limpopo Belt, LDS: Lebombo Dyke Swarm, LM: Lebombo Monocline, MB: Mozambique Basin, MCP: Mozambique Coastal Plains, MozB: Mozambique Belt, MozR: Mozambique Ridge, MSM: Mateke-Sabi Monocline, NNB: Namaqua-Natal Belt, NV: Natal Valley, ODS: Okavango Dyke Swarm, RRDS: Rooi Rand Dyke Swarm, SDR: Seaward Dipping Reflector, ZB: Zambezi Belt, ZC: Zimbabwe Craton.

magmatic material prior to the onset of drifting of about 5 Ma (Fig. 5.7). A similar chronology is known for the break-up related emplacement of other continental flood basalts (Jourdan et al., 2007). For example, the Parana-Etendeka traps are characterized by a similar duration of magmatism, but with a slightly longer preceding phase of about 7 Ma (Jourdan et al., 2007). However, to verify the validity for the entire Karoo LIP and to draw conclusions on the kind of the magmatic source, further investigations are required especially in the area of the MCP and the adjacent Mozambique Basin.

5.5 Conclusion

[1] The identified HVLCB along the margin of Central Mozambique shows a homogeneous spatial extent of about 190-220 km and an uniform maximal emplacement time up to the magnetic chron M29r (159 Ma; Ogg, 2012).

[2] The edge effect of the transition from the thick distinct continental crust of Mozambique to the thinner one in the Mozambique Basin causes only a half of the observed negative magnetic anomaly. Typical magnetizations of extrusive and intrusive volcanic rocks characterize the additional required magnetic sources.

[3] In agreement to findings based on seismic reflection data, magmatic intrusions contribute to the coast-parallel positive magnetic anomaly along the coast of Central Mozambique and in the centre of Beira High. Additionally, SDRs are located at the north-eastern margin of Central Mozambique. These obtained their reversed polarization during the emplacement at about 168.5-166.8 Ma (M42-M40), when 3/4 of the period was characterized by a reversed polarization of the earth magnetic field. In contrast, the lava flows at the north-western flank of Beira High show a normal polarization and are emplaced sometime between 168.5-164.1 (M42-M38) Ma. The subsequent onset of the first oceanic crust is accompanied by the emplacement of the oldest magnetic spreading anomaly M38n.2n (164.1 Ma; Ogg, 2012).

[4] At the conjugated margin in the Riiser-Larsen Sea, the coast-parallel positive magnetic anomaly is as well caused by intrusions. At the COT, the magnetic anomaly shows a limb typical for SDRs, which exhibited polarity reversals. This suggests the presence of SDRs at this margin, too. The distinct similarity of the magnetic anomaly to the area of Beira High, leads to the assumption that both are emplaced by the same magmatic event. This supports the idea of Beira High as former part of the continental margin of Antarctica. The normal polarized intrusions, emplaced by a late stage of rift

volcanism, pinch through the basement and partly overprint the magnetic signature of the SDRs and cause the difference in polarization between the two margins. The emplacement of the SDRs in two distinct magmatic episodes reveals a clear similarity to the emplacement of the Explora Wedge in the Lazarev Sea. Furthermore, the similarity of the observed magnetic anomaly to the margin of Central Mozambique in the oceanic domain, allows the identification of magnetic spreading anomalies up to M38n.2n in the Riiser-Larsen Sea, too.

[5] The north-eastern branch of the triple junction of the Karoo LIP can be traced across the Mateke-Sabi monocline to the east and terminates close to Davie Ridge. A continuous magmatism of at least 12 Ma affected the central coast of Mozambique, comprising 5 Ma before the onset of oceanic crust and 7 Ma afterwards.

Acknowledgements

We thank the Polar Marine Geosurvey Expedition for providing the multichannel seismic (MCS) data at the Antarctic Seismic Data Library System and making it available for public access. Furthermore, our thanks go to Schlumberger Multiclient for providing insights into some regional MCS and magnetic data at the Mozambican margin. For their support with the software SOFI2D we thank Thomas Bohlen and Tilman Metz. This project is funded through a grant by the German Federal Ministry of Education and Research (BMBF, 03G0230A) and by AWI internal funding.

6 The initial Gondwana break-up in the Africa-Antarctica Corridor – A reconstruction based on new magnetic data

Christian Olaf Mueller¹, Wilfried Jokat^{1,2}, Bernd Schreckenberger³

¹ *Alfred Wegener Institute, Bremerhaven, Germany*

² *University of Bremen, Bremen, Germany*

³ *Federal Institute for Geosciences and Natural Resources, Hanover, Germany*

Abstract

The opening of the Africa-Antarctica Corridor, in the heart of the initial Gondwana break-up, is still enigmatic due to missing information on the origin of major crustal features and the exact timing of the onset of the first oceanic crust in the Jurassic. Therefore, in 2014, new shipborne magnetic data were systematically acquired in the northern Mozambique Basin and across Beira High. These are integrated in a compilation of magnetic data covering nearly the entire Mozambique Basin. Herein, distinct magnetic lineations are observed, which allow the identification of a whole set of Jurassic magnetic spreading anomalies, constraining the timing of the initial break-up, beginning at M38n.2n (164.1 Ma). Magnetic data onshore the Mozambique Coastal Plains reveal a striking similarity to oceanic crust in the adjacent Mozambique Basin, which allowed the tentative identification of the magnetic chrons M28n.2r-M21r (158.2-149.6 Ma) in the southern part of the Mozambique Coastal Plains. The consecutive spreading anomalies are observed at the Mozambique Ridge, which entirely represents an oceanic LIP, formed between M19n.2n-CNS (145.7-115 Ma). An extinct mid-ocean ridge in the Northern Natal Valley separated the Mozambique Ridge from

the Inharrime Ridge, being active from latest M10Nr to M1n (135.2-127.3 Ma). Well-expressed fracture zones can be traced throughout the Africa-Antarctica Corridor and allow the precise rotation of Antarctica back to Africa. The initial fit depicts striking continuations of onshore tectonic features across the plate boundaries. Within a tight Gondwana fit, the Beira High can be restored. It represents a continental fragment, which got detached from Antarctica along the major sinistral Namama-Orvin Shear Zone of the East African-Antarctic Orogen, by 159 Ma at the latest. A refined kinematic break-up model is presented describing consistently the opening of the Africa-Antarctica Corridor and the Somali Basin by the same rotation poles, including the southwards journey of Madagascar.

6.1 Introduction

The Africa-Antarctica Corridor (AAC) extends from the coast of Mozambique in SE-Africa to the coast of the Dronning Maud Land (DML) in East Antarctica (Fig. 6.1). The Early Jurassic break-up of Gondwana led to the emplacement of oceanic crust that forms the basement of the AAC, which preserves a complete plate kinematic record of the separation of East and West Gondwana. Many publications have addressed the early stages of the Gondwana break-up in plate reconstructions (e.g. Cox, 1992; Eagles and König, 2008; Jokat et al., 2003; Lawver et al., 1998; Leinweber and Jokat, 2012; Martin and Hartnady, 1986; Norton and Sclater, 1979). Especially details on the link between the initial, massive onshore volcanism along the Lebombo Monocline in SE-Africa and the onset of the formation of oceanic crust is of specific interest. While the onshore volcanism is well dated, the age of the onset of oceanic crust is still debated. Due to the lack of high quality geophysical data along the conjugate margins, constraining the origin and age of the crust, the published reconstructions clearly differ in their pre-break-up fit and plate motions in Jurassic and Early Cretaceous times. An additional aggravating factor for determining a consistent age model is the weak earth's geomagnetic field during the Jurassic magnetic quiet period (Tominaga et al., 2015), which impairs the identification of early magnetic spreading anomalies close to the margins. Thus, several problems in interpreting the various structural elements in the AAC remained.

Despite this, recent investigations have confirmed the existence of normal oceanic crust close to the coast of Central Mozambique (Leinweber et al., 2013; Mueller and Jokat, 2017) and dated its initial formation in the Mozambique Basin (MB) and in the Riiser-Larsen Sea (RLS) to 164.1 Ma (M38n.2n) (Mueller and Jokat, 2017). Furthermore, the Beira High was characterized as a continental fragment (Mueller et al., 2016)

sitional crust at the MCP (Domingues et al., 2016; Fonseca et al., 2014). South of the MCP, a possible trend of the continent-ocean boundary (COB) in this area extends along the southern termination of the Northern Natal Valley (NNV) towards the prominent basement high of the South Tugela Ridge (Fig. 6.2) implying that the NNV is floored by stretched continental crust (Goodlad et al., 1982; Martin et al., 1982; Raillard, 1990). On the contrary, Marks and Tikku (2001) proposed on the base of sparse magnetic data the existence of an E-W aligned extinct ridge in the area of the NNV. Based on systematically acquired magnetic data, Leinweber and Jokat (2011) depicted NE-SW directed magnetic lineations in the NNV, which support an oceanic origin.

Southwards of the NNV, the crustal nature of the MozR has also been the subject of debate. Numerous studies have proposed an entirely or partially continental origin, based on dredge sampling (e.g. Ben-Avraham et al., 1995; Hartnady et al., 1992; Mougnot et al., 1991; Raillard, 1990; Tikku et al., 2002), which leads to an overlap with East Antarctica in plate kinematic reconstructions. Drilling of the northern MozR (DSDP leg 25, Site 249; Fig. 6.2), however only proved the presence of Neocomian age sediments overlying the basement (Simpson et al., 1974). Recent seismic investigations (Fischer et al., 2016; Gohl et al., 2011) have been interpreted in terms of multistage magmatism affecting the MozR, and lead to its classification as an oceanic large igneous province (LIP). The presence of linear magnetic reversal anomalies over the MozR support this conclusion (König and Jokat, 2010; Leinweber and Jokat, 2011). However, continuous magnetic spreading anomalies are not observed. Hence the time of emplacement of entire MozR was supposed between 140-122 Ma (König and Jokat, 2010). Irrespective of its crustal nature, a precise timing for the emplacement or the separation of the MozR is essential for a consistent break-up model of the AAC.

Figure 6.1 (cont.): The yellow dashed lines represent the outline of the AAC. White dashed lines mark the areas shown in detail in Figs. 6.2 and 6.3. Abbreviations: ABFZ: Andrew Bain Fracture Zone, AFFZ: Agulhas Falkland Fracture Zone, AFR: Africa, AFZ: Astrid Fracture Zone, ANT: Antarctica, AP: Agulhas Plateau, AR: Astrid Ridge, BH: Beira High, BI: Bassas da India, CP: Crozet Plateau, CR: Conrad Rise, CS: Cosmonaut Sea, DFZ: Davie Fracture Zone, DIFZ: Discovery II Fracture Zone, DuFZ: Du Toit Fracture Zone, EB: Enderby Basin, ESFZ: Edward Simpson Fracture Zone, GR: Gunnerus Ridge, LS: Lazarev Sea, MAD: Madagascar, MadR: Madagascar Ridge, MB: Mozambique Basin, MCP: Mozambique Coastal Plains, MFZ: Mozambique Fracture Zone, MozR: Mozambique Ridge, MR: Maud Rise, NV: Natal Valley, PEFZ: Prince Edward Fracture Zone, RLS: Riiser-Larsen Sea, SB: Somali Basin, SWIR: Southwest Indian Ridge, WS: Weddell Sea.

Therefore, at the beginning of 2014, new high quality magnetic data were systematically acquired in the MB to densify the data closer to the MB continental margin. Here, we present and investigate the new data, integrated in a compilation of all available magnetic data in the MB and adjacent Natal Valley. Newly identified magnetic spreading anomalies provide evidence for the early motion of East Antarctica, the separation of Beira High and for the crustal origin and emplacement of the MCP, Natal Valley and MozR. Pre-rift boundaries and the track of the major fracture zones at the conjugate margins are assigned by the combined investigation of gravity and magnetic data. Finally, a refined kinematic break-up model of the AAC is presented.

6.2 Structural elements and their tectonic setting

6.2.1 Archean to Paleozoic

Onshore SE-Africa, the former Kalahari Craton consists of the Archean Kaapvaal and Zimbabwe cratons, separated by the collisional (~ 2.6 Ga) Limpopo Belt (Kröner, 1977) (Fig. 6.2). Till Jurassic times, the Kalahari Craton was juxtaposed with the Archean Grunehogna Craton of Antarctica (Fig. 6.3) (Groenewald et al., 1991). In the Mesoproterozoic, the assembly of the supercontinent Rodinia caused the Kibaran orogeny (~ 1.1 Ga) and led to the extensive formation of the Namaqua-Natal-Maud-Belt in South Africa, northern Mozambique (Fig. 6.2) and western DML (Grantham et al., 2003) (Fig. 6.3).

In East Antarctica, a recent study of Jacobs et al. (2015) proposes a Tonian (1.0-0.9 Ga) oceanic arc super terrane (TOAST) flooring the crust in the eastern part of Dronning Maud Land (Fig. 6.3). The TOAST extends from the Orvin Shear Zone (OSZ) and the Forster magnetic anomaly (FMA, Riedel et al., 2013) in the west, across the area of Sør Rondane, towards the Yamato mountains in the east (Jacobs et al., 2015). Much of the continental crust of Africa and Antarctica was reworked during the late Neoproterozoic assembly of Gondwana, which led to the formation of the East African-Antarctic Orogen (EAAO) (Jacobs et al., 1998). The orogen's components, the Zambezi Belt and Mozambique Belt formed in SE-Africa (Fig. 6.2). In northern Mozambique, prominent shear zones with diverse orientations, like the SW-NE trending Lurio Belt and the NNE-SSW trending Namama Shear Zone (NMS), testify to the complex polyphase history of the Pan-African Orogeny (Ueda et al., 2012; Viola et al., 2008). In Antarctica, metamorphism affected much of DML (Jacobs et al., 1998). This is especially expressed by the Pan-African overprint at the exposures of the Maud Belt, e.g. at Heimefrontfjella, Kirwanveggen, Sverdrupfjella, the Mühlig-

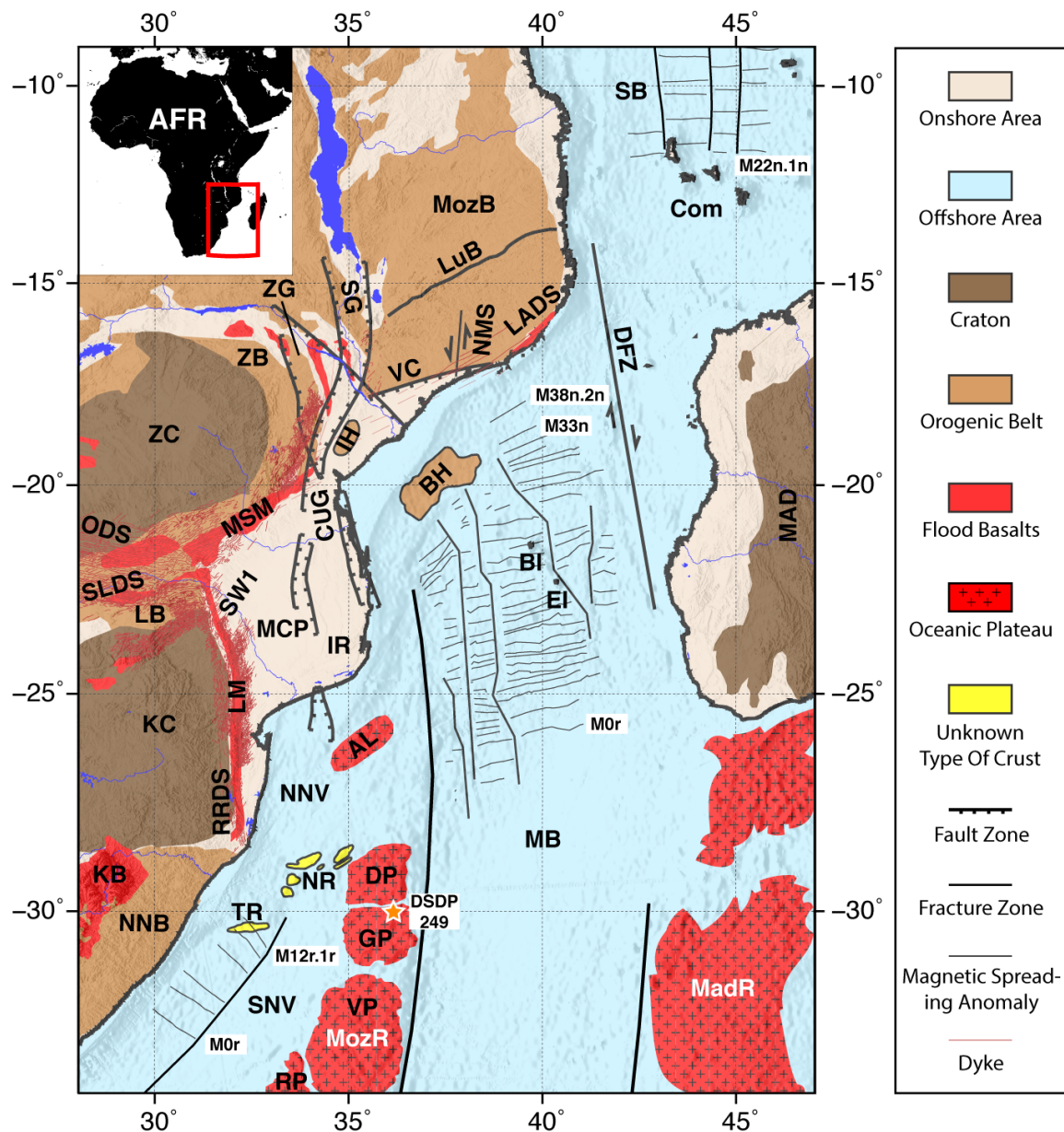


Figure 6.2: Tectonic setting of SE-Africa and the Mozambique Basin at the African end of the AAC. The terrains are digitized after [Eales et al. \(1984\)](#), [Nguuri et al. \(2001\)](#) and [Sahu \(2000\)](#). Fault systems are based on [De Buyl and Flores \(1986\)](#), the position of the Vila Candida hinge line on [Lafourcade \(1984\)](#) and the location of the Lurio Belt and the Namama Shear Zone on [Viola et al. \(2008\)](#). The locations of the dykes are based on the publications of [Mekonnen \(2004\)](#), [Reeves \(2000\)](#) and [Reeves et al. \(2016\)](#). The outline of Beira High is taken from [Mahanjane \(2012\)](#). The outline of the main plateaus of the Mozambique Ridge and the Madagascar Ridge follows the 2500 m isoline of the bathymetry of the GEBCO_2014 grid (version 20150318; [Weatherall et al., 2015](#)). The outlines of the Naude Ridge and the South Tugela Ridge are taken from [Raillard \(1990\)](#). The locations of the magnetic spreading anomalies in the Somali Basin are taken from [Cochran \(1988\)](#), in the Mozambique Basin from [Leinweber and Jokat \(2012\)](#) and in the Southern Natal Valley from [Goodlad et al. \(1982\)](#). Continues ...

Hofmann Mountains, Wohlthat Massif, SR and YM (Jacobs et al., 1998) (Fig. 6.3). Ongoing debate addresses the question of whether the main shear zone at the Heimefrontfjella represents the western termination of the EAAO (Jacobs and Thomas, 2004; Mieth and Jokat, 2014).

6.2.2 Mesozoic to Present

In Early Jurassic times, the emplacement of the Karoo flood basalts in SE-Africa and of the Ferrar flood basalts in East Antarctica are the first indication for the subsequent initial Gondwana break-up (Figs. 6.2 and 6.3). The main phase of magmatic activity in the Karoo Province is suggested to span from 184 until 172 Ma (Jourdan et al., 2007) and to have formed the volcanic Lebombo (LM) and Matake-Sabi (MSM) monoclines, as well as giant dyke swarms. Onshore the conjugate margin of Antarctica, rocks emplaced during this Jurassic magmatism are restricted to a small number of samples, mostly collected along the Jutul-Penck Graben and at the outer rim of the Grunehogna Province (Zhang et al., 2003). Similar to the Karoo LIP, these yield ages of 182-175 Ma (Hastie et al., 2014). Offshore DML in the Weddell Sea and the Lazarev Sea (Fig. 6.3), an extensive sequence of seaward dipping reflectors (SDRs) of the volcanic Explora Wedge manifests the large-scale Jurassic magmatism emplaced along the margin of East Antarctica (Hinz and Krause, 1982). The Explora Wedge is composed of a voluminous sequence of inner SDRs and a less distinct one of outer SDRs, indicating an emplacement in at least two different magmatic phases (Hinz et al., 2004; Kristoffersen et al., 2014). This is supported by a study of Mueller and Jokat (2017), suggesting a first magmatic event at 168.5-166.8 Ma (magnetic chrons M42-M40) emplacing reverse polarized SDRs in the Lazarev Sea and RLS. At 166.8-164.1 Ma (M39-M38), a second

Figure 6.2 (cont.): Abbreviations: AFR: Africa, AL: Almirante Leite Bank, BH: Beira High, BI: Bassas da India, Com: Comoros, CUG: Chissenga-Urema Graben System, DP: Dana Plateau, DFZ: Davie Fracture Zone, EI: Europa Island, GP: Galathea Plateau, IH: Inhaminga High, IR: Inharrime Ridge, KB: Karoo Basalts, KC: Kaapvaal Craton, LADS: Limpopo-Angoche Dyke Swarm, LB: Limpopo Belt, LM: Lebombo Monocline, LuB: Lurio Belt, MAD: Madagascar, MadR: Madagascar Ridge, MB: Mozambique Basin, MCP: Mozambique Coastal Plains, MozB: Mozambique Belt, MozR: Mozambique Ridge, MSM: Mateke-Sabi Monocline, NMS: Namama Shear Zone, NNB: Namaqua-Natal Belt, NNV: Northern Natal Valley, NR: Naude Ridge, ODS: Okavango Dyke Swarm, RP: Robert-Giraud Plateau, RRDS: Rooi Rand Dyke Swarm, SB: Somali Basin, SG: Shire Graben, SLDS: Save-Limpopo Dyke Swarm, SNV: Southern Natal Valley, SW1: SW1 Dyke Swarm, TR: South Tugela Ridge, VC: Vila Candida Hinge Line, VP: Vauban Plateau, ZB: Zambezi Belt, ZC: Zimbabwe Craton, ZG: Zambezi Graben.

magmatic event caused the effusion of normal polarized SDRs in front of the Explora Wedge in the Lazarev Sea and intrusions in the volcanic sequences erupted along RLS margin (Mueller and Jokat, 2017). In contrast, along the conjugate Central Mozambican margin, so far only magnetically reversed polarized SDRs are identified (Mueller and Jokat, 2017; Reichert and Neben, 2008). A thick Cretaceous and Cenozoic sediment cover hinders the search for SDRs beneath the MCP. Furthermore, no details are known about the nature of the crust at the MCP and the NNV (Fig. 6.2), leaving their origin and the location of the COB in this area ambiguous.

Offshore Mozambique, a prominent basement high, the Beira High (Fig. 6.2), consists of stretched and highly intruded continental crust and represents a continental fragment (Mueller et al., 2016), detached either from the African or the Antarctic plate. Further east along the coast of Central Mozambique, the onset of the first oceanic crust is dated to 164.1 Ma (M38n.2n; Mueller and Jokat, 2017). The track of the subsequent opening of the MB, RLS and Lazarev Sea is indicated by the trends of major fracture zones. The Mozambique Fracture Zone (MFZ) borders the MB in the west and the Natal Valley in the east (Fig. 6.1), fringing the volcanic plateaus of the MozR. According to recent seismic studies, the main parts of the MozR are of volcanic origin and form a LIP of Early Cretaceous age (Fischer et al., 2016; König and Jokat, 2010; Leinweber and Jokat, 2011). The Astrid Fracture Zone (AFZ) represents the counterpart of the MFZ at the conjugate margin (Figs. 6.2 and 6.3). The Astrid Ridge (AR) is divided into a northern and southern part by the AFZ (Fig. 6.3). Identified magnetic lineations at both parts of the AR suggest its composition of thickened oceanic crust (Hinz et al., 2004; Leinweber and Jokat, 2012). The AR terminates the Lazarev Sea to the east and separates it from the RLS. The most-likely continental Gunnerus Ridge (Leitchenkov et al., 2008; Roeser et al., 1996; Saki et al., 1987) borders the RLS to the east (Fig. 6.3).

Onshore Mozambique, rift systems are superimposed along parts of the EAAO. A first initial rifting episode might be dated back to Carboniferous to Triassic times, as response to compressional and transpressional deformations in East-Central Africa (Delvaux, 2001; Frizon De Lamotte et al., 2015). In a second rifting episode, the Zambezi Tectonic System (ZTS), comprising the Zambezi Graben, has developed at least since Early Cretaceous times (Flores, 1973) and runs predominantly NW-SE (Fig. 6.2). The Inhanga Tectonic System (ITS) developed since the uplift of the Inhanga High in Late Cretaceous times. Here, the Urema Graben crosscuts the ZTS in a NE-SW direction and turns N-S into the Chissenga Graben (Fig. 6.2). All of these old rift structures have experienced reactivation related to the development of the Cenozoic East African Rift System.

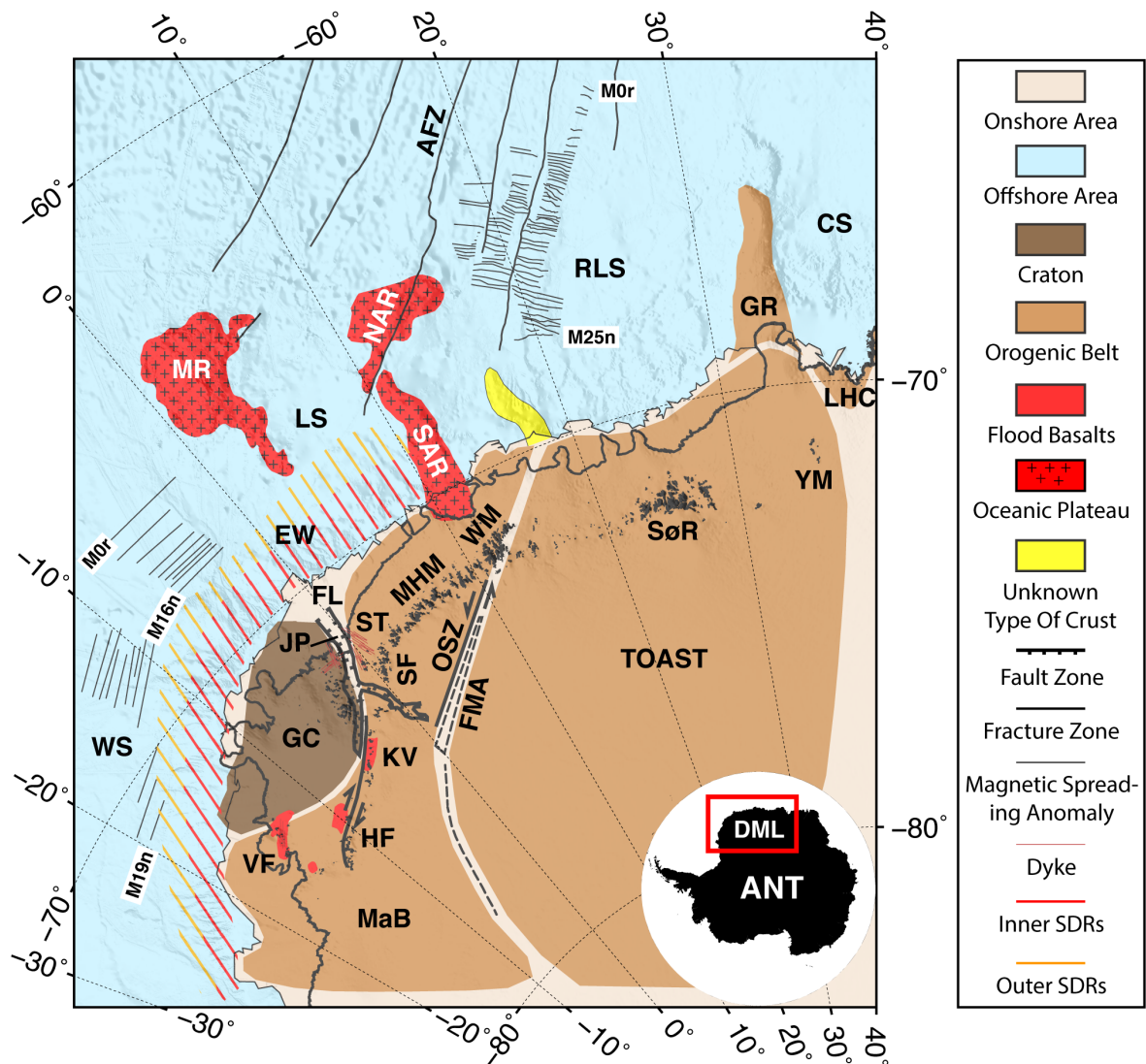


Figure 6.3: Tectonic setting of Dronning Maud Land (DML) and its offshore basins at the Antarctic end of the AAC. Onshore terrains are digitized after [Marschall et al. \(2010\)](#), [Mieth and Jokat \(2014\)](#) and [Jacobs et al. \(2015\)](#). The areas of the MaB and the TOAST are overprinted by the Pan-African orogeny, hence both areas are categorized as orogenic belt. Offshore terrains are digitized after [Leinweber and Jokat \(2012\)](#) and [Leitchenkov et al. \(2008\)](#). The locations of magnetic spreading anomalies are based on studies of [Jokat et al. \(2003\)](#) and [Leinweber and Jokat \(2012\)](#). Abbreviations: AFZ: Astrid Fracture Zone, ANT: Antarctica, CS: Cosmonaut Sea, EW: Explora Wedge, FL: Fimbulisen, FMA: Forster Magnetic Anomaly, GC: Grunehogna Craton, GR: Gunnerus Ridge, HF: Heimfrontfjella, JP: Jutul-Penck Graben System, KV: Kirvanveggen, LHC: Lützw-Holm Complex, LS: Lazarev Sea, MaB: Maud Belt, MHM: Mühlig-Hofmann Mountains, MR: Maud Rise, NAR: Northern Astrid Ridge, OSZ: Orvin Shear Zone, RLS: Riiser-Larsen Sea, SAR: Southern Astrid Ridge, SF: Sverdrupfjella, Sør: Sør Rondane, ST Straumsvola/Tvora: TOAST: Tonian Oceanic Arc Super Terrene, VF: Vestfjella, WM: Wohlthat Massif, WS: Weddell Sea, YM: Yamato Mountains.

The Jutul-Penck Graben in Antarctica (Fig. 6.3, JP) is suggested to have formed as a rift, which has failed in Jurassic times (Ferraccioli et al., 2005; Grantham and Hunter, 1991; Riedel et al., 2013) and might be considered as a counterpart to the rift structures in Mozambique.

6.3 Magnetic data acquisition and processing

6.3.1 New magnetic data

From January to March 2014, the cruises SO230 (Jokat, 2014) and SO231 (Franke, 2014) with the research vessel Sonne acquired new shipborne magnetic data in the Mozambique Basin and the southern Somali Basin (Fig. 6.4, bold red lines). To obtain a complete coverage with systematically acquired magnetic data in the MB, the new profiles were aligned parallel to previously acquired magnetic lines in this area (MoBaMaSis-Cruise, Reichert and Neben, 2008; Leinweber and Jokat, 2012), and are running perpendicular towards the central coast of Mozambique (Fig. 6.4, red lines). Here, the average line spacing is about 25 km. The ship's speed varied between 5 and 10 kn during acquisition. In the southern Somali Basin, the magnetic data were acquired during the seismic data acquisition, and hence are not regularly spaced. The dense pattern of magnetic lines in the Rovuma Basin originates from the simultaneous acquisition of a high-resolution bathymetric dataset in this area.

The magnetic data were continuously acquired with an array of a SeaSpy gradient magnetometer with two Overhauser sensors separated by 150 m and a Magson vector magnetometer sensor in between. The entire array was towed 750 m behind the vessel. The almost variation-free total magnetic field intensity is obtained by the integration of the gradients over the distance of the ship track. SeaLink software and an internal BGR code were used for onboard processing. Geosoft Oasis Montaj was used for the subsequent processing and graphical output. The ship-towed sensor data were de-spiked and corrected for the core-field (IGRF-12). Additionally, an upward continuation to 350 m and levelling was applied.

6.3.2 Compilation of magnetic data in the MB

A compilation of multiple magnetic surveys from the last 12 years in the MB, where the AWI participated in, is shown in Figure 6.5. This comprises the magnetic profiles of the AISTEK-II (Jokat, 2005) and AISTEK-III (Jokat, 2009), MoBaMaSis (Reichert and Neben, 2008), SO230 (Jokat, 2014) and SO231 (Franke, 2014) cruises. Additional

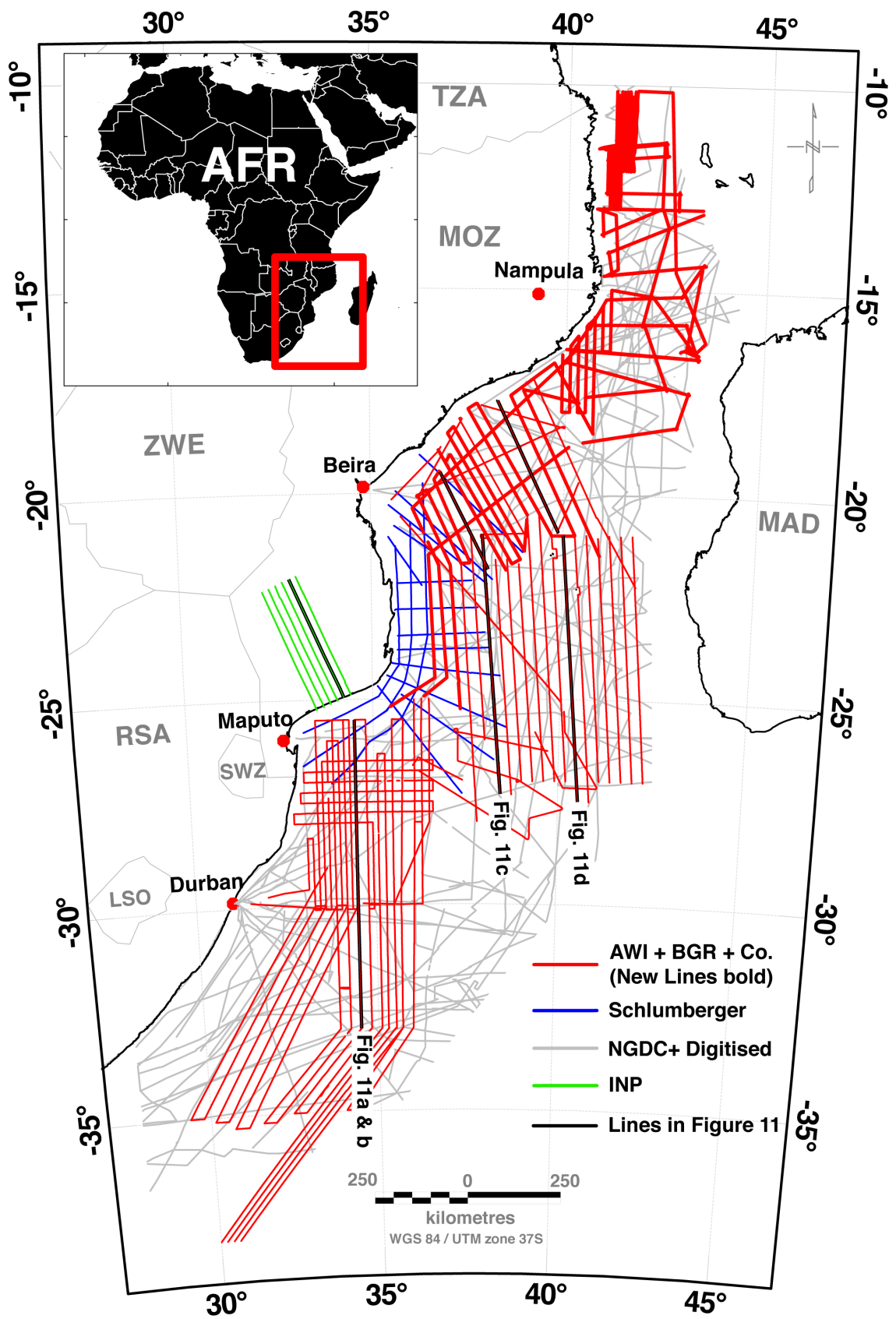


Figure 6.4: Line coverage for compilation of magnetic data in the Mozambique Basin.

Schlumberger multicient data complete our dataset towards the MCP (Fig. 6.4, blue lines). To enhance coverage in the MB, older magnetic profiles from the NGDC (National Geophysical Data Center) database and the lines MDU02 and MDU07 (König and Jokat, 2010) were incorporated (Fig. 6.4, grey lines). Finally, magnetic profiles published by Goodlad et al. (1982) and Reznikov et al. (2005) were digitized and added to the compilation. In total, the database consists of 156000 km of shipborne magnetic data and covers an area of 2.1 Mio km². Based on the irregular distribution of the magnetic profiles it is not possible to assign measurement lines and tie lines. Therefore, for levelling of the whole database the ‘random line levelling’ technique of Mieth (2014) was applied, which is an adaption of the procedure of Mairing et al. (2002). The mean absolute crosspoint error was reduced from 31.1 ± 54.3 nT to 2.93 ± 5.54 nT by the levelling algorithm.

Differential reduction to pole (Arkani-Hamed, 1988) was applied to the dataset (Fig. 6.6a) to allow a direct comparison of the location of identified boundaries and lineations in the magnetic data to the gravity data and for a simple interpretation of the magnetic signatures. The additional calculation of the analytic signal (Fig. 6.6b) reveals the position of magnetic contacts and sheets in the survey area.

6.4 Results and Interpretation

6.4.1 Fractures in the Mozambique Basin

The complete magnetic data and its derivatives are shown in Figs. 6.5 and 6.6 and the gravity data in Fig. 6.7. The data allow the tracing of several fractures back to the coast of the Central Mozambique. We propose four major fractures that separate areas of distinct differences in gravity and magnetic fields as well as areas separated by a distinct offset of identified magnetic spreading anomalies of the same age (Fig. 6.8).

The easternmost fracture runs in the area of Davie Ridge and borders the MB to the Somali Basin (Figs. 6.5 and 6.7). The relative southwards motion of Madagascar during the Gondwana break-up might have caused an overprint of the fracture in this area. South of Madagascar, the fracture extends close to the western boundary of the Madagascar Ridge and joins the Discovery II Fracture Zone at the SWIR (Fig. 6.1). At the Antarctic plate the conjugate fracture elongates along the Conrad Rise and terminates in the area of Gunnerus Ridge (Fig. 6.1).

The central MB is divided by a major fracture originating east of Beira High. At the SWIR, this fracture coincides with the Prince Edward Fracture Zone (Bergh and Norton, 1976). Off East Antarctica, the fracture terminates at a basement high (Figs.

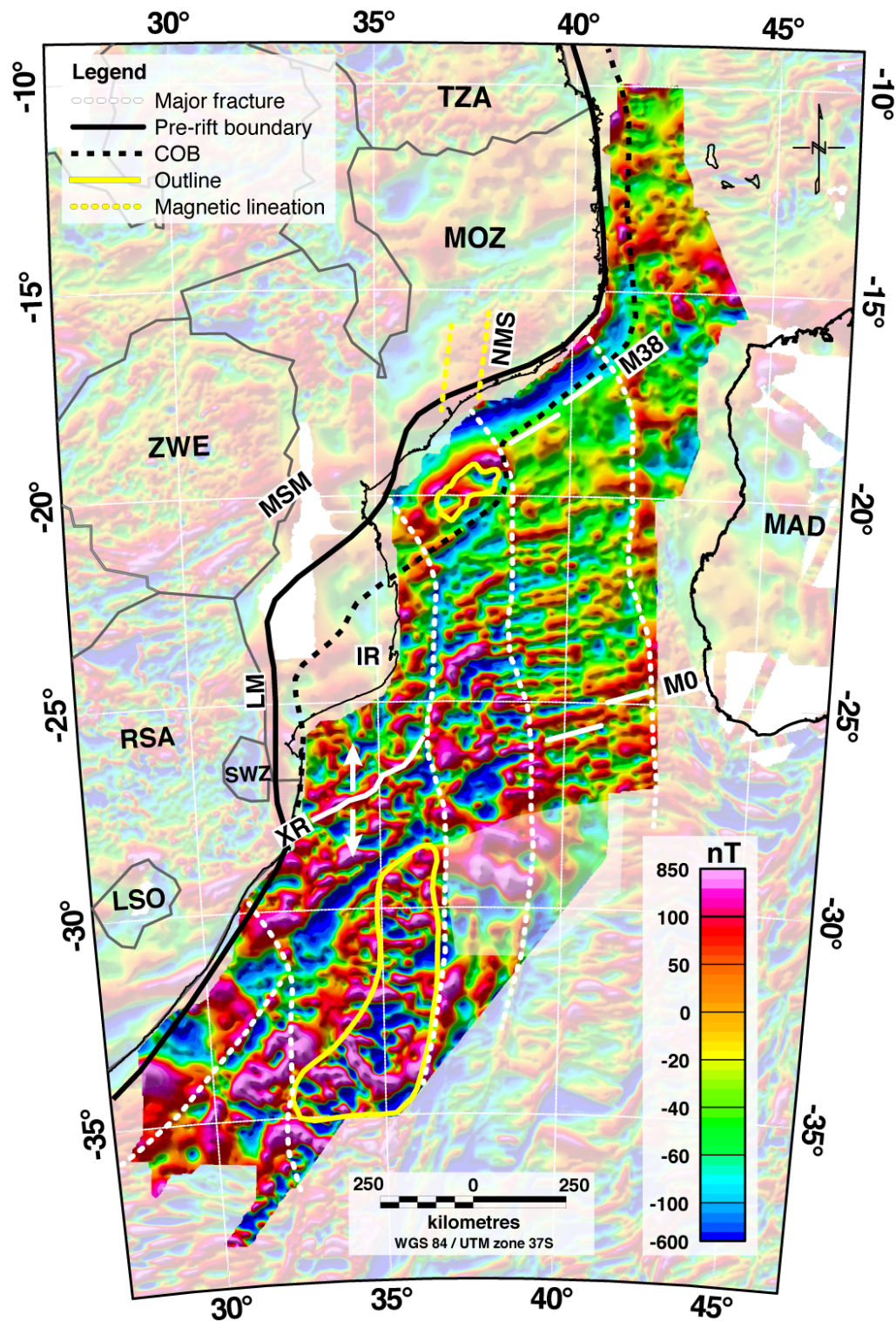


Figure 6.5: Anomaly map of the total magnetic field intensity in the Mozambique Basin. The new compilation of the magnetic data is coloured, whereas the global EMAG2 grid (version 2; Maus et al., 2009) is shown in pale colours in the background. The slightly transparent area east of the Mozambique Ridge is covered by a small number of magnetic profiles. The yellow lines mark the respective positions of Beira High and the Mozambique Ridge. Abbreviations of tectonic features: LM: Lebombo Monocline, MSM: Mateke-Sabi Monocline, NMS: Namama Shear Zone, XR: Extinct Ridge.

6.3 (yellow coloured unknown type of crust), 6.9, 6.10) in the RLS (Hinze et al., 2004; Leinweber and Jokat, 2012)

Another boundary separates the Beira High to the area of the MCP (Figs. 6.5 and 6.7). In the north, this follows the Mozambique Fracture Zone, whereas south of the MozR it turns into the Andrew Bain Fracture Zone (Fig. 6.1). The conjugate feature in Antarctica is the Astrid Fracture Zone (Figs. 6.9 and 6.10).

The Lebombo monocline is part of the western boundary of the AAC. Here, no definite fracture is identified in the potential field data, but revealed a distinct tectonic boundary (Fig. 6.7). South of the LM, the location of the boundary is ambiguous, due to the complex tectonic setting in the Natal Valley. Likely is a transition into the Du Toit Fracture Zone (Sclater et al., 1997) (Fig. 6.1). At the Antarctic plate, the fracture extends towards the western boundary of the Grunehogna Craton (Figs. 6.9 and 6.10).

Based on the identification of these major fractures, three discrete segments can be assigned for the AAC off- and onshore Mozambique: a NE-Segment, the Beira-High-Segment (BH-Segment) and the MCP-Segment (Fig. 6.8). Results of detailed geophysical interpretations of these segments are described in the following section.

6.4.2 NE-Segment

Pronounced magnetic reversal anomalies characterize the western part of the NE-Segment, whereas towards Davie Ridge their amplitude diminishes (Fig. 6.5). In the south, the spreading anomalies are mainly directed ENE-WSW and turn NE-SW closer to the coast. The last magnetic spreading anomaly M0r, before the onset of the Cretaceous Normal Superchron (CNS), is consistently determined in the south of this segment (Fig. 6.8, NE-Segment). Besides minor differences, the subsequent identification of the Cretaceous magnetic chrons confirmed the results of König and Jokat (2010) and Leinweber and Jokat (2012). In general, the amplitude of these magnetic anomalies in this segment is about -200 to +200 nT. Jurassic magnetic spreading anomalies are located closer to the coast in the area between 18°S to 20°S (Fig. 6.8), but are difficult to identify because of a reduction in amplitude into the -50 to -20 nT range. Small amplitudes like these are characteristic of the so-called Jurassic Magnetic Quiet Period (Tominaga et al., 2015), but also reflect the deepening basement in this area (Castelino et al., 2015; Leinweber et al., 2013). Here, our interpretation of magnetic isochrons differs from that of Leinweber and Jokat (2012) owing to the denser line coverage of magnetic data available to us, and to refinements in the Jurassic parts of the magnetic polarity timescale (Ogg and Smith, 2004; Ogg, 2012). The oldest magnetic spreading

6. THE INITIAL GONDWANA BREAK-UP IN THE AFRICA-ANTARCTICA CORRIDOR

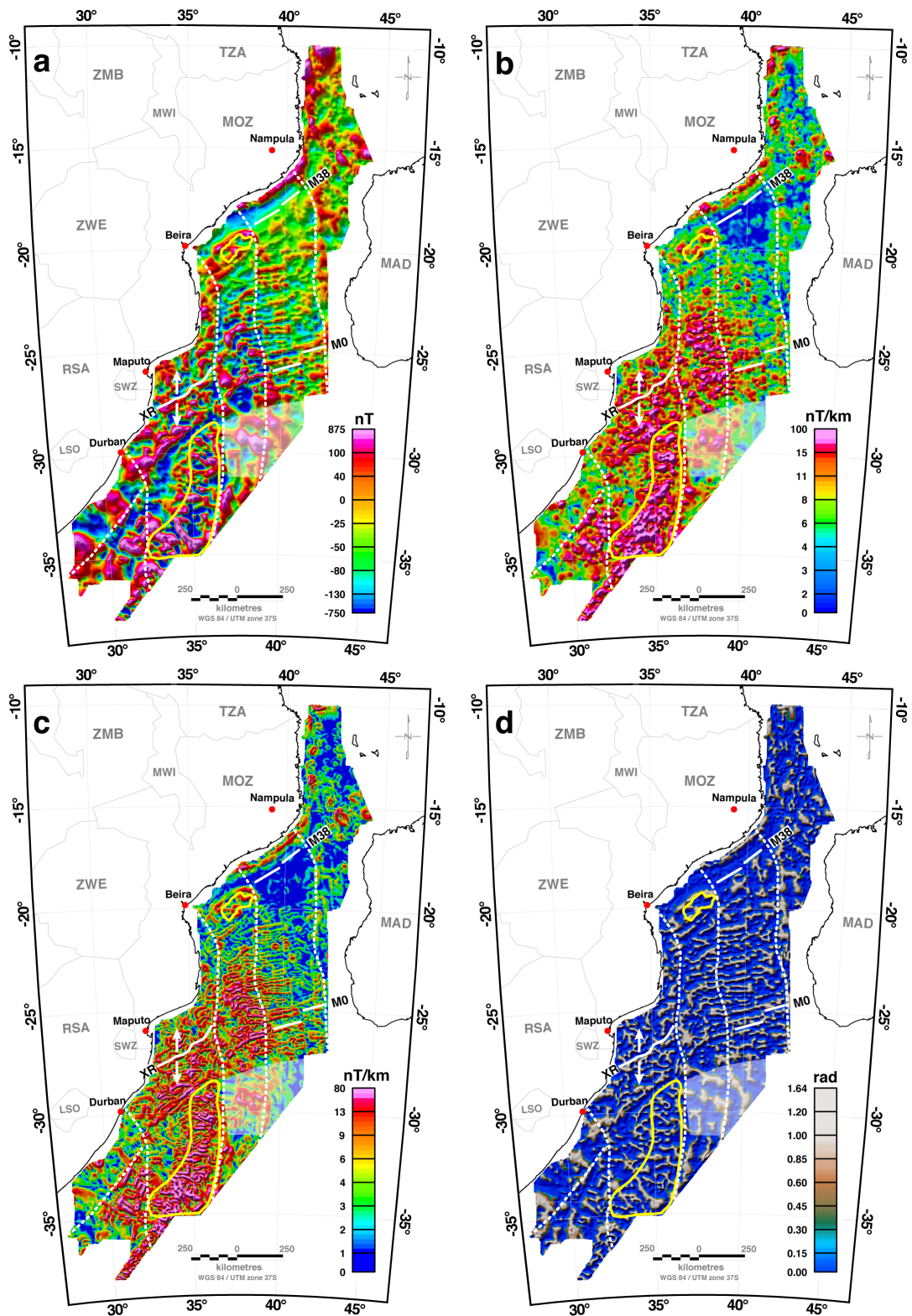


Figure 6.6: Derivative maps of the TMI anomaly in the Mozambique Basin. a) Differential reduction to the pole, b) Analytic signal, c) Enhanced horizontal derivative, d) Positive tilt derivative. The slightly transparent area east of the Mozambique Ridge is covered by a small number of magnetic profiles. The yellow lines outline the positions of Beira High and the Mozambique Ridge.

anomalies in the MB are identified in this segment. In agreement with [Mueller and Jokat \(2017\)](#), the onset of the first oceanic crust accords to chron M38n.2n (164.1 Ma; [Ogg, 2012](#)). Northwards of this, reverse polarized SDRs sequences cause a striking coast-parallel negative magnetic anomaly ([Leinweber et al., 2013](#); [Mueller and Jokat, 2017](#)) (Figs. 6.5 and 6.6a). Close to the coast, the reduced to the pole magnetic data (Fig. 6.6a) show a coast-parallel positive anomaly that coincides with the position of a distinct gravity contrast (Fig. 6.7). Here, seismic refraction studies and potential field modelling ([Leinweber et al., 2013](#); [Mueller and Jokat, 2017](#)) constrain the transition towards > 30 km thick continental crust of the Mozambique Belt in this area.

6.4.3 BH-Segment

Magnetic spreading anomalies are well expressed in the south-eastern part of the BH segment, but become difficult to trace westwards (Fig. 6.5). The anomalies show a similar signature compared to the NE-Segment, but are clearly offset (Fig. 6.8). In the south, the magnetic anomalies show high amplitudes of between -350 and +500 nT (Fig. 6.11c). Here, the gravity data depict a distinct N-S trending high (Fig. 6.7), which in some publications is considered as a northward extension of the MozR (e.g. [Eagles and König, 2008](#); [Reeves et al., 2016](#)) In the same area, the analytic signal of the magnetic data (Fig. 6.6b) reveals a strong gradient, indicating an elevated basement and allowing the interpretation of intruded magmatic material. The identification of mainly ENE-WSW trending Cretaceous magnetic spreading anomalies is conform to the results of [König and Jokat \(2010\)](#) and [Leinweber and Jokat \(2012\)](#) in this area. Concerning the Jurassic, [Leinweber and Jokat \(2012\)](#) reported M33n as the oldest spreading anomaly south of Beira High. However, a reconstruction, based on this identification is difficult ([Leinweber and Jokat, 2012](#)). Based on the newly investigated continental origin of Beira High ([Mueller et al., 2016](#)) and the new magnetic profiles in this area, we consider the oldest identified magnetic chron south of Beira High to be M28n.2r (158.2 Ma; [Ogg, 2012](#)) (Fig. 6.8, BH-Segment). North of this, the magnetic signature of Beira High does not correlate with the Jurassic anomalies in the NE-Segment (Fig. 6.11c, d). Seismic studies depict a NE-SW trending faulted southern margin to Beira High ([Mahanjane, 2012](#); [Mueller et al., 2016](#)). This margin is also characterized by the presence of volcanic and intrusive rocks that raise a positive NE-SW-trending anomaly north of M28n.2r ([Mueller et al., 2016](#)) (Figs. 6.5, 6.6a, d). Seismic reflection data and magnetic modelling suggest the presence of large sills coincident with a circular anomaly at 20°S on Beira High ([Mueller and Jokat, 2017](#)) (Fig. 6.6c). A strong positive anomaly at the northern flank of Beira High (Figs. 6.5

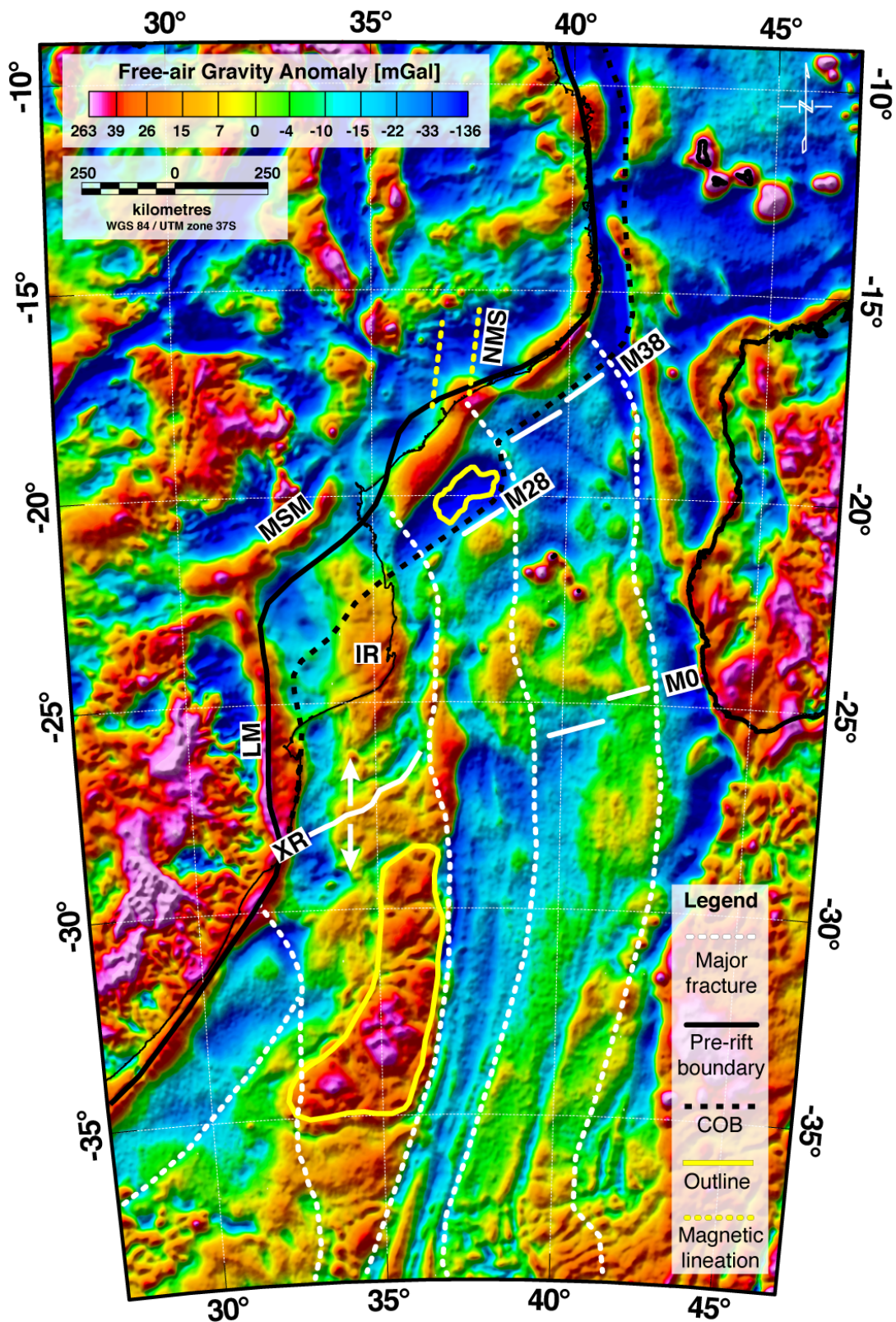


Figure 6.7: Satellite derived free-air gravity anomaly of SE-Africa and the Mozambique Basin (Sandwell et al., 2014). The yellow lines mark the respective positions of Beira High and the Mozambique Ridge. Abbreviations of tectonic features: LM: Lebombo Monocline, MSM: Mateke-Sabi Monocline, NMS: Namama Shear Zone, XR: Extinct Ridge.

and 6.6a) is attributed to the presence of SDRs and lava flows (Mueller et al., 2016; Mueller and Jokat, 2017). In addition, when compared to the NE-Segment, the reduced to the pole magnetic data (Fig. 6.6a) show a wider negative coast-parallel magnetic anomaly. Here, a thick sequence of lava flows is reported (Mahanjane, 2012) to overlie the basement in the Zambezi Delta Depression. According to the gravity and magnetic signature in this coastal segment (Figs. 6.5 and 6.7) as well as the results of potential field modelling (Mueller et al., 2016; Mueller and Jokat, 2017; Watts, 2001), show that the transition towards thick continental crust might be located onshore Mozambique (Figs. 6.5 and 6.7, pre-rift boundary).

6.4.4 MCP-Segment

The interpretation of magnetic data in this segment is challenging, due to a multistage magmatism in the Late Jurassic and Cretaceous that affected this area, as well as recent magmatism along the western branch of the East African Rift System, extending into this segment. Since the 80's, several plate reconstructions of the initial Gondwana break-up already stated a more complex break-up scenario in this segment as in the adjacent Mozambique Basin. So far, magnetic studies in this segment were limited to offshore magnetic data (König and Jokat, 2010; Leinweber and Jokat, 2011; Tikku et al., 2002), which did not allow an assignment of magnetic chrons and could only suppose the presence of rift jumps to obtain a consistent break-up model in this segment (Leinweber and Jokat, 2012). For this study a small amount of high-resolution magnetic data onshore the MCP is available (Fig. 6.4, green lines). The data are located in the central and western part of the MCP. Here, in general, NE-SW directed magnetic lineations are observed in the central part of the MCP (Fig. 6.8). A comparison to corresponding synthetic magnetic waveforms and to the magnetic data in the BH-Segment (Fig. 6.13b, c) reveals a similarity of the magnetic signature of both segments. On the basis of this similarity, we tentatively interpret magnetic reversal anomalies over the southern part of the MCP to document the formation of igneous crust in the period since M28n.2r, and the northern part of the MCP to consist of transitional crust (Fig. 6.11b, d). At the southern coast of the MCP, chron M21r (149.6 Ma; Ogg, 2012) is interpreted at the southern termination of the profiles (Figs. 6.4 and 6.8). These new evidences of the magnetic data at the MCP allow us a re-evaluation of the magnetic data in NNV and across the MozR.

In view of the general southwards opening of the AAC and in consideration of the results of our interpretation in the NE- and BH-Segment, Cretaceous magnetic spreading anomalies trending ENE-WSW might be expected to lie south of the MCP in the

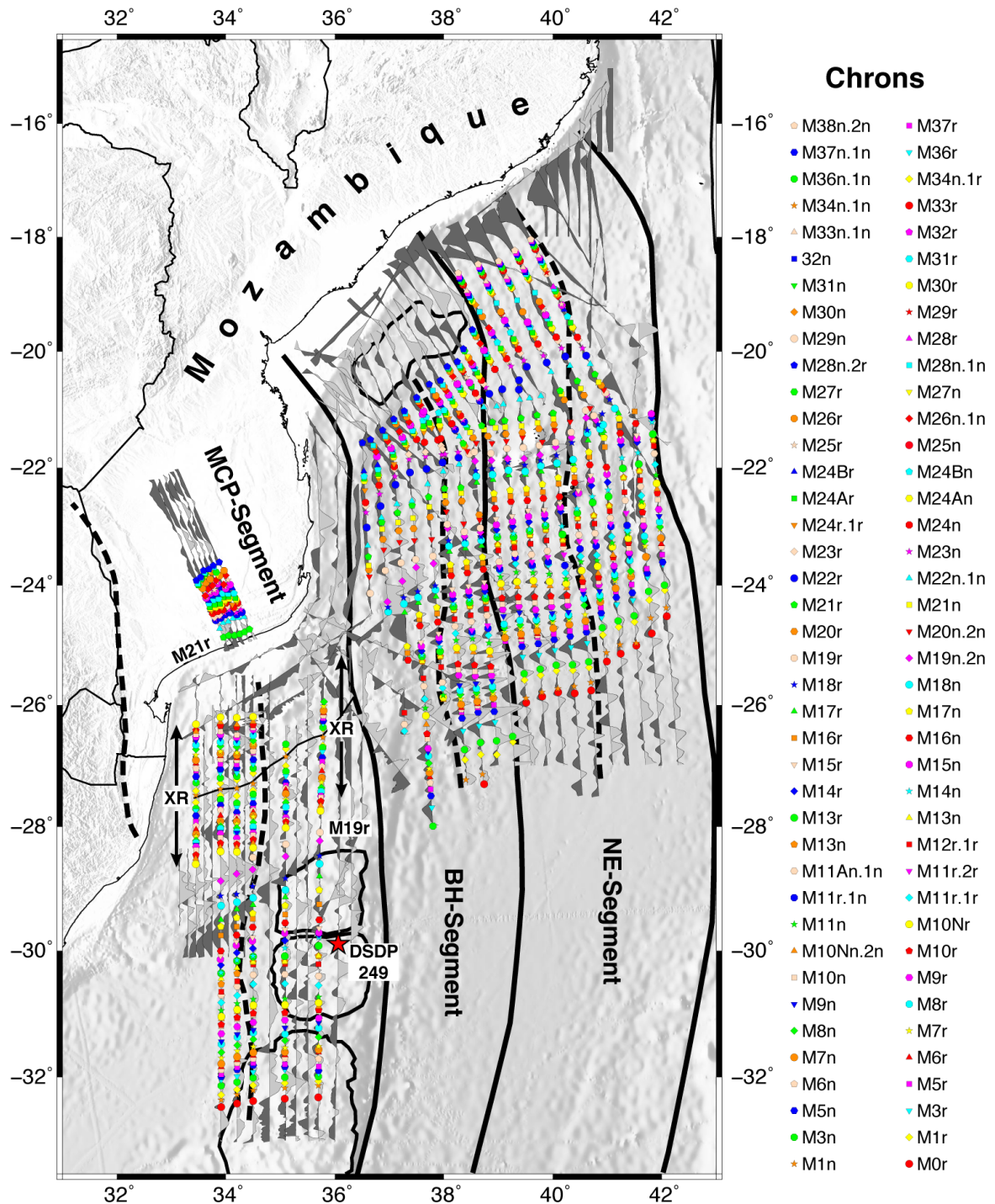


Figure 6.8: New magnetic anomaly picks with their according chron in the Mozambique Basin and the Northern Natal Valley and over the Mozambique Coastal Plains and Mozambique Ridge. In this study the geomagnetic polarity time scale of Ogg (2012) based on a mid-depth deep-tow model was used. Based on the difficulty in picking the flanks of the weak anomalies during the Jurassic Quiet Period and to be consistent with the picks of Leinweber and Jokat (2012), we decided to pick as well at the minima and maxima of the anomalies. Solid black lines mark major fracture zones, which divide the survey area in three segments.

NNV. However, mostly NE-SW directed magnetic lineations are observed in the NNV, and in detail the waveforms are difficult to interpret as a younging continuation of the sequence beyond M21r. Instead, the magnetic lineations seem to be symmetrical about a NW-SE trending magnetic high in the centre of the NNV, implying the presence of an extinct mid-ocean ridge (Fig. 6.5, XR). Based on waveform modelling, this extinction can be dated to chron M1n (127.3 Ma) (Fig. 6.8). Each side of the ridge, magnetic isochrons are interpretable outwards to M10Nr (135.2 Ma). Consistent with this interpretation, the gravity data suggest the presence of NE-SW trending basement features superimposed on a relative low at the NNV (Fig. 6.7), and situated between symmetrical relative highs centred on the MCP and MozR. The eastwards continuation of this extinct ridge is challenging to interpret. A strong negative magnetic anomaly centred on the Ariel Graben, which separates the NNV from the Southern Natal Valley (SNV) and MozR, does not correlate with any of the modelled magnetic isochrons. The analytic signal (Fig. 6.6b) reveals a high gradient in the Ariel Graben that implies the presence of intruded volcanic material.

A variety of magnetic lineations are observed in the SNV and at the MozR. A proposed extinct ridge between the Dana and Galathea Plateau (Leinweber and Jokat, 2011) can not be confirmed. In contrast, we interpret a continuous sequence of magnetic isochrons (Fig. 6.8, MCP-Segment) that indicate emplacement of the Dana Plateau between M19n.2n and M15n (145.7-139.7 Ma) and the Galathea Plateau between M14n and M9r (138.8-133.4 Ma). In the centre of the MozR, the Vauban Plateau developed between M8r (132.9 Ma) and some time during the CNS that we estimate to 118 Ma by assuming a constant spreading rate after chron M0r (126.1 Ma). Consequently, no magnetic lineations are expected or interpreted over the Rennel Plateau, whose emplacement is estimated for the period 118-115 Ma. Magnetic reversal isochrons could not be unequivocally identified across the Robert-Giraud Plateau, the south-western part of the MozR (Fig. 6.2). However, the observed magnetic lineations at this plateau (Fig. 6.5) show a clear similarity to the northern part of the Vauban Plateau at the centre of the MozR and thus imply simultaneous formation in the period between chrons M7r and M0r (132.4-124 Ma).

6.5 Discussion

6.5.1 Pre-rift boundaries

Besides the identification of all relevant tectonic units in the AAC, their pre-rift boundaries are essential for the construction of a consistent break-up model (Figs. 6.5, 6.7,

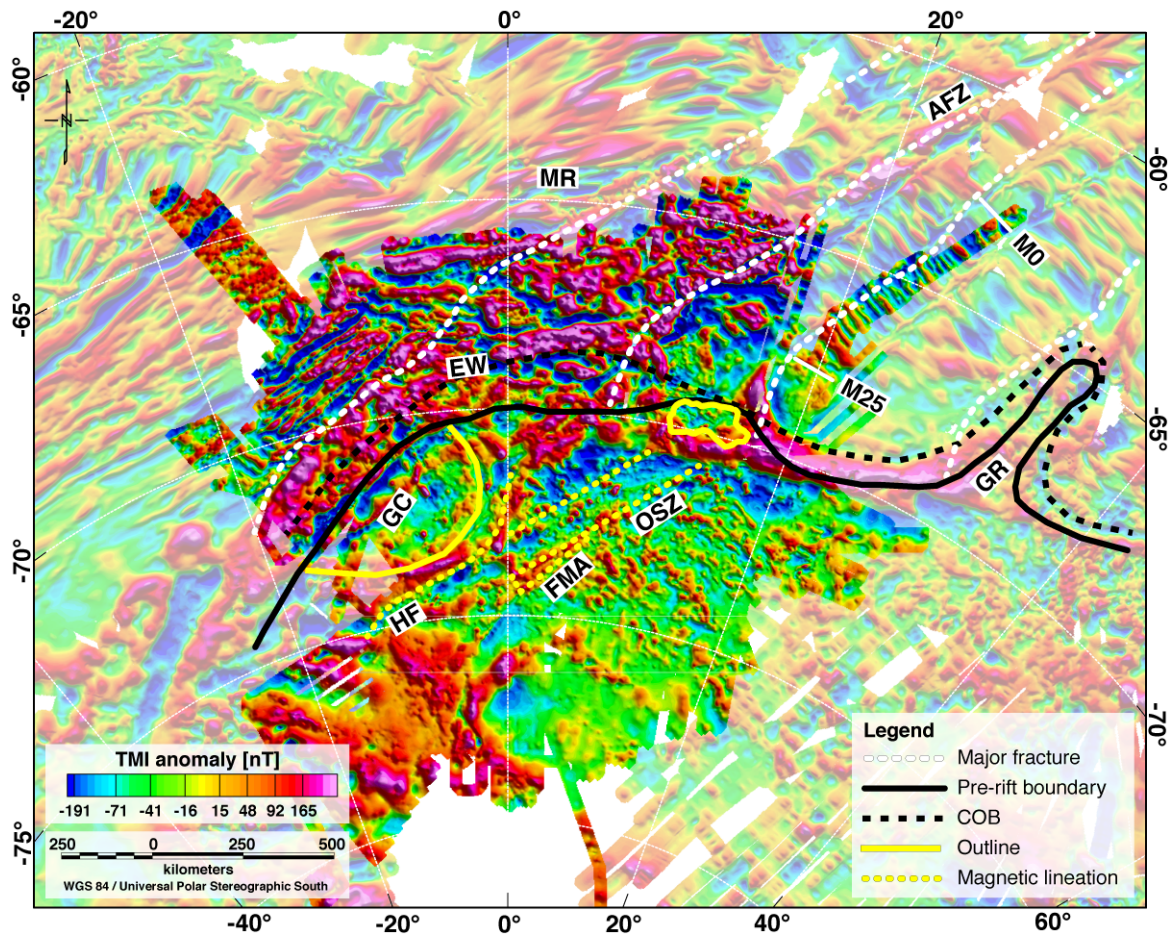


Figure 6.9: Anomaly of the total magnetic field intensity in Dronning Maud Land and its offshore basins. The intensely coloured data are based on a compilation of high-resolution aeromagnetic data by [Mieth \(2014\)](#), whereas the global EMAG2 grid (version 2; [Maus et al., 2009](#)) is shown in pale colours in the background. The solid yellow lines mark the position of the Grunehogna Craton and the pre-rift position of Beira High at the margin of Antarctica. Abbreviations: AFZ: Astrid Fracture Zone, EW: Explora Wedge, FMA: Forster Magnetic Anomaly, GC: Grunehogna Craton, GR: Gunnerus Ridge, HF: Heimefrontfjella, MR: Maud Rise, OSZ: Orvin Shear Zone.

6.9, 6.10, pre-rift boundary). Seismic refraction studies and gravity models reveal evidence for the location of the continent-ocean transitions in the BH and NE segments. A narrow transition from thin oceanic crust towards up to 40 km thick continental crust is located at the Mozambican coast in the NE-Segment ([Leinweber et al., 2013](#); [Mueller and Jokat, 2017](#)). In contrast, thin crust of about 7 km underlies the coast in the BH-Segment and implies the transition to unrifted crust lies onshore in Mozambique ([Mueller et al., 2016](#)). Here, seismic reflection lines depict SDRs and the Nhamura-1 well encountered volcanics of the Middle to Upper Jurassic Stormberg series onshore the Zambezi Delta ([Lafourcade, 1984](#)). Furthermore, in the BH-Segment, the prominent coast-parallel negative magnetic anomaly (Fig. 6.5) ([Mueller and Jokat, 2017](#);

Reichert and Neben, 2008) turns towards onshore Mozambique and is attributed to the presence of SDRs. About 100 km onshore Mozambique, north of these inferred SDRs, the gravity models of Mueller and Jokat (2017) and Watts (2001) suggest the presence of about 35 km thick unrifted crust. Here, the Vila Candida hinge line (Zone de flexure de Vila Candida (Lafourcade, 1984) or Limpopo lineament (Cox, 1992)) (Fig. 6.2, VC) marks the southern termination of the Mozambique Belt. Based on fission-track data, Daszinnies et al. (2009) propose the existence of a rift flank in the area of the Vila Candida hinge line, whose location we therefore interpret as a pre-rift boundary in the BH-Segment. Further west, the Urema Graben separates the Inhaminga High (Fig. 6.2, IH) from the adjacent Zambezi Belt. Most likely, this basement high is of continental origin and was separated from the Zambezi Belt by the activity of the Cretaceous Inhaminga Tectonic System (Flores, 1973). This suggests a continuation of the pre-rift boundary south of the Inhaminga High (Figs. 6.5 and 6.7, pre-rift boundary). The availability of additional space between the Zambezi Belt and Mozambique Belt to accommodate the northernmost parts of the Mozambique Ridge, if they are to be interpreted as of continental origin (Eagles and König, 2008), seems unlikely due to the proximity of the orogenic belts and the presence of the Inhaminga High.

This study has given additional evidence for the presence of oceanic crust beneath the southern part of the MCP. Here, the Lebombo and Mateke-Sabi monoclines are considered as major tectonic boundaries between the MCP and the adjacent cratons and mobile belts (Fig. 6.2, LM, MSM). The prominent gravity highs over the monoclines are attributable to a combination of edge effects related to a distinct change in crustal thickness and the presence of dense intruded volcanic material (Gwavava et al., 1992; Watts, 2001). On the contrary, a recent seismological study of Domingues et al. (2016) and the gravity inversion of Nguyen et al. (2016) suggest that thick crust of the Zimbabwe Craton and the Limpopo Belt terminate slightly south-east of the Mateke-Sabi monocline. Consequently, here the pre-rift boundary at the MCP is assumed to extend slightly south of the MSM and close to the LM.

Little is known about the crustal composition of the extended continental crust of the East Antarctic margin, due to a several hundred-meter thick ice sheet, covering much of the shelf areas. However, new compilations of gravity data in Antarctica (Scheinert et al., 2016) (Fig. 6.10) and magnetic data in DML (Mieth, 2014) (Fig. 6.9) reveal valuable evidence for the extents of the major tectonic units. A strong positive gravity anomaly is observed along the entire margin of DML (Fig. 6.10), trending close to the ice sheet grounding line. Like its conjugate margin in the NE-Segment of Central Mozambique, seismic reflection data reveal no significant width of the shelf in the RLS (Hinz et al., 2004; Leitchenkov et al., 2008), which could mask the gravity signal of

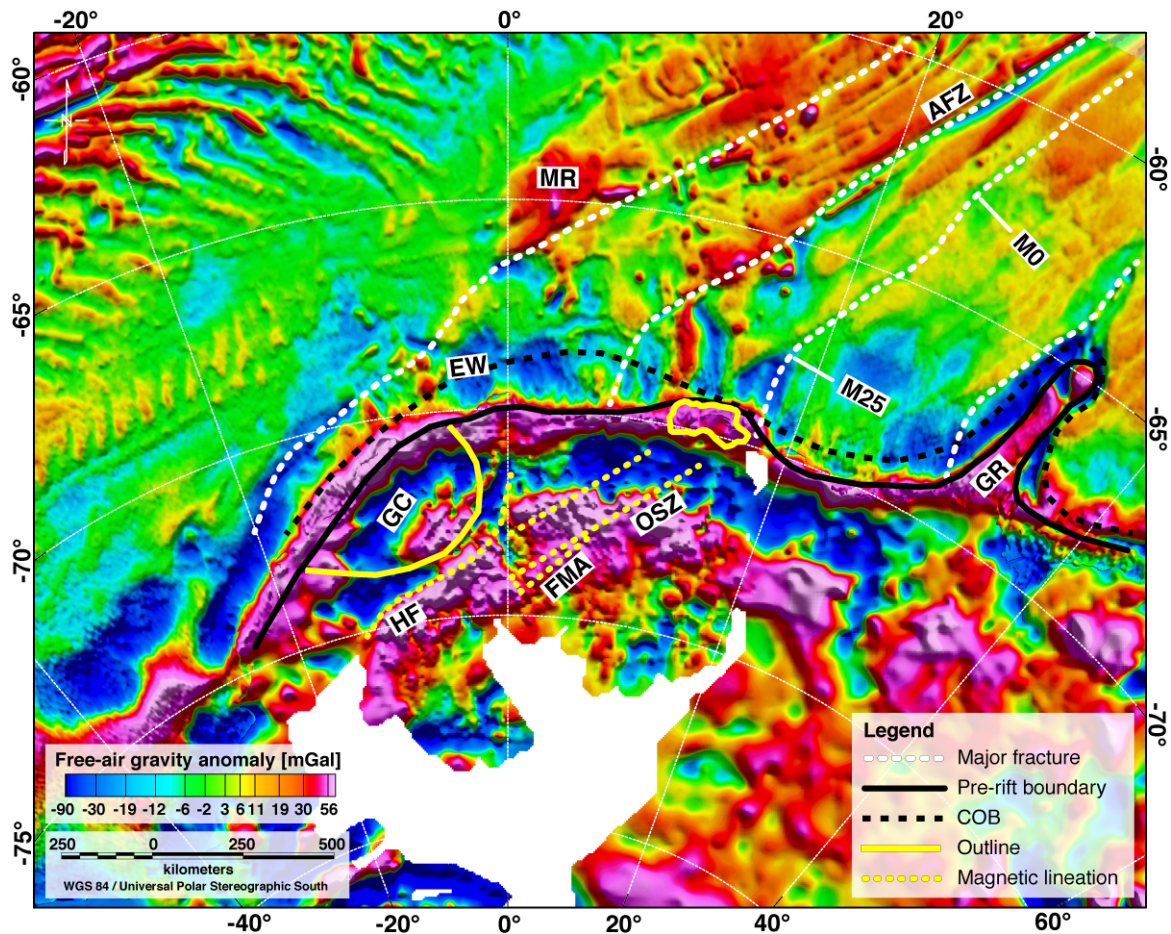


Figure 6.10: Free-air gravity anomaly of Dronning Maud Land and its offshore basins. The compilation of Scheinert et al. (2016) is used for onshore Antarctica, whereas the data of Sandwell et al. (2014) are shown in the offshore areas. The solid yellow lines mark the position of the Grunehogna Craton and the pre-rift position of Beira High at the margin of Antarctica. Abbreviations: AFZ: Astrid Fracture Zone, EW: Explora Wedge, FMA: Forster Magnetic Anomaly, GC: Grunehogna Craton, GR: Gunnerus Ridge, HF: Heimefrontfjella, MR: Maud Rise, OSZ: Orvin Shear Zone.

the continent-ocean transition (Watts and Fairhead, 1999). Gravity modelling in the RLS suggests up to 35 km thick continental crust in the area of the coast-parallel gravity high (Leitchenkov et al., 2008). Therefore, it is assumed that the strong gravity anomaly marks the northern limit of unrifted crust in DML and serves as pre-rift boundary. Seismic refraction studies in the eastern Weddell Sea (Hübscher et al., 1996; Jokat et al., 2004; Kudryavtzev et al., 1991) and the Lazarev Sea (Jokat et al., 2004) yield additional support for this assumption. Here, about 40 km thick unrifted crust thins northwards near the ice edge (Hübscher et al., 1996), which coincides as well with the gravity high.

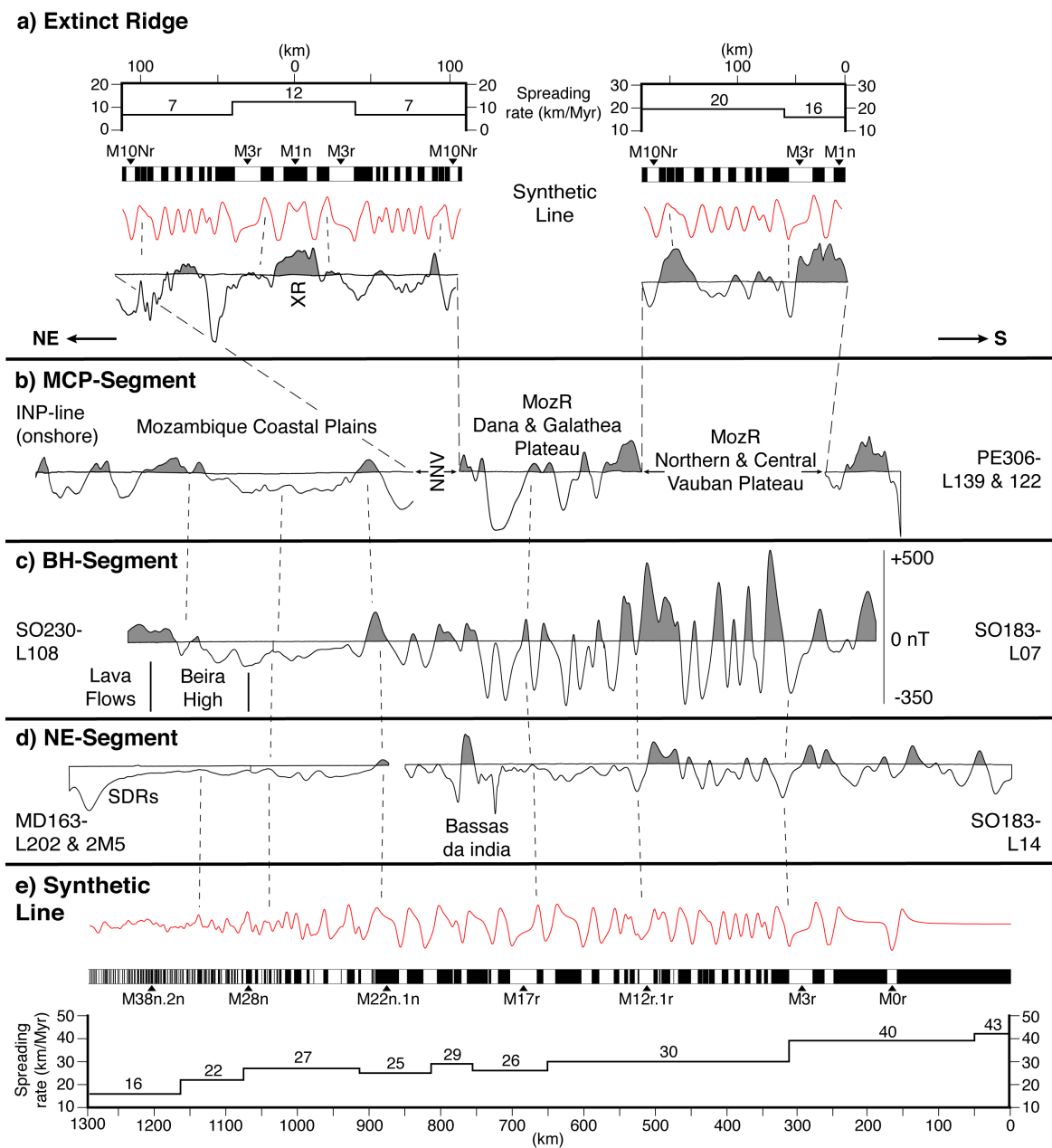


Figure 6.11: Comparison of a synthetic magnetic anomaly sequence to magnetic profiles over the various segments of the Mozambique Basin (locations in Fig. 6.4). The synthetic line is based on the plate kinematic model of this study and the geomagnetic polarity timescale of Ogg (2012). The section of the magnetic profile across the extinct ridge in the Northern Natal Valley (NNV) and at the Vauban Plateau is enlarged for a better visibility.

6.5.2 Initial Fit

A tight fit between the identified pre-rift boundaries of East and West Gondwana is proposed in the future area of the AAC (Fig. 6.12). The tightness suggests that large-scale continental fragments within the present AAC are only to be found at Beira High

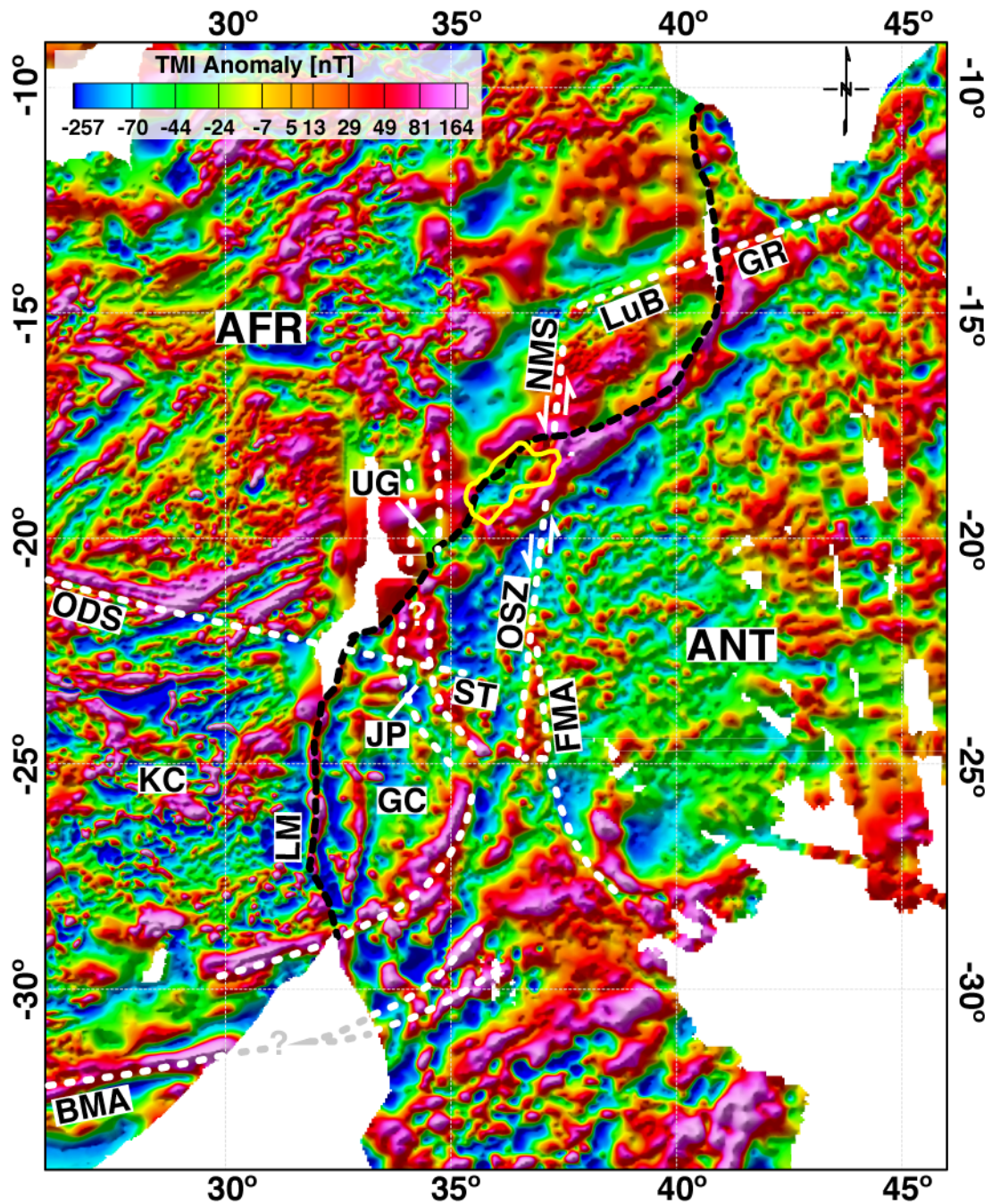


Figure 6.12: Initial fit between Africa and Antarctica. Antarctica is rotated back to a fixed African plate by the rotations suggested in this study for 182 Ma (Table 6.1). Both plates are linked at their pre-rift boundaries (dashed black line). The distinct alignments between the tectonic features of both plates are described in the text. For Antarctica, the magnetic data compilation of Mieth (2014) is merged with the EMAG2 grid (version 2; Maus et al., 2009). For Africa, only the EMAG2 grid is shown with the same colour scale as for Antarctica. Abbreviations: AFR: Africa, ANT: Antarctica, BMA: Beattie Magnetic Anomaly, FMA: Forster Magnetic Anomaly, GC: Grunehogna Craton, GR: Gunnerus Ridge, JP: Jutul-Penck Graben System, KC: Kaapvaal Craton, LM: Lebombo Monocline, LuB: Lurio Belt, NMS: Namama Shear Zone, ODS: Okavango Dyke Swarm, OSZ: Orvin Shear Zone, ST: Straumsvola/Tvora, UG: Urema Graben.

and, possibly, the smaller South Tugela Ridge (Bhattacharya and Duval, 2016). The reconstructed magnetic anomalies reveal several lineations that can be traced between conjugate pairs of continents. Clearly visible is the continuation of the strong magnetic anomaly at the southern edge of the Kaapvaal Craton in SE-Africa to the corresponding edge of the Grunehogna Craton in East Antarctica (Fig. 6.12). The reconstruction unites the Okavanga and Straumsvola dyke swarms, which were both emplaced about 178 Ma and trend WNW-ESE (Hastie et al., 2014). The Jutul-Penck Graben can be aligned with the Urema Graben of the ITS in Mozambique, implying a shared initiation as rift structures in latest Jurassic times. It is likely that the suggested Cretaceous emplacement of the ITS (Flores, 1973) reactivated existing structures of the EAAO. There is also remarkable north-eastward continuity between the Forster Magnetic Anomaly via the Orvin Shear Zone in DML to the Pan-African Namama Shear Zone (NMS) in Central Mozambique (Fig. 6.12). The sinistral NMS displaces structures flanking it by at least 50 km (Macey et al., 2010; Viola et al., 2008). In agreement, the Orvin Shear Zone shows as well a sinistral sense and is assumed, along with the Forster Magnetic Anomaly, to mark a major tectonic boundary within or at the edge of the EAAO (Grantham et al., 2003; Jacobs et al., 1998; Riedel et al., 2013). Minor features within the EAAO might be expected to show continuity east and west of the Namama-Orvin Shear Zone, too. A surprising observation is that the magnetic signature of the Lurio Belt in NE-Mozambique seems to extend across Gunnerus Ridge (Fig. 6.12, LuB, GR) to run either along the coast of the Cosmonaut Sea or along a thrust zone in Sri Lanka (Reeves and De Wit, 2000).

6.5.3 Onset of Jurassic Rifting

A crucial boundary condition for the reconstruction of the AAC is the timing for the onset of rifting between East and West Gondwana. In general, the initial emplacement of the Karoo flood basalts in SE-Africa and the Ferrar flood basalts in East Antarctica are considered as indicators for the onset of the Jurassic rifting (Figs. 6.2 and 6.3). The main phase of Karoo basalt emplacement happened at 184-181 Ma in the southern part of SE-Africa (Hastie et al., 2014). Jourdan et al. (2008) report a subsequent northwards shift of the magmatic activity, constrained by volcanics that date to between 182 and 178 Ma. The Ferrar flood basalts and dyke swarms in DML were emplaced in the same period (Hastie et al., 2014). Furthermore, Mueller and Jokat (2017) suggest a slightly later onset, but continuous magmatism to the east of Central Mozambique. An emplacement of the Save-Limpopo dyke swarm and the Mwenezi intrusions between 178-174 Ma (Hastie et al., 2014), the SW-1 dyke swarm about 170 Ma (Hastie et al.,

2014; Mekonnen, 2004) as well as an age of 177 ± 3 Ma of the oldest volcanics in the Moma district (Jaritz et al., 1977) support this model.

Brune et al. (2016) have suggested a general pattern of plate divergence during continental fragmentation and dispersal. Initially, during the onset of rifting, plate divergence is expected to be slow at about 2-5 km/Myr whilst the continental lithosphere weakens. Subsequently, during an ~ 10 Myr-long speed-up phase, the plate divergence velocity increases as the lithosphere weakens. As a consequence, continental rifting eventually gives way to seafloor spreading. Applying these ideas in the AAC, we might expect that initial (~ 182 Ma) Jurassic rifting, at which time magmatism was affecting both conjugate margins, occurred at slow divergence rates, and that the onset of faster rates had occurred by 177 Ma at the earliest, when the entire margin of Southern and Central Mozambique was affected by magmatism (Mueller and Jokat, 2017). The 174-172 Ma emplacement of the Rooi Rand dyke swarm at the southern tip of the Lebombo monocline is interesting in this context (Hastie et al., 2014). Their MORB-like composition might not indicate the onset of oceanization (Jourdan et al., 2008), but instead an enhancement of decompression melting in response to more rapid lithospheric thinning as the rate of plate divergence accelerated, according to the rotations in Table 6.1, to about 16 km/Myr. The NE-SW orientation of the SW-1 dyke swarm at the MCP (Mekonnen, 2004) and of the Limpopo-Angoche dyke swarm along the coast of Central Mozambique (Reeves et al., 2016) reveals a margin-normal (NW-SE directed) stress field during rifting. The trends of fracture zones close to the ice shelf in the RLS (Fig. 6.13a, c) and of synthetic flowlines (Fig. 6.13a) suggest that this stress field had changed little by 164.1 Ma, with development of the first oceanic crust in the AAC (Mueller and Jokat, 2017).

Leinweber and Jokat (2012) noted the apparent 8 Myr long delay between the youngest volcanism on the Lebombo Monocline and this oldest oceanic crust further east, and suggested it records a response to early anticlockwise rotation of East Gondwana, leading to east-directed rifting beneath the MCP-Segment. This rotation does not reproduce the pre-rift alignments that are possible with our initial fit, and leads to untenable overlap of the Grunehogna Craton with the Kaapvaal Craton whilst it occurs. An alternative explanation of the delay is as an indication of diachronous west-to-east break-up. If this is to be seen as consistent with our assumption of a two-plate scenario, it would require intra-Antarctic or intra-Africa tectonics to transform the divergent plate boundary in the MCP into one or both of the neighbouring continental interiors. The ZTS, ITS, and Jutulstraumen-Penck rifts might be considered as such features.

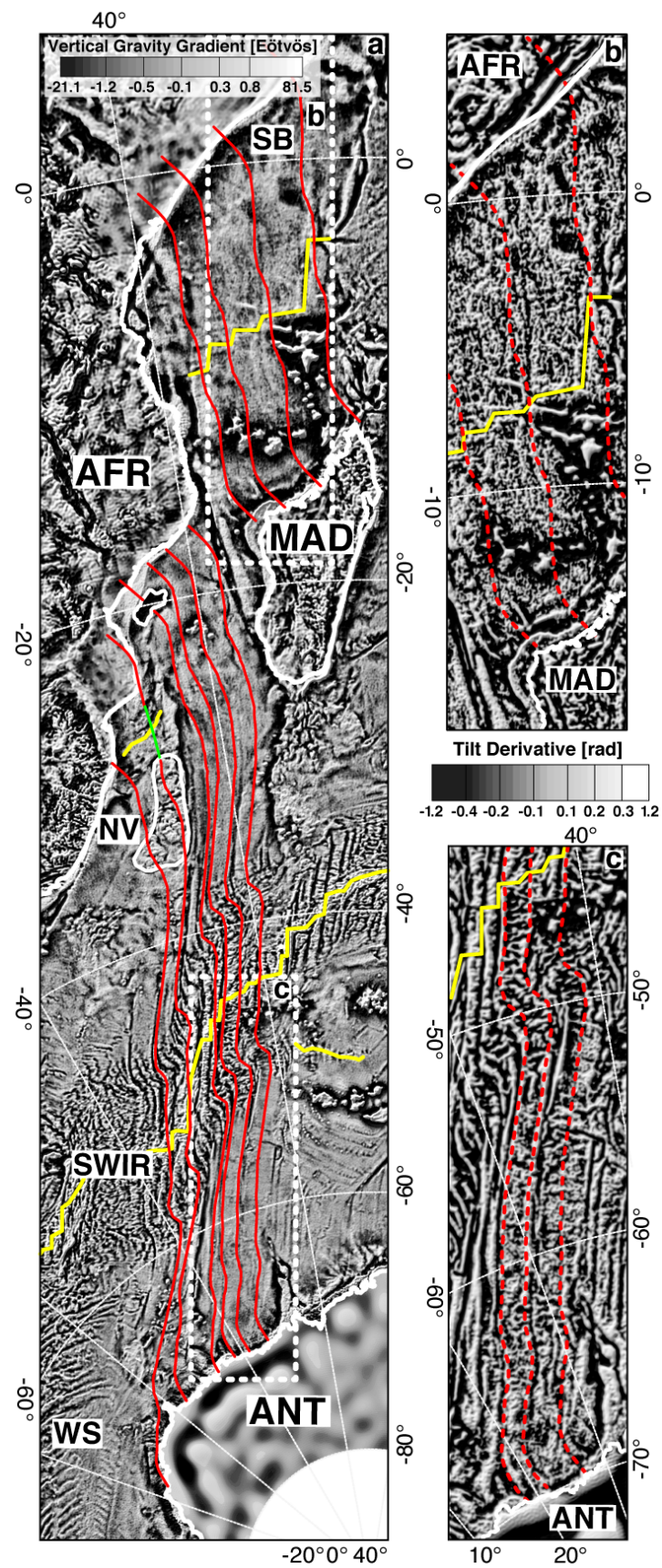


Figure 6.13: Synthetic flowlines (red) calculated by the rotations in Table 6.1. Continues ...

6.5.4 The Beira High Drift

Recent seismic studies revealed the continental nature of Beira High (Mahanjane, 2012; Mueller et al., 2016). Its interior consists of stretched, but highly intruded continental crust. Gravity modelling indicates that the margins of the BH-Segment in Central Mozambique and the north-western flank of Beira High host crust that is similarly broad and thin (Mueller et al., 2016; Mueller and Jokat, 2017). In contrast, the south-eastern margin of Beira High towards normal oceanic crust in the Mozambique Basin is much narrower (Mueller et al., 2016). Seismic reflection data and magnetic modelling over Beira High depict the extrusion of SDR-like lava flows at its north-western flank and the presence of additional sill-like intrusions in its central part (Mahanjane, 2012; Mueller and Jokat, 2017). Furthermore, Mueller and Jokat (2017) report similarities between the magnetic signatures of the north-western flank of Beira High and the central margin in the RLS, which might indicate that both are affected by the same magmatic events and implies a shared history. These observations led Mueller et al. (2016) to suggest the isolation of Beira High in the MB by a rift jump from an initial location on its African side to a later one on its Antarctic side.

By means of the newly assigned pre-rift boundaries, it is possible to accommodate Beira High between East and West Gondwana. The eastern boundary of Beira High within the initial fit coincides with the southern termination of the prominent sinistral Namama Shear Zone in Mozambique and its continuation towards the Orvin Shear Zone in DML. This zone of weakness might have accommodated a transform fault between the early African-Beira rift until its abandonment in favour of the Antarctica-Beira successor rift.

We note the change in geophysical signature in those parts of the RLS margin to which Beira High reconstructs. Here, between southern Astrid Ridge and a basement high of unknown origin at 16-18°E (Fig. 6.3, yellow coloured unknown type of crust), the positive gravity anomaly broadens significantly (Fig. 6.10), and the smooth high-

Figure 6.13 (cont.): a) Synthetic flowlines in the AAC and the Somali Basin, overlain on the vertical gravity gradient data of Sandwell et al. (2014). The flow lines meet at the active mid-ocean ridge (yellow). The green flow line represents additional spreading in the Northern Natal Valley between the African plate and a micro plate of the MozR by a ridge, which was active between M10Nr and M1n. The rift jump at Beira High causes the separation of the flowline in this area. b) and c) synthetic flowlines in the Somali Basin and the Riiser-Larsen Sea, overlain on the tilt derivative of the vertical gravity gradient. Remarkable is the clear expression of the fractures in the Riiser-Larsen Sea until close to the ice shelf (white line). Abbreviations: AFR: Africa, ANT: Antarctica, MAD: Madagascar, NV: Natal Valley, SB: Somali Basin, SWIR: Southwest Indian Ridge, WS: Weddell Sea.

intensity magnetic anomaly of the RLS margin begins to give way to more localised and weaker anomalies in the direction of the Explora Wedge in the Lazarev Sea (Fig. 6.9, outline of Beira High). Conspicuously, the magnetic anomaly at the north-western flank of Beira High (Fig. 6.5) may represent the missing westwards continuation of the marginal magnetic signature of the RLS. The changed geophysical signatures of the RLS margin between Astrid Ridge and 16-18°E can thus be explained as the result of later rifting there, which transferred Beira High to what was to become the African plate. Seismic reflection data indicate a thick layer of volcanic and magmatic material in the apron of Astrid Ridge filling this newly formed deep basin (Hinz et al., 2004). The dense volcanic rocks cause the wider gravity high and the magnetic anomalies (Leinweber and Jokat, 2012) in this area. Volcanic rocks and old sediments are interpreted to onlap both sides of the intra-basin high at 16-18°E (Fig. 6.3, yellow colour) (Hinz et al., 2004; Leitchenkov et al., 2008). Similar to Beira High, this intra-basin high is characterised by a negative gravity anomaly (Fig. 6.10) and magnetic anomalies (Fig. 6.9) associated with magmatic intrusions, inviting its interpretation also as a detached continental sliver.

The Beira High rift jump is assumed to have followed the emplacement of lava flows at the high's north-western flank around 159 Ma. This coincides with a change in plate divergence direction between east and west Gondwana and the development of magnetic reversal isochron M28n.2r (158.2 Ma) south-east of Beira High. It is likely that the flows formed towards the end of an early (beginning 166.3 Ma; Table 6.1) period of stretching affecting Beira High that also led to its intrusion by gabbroic melts. Beira High is not palinspastically restored in our reconstruction to take account of this stretching.

Based on its restored position to the east of the major sinistral Namama-Orvin Shear Zone at the coast of DML, it is possible to speculate that Beira High might ultimately have originated as part of the Maud Belt. Its subsequent history would thus have involved overprint during the Pan-African orogeny prior to its extension and intrusion during Gondwana break-up.

6.5.5 The extinct ridge in the NNV and the emplacement of the MozR

The interpretation of magnetic reversal isochrons in the MCP-Segment (Fig. 6.8, MCP-Segment) results in implications for the break-up in this segment. The isochrons are interpreted as M21r (149.6 Ma) at the southern coast of the MCP. The ensuing sequence is identified far to the south, beginning just slightly north of the MozR, where isochrons

M19n.2n (145.7) until M0 and into the CNS (115 Ma) are interpretable. For the intervening space and time, we interpret the presence and action of an extinct ridge in the NNV (Fig. 6.8, XR), flanked by magnetic isochrons that show it was active at least in the period M10Nr to M1n (135.2-127.3 Ma). Plate divergence at this ridge caused southwards displacement of the MozR. Three additional observations support the existence of this extinct ridge:

1. The symmetrical gravity anomaly highs over the Inharrime and northern Mozambique ridges are separated by a distinct lower anomaly of the NNV.
2. Already [Martin and Hartnady \(1986\)](#) observed the asymmetry of African and Antarctic sea floor aged older than M2. Based on a pre-rift boundary close to the Lebombo and Mateke-Sabi monocline, hypothetical flow lines of a reconstruction (Fig. 6.13a) without additional formed crust end up still on the African plate and do not meet midway at the SWIR.
3. In a similar sense, without additional formed crust in the MCP-Segment, it is not possible to account for the reported Valanginian to Hauterivian age (139.4-130.8 Ma; [Gradstein et al., 2012](#)) of the oldest sediments at DSDP site 249 (Fig. 6.2) at the Galathea Plateau ([Simpson et al., 1974](#)).

An extinct ridge in the NNV was originally proposed by [Tikku et al. \(2002\)](#). They suggested an E-W trending axis that had been active about M11-M2, defining an independently rotating plate bearing parts of the MozR. Based on the data in our newer magnetic compilation, a NE-SW orientation seems more likely for the ridge, and its extinction date refined to M1n. The onset of spreading at the extinct ridge is more challenging to date, due to the weakening of magnetic anomalies away from its axis (Fig. 6.11a). Like that of [Tikku et al. \(2002\)](#) our synthetic magnetic anomaly profile allows for tentative identification of paired M10Nr isochrons. During the ridge's activity the MozR was part of a small micro plate, with simultaneous spreading at different rates at two ridges (Fig. 6.14, M8n). One existed between the African plate and the northern boundary of the micro plate in the NNV, and a second at the southern tip of the micro plate and the Antarctic plate. Regarding the spreading velocities, at the beginning of M3r, a full spreading rate of 24 km/Ma is observed at the ridge in the NNV and a half-spreading rate of 16 km/Ma at the spreading centre at the Vauban Plateau of the MozR (Fig. 6.11a). This results in a total plate divergence rate of 40 km/Ma over two mid-ocean ridges at this time in the MCP-Segment, similar to that across the single African-Antarctic ridge segment in the adjacent BH-Segment. However, prior to M3r, a similar balance can only be achieved if the NNV ridge is assumed to have been active since M12r.1r (Fig. 6.11e).

As a consequence of the active ridge in the NNV, the additional southwards motion of the MozR accompanied the proposed simultaneous southwards motion of the magmatic source, which might caused a longer magmatic influence on the MozR and explain the observed multistage magmatism (Fischer et al., 2016). Furthermore, ash-rich silt- and claystones as well as volcanic glass of Valanginian to Early Cenomanian age (139-100 Ma; Gradstein et al., 2012), encountered at DSDP Site 249 (Fig. 6.2) at the northern MozR (Simpson et al., 1974), testify to the long-lasting Cretaceous magmatism in this area.

Conspicuous magnetic anomalies, coincident with free-air gravity highs, located directly east of the extinct ridge in the BH-Segment (Figs. 6.5 and 6.7), indicate as well an enhanced magma supply to the ridge's eastern end. These features have previously been considered as a possible northward extension of the MozR (Eagles and König, 2008; Reeves et al., 2016; Tikku et al., 2002).

6.5.6 Link to the plates of Madagascar and South America

Recent geophysical studies dealing with the opening of the Somali Basin indicate clockwise rotation of Madagascar in its early stage (e.g. Eagles and König, 2008; Davis et al., 2016; Phethean et al., 2016; Reeves et al., 2016). In general, this motion is compatible with our results in the AAC. However, in comparison to those studies, we have been able to interpret Jurassic magnetic reversal anomalies close to the COB, as well as the presence of SDRs, and so assign a detailed timing for the initial break-up. According to our study, the Mozambique and Somali basins opened simultaneously since the Jurassic between just two plates. The same rotation as for the opening of the AAC can be applied to Madagascar to restore it from its initial position at the African margin, fringing around Bur Acaba, to its present position (Table 6.1). However, the trend of the calculated synthetic flowlines slightly differs to the proposed fracture zones of Phethean et al. (2016) or those interpretable from the vertical gradient of gravity (Fig. 6.13).

Furthermore, for the time at about 150 Ma, seismic reflection data across Davie Ridge depict a compressional phase west of Davie Ridge and extension east of it (Mahanjane, 2014). Those authors suggest a clockwise rotation of Madagascar about a pivot in the proximity of the Angoche Basin at this time (Mahanjane, 2014). About 150 Ma, a distinct clockwise rotation is also produced in our model (Fig. 6.14, M16n), albeit about a different rotation pole (Table 6.1). It might be that the rotation at this time predicted by our model was either more complicated or a complex rift propagation caused short-lived compressional forces at the ridge.

The emplacement of the extinct ridge sometime between M12r.1r and M10Nr (138–135 Ma) in the NNV coincides with the onset of the separation of Africa and South America at 138 Ma (Pérez-Díaz and Eagles, 2014). Prior to this rifting, Figure 6.14 suggests a tight fit of Maurice Ewing Bank to Africa and Antarctica, at the southwestern boundary of the South Tugela Ridge (Fig. 6.14, Gondwana Fit (182 Ma)). Based on seismic reflection data, Bhattacharya and Duval (2016) postulate that South Tugela Ridge is a continental sliver. This conclusion is supported by the ridge’s similarities to the Beira High in potential field data, and consequently might represent a continental sliver detached either from Maurice Ewing Bank or the African continent.

6.6 The new kinematic break-up model of the AAC

Together with previously interpreted isochrons in the RLS (Leinweber and Jokat, 2012), the newly interpreted magnetic isochrons of the Mozambique Basin serve as a base for the calculation of new rotation parameters. Additional constraints are provided by fracture zones that can be traced throughout the AAC, to which we fit synthetic flowlines (Fig. 6.13). The open-source software GPlates (Boyden et al., 2011) is used for the reconstruction. The new rotation parameters, for East Antarctica with respect to a fixed African plate, are listed in Table 6.1. For times after the CNS, we use the rotations of Matthews et al. (2016). In the following, the reconstruction model (Fig. 6.14) is described at important stages.

Rifting (182 -164.1 Ma): Prior to rifting, there is a tight fit between East and West Gondwana (Fig. 6.14, Gondwana Fit). Since 182 Ma, magmatism affected the African and Antarctic continent (Hastie et al., 2014) alongside the onset of NW-SE oriented tensional forces. This led to a period of slow (2-5 km/Myr) SE directed divergence of east and west Gondwana (Brune et al., 2016). By 177 Ma at the earliest, magmatism came to affect the entire Southern and Central Mozambican margin (Mueller and Jokat, 2017), heralding the onset of a ~ 10 Myr long period of increasing plate divergence rates. The emplacement of the Rooi Rand dyke swarm at 174-172 Ma (Hastie et al., 2014) and most likely of the SW-1 and Limpopo-Angoche dyke swarms, accompanied this phase. Identified high-velocity lower crustal bodies along the central coast of Mozambique (Leinweber et al., 2013; Mueller et al., 2016) and at the Antarctic margin in the Lazarev (Jokat et al., 2004) and Weddell seas (Hübscher et al., 1996; Kudryavtzev et al., 1991) suggest magmatic material underplating the stretched continental crust. Reverse polarized SDRs at the margin of Central Mozambique as well as the inner SDRs at the Explora Wedge emerge between 168.5 and 166.8 Ma

Table 6.1: Finite rotations for the opening of the AAC and the Somali Basin. Unless otherwise noted, stated ages correspond to the mid interval time of the respective magnetic chron of the geomagnetic polarity time scale of [Ogg \(2012\)](#).

Chron	Age	Latitude	Longitude	Angle	Reference
Antarctica with respect to Africa					
Present	0.00	90.00	0.00	0.00	
C5n.2no	11.06	8.20	-49.40	1.53	(Royer and Chang, 1991)
C6no	19.72	10.70	-47.90	2.78	(Royer and Chang, 1991)
C13ny	33.16	12.00	-48.40	5.46	(Royer and Chang, 1991)
C21no	47.35	9.73	-40.67	8.82	(Cande et al., 2010)
C25ny	57.10	9.86	-45.24	10.49	(Cande et al., 2010)
C31ny	68.37	0.10	-45.56	11.70	(Bernard et al., 2005)
C33n	77.10	-4.60	-40.60	14.39	(Bernard et al., 2005)
C34ny	83.64	-1.17	-40.52	16.92	This study
CNS	102.00	-2.32	-33.32	28.09	This study (To fit fractures)
CNS	113.00	-6.74	-28.95	34.57	This study (To fit fractures)
CNS	120.00	-8.77	-27.49	37.48	This study (To fit fractures)
M0r	126.12	-10.41	-26.02	41.09	This study
M3n	128.89	-9.55	-27.19	42.30	This study
M5n	131.02	-9.36	-27.58	43.01	This study
M8n	132.68	-8.86	-28.44	43.21	This study
M10n	133.73	-8.93	-28.71	43.65	This study
M11n	135.62	-8.89	-29.17	44.42	This study
M13n	138.34	-8.99	-29.57	44.96	This study
M16n	141.03	-8.58	-30.20	46.64	This study
M17r	143.29	-8.20	-30.20	47.86	This study

6. THE INITIAL GONDWANA BREAK-UP IN THE AFRICA-ANTARCTICA CORRIDOR

M20n.2n	147.34	-7.41	-30.99	49.17	This study
M22n.1n	150.56	-7.00	-31.46	50.30	This study
M22r	151.79	-6.74	-31.71	50.88	This study
M25n	155.70	-6.45	-31.96	52.67	This study
M28n.2r	158.24	-6.55	-32.30	53.59	This study
M30n	159.50	-6.63	-32.42	53.87	This study
M33n.1n	160.83	-6.70	-32.57	54.23	This study
M38n.2n	164.10	-7.02	-32.97	55.05	This study
Speed-up	177.00	-7.79	-33.86	56.72	This study
FIT	182.00	-7.96	-33.86	56.91	This study
Madagascar with respect to Africa					
Present	0.00	90.00	0.00	0.00	
M0r	126.12	90.00	0.00	0.00	This study
Madagascar with respect to Antarctica					
M0r	126.12	-10.41	-26.03	-41.08	This study
FIT	182.00	-10.41	-26.03	-41.08	This study
Beira High with respect to Africa					
Present	0.00	90.00	0.00	0.00	
	166.30	-7.25	-33.18	-55.49	This study
Beira High with respect to Antarctica					
	166.30	-7.25	-33.18	-55.49	This study
FIT	182.00	-7.25	-33.18	-55.49	This study
Mozambique Ridge with respect to Africa					
Present	0.00	90.00	0.00	0.00	
M1n	126.70	90.00	0.00	0.00	This study
M3n	128.89	-26.28	-0.25	1.31	This study
M5n	131.02	-26.75	-3.19	2.82	This study
M8n	132.68	-26.78	-6.43	3.93	This study
M10Nro	135.32	-26.72	-8.70	5.54	This study
M20r	148.08	90.00	0.00	0.00	This study

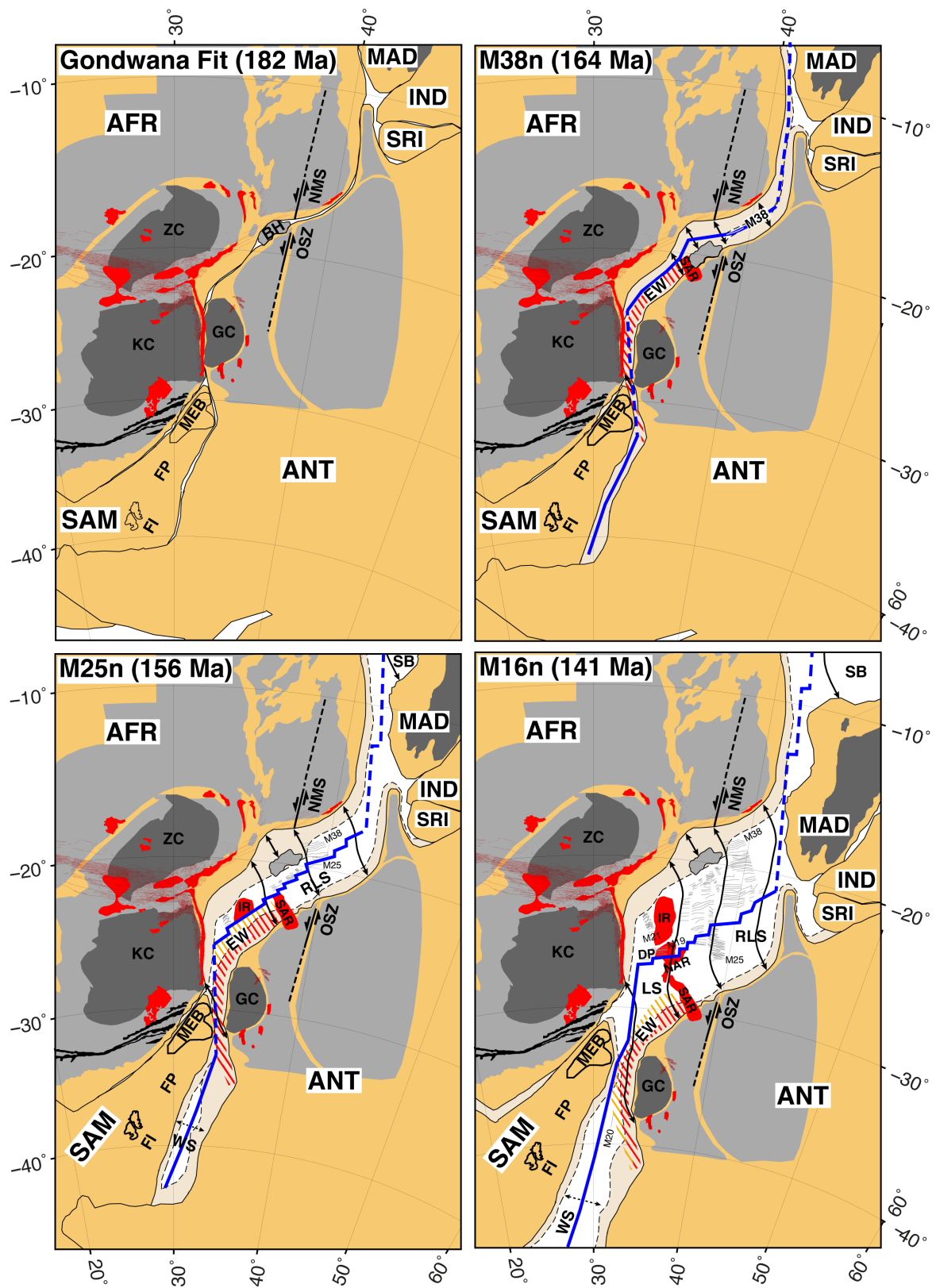


Figure 6.14: Reconstruction of the initial Gondwana break-up in the AAC for 6 times. Continues ...

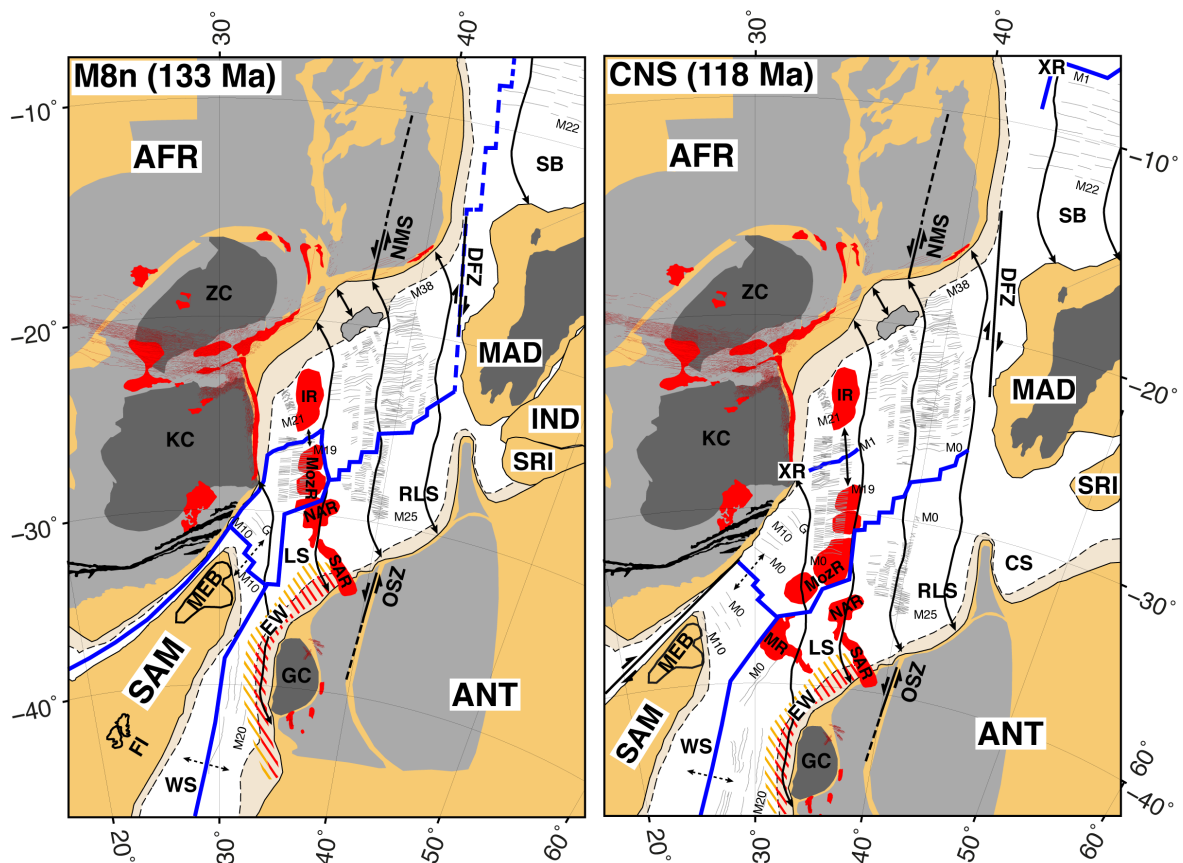


Figure 6.14 (cont.): A solid black line along the continents depicts the pre-rift boundary, whereas the dashed line marks the assumed COB. Dark grey areas are cratons and light grey areas are orogenic belts. Red areas represent flood basalts and volcanic ridges. The blue line depicts the positions of the mid-ocean ridges at the respective time. Thick solid black lines with arrows are synthetic flowlines. Hatched areas mark the location of known SDRs (red: inner SDRs, orange: outer SDRs). Thin grey lines represent magnetic spreading anomalies. In the Mozambique Basin, the magnetic spreading anomalies are based on this study and in the Riiser-Larsen Sea on [Leinweber and Jokat \(2012\)](#). In the Somali Basin these are taken from [Cochran \(1988\)](#). The separation of the South America from Africa is constrained by the magnetic isochrons of [Goodlad et al. \(1982\)](#). Magnetic isochrons used for the opening of the Weddell Sea are based on [Jokat et al. \(2003\)](#) and [König and Jokat \(2006\)](#). Abbreviations: AFR: Africa, ANT: Antarctica, CS: Cosmonaut Sea, DFZ: Davie Fracture Zone, DP: Dana Plateau (MozR), EW: Explora Wedge, FI: Falkland Islands, FP: Falkland Plateau, GC: Grunehogna Craton, IND: India, IR: Inharrime Ridge, KC: Kaapvaal Craton, LS: Lazarev Sea, MAD: Madagascar, MEB: Maurice Ewing Bank, MozR: Mozambique Ridge, MR: Maud Rise, NAR: Northern Astrid Ridge, NMS: Namama Shear Zone, OSZ: Orvin Shear Zone, RLS: Riiser-Larsen Sea, SAM: South America, SAR: Southern Astrid Ridge, SB: Somali Basin, SRI: Sri Lanka, WS: Weddell Sea, XR: Extinct Ridge, ZC: Zimbabwe Craton.

([Kristoffersen et al., 2014](#)). During this period, Beira High is part of the Antarctic plate with a rift axis separating it from the continental interior of Africa (Fig. 6.14, Gondwana Fit).

M38n.2n – M28n.2r (164.1-158.2 Ma): The oldest oceanic crust is identified in the NE-Segment in the Mozambique Basin (Fig. 6.14, M38n) with the interpretation of isochron M38n.2n (164.1 Ma) (Mueller and Jokat, 2017). At this time, another phase of volcanism affects mainly the margin of DML. This results in the effusion of the normal polarized outer SDRs at the Explora Wedge in the Lazerev Sea and intrusion of the continental margin in the RLS, leading to observable differences in the magnetic signatures of these margins and their conjugates. By 159 Ma at the latest, the locus of rifting switches from north of Beira High to south of it, leading to its separation from East Gondwana. Thickened oceanic crust is emplaced at the southern Astrid Ridge.

M28n.2r – M21r (158.2-149.6 Ma): The oldest interpreted magnetic isochron south of Beira High and on the MCP is M28n.2r (Fig. 6.14, M25n). In this period, the divergence of East Gondwana rotates clockwise and changes its spreading direction from SE to SSW. Consequently, the development of the southern Astrid Ridge abates. Furthermore, the rotation results in a complex rift reorganisation in the western Somali Basin, at which a set of NE-trending mid-ocean ridge segments separated by SE-trending transform faults rotate and merge to form the long-offset N-S trending Davie Ridge, leading to localised zones of compression and extension in an overall transform setting.

M21r – M14n (149.6-138.8 Ma): By now, the southern MCP are floored by thick oceanic crust. At M21r, the spreading centre is located at what is at present the southern coast of the MCP. Subsequently, from M19n.2n until M15n (145.7-139.7 Ma), the Dana Plateau of the MozR emerges by seafloor spreading at a mid-ocean ridge affected by excess melt production (Fig. 6.14, M16n). At the same time, the northern Astrid Ridge starts to develop along the Astrid Fracture Zone.

M14n – M12r.1r (138.8-137.4 Ma): Fracture zones in the Riiser-Larsen Sea clearly depict the onset of a slight anticlockwise rotation of East Gondwana at this time. Fracture zones in the Mozambique Basin reveal the same change in less distinct gravity anomalies, but it is questionable if a similar change is evident in the fracture zones of the Somali Basin (Fig. 6.13) (Phethean et al., 2016). From M14n (138.8 Ma) on, the emplacement of the Galathea Plateau of the MozR begins.

M12r.1r – M1n (137.4-127.3 Ma): At about M12 to M10, the South American plate starts to separate from the African plate. A continental sliver is likely to have separated from Maurice Ewing Bank in the process, leading to the formation of the

South Tugela Ridge off the South African coast. Combined with increased magmatism, this separation might have triggered the onset of spreading at an additional NE-SW oriented ridge in the NNV between the Inharrime Ridge and the Dana Plateau. During this period, the MozR moves as part of a small plate within the large-scale plate boundary between East Antarctica and Africa. Based on the opening of the NNV, the MozR moves southwards like the magmatic source and results in a longer lasting magmatism affecting the MozR that is responsible for its topographic expression. Simultaneously, ongoing spreading at the small plate's southern boundary leads to formation of parts of the Vauban (Fig. 6.14, M8n) and Robert-Giraud plateaus. The increased magmatism at this time also affects the adjacent segment of the Mozambique Basin, leading to emplacement of the northern reaches of the MozR there.

M1n – CNS (127.3-115 Ma): By now, the ridge in the NNV has ceased and excess magmatism in the Mozambique Basin has abated (Fig. 6.14, CNS). Around the same time, southwards motion of Madagascar ended with the extinction of the mid-ocean ridge in the Somali Basin (Davis et al., 2016). This can be seen as consistent with the absence of M-series magnetic isochrons in the western Enderby Basin (Jokat et al., 2010), to the region north of which our rotations reconstruct Madagascar.

CNS (115 Ma): The initial development of the MozR ends with the emplacement of the Rennel Plateau at about 115 Ma. However, cored ash-rich silt- and clay-stones of Valanginian to Cenomanian age (~139-100 Ma) (Simpson et al., 1974) depict an ongoing history of magmatism in this area. Subsequent plate motions accompany the formation and rifting apart of a large igneous province at Maud Rise-Agulhas Plateau (Fig. 6.14, CNS) and the emplacement of Transkei Rise between them and the MozR.

6.7 Conclusion

This study is based on the interpretation of newly acquired magnetic data off the central and northern coasts of Mozambique. These data are integrated into a new compilation of all available magnetic profiles in the Mozambique Basin. Their investigation allows the set-up of a self-consistent reconstruction scheme that aims to explain the history of continental break-up and seafloor spreading that led to the simultaneous formation of the AAC and Somali Basin. The main conclusions are:

[1] By means of the identified pre-rift boundaries, a tight initial fit between East and West Gondwana is proposed, wherein the Beira High is located in the western RLS and

no space is available to restore the MozR (Fig. 6.14, Gondwana Fit). Prior to rifting, several pairs of geological structures can be identified as conjugates that were originally continuous features in Gondwana (Fig. 6.12). These include a major sinistral shear zone in the EAAO that comprises the Namama Shear Zone in Mozambique and the Orvin Shear Zone in DML. Initial rifting of East Gondwana starts in a SE orientation at about 182 Ma.

[2] Jurassic magnetic spreading anomalies can be continuously interpreted in the Northern Mozambique Basin (Fig. 6.8). The first oceanic crust is emplaced in the eastern part of the AAC at M38n.2n (164.1 Ma). At about 155 Ma, East Gondwana rotates clockwise and the direction of its separation from West Gondwana changes from SE to SSW.

[3] The Beira High represents a continental fragment that stayed fixed to the Antarctic plate during the first instance of rifting. It was detached from the Antarctic plate and won for the African plate by a rift jump to its southern side by 159 Ma at the latest. Well-expressed fracture zones throughout the AAC reveal its palaeo-position at the Antarctic margin where the Riiser-Larsen Sea gives way to the Lazarev Sea. A deep basin filled by volcanic rocks occupies the Antarctic location that was vacated by the Beira High.

[4] Tentatively identified magnetic spreading anomalies at the southern part of the MCP, the NNV and the MozR point to an oceanic origin of these structures. The thickened oceanic crust in the southern part of the MCP seems to be emplaced from M28n.2r-M21r (158.2-149.6 Ma). The subsequent magnetic spreading anomalies are continuously observed at the MozR, which formed between M19n.2n-CNS (145.7-115 Ma).

[5] There is evidence for a NE-SW oriented extinct ridge in the NNV, separating the Dana Plateau of the MozR from its conjugate, the Inharrime Ridge at the MCP. The formation of the ridge was a response to the independent rotation of a small plate that started at the latest by M10Nr (135.2 Ma), and might have been triggered by the simultaneous onset of drifting of the South American plate.

[6] A break-up model for eastern Africa (Fig. 6.14) is introduced constrained by the most extensive magnetic data set. It consistently describes the opening of the AAC and the Somali Basin using a single set of rotations.

Acknowledgements

We thank captain Detlef Korte and his crew of R/V Sonne for their support and assistance during the cruises SO230 and SO231. We acknowledge Ingo Heyde for supporting the gravity and magnetic data acquisition. Furthermore thanks go to Schlumberger Multiclient for providing insights into some regional MCS and magnetic data at the Mozambican margin. Additionally we thank INP for the provision of magnetic data onshore Mozambique. Furthermore thanks go to Graeme Eagles for improving the grammar. This project is funded through a grant by the German Federal Ministry of Education and Research (BMBF, 03G0230A) and by AWI internal funding.

7 Conclusion

This thesis provides new insights into the crustal structure along the continental margin of Central Mozambique by means of seismic and potential field data. The findings are incorporated in a new reconstruction of the initial Gondwana break-up in the Africa-Antarctica Corridor, which contributes to our understanding of the tectonic evolution of the conjugate margins of Mozambique and Dronning Maud Land. Subsequently, the main results are summarized and related to the research questions addressed in section [1.4](#).

Crustal structure along the continental margin of Central Mozambique

The study of the new seismic refraction data revealed normal oceanic crust of 5.5-7 km thickness south of Beira High in the Mozambique Basin. High upper crustal (layer 2) velocities of ≥ 5.6 km/s as well as lower crustal (layer 3) velocities of 6.5-7.0 km/s with the absence of a HVLCB are in agreement with the distinct oceanic crust in the NE-part of the margin ([Leinweber et al., 2013](#)). A steep flank marks the sharp transition from the oceanic crust towards an up to 23 km thick crust at Beira High. Here, a constant small increase in velocity and a velocity contrast of 7.0 to 8.0 km/s at the Moho is observed. A comparison with the velocity structure of continental fragments reveals striking similarities and clear differences to oceanic plateaus. Comparably low densities in the lower crust, indicating the presence of felsic material, as well as sill-like intrusions observed in the seismic reflection data and expressed in the magnetic data, reveal Beira High to represent a major tectonic feature that consists of stretched, but partly highly intruded continental crust. A wider transition is observed at the north-western flank of Beira High towards about 7 km thin crust in the Zambezi Delta Depression. Here, the velocity structure depicts similar velocities to the shelf area in the NE-part of the margin and is as well underlain by a pronounced HVLCB. The re-evaluation of the seismic refraction data at the NE-part of the margin shows a uniform 190-220 km wide extent of the up to 7 km thick HVLCB with maximal basal velocities of about 7.4 km/s along the margin of Central Mozambique. However, in the SW-part of the margin, the COT seems to extend below the present coast of Mozambique and does not

verify the presence of a narrow transition as observed in the NE-part. This identified crustal diversity at the continental margin of Central Mozambique is in agreement with observed distinct basement blocks at the conjugate margin in the Riiser-Larsen Sea ([Leitchenkov et al., 2008](#)) and points towards an asymmetric break-up.

Distribution and age of the break-up related magmatism along the continental margin of Central Mozambique

At the NE-part of the continental margin of Central Mozambique, magnetic modelling supports the findings of weak SDRs identified in seismic reflection data, which contribute to the prominent coast-parallel negative magnetic anomaly. These are less voluminous as known SDRs from the Explora Wedge in Antarctica that might indicate its greater offset to the magmatic source. Seawards of the SDRs at the Mozambican margin, the onset of oceanic crust is dated to M38n.2n (164.1 Ma) and implies the prior emplacement of SDRs in the period of 168.5-166.8 Ma, when the Earth's magnetic field was mainly reverse polarized. At the East Antarctic margin, [Kristoffersen et al. \(2014\)](#) noticed the difference between the mostly reverse polarized inner SDRs of the Explora Wedge in the Lazarev and Weddell Sea, and their additional distinct normal polarized outer SDRs. A likely origin of the outer SDRs is a late stage of rift volcanism that mainly affected the margin of Antarctica. This caused the emplacement of the normal polarized outer SDRs as well as the intrusions in the Riiser-Larsen Sea, observed in the seismic reflection data. The intrusions pinch through the basement in the lowermost sediment layer and might cause an overprint of weak expressed SDRs and consequently the different magnetic signature of the conjugate margins.

Onshore Mozambique, there are several evidences for additional volcanics. Their distribution reveals a clear extension of the north-eastern branch of the Karoo LIP along the entire Central Mozambique continental margin. Only a single sample provides an indication for the onset of magmatism at 177 Ma along the margin of Central Mozambique, whereas several ones imply a main magmatic phase between 169-157 Ma. An earlier onset of magmatism at 184-180 Ma in SE-Africa and Zimbabwe ([Jourdan et al., 2008](#)) implies an initial position of the magmatic source west of the margin of Central Mozambique. By means of our new findings and putting it into context with the findings of previous studies, magmatism seemed to be continuous in SE-Africa during the initial break-up, which raises the possibility of either a mantle plume or a thermal anomaly as source for the emplacement of the Karoo LIP and trigger for the break-up.

Initial Gondwana break-up in the Africa-Antarctica Corridor

The new magnetic data compilation for the Mozambique Basin shows pronounced magnetic spreading anomalies in the NE-part of the basin, which confirms the presence of oceanic crust bordering close to the margin. Magnetic chron M38n.2n (164.1 Ma) marks the onset of oceanic crust in the NE-part of the basin, whereas south of Beira High the oldest chron is dated to M28n.2r (158.2 Ma). Several fractures, describing the continent's motion, can be observed in the AAC and were traced throughout most parts, especially closest to the ice shelf in the Riiser-Larsen Sea. The assigned pre-rift boundaries along the margins reveal a tight Gondwana fit in the reconstruction, where no large-scale fragments can be restored, except Beira High. Additionally, the initial fit depicts several magnetic lineations that can be linked between the African and Antarctic plate. Worth mentioning is a possible continuation of the Okavango dyke swarm towards the same-aged dykes at Straumsvola/Tvora as well as a potential continuation of the Lurio Belt across Gunnerus Ridge. Remarkable is the alignment of the sinistral Namama Shear Zone on the African plate with the sinistral Orvin Shear Zone and its possible southwards extension along the Forster Magnetic Anomaly in Antarctica. Together, these might mark a major tectonic boundary of the East African-Antarctic Orogen. Furthermore, it is likely that this zone of weakness triggered the separation of Beira High at this position. During the initial break-up, first Beira High moved southwards with East Gondwana, but by constant stretching it got detached from the Antarctic plate latest at 159 Ma. Nowadays, a deep basin filled by volcanics is observed at Beira High's palaeo-position at the Antarctic margin.

The break-up in the adjacent segment of Mozambique Ridge cannot be only explained by the same rotations as in the Mozambique Basin, which would lead to contradictions with either the geophysical, geological or geodynamic constraints. However, magnetic data onshore the southern MCP reveal a similarity with the magnetic spreading anomalies south of Beira High and imply the emplacement of the southern MCP between M28n.2r to M21r (158.2-149.6 Ma). The continuous spreading anomalies are tentatively identified at the Mozambique Ridge, which seems to be emplaced between M19n.2n to CNS (145.7-115 Ma). The identified magnetic chron M13r (138.5 Ma) close to the DSDP site 249 at the Galathea Plateau is in great agreement with the basement overlying sediments of Valanginian to Hauterivian age (139.4-130.8 Ma) at DSDP site 249 (Simpson et al., 1974). By following the idea of Tikku et al. (2002), an extinct ridge was active in the Northern Natal Valley (NNV) and might have caused the separation of Mozambique Ridge from the Inharrime Ridge at the MCP. In the new magnetic compilation a ridge-like structure is observed in the middle of the NNV and its extinction

7. CONCLUSION

can be dated to M1n. However, the identification towards older magnetic spreading anomalies gets more complicated, due to the presence of young volcanism. The ridge's activity can only tentatively suggested between latest M10Nr to M1n (135.2-127.3Ma). At this time the Mozambique Ridge moved as part of a micro plate. This model represents a possible solution for the emplacement of the Mozambique Ridge by accounting for the present-day available constraints.

Furthermore, the same rotations as applied for the opening of the AAC can be used for the rotation of Madagascar from its palaeo-position to its present one. However, the trend of calculated hypothetical flowlines show slight differences to postulated fractures zones in the Somali Basin ([Phethean et al., 2016](#)).

8 Outlook

This thesis addressed several research questions concerning the tectonic setting of the Gondwanian margins and the break-up itself. However, such a complex process cannot be sufficiently explained in a single simplified model. Consequently, the findings of this study might guide us to specify some general questions and point out new regional ones.

Geological links and the pre-rift position of Sri Lanka

The identified initial fit between the African and Antarctic plate bears the potential for further identifications of links between the onshore geology of both continents and might allow a more reliable assignment of tectonic structures in Dronning Maud Land. In this context, a compilation of the by now available high-resolution magnetic data onshore Mozambique and its integration to the offshore compilation of this study would result in an enhanced identification of major boundaries across the continents and the observation of further small-scale connections. These might serve as a-priori information for upcoming geological and geophysical studies onshore Antarctica and ease the interpretation of this data.

In the light of an upcoming AWI cruise to the continental margin of Sri Lanka during summer this year and its geophysical investigation, a special focus should be set on the surprising continuation of the magnetic signature of the Lurio Belt across Gunnerus Ridge. Likely is a pre-rift position of Sri Lanka directly east of Gunnerus Ridge in the present-day Enderby Basin. However, the absence of magnetic spreading anomalies in the Enderby Basin ([Jokat et al., 2010](#)) indicate the onset of drifting of Sri Lanka during the CNS and identified Mesozoic chrons at the southern margin of Sri Lanka ([Desa et al., 2006](#)) are still in question. Consequently, main constraints for the palaeo-position of Sri Lanka in the assemblage of Gondwana might be only obtained by tracing major tectonic boundaries across Sri Lanka and its surrounding plates. A likely link to the African plate might be a continuation of the connection of Lurio Belt across Gunnerus Ridge towards a thrust front onshore Sri Lanka, as supposed by [Grantham et al. \(2003\)](#), or to observed structures slightly north of the Lurio Belt. To allow a

verification of this hypothesis, additional systematically acquired magnetic data are required at least across the southern Gunnerus Ridge and could be extended towards the eastern margin of the Riiser-Larsen Sea. On the one hand this would supplement the previous surveys in the Enderby Basin (Jokat et al., 2010) and across Sør Rondane in eastern Dronning Maud Land (Mieth et al., 2014). On the other hand, the following four main research questions could be addressed by this single survey:

1. Is Gunnerus Ridge entirely of continental origin or can magnetic spreading anomalies be observed? By now, only sonobuoy data (Saki et al., 1987) and gravity modelling (Leitchenkov et al., 2008) constrain the proposed entire continental origin.
2. Does the Lurio Belt continue across Gunnerus Ridge towards the margin in the Cosmonaut Sea or onshore Sri Lanka?
3. Are there Late to Middle Jurassic magnetic spreading anomalies in the eastern Riiser-Larsen Sea, as observed at the conjugate Mozambican margin? Does the new data still support the presence of late stage magmatism that overprints the magnetic signature of weak expressed SDRs?
4. Is there an eastward continuation of the south-eastern Dronning Maud Land Province (Mieth, 2014)?

Crustal origin of the MCP and the Mozambique Ridge

In the scope of this thesis, magnetic spreading anomalies could only be tentatively identified at the southern MCP, NNV and Mozambique Ridge and still do not allow a distinct classification of the origin. In the nearest future, there will be results from a French research cruise available, which investigated the southern MCP and NNV by seismic refraction, seismic reflection and potential field data. It will be interesting to see how their new findings can be related to the here outlined problems in the MCP-Segment. However, based on the results of this thesis, it might be that the French survey did not cover the COT and for sure not the pre-rift boundary in this segment. Consequently, there might be still uncertainty in the formation of the MCP, which can only be identified by a seismic refraction profile running onshore from the northern part of the MCP towards the offshore area south of Beira High.

Furthermore, it is still questionable if there are small continental fragments at the Mozambique Ridge (e.g. at the Vauban Plateau), covered by the intense volcanism. Such a finding would have major influences on the reconstruction of the margins at the MCP and the Lazarev Sea in Antarctica. Evidence might provide another seismic refraction study with one profile running north-south across the Dana-Plateau down

to the small Rennel Plateau and at least two E-W running transects, one across the Vauban Plateau and a second across the DSDP site 249 in the northern part of the Galathea Plateau.

Magmatism along the margin of DML and the driving forces of the break-up

This thesis provides a consistent break-up model of the AAC as well as insights into the distribution and duration of the break-up related volcanism of the Karoo LIP. However, a detailed investigation of the driving forces and the magnetic source were beyond the scope of this thesis. A possible subsequent study might focus on the investigation of the origin of the HVLCB and the mantle-lithosphere interactions as outlined by [Leinweber et al. \(2013\)](#). In combination with geochemical investigations it might be possible to address the kind of the magmatic source and its origin. Furthermore, additional magnetic modelling along the margin of Dronning Maud Land (e.g. along the few seismic refraction profiles) might allow an enhanced characterization of the Explora Wedge and could provide evidence for the presence of a late stage of rift volcanism.

References

- Arkani-Hamed, J. (1988), Differential reduction-to-the-pole of regional magnetic anomalies, *Geophysics*, *53*(12), 1592–1600, doi:[10.1190/1.1442441](https://doi.org/10.1190/1.1442441).
- Arkani-Hamed, J. (1993), The bulk magnetization contrast across the ocean-continent boundary in the east coast of North America, *Geophysical Journal International*, *115*(1), 152–158, doi:[10.1111/j.1365-246X.1993.tb05595.x](https://doi.org/10.1111/j.1365-246X.1993.tb05595.x).
- Artemieva, I. M. (2006), Global 1x1 thermal model TC1 for the continental lithosphere: Implications for lithosphere secular evolution, *Tectonophysics*, *416*(1-4), 245–277, doi:[10.1016/j.tecto.2005.11.022](https://doi.org/10.1016/j.tecto.2005.11.022).
- Aubourg, C., G. Tshoso, B. Le Gall, H. Bertrand, J.-J. Tiercelin, A. Kampunzu, J. Dymant, and M. Modisi (2008), Magma flow revealed by magnetic fabric in the Okavango giant dyke swarm, Karoo igneous province, northern Botswana, *Journal of Volcanology and Geothermal Research*, *170*(3-4), 247–261, doi:[10.1016/j.jvolgeores.2007.10.013](https://doi.org/10.1016/j.jvolgeores.2007.10.013).
- Barritt, S. D. (1993), The African Magnetic Mapping Project, *ITC Journal*, (2), 122–131.
- Barton, P. J. (1986), The relationship between seismic velocity and density in the continental crust - a useful constraint?, *Geophysical Journal of the Royal Astronomical Society*, *87*(1), 195–208, doi:[10.1111/j.1365-246X.1986.tb04553.x](https://doi.org/10.1111/j.1365-246X.1986.tb04553.x).
- Ben-Avraham, Z., C. J. Hartnady, and A. P. Roex (1995), Neotectonic activity on continental fragments Agulhas Plateau and Mozambique Ridge, *Journal of Geophysical Research*, *100*(B4), 6199–6211, doi:[10.1029/94JB02881](https://doi.org/10.1029/94JB02881).
- Bergh, H. W. (1971), Sea-floor spreading in the southwest Indian Ocean, *Journal of Geophysical Research*, *76*(26), 6276–6282, doi:[10.1029/JB076i026p06276](https://doi.org/10.1029/JB076i026p06276).
- Bergh, H. W., and I. O. Norton (1976), Prince Edward Fracture Zone and the evolution of the Mozambique Basin, *Journal of Geophysical Research*, *81*(29), 5221–5239, doi:[10.1029/JB081i029p05221](https://doi.org/10.1029/JB081i029p05221).

- Bhattacharya, M., and G. Duval (2016), A snapshot of the geotectonics and petroleum geology of the Durban and Zululand Basins, offshore South Africa, *First Break*, *34*(12), 45–51.
- Bohlen, T. (1998), Viskoelastische FD-Modellierung seismischer Wellen zur Interpretation gemessener Seismogramme, Ph.D. thesis, Christian-Albrechts-Universität zu Kiel.
- Bohlen, T. (2002), Parallel 3-D viscoelastic finite difference seismic modelling, *Computers and Geosciences*, *28*(8), 887–899, doi:[10.1016/S0098-3004\(02\)00006-7](https://doi.org/10.1016/S0098-3004(02)00006-7).
- Bohlen, T., D. De Nil, S. Dunkl, L. Groos, S. Heider, O. Hellwig, S. Jetschny, D. Koehn, A. Kurzmann, M. Tilman, and M. Schaefer (2015a), SOFI2D - seismic modeling with finite differences 2D, v2015_05_15. Karlsruhe Institute of Technology, Karlsruhe.
- Bohlen, T., D. De Nil, K. Daniel, and S. Jetschny (2015b), SOFI2D, seismic modeling with finite differences 2D - elastic and viscoelastic version, User's Guide, *Tech. rep.*, Karlsruhe Institute for Technology, Karlsruhe.
- Boyden, J. A., R. D. Müller, M. Gurnis, T. H. Torsvik, J. A. Clark, M. Turner, H. Ivey-Law, R. J. Watson, and J. J. Cannon (2011), Next-generation plate-tectonic reconstructions using GPlates, in *Geoinformatics : Cyberinfrastructure for the Solid Earth Sciences*, edited by G. R. Keller and C. Baru, pp. 95–114, Cambridge University Press, Cambridge.
- Brocher, T. M. (2005), Compressional and Shear Wave Velocity Versus Depth in the San Francisco Bay Area , California : Rules for USGS Bay Area Velocity Model 05.0.0, *Tech. rep.*, U.S. Geological Survey, Menlo Park, California, USA.
- Brocher, T. M. (2008), Compressional and shear-wave velocity versus depth relations for common rock types in northern California, *Bulletin of the Seismological Society of America*, *98*(2), 950–968, doi:[10.1785/0120060403](https://doi.org/10.1785/0120060403).
- Brune, S., S. E. Williams, N. P. Butterworth, and R. D. Müller (2016), Abrupt plate accelerations shape rifted continental margins, *Nature*, *536*(7615), 201–204, doi:[10.1038/nature18319](https://doi.org/10.1038/nature18319).
- Burke, K., and J. F. Dewey (1973), Plume-Generated Triple Junctions: Key Indicators in Applying Plate Tectonics to Old Rocks, *The Journal of Geology*, *81*(4), 406–433, doi:[10.1086/627882](https://doi.org/10.1086/627882).

- Carlson, R. L., and G. S. Raskin (1984), Density of the ocean crust, *Nature*, *311*(5986), 555–558, doi:[10.1038/311555a0](https://doi.org/10.1038/311555a0).
- Carlson, R. L., N. I. Christensen, and R. P. Moore (1980), Anomalous crustal structures in ocean basins: Continental fragments and oceanic plateaus, *Earth and Planetary Science Letters*, *51*(1), 171–180, doi:[10.1016/0012-821X\(80\)90264-2](https://doi.org/10.1016/0012-821X(80)90264-2).
- Castelino, J. A., C. Reichert, F. Klingelhoefer, D. Aslanian, and W. Jokat (2015), Mesozoic and Early Cenozoic sediment influx and morphology of the Mozambique Basin, *Marine and Petroleum Geology*, *66*(4), 890–905, doi:[10.1016/j.marpetgeo.2015.07.028](https://doi.org/10.1016/j.marpetgeo.2015.07.028).
- Charvis, P., and S. Operto (1999), Structure of the Cretaceous Kerguelen Volcanic Province (southern Indian Ocean) from wide-angle seismic data, *Journal of Geodynamics*, *28*(1), 51–71, doi:[10.1016/S0264-3707\(98\)00029-5](https://doi.org/10.1016/S0264-3707(98)00029-5).
- Chian, D., I. D. Reid, and H. R. Jackson (2001), Crustal structure beneath Orphan Basin and implications for nonvolcanic continental rifting, *Journal of Geophysical Research*, *106*(B6), 10,923–10,940, doi:[10.1029/2000JB900422](https://doi.org/10.1029/2000JB900422).
- Christensen, N. I., and W. D. Mooney (1995), Seismic velocity structure and composition of the continental crust: A global view, *Journal of Geophysical Research*, *100*(B6), 9761–9788, doi:[10.1029/95JB00259](https://doi.org/10.1029/95JB00259).
- Cochran, J. R. (1988), Somali Basin, Chain Ridge, and origin of the Northern Somali Basin gravity and geoid low, *Journal of Geophysical Research*, *93*(B10), 11,985–12,008, doi:[10.1029/JB093iB10p11985](https://doi.org/10.1029/JB093iB10p11985).
- Cox, K. G. (1992), Karoo igneous activity, and the early stages of the break-up of Gondwanaland, *Geological Society, London, Special Publications*, *68*(1), 137–148, doi:[10.1144/GSL.SP.1992.068.01.09](https://doi.org/10.1144/GSL.SP.1992.068.01.09).
- Da Silva Schmitt, R., R. A. J. Trouw, W. R. Van Schmus, and M. M. Pimentel (2004), Late amalgamation in the central part of West Gondwana: New geochronological data and the characterization of a Cambrian collisional orogeny in the Ribeira Belt (SE Brazil), *Precambrian Research*, *133*(1-2), 29–61, doi:[10.1016/j.precamres.2004.03.010](https://doi.org/10.1016/j.precamres.2004.03.010).
- Daszinnies, M. C., J. Jacobs, J.-A. Wartho, and G. H. Grantham (2009), Post Pan-African thermo-tectonic evolution of the north Mozambican basement and its implication for the Gondwana rifting. Inferences from $^{40}\text{Ar}/^{39}\text{Ar}$ hornblende, biotite and

- titanite fission-track dating, *Geological Society, London, Special Publications*, 324(1), 261–286, doi:[10.1144/SP324.18](https://doi.org/10.1144/SP324.18).
- Davies, T. A., B. P. Luyendyk, K. S. Rodolfo, D. Kempe, B. C. McKelvey, R. D. Leidy, G. J. Horvath, R. D. Hyndman, H. R. Thierstein, R. C. Herb, E. Boltovskoy, and P. Doyle (1974), Site 250, in *Initial Reports of the Deep Sea Drilling Project*, 26, edited by T. A. Davies and B. P. Luyendyk, pp. 21–73, U.S. Government Printing Office, doi:[10.2973/dsdp.proc.26.103.1974](https://doi.org/10.2973/dsdp.proc.26.103.1974).
- Davis, J. K., L. A. Lawver, I. O. Norton, and L. M. Gahagan (2016), New Somali Basin Magnetic Anomalies and a Plate Model for the Early Indian Ocean, *Gondwana Research*, 34, 16–28, doi:[10.1016/j.gr.2016.02.010](https://doi.org/10.1016/j.gr.2016.02.010).
- De Buyl, M., and G. Flores (1986), The Southern Mozambique Basin: The Most Promising Hydrocarbon Province Offshore East Africa, in *Future Petroleum Provinces of the World*, edited by M. T. Halbouty, pp. 399–425, AAPG Memoir, 40.
- Delius, H., T. S. Brewer, and P. K. Harvey (2003), Evidence for textural and alteration changes in basaltic lava flows using variations in rock magnetic properties (ODP Leg 183), *Tectonophysics*, 371(1-4), 111–140, doi:[10.1016/S0040-1951\(03\)00202-6](https://doi.org/10.1016/S0040-1951(03)00202-6).
- Delvaux, D. (2001), Tectonic and palaeostress evolution of the Tanganyika-Rukwa-Malawi rift segment, East African Rift System, in *Peri-Tethys Memoir 6: Peri-Tethyan Rift/Wrench Basins and Passive Margins*, edited by P. A. Ziegler, W. Cavazza, A. H. F. Robertson, and S. Crasquin-Solea, memoires d' ed., chap. 17, pp. 545–567, Museum National D'histoire, Paris.
- Desa, M., M. V. Ramana, and T. Ramprasad (2006), Seafloor spreading magnetic anomalies south off Sri Lanka, *Marine Geology*, 229(3-4), 227–240, doi:[10.1016/j.margeo.2006.03.006](https://doi.org/10.1016/j.margeo.2006.03.006).
- Direen, N., and a.J. Crawford (2003), Fossil seaward-dipping reflector sequences preserved in southeastern Australia: a 600 Ma volcanic passive margin in eastern Gondwanaland, *Journal of the Geological Society, London*, 160(6), 985–990, doi:[10.1144/0016-764903-010](https://doi.org/10.1144/0016-764903-010).
- Domingues, A., G. Silveira, A. M. Ferreira, S.-J. Chang, S. Custódio, and J. F. Fonseca (2016), Ambient noise tomography of the East African Rift in Mozambique, *Geophysical Journal International*, 204(3), 1565–1578, doi:[10.1093/gji/ggv538](https://doi.org/10.1093/gji/ggv538).
- Du Toit, S. R., A. G. Kidston, and O. L. Slind (1997), *The hydrocarbon potential of the East Africa continental margin*, 1–132 pp., Alconsult International Ltd., Calgary.

- Duncan, R. A., P. R. Hooper, J. Rehacek, J. S. Marsh, and A. R. Duncan (1997), The timing and duration of the Karoo igneous event, southern Gondwana, *Journal of Geophysical Research*, *102*(B8), 18,127–18,138, doi:[10.1029/97JB00972](https://doi.org/10.1029/97JB00972).
- Eagles, G., and M. König (2008), A model of plate kinematics in Gondwana breakup, *Geophysical Journal International*, *173*(2), 703–717, doi:[10.1111/j.1365-246X.2008.03753.x](https://doi.org/10.1111/j.1365-246X.2008.03753.x).
- Eagles, G., L. Pérez-Díaz, and N. Scarselli (2015), Getting over continent ocean boundaries, *Earth-Science Reviews*, *151*, 244–265, doi:[10.1016/j.earscirev.2015.10.009](https://doi.org/10.1016/j.earscirev.2015.10.009).
- Eales, H. V., J. S. Marsh, and K. G. Cox (1984), The Karoo Igneous Province: An Introduction, in *Petrogenesis of the Volcanic Rocks of the Karoo Province*, edited by A. J. Erlank, pp. 1–26, Geological Society of South Africa Special Publication 13.
- Encarnación, J., T. H. Fleming, D. H. Elliot, and H. V. Eales (1996), Synchronous emplacement of Ferrar and Karoo dolerites and the early breakup of Gondwana, *Geology*, *24*(6), 535–538, doi:[10.1130/0091-7613\(1996\)024<0535:SEOFAK>2.3.CO;2](https://doi.org/10.1130/0091-7613(1996)024<0535:SEOFAK>2.3.CO;2).
- Fairhead, J. D., A. B. Watts, P. Chevalier, B. El-Haddadeh, C. M. Green, G. W. Stuart, K. A. Whaler, and I. Whindle (1988), African Gravity Project. Technical Report, *Tech. rep.*, University of Leeds Industrial Services Ltd., Leeds, United Kingdom.
- Fedi, M., and G. Florio (2001), Detection of potential fields source boundaries by enhanced horizontal derivative method, *Geophysical Prospecting*, *49*(1), 40–58, doi:[10.1046/j.1365-2478.2001.00235.x](https://doi.org/10.1046/j.1365-2478.2001.00235.x).
- Ferraccioli, F., P. C. Jones, M. L. Curtis, P. T. Leat, and T. R. Riley (2005), Tectonic and magmatic patterns in the Jutulstraumen rift (?) region, East Antarctica, as imaged by high-resolution aeromagnetic data, *Earth, Planets and Space*, *57*(8), 767–780, doi:[10.1186/BF03351856](https://doi.org/10.1186/BF03351856).
- Ferré, E. C., S. A. Friedman, F. Martín-Hernández, J. M. Feinberg, J. L. Till, D. A. Ionov, and J. A. Conder (2014), Eight good reasons why the uppermost mantle could be magnetic, *Tectonophysics*, *624-625*, 3–14, doi:[10.1016/j.tecto.2014.01.004](https://doi.org/10.1016/j.tecto.2014.01.004).
- Fischer, M. D., G. Uenzelmann-Neben, G. Jacques, and R. Werner (2016), The Mozambique Ridge: a document of massive multi-stage magmatism, *Geophysical Journal International*, doi:[10.1093/gji/ggw403](https://doi.org/10.1093/gji/ggw403).
- Flores, G. (1964), On the age of the Lupata rocks, lower Zambezi River, Mozambique, *Transactions of the Geological Society of South Africa*, *67*, 111–118.

- Flores, G. (1973), The Cretaceous and Tertiary Sedimentary Basins of Mozambique and Zululand, in *Sedimentary Basins of South and Eastern Africa Coasts, Part 2*, edited by G. T. Blant, pp. 81–111, Association of African Geological Survey, Paris.
- Fonseca, J. F. B. D., J. Chamussa, A. L. Domingues, G. Helffrich, E. Antunes, G. van Aswegen, L. V. Pinto, S. Custódio, and V. J. Manhica (2014), MOZART: A Seismological Investigation of the East African Rift in Central Mozambique, *Seismological Research Letters*, *85*(1), 108–116, doi:[10.1785/0220130082](https://doi.org/10.1785/0220130082).
- Franke, D. (2013), Rifting, lithosphere breakup and volcanism: Comparison of magma-poor and volcanic rifted margins, *Marine and Petroleum Geology*, *43*, 63–87, doi:[10.1016/j.marpetgeo.2012.11.003](https://doi.org/10.1016/j.marpetgeo.2012.11.003).
- Franke, D. (2014), The passive and rifted continental margin off Mozambique: Early dispersal of Gondwana and the recent influence of the East African rift system) (PAGE-Four), *Cruise report*.
- Frizon De Lamotte, D., B. Fourdan, S. Leleu, F. Leparmentier, and P. De Clarens (2015), Style of rifting and the stages of Pangea breakup, *Tectonics*, *34*(5), 1009–1029, doi:[10.1002/2014TC003760](https://doi.org/10.1002/2014TC003760).
- Fromm, T. (2016), PRay – A graphical user interface for interactive visualization and modification of rayinvr models, *Journal of Applied Geophysics*, *124*, 1–3, doi:[10.1016/j.jappgeo.2015.11.004](https://doi.org/10.1016/j.jappgeo.2015.11.004).
- Funck, T., M. S. Andersen, J. K. Neish, and T. Dahl-Jensen (2008), A refraction seismic transect from the Faroe Islands to the Hatton-Rockall Basin, *Journal of Geophysical Research: Solid Earth*, *113*(B12), 405–429, doi:[10.1029/2008JB005675](https://doi.org/10.1029/2008JB005675).
- Gardner, G. H. F. (1974), Formation velocity and density - the diagnostic basics for stratigraphic traps, *Geophysics*, *39*(6), 770–780, doi:[10.1190/1.1440465](https://doi.org/10.1190/1.1440465).
- Gee, J. S., and D. V. Kent (2007), Source of Oceanic Magnetic Anomalies and the Geomagnetic Polarity Timescale, *Treatise on Geophysics*, *5*, 455–507, doi:[10.1016/B978-044452748-6.00097-3](https://doi.org/10.1016/B978-044452748-6.00097-3).
- Gerlings, J., K. E. Loudon, and H. R. Jackson (2011), Crustal structure of the Flemish Cap Continental Margin (eastern Canada): An analysis of a seismic refraction profile, *Geophysical Journal International*, *185*(1), 30–48, doi:[10.1111/j.1365-246X.2011.04931.x](https://doi.org/10.1111/j.1365-246X.2011.04931.x).

- Ghidella, M. E., L. M. Gahagan, and L. A. Lawver (2007), Break-up of Gondwana and opening of the South Atlantic; review of existing plate tectonic models, in *Antarctica: A Keystone in a Changing World - Online Proceedings for the 10th International Symposium on Antarctic Earth Sciences*, vol. 1047, edited by C. Raymond, pp. 1–5, U.S. Geological Survey, Santa Barbara, doi:[10.3133/of2007-1047.srp055](https://doi.org/10.3133/of2007-1047.srp055).
- Godfrey, N. J., B. C. Beaudoin, and S. L. Klemperer (1997), Ophiolitic basement to the Great Valley forearc basin, California, from seismic and gravity data: Implications for crustal growth at the North American continental margin, *Geological Society of America Bulletin*, 109(12), 1536–1562, doi:[10.1130/0016-7606\(1997\)109<1536:OBTTGV>2.3.CO;2](https://doi.org/10.1130/0016-7606(1997)109<1536:OBTTGV>2.3.CO;2).
- Gohl, K., G. Uenzelmann-Neben, and N. Grobys (2011), Growth and dispersal of a Southeast African large igneous province, *South African Journal of Geology*, 114(3–4), 379–386, doi:[10.2113/gssajg.114.3-4.379](https://doi.org/10.2113/gssajg.114.3-4.379).
- Golynsky, A., D. Blankenship, M. Chiappini, D. Damaske, F. Ferraccioli, C. Finn, D. Golynsky, A. Goncharov, T. Ishihara, S. Ivanov, W. Jokat, H. R. Kim, M. König, V. Masolov, Y. Nogi, M. Sand, M. Studinger, R. von Frese, and A. W. Group (2007), New Magnetic Anomaly Map of East Antarctica and Surrounding Regions, in *Antarctica: A Keystone in a Changing World - Online Proceedings for the 10th International Symposium on Antarctic Earth Sciences*, vol. 1047, edited by C. Raymond, pp. 1–4, U.S. Geological Survey, Santa Barbara, doi:[10.3133/of2007.srp050](https://doi.org/10.3133/of2007.srp050).
- Goodlad, S. W., A. K. Martin, and C. J. H. Hartnady (1982), Mesozoic magnetic anomalies in the southern Natal Valley, *Nature*, 295(5851), 686–688, doi:[10.1038/295686a0](https://doi.org/10.1038/295686a0).
- Götze, H.-J. (2007), IGMAS+, Interactive Geophysical Modelling Assistant, v1.1.1892.1, Transinsight GmbH, Dresden.
- Götze, H.-J., and B. Lahmeyer (1988), Application of three-dimensional interactive modeling in gravity and magnetics, *Geophysics*, 53(8), 1096–1108, doi:[10.1190/1.1442546](https://doi.org/10.1190/1.1442546).
- Gradstein, F., and J. Ogg (2004), Geologic Time Scale 2004 - why, how, and where next!, *Lethaia*, 37(2), 175–181, doi:[10.1080/00241160410006483](https://doi.org/10.1080/00241160410006483).
- Gradstein, F. M., J. G. Ogg, and F. J. Hilgen (2012), On The Geologic Time Scale, *Newsletters on Stratigraphy*, 45(2), 171–188, doi:[10.1127/0078-0421/2012/0020](https://doi.org/10.1127/0078-0421/2012/0020).

- Grantham, G. H., and D. R. Hunter (1991), The timing and nature of faulting and jointing adjacent to the Pencksökket, western Dronning Maud Land, Antarctica, in *Geological Evolution of Antarctica; Proceedings of the Fifth International Symposium on Antarctic Earth Science*, edited by J. Thomson, M.R.A.; Crame, J.A.; Thomson, pp. 47–52, Cambridge University Press, New York.
- Grantham, G. H., M. A. H. Maboko, and B. M. Eglinton (2003), A review of the evolution of the Mozambique Belt and implications for the amalgamation and dispersal of Rodinia and Gondwana, *Geological Society, London, Special Publications*, 206(1), 401–425, doi:[10.1144/GSL.SP.2003.206.01.19](https://doi.org/10.1144/GSL.SP.2003.206.01.19).
- Green, R. W. E., and A. L. Hales (1966), Seismic refraction measurements in the southwestern Indian Ocean, *Journal of Geophysical Research*, 71(6), 1637–1647, doi:[10.1029/JZ071i006p01637](https://doi.org/10.1029/JZ071i006p01637).
- Groenewald, P. B., G. H. Grantham, and M. K. Watkeys (1991), Geological evidence for a Proterozoic to Mesozoic link between southeastern Africa and Dronning Maud Land, Antarctica, *Journal of the Geological Society*, 148(6), 1115–1123, doi:[10.1144/gsjgs.148.6.1115](https://doi.org/10.1144/gsjgs.148.6.1115).
- Gwavava, O., C. J. Swain, F. Podmore, and J. D. Fairhead (1992), Evidence of crustal thinning beneath the Limpopo Belt and Lebombo monocline of southern Africa based on regional gravity studies and implications for the reconstruction of Gondwana, *Tectonophysics*, 212(1-2), 1–20, doi:[10.1016/0040-1951\(92\)90136-T](https://doi.org/10.1016/0040-1951(92)90136-T).
- Harrison, C. G. A. (1976), Magnetization of the oceanic crust, *Geophysical Journal of the Royal Astronomical Society*, 47(2), 257–283, doi:[10.1111/j.1365-246X.1976.tb01273.x](https://doi.org/10.1111/j.1365-246X.1976.tb01273.x).
- Hartnady, C. J. H., Z. Ben-Avraham, and J. Rogers (1992), Deep-ocean basins and submarine rises off the continental margin of south-eastern Africa: new geological research, *South African Journal of Science*, 88(11-12), 534–539.
- Hastie, W. W., M. K. Watkeys, and C. Aubourg (2014), Magma flow in dyke swarms of the Karoo LIP: Implications for the mantle plume hypothesis, *Gondwana Research*, 25(2), 736–755, doi:[10.1016/j.gr.2013.08.010](https://doi.org/10.1016/j.gr.2013.08.010).
- Heirtzler, J. R., and R. H. Burroughs (1971), Madagascar's Paleoposition: New Data from the Mozambique Channel, *Science*, 174(4008), 488–490, doi:[10.1126/science.174.4008.488](https://doi.org/10.1126/science.174.4008.488).

- Hemant, K. (2003), Modelling and Interpretation of Global Lithospheric Magnetic Anomalies, Ph.D. thesis, FU Berlin.
- Hinz, K. (1981), A hypothesis on terrestrial catastrophes. Wedges of very thick oceanward dipping layers beneath passive continental margins - their origin and paleoenvironmental significance, in *Geologisches Jahrbuch*, E22, pp. 3–28.
- Hinz, K., and W. Krause (1982), The Continental Margin of Queen Maud Land/Antarctica: Seismic Sequences, Structural Elements and Geological Development, in *Geologisches Jahrbuch*, E23, pp. 17–41.
- Hinz, K., S. Neben, Y. B. Gouseva, and G. A. Kudryavtsev (2004), A compilation of geophysical data from the Lazarev Sea and the Riiser-Larsen Sea, Antarctica, *Marine Geophysical Researches*, 25(3-4), 233–245, doi:[10.1007/s11001-005-1319-y](https://doi.org/10.1007/s11001-005-1319-y).
- Hochmuth, K., K. Gohl, G. Uenzelmann-Neben, and R. Werner (2014), The diverse crustal structure and magmatic evolution of the Manihiki Plateau, central Pacific, *Solid Earth Discussions*, 6(2), 1863–1905, doi:[10.5194/sed-6-1863-2014](https://doi.org/10.5194/sed-6-1863-2014).
- Hübscher, C., W. Jokat, and H. Miller (1996), Crustal structure of the Antarctic continental margin in the eastern Weddell Sea, *Geological Society, London, Special Publications*, 108(1), 165–174, doi:[10.1144/GSL.SP.1996.108.01.12](https://doi.org/10.1144/GSL.SP.1996.108.01.12).
- Jacobs, J., and R. J. Thomas (2004), Himalayan-type indenter-escape tectonics model for the southern part of the late Neoproterozoic-early Paleozoic East African-Antarctic orogen, *Geology*, 32(8), 721–724, doi:[10.1130/G20516.1](https://doi.org/10.1130/G20516.1).
- Jacobs, J., C. M. Fanning, F. Henjes-Kunst, M. Olesch, and H.-J. Paech (1998), Continuation of the Mozambique Belt Into East Antarctica: Grenville-Age Metamorphism and Polyphase Pan-African High-Grade Events in Central Dronning Maud Land, *The Journal of Geology*, 106(4), 385–406, doi:[10.1086/516031](https://doi.org/10.1086/516031).
- Jacobs, J., M. Elburg, A. Läufer, I. C. Kleinhanns, F. Henjes-Kunst, S. Estrada, A. S. Ruppel, D. Damaske, P. Montero, and F. Bea (2015), Two distinct Late Mesoproterozoic/Early Neoproterozoic basement provinces in central/eastern Dronning Maud Land, East Antarctica: The missing link, 15-21E, *Precambrian Research*, 265, 249–272, doi:[10.1016/j.precamres.2015.05.003](https://doi.org/10.1016/j.precamres.2015.05.003).
- Jaritz, W., J. Kreutzer, P. Müller, and W. Harre (1977), Die Vulkanitserien im Küstengebiet von Nordmoçambique, in *Geologisches Jahrbuch*, B26, pp. 147–165.

- Jokat, W. (2005), Southeastern Atlantic and southwestern Indian Ocean : reconstruction of the sedimentary and tectonic development since the Cretaceous AISTEK-II: Mozambique Ridge and Mozambique Basin, *Cruise report*, Alfred Wegener Institute, Helmholtz Centre for Polar and Marine Research, Bremerhaven, Germany.
- Jokat, W. (2009), The expedition of the research vessel "Pelagia" to the Natal Basin and the Mozambique Ridge in 2009 (Project AISTEK III), *Cruise report*, Alfred Wegener Institute, Helmholtz Centre for Polar and Marine Research, Bremerhaven, Germany.
- Jokat, W. (2014), The expedition of the research vessel "Sonne" to the Mozambique Basin in 2014 (SO230), *Cruise report*, Alfred Wegener Institute, Helmholtz Centre for Polar and Marine Research, Bremerhaven, Germany.
- Jokat, W., and M. C. Schmidt-Aursch (2007), Geophysical characteristics of the ultraslow spreading Gakkel Ridge, Arctic Ocean, *Geophysical Journal International*, *168*(3), 983–998, doi:[10.1111/j.1365-246X.2006.03278.x](https://doi.org/10.1111/j.1365-246X.2006.03278.x).
- Jokat, W., T. Boebel, M. König, and U. Meyer (2003), Timing and geometry of early Gondwana breakup, *Journal of Geophysical Research*, *108*(B9), 2428–2842, doi:[10.1029/2002JB001802](https://doi.org/10.1029/2002JB001802).
- Jokat, W., O. Ritzmann, C. Reichert, and K. Hinz (2004), Deep crustal structure of the continental margin off the Explora Escarpment and in the Lazarev Sea, East Antarctica, *Marine Geophysical Researches*, *25*(3-4), 283–304, doi:[10.1007/s11001-005-1337-9](https://doi.org/10.1007/s11001-005-1337-9).
- Jokat, W., Y. Nogi, and V. Leinweber (2010), New aeromagnetic data from the western Enderby Basin and consequences for Antarctic-India break-up, *Geophysical Research Letters*, *37*(21), 1–5, doi:[10.1029/2010GL045117](https://doi.org/10.1029/2010GL045117).
- Jones, D. L., R. A. Duncan, J. C. Briden, D. E. Randall, and C. MacNiocaill (2001), Age of the Batoka basalts, northern Zimbabwe, and the duration of Karoo Large Igneous Province magmatism, *Geochemistry, Geophysics, Geosystems*, *2*(2), 1–14, doi:[10.1029/2000GC000110](https://doi.org/10.1029/2000GC000110).
- Jourdan, F., G. Féraud, H. Bertrand, A. B. Kampunzu, G. Tshoso, M. K. Watkeys, and B. Le Gall (2005), Karoo large igneous province: Brevity, origin, and relation to mass extinction questioned by new $^{40}\text{Ar}/^{39}\text{Ar}$ age data, *Geology*, *33*(9), 745–748, doi:[10.1130/G21632.1](https://doi.org/10.1130/G21632.1).

- Jourdan, F., G. Féraud, H. Bertrand, and M. K. Watkeys (2007), From flood basalts to the inception of oceanization: Example from the $^{40}\text{Ar}/^{39}\text{Ar}$ high-resolution picture of the Karoo large igneous province, *Geochemistry, Geophysics, Geosystems*, 8(2), 1–20, doi:[10.1029/2006GC001392](https://doi.org/10.1029/2006GC001392).
- Jourdan, F., G. Féraud, H. Bertrand, M. K. Watkeys, and P. R. Renne (2008), The $^{40}\text{Ar}/^{39}\text{Ar}$ ages of the sill complex of the Karoo large igneous province: Implications for the Pliensbachian-Toarcian climate change, *Geochemistry, Geophysics, Geosystems*, 9(6), 1–20, doi:[10.1029/2008GC001994](https://doi.org/10.1029/2008GC001994).
- Kaus, B. J. P. (2013), Solid Earth: Heating glaciers from below, *Nature Geoscience*, 6(9), 683–684, doi:[10.1038/ngeo1919](https://doi.org/10.1038/ngeo1919).
- Klausen, M. B. (2009), The Lebombo monocline and associated feeder dyke swarm: Diagnostic of a successful and highly volcanic rifted margin?, *Tectonophysics*, 468(1–4), 42–62, doi:[10.1016/j.tecto.2008.10.012](https://doi.org/10.1016/j.tecto.2008.10.012).
- Klingelhoefer, F., Y. Lafoy, J. Collot, E. Cosquer, L. Géli, H. Nouzé, and R. Vially (2007), Crustal structure of the basin and ridge system west of New Caledonia (south-west Pacific) from wide-angle and reflection seismic data, *Journal of Geophysical Research: Solid Earth*, 112(B11), 102–119, doi:[10.1029/2007JB005093](https://doi.org/10.1029/2007JB005093).
- König, M., and W. Jokat (2006), The Mesozoic breakup of the Weddell Sea, *Journal of Geophysical Research: Solid Earth*, 111(12), 1–28, doi:[10.1029/2006JB004035](https://doi.org/10.1029/2006JB004035).
- König, M., and W. Jokat (2010), Advanced insights into magmatism and volcanism of the Mozambique Ridge and Mozambique Basin in the view of new potential field data, *Geophysical Journal International*, 180(1), 158–180, doi:[10.1111/j.1365-246X.2009.04433.x](https://doi.org/10.1111/j.1365-246X.2009.04433.x).
- Kristoffersen, Y., C. Hofstede, A. Diez, R. Blenkner, A. Lambrecht, C. Mayer, and O. Eisen (2014), Reassembling Gondwana: A new high quality constraint from vibroseis exploration of the sub-ice shelf geology of the East Antarctic continental margin, *Journal of Geophysical Research: Solid Earth*, 119(12), 9171–9182, doi:[10.1002/2014JB011479](https://doi.org/10.1002/2014JB011479).
- Kröner, A. (1977), Precambrian mobile belts of southern and eastern africa – ancient sutures or sites of ensialic mobility? a case for crustal evolution towards plate tectonics, *Tectonophysics*, 40(1–2), 101–135, doi:[10.1016/0040-1951\(77\)90031-2](https://doi.org/10.1016/0040-1951(77)90031-2).

- Kudryavtzev, G. A., V. V. Butzenko, and I. N. Kadmina (1991), Crustal section across western Dronning Maud Land continental margin from geophysical data, in *Abstracts, Sixth international symposium on Antarctic earth sciences*, pp. 330–335.
- Lafourcade, M. P. (1984), Étude géologique et géophysique de la marge continentale du sud Mozambique, 17S à 28S, Ph.d. thesis, Université Pierre et Marie Curie Paris VI.
- Lawver, L. A., L. M. Gahagan, and I. W. Dalziel (1998), A Tight fit-Early Mesozoic Gondwana, a Plate Reconstruction Perspective, *Memoirs of National Institute of Polar Research. Special issue*, 53, 214–229.
- Leinweber, V. T., and W. Jokat (2011), Is there continental crust underneath the northern Natal Valley and the Mozambique Coastal Plains?, *Geophysical Research Letters*, 38(14), 1–7, doi:[10.1029/2011GL047659](https://doi.org/10.1029/2011GL047659).
- Leinweber, V. T., and W. Jokat (2012), The Jurassic history of the Africa-Antarctica corridor - new constraints from magnetic data on the conjugate continental margins, *Tectonophysics*, 530-531, 87–101, doi:[10.1016/j.tecto.2011.11.008](https://doi.org/10.1016/j.tecto.2011.11.008).
- Leinweber, V. T., F. Klingelhoefer, S. Neben, C. Reichert, D. Aslanian, L. Matias, I. Heyde, B. Schreckenberger, and W. Jokat (2013), The crustal structure of the Central Mozambique continental margin - Wide-angle seismic, gravity and magnetic study in the Mozambique Channel, Eastern Africa, *Tectonophysics*, 599, 170–196, doi:[10.1016/j.tecto.2013.04.015](https://doi.org/10.1016/j.tecto.2013.04.015).
- Leitchenkov, G., J. Guseva, V. Gandyukhin, G. Grikurov, Y. Kristoffersen, M. Sand, A. Golynsky, and N. Aleshkova (2008), Crustal structure and tectonic provinces of the Riiser-Larsen Sea area (East Antarctica): Results of geophysical studies, *Marine Geophysical Researches*, 29(2), 135–158, doi:[10.1007/s11001-008-9051-z](https://doi.org/10.1007/s11001-008-9051-z).
- Ljones, F., A. Kuwano, R. Mjelde, A. Breivik, H. Shimamura, Y. Murai, and Y. Nishimura (2004), Crustal transect from the North Atlantic Knipovich Ridge to the Svalbard Margin west of Hornsund, *Tectonophysics*, 378(1-2), 17–41, doi:[10.1016/j.tecto.2003.10.003](https://doi.org/10.1016/j.tecto.2003.10.003).
- Lort, J. M., W. Q. Limond, J. Segoufin, P. Patriat, J. R. Deltail, and B. Damotte (1979), New seismic data in the Mozambique Channel, *Marine Geophysical Researches*, 4(1), 71–89, doi:[10.1007/BF00286146](https://doi.org/10.1007/BF00286146).

- Ludwig, W. J., J. E. Nafe, E. S. W. Simpson, and S. Sacks (1968), Seismic-refraction measurements on the Southeast African Continental Margin, *Journal of Geophysical Research*, *73*(12), 3707, doi:[10.1029/JB073i012p03707](https://doi.org/10.1029/JB073i012p03707).
- Macey, P. H., R. J. Thomas, G. H. Grantham, B. A. Ingram, J. Jacobs, R. A. Armstrong, M. P. Roberts, B. Bingen, L. Hollick, G. S. de Kock, G. Viola, W. Bauer, E. Gonzales, T. Bjerkgård, I. H. C. Henderson, J. S. Sandstad, M. S. Cronwright, S. Harley, A. Solli, Ø. Nordgulen, G. Motuza, E. Daudi, and V. Manhiça (2010), Mesoproterozoic geology of the Nampula Block, northern Mozambique: Tracing fragments of Mesoproterozoic crust in the heart of Gondwana, *Precambrian Research*, *182*(1-2), 124–148, doi:[10.1016/j.precamres.2010.07.005](https://doi.org/10.1016/j.precamres.2010.07.005).
- Mahanjane, E. S. (2012), A geotectonic history of the northern Mozambique Basin including the Beira High - A contribution for the understanding of its development, *Marine and Petroleum Geology*, *36*(1), 1–12, doi:[10.1016/j.marpetgeo.2012.05.007](https://doi.org/10.1016/j.marpetgeo.2012.05.007).
- Mahanjane, E. S. (2014), The Davie Fracture Zone and adjacent basins in the offshore Mozambique Margin - A new insights for the hydrocarbon potential, *Marine and Petroleum Geology*, *57*, 561–571, doi:[10.1016/j.marpetgeo.2014.06.015](https://doi.org/10.1016/j.marpetgeo.2014.06.015).
- Marello, L. (2012), Basin Architecture and Lithospheric Structure of the Barents Sea Region from Geophysical Modelling, Ph.D. thesis, NTNU Trondheim.
- Marello, L., J. Ebbing, and L. Gernigon (2010), Magnetic basement study in the Barents Sea from inversion and forward modelling, *Tectonophysics*, *493*(1-2), 153–171, doi:[10.1016/j.tecto.2010.07.014](https://doi.org/10.1016/j.tecto.2010.07.014).
- Marello, L., J. Ebbing, and L. Gernigon (2013), Basement inhomogeneities and crustal setting in the Barents Sea from a combined 3D gravity and magnetic model, *Geophysical Journal International*, *193*(2), 557–584, doi:[10.1093/gji/ggt018](https://doi.org/10.1093/gji/ggt018).
- Marks, K. M., and A. A. Tikku (2001), Cretaceous reconstructions of East Antarctica, Africa and Madagascar, *Earth and Planetary Science Letters*, *186*(3-4), 479–495, doi:[10.1016/S0012-821X\(01\)00262-X](https://doi.org/10.1016/S0012-821X(01)00262-X).
- Marschall, H. R., C. J. Hawkesworth, C. D. Storey, B. Dhuime, P. T. Leat, H. P. Meyer, and S. Tamm-Buckle (2010), The Annandagstoppane Granite, East Antarctica: Evidence for Archaean Intracrustal recycling in the Kaapvaal-Grunehogna Craton from zircon O and Hf isotopes, *Journal of Petrology*, *51*(11), 2277–2301, doi:[10.1093/petrology/egq057](https://doi.org/10.1093/petrology/egq057).

- Martin, A., and C. Hartnady (1986), Plate tectonic development of the South West Indian Ocean: A revised reconstruction of East Antarctica and Africa, *Journal of Geophysical Research*, *91*(B5), 4767–4786, doi:[10.1029/JB091iB05p04767](https://doi.org/10.1029/JB091iB05p04767).
- Martin, A. K., S. W. Goodlad, C. J. H. Hartnady, and A. du Plessis (1982), Cretaceous palaeopositions of the Falkland Plateau relative to southern Africa using Mesozoic seafloor spreading anomalies, *Geophysical Journal of the Royal Astronomical Society*, *71*(3), 567–579, doi:[10.1111/j.1365-246X.1982.tb02784.x](https://doi.org/10.1111/j.1365-246X.1982.tb02784.x).
- Matthews, K. J., K. T. Maloney, S. Zahirovic, S. E. Williams, M. Seton, and R. D. Müller (2016), Global plate boundary evolution and kinematics since the late Paleozoic, *Global and Planetary Change*, *146*, 226–250, doi:[10.1016/j.gloplacha.2016.10.002](https://doi.org/10.1016/j.gloplacha.2016.10.002).
- Mauring, E., L. P. Beard, O. Kihle, and M. A. Smethurst (2002), A comparison of aeromagnetic levelling techniques with an introduction to median levelling, *Geophysical Prospecting*, *50*(1), 43–54, doi:[10.1046/j.1365-2478.2002.00300.x](https://doi.org/10.1046/j.1365-2478.2002.00300.x).
- Maus, S., U. Barckhausen, H. Berkenbosch, N. Bournas, J. Brozena, V. Childers, F. Dostaler, J. D. Fairhead, C. Finn, R. R. B. Von Frese, C. Gaina, S. Golynsky, R. Kucks, H. Lühr, P. Milligan, S. Mogren, R. D. Müller, O. Olesen, M. Pilkington, R. Saltus, B. Schreckenberger, E. Thébault, and F. C. Tontini (2009), EMAG2: A 2-arc min resolution Earth Magnetic Anomaly Grid compiled from satellite, airborne, and marine magnetic measurements, *Geochemistry, Geophysics, Geosystems*, *10*(8), 1–12, doi:[10.1029/2009GC002471](https://doi.org/10.1029/2009GC002471).
- Mekonnen, T. K. (2004), Interpretation & Geodatabase of Dykes Using Aeromagnetic Data of Zimbabwe and Mozambique, Master's thesis, ITC Enschede, The Netherlands.
- Menzies, M., S. Klemperer, C. Elbinger, and J. Baker (2002), Characteristics of volcanic rifted margins, *Geological Society of America*, *362*, 1–14, doi:[10.1130/0-8137-2362-0.1](https://doi.org/10.1130/0-8137-2362-0.1).
- Mieth, M. (2014), Aerogeophysical constraints for the geodynamic evolution of Dronning Maud Land, East Antarctica, Ph.D. thesis, Bremen, Germany.
- Mieth, M., and W. Jokat (2014), New aeromagnetic view of the geological fabric of southern Dronning Maud Land and Coats Land, East Antarctica, *Gondwana Research*, *25*(1), 358–367, doi:[10.1016/j.gr.2013.04.003](https://doi.org/10.1016/j.gr.2013.04.003).

- Mieth, M., J. Jacobs, A. Ruppel, D. Damaske, A. Läufer, and W. Jokat (2014), New detailed aeromagnetic and geological data of eastern Dronning Maud Land: Implications for refining the tectonic and structural framework of Sør Rondane, East Antarctica, *Precambrian Research*, *245*, 174–185, doi:[10.1016/j.precamres.2014.02.009](https://doi.org/10.1016/j.precamres.2014.02.009).
- Miltitzer, H., and R. Scheibe (1981), Grundlagen der angewandten Geomagnetik, *Freiberger Forschungsheft, C*(352), 1–314.
- Miura, S., K. Suyehiro, M. Shinohara, N. Takahashi, E. Araki, and A. Taira (2004), Seismological structure and implications of collision between the Ontong Java Plateau and Solomon Island Arc from ocean bottom seismometer-airgun data, *Tectonophysics*, *389*(3-4), 191–220, doi:[10.1016/j.tecto.2003.09.029](https://doi.org/10.1016/j.tecto.2003.09.029).
- Mjelde, R., J. Kasahara, H. Shimamura, A. Kamimura, T. Kanazawa, S. Kodaira, T. Raum, and H. Shiobara (2002), Lower crustal seismic velocity-anomalies; magmatic underplating or serpentinitized peridotite? Evidence from the Vøring Margin, NE Atlantic, *Marine Geophysical Researches*, *23*(2), 169–183, doi:[10.1023/A:1022480304527](https://doi.org/10.1023/A:1022480304527).
- Mjelde, R., J. I. Faleide, A. J. Breivik, and T. Raum (2009), Lower crustal composition and crustal lineaments on the Vøring Margin, NE Atlantic: A review, *Tectonophysics*, *472*(1-4), 183–193, doi:[10.1016/j.tecto.2008.04.018](https://doi.org/10.1016/j.tecto.2008.04.018).
- Mooney, W. D., C. Prodehl, and N. I. Pavlenkova (2002), Seismic velocity structure of the continental lithosphere from controlled source data, in *International Handbook of Earthquake and Engineering Seismology, Part A, Vol. 81A*, edited by W. H. Lee, H. Kanamori, P. C. Jennings, and C. Kisslinger, 1 ed., chap. 54, pp. 887–910, Academic Press, doi:[10.1016/S0074-6142\(02\)80261-3](https://doi.org/10.1016/S0074-6142(02)80261-3).
- Mougenot, D., M. Recq, P. Virlogeux, and C. Lepvrier (1986), Seaward extension of the East African Rift, *Nature*, *321*(6070), 599–603, doi:[10.1038/321599a0](https://doi.org/10.1038/321599a0).
- Mougenot, D., M. Gennesseaux, J. Hernandez, C. Lepvrier, J. Malod, S. Raillard, J. Vanney, and M. Villeneuve (1991), The Mozambique Ridge (Indian Ocean): a continental fragment shaped during the transform motion of American and Antarctic plates along East-Africa?, *Comptes Rendus de l'Académie des Sciences Paris, Série II*, *312*(6), 655–662.
- Mueller, C. O., and W. Jokat (2017), Geophysical evidence for the crustal variation and distribution of magmatism along the central coast of Mozambique, *submitted to Tectonophysics*.

- Mueller, C. O., W. Jokat, and B. Schreckenberger (2016), The crustal structure of Beira High, central Mozambique – Combined investigation of wide-angle seismic and potential field data, *Tectonophysics*, 683, 233–254, doi:[10.1016/j.tecto.2016.06.028](https://doi.org/10.1016/j.tecto.2016.06.028).
- Mutter, J. C., M. Talwani, and P. L. Stoffa (1982), Origin of seaward-dipping reflectors in oceanic crust off the Norwegian margin by "subaerial sea-floor spreading", *Geology*, 10(7), 353–357, doi:[10.1130/0091-7613\(1982\)10<353:OOSRIO>2.0.CO;2](https://doi.org/10.1130/0091-7613(1982)10<353:OOSRIO>2.0.CO;2).
- Nairn, A. E. M., I. Lerche, and J. E. Iliffe (1991), Geology, basin analysis, and hydrocarbon potential of Mozambique and the Mozambique Channel, *Earth-Science Reviews*, 30(1-2), 81–123, doi:[10.1016/0012-8252\(91\)90014-7](https://doi.org/10.1016/0012-8252(91)90014-7).
- Nguuri, T. K., J. Gore, D. E. James, S. J. Webb, C. Wright, T. G. Zengeni, O. Gwavava, and J. A. Snoke (2001), Crustal structure beneath southern Africa and its implications for the formation and evolution of the Kaapvaal and Zimbabwe cratons, *Geophysical Research Letters*, 28(13), 2501–2504, doi:[10.1029/2000GL012587](https://doi.org/10.1029/2000GL012587).
- Nguyen, L. C., S. A. Hall, D. E. Bird, and P. J. Ball (2016), Reconstruction of the East Africa and Antarctica continental margins, *Journal of Geophysical Research: Solid Earth*, 121(6), 4156–4179, doi:[10.1002/2015JB012776](https://doi.org/10.1002/2015JB012776).
- Nicolas, A., and F. Boudier (2000), Large mantle upwellings and related variations in crustal thickness in the Oman ophiolite, in *Special Paper 349: Ophiolites and oceanic crust: new insights from field studies and the Ocean Drilling Program*, pp. 67–73, Geological Society of America, doi:[10.1130/0-8137-2349-3.67](https://doi.org/10.1130/0-8137-2349-3.67).
- Norton, I. O., and J. G. Sclater (1979), A model for the evolution of the Indian Ocean and the breakup of Gondwanaland, *Journal of Geophysical Research*, 84(B12), 6803–6830, doi:[10.1029/JB084iB12p06803](https://doi.org/10.1029/JB084iB12p06803).
- Ogg, J., L. Hinnov, and C. Huang (2012), Jurassic, in *The Geologic Time Scale 2012*, edited by F. M. Gradstein, J. G. Ogg, M. Schmitz, and G. Ogg, 1 ed., chap. 26, pp. 731–791, Elsevier, doi:[10.1016/B978-0-444-59425-9.00026-3](https://doi.org/10.1016/B978-0-444-59425-9.00026-3).
- Ogg, J. G. (2012), Geomagnetic Polarity Time Scale, in *The Geologic Time Scale 2012*, vol. 1-2, edited by F. M. Gradstein, J. G. Ogg, M. Schmitz, and G. Ogg, 1 ed., chap. 5, pp. 85–113, Elsevier, doi:[10.1016/B978-0-444-59425-9.00005-6](https://doi.org/10.1016/B978-0-444-59425-9.00005-6).
- Ogg, J. G., and A. G. Smith (2004), The geomagnetic polarity time scale, in *A Geological Time Scale 2004*, edited by F. M. Gradstein, J. G. Ogg, and A. G. Smith, 1 ed., chap. 5, pp. 63–86, Cambridge University Press, doi:[10.1017/CBO9780511536045.006](https://doi.org/10.1017/CBO9780511536045.006).

- O'Reilly, B., F. Hauser, C. Ravaut, P. Shannon, and P. Readman (2006), Crustal thinning, mantle exhumation and serpentinization in the Porcupine Basin, offshore Ireland: evidence from wide-angle seismic data, *Journal of the Geological Society*, *163*(5), 775–787, doi:[10.1144/0016-76492005-079](https://doi.org/10.1144/0016-76492005-079).
- Parsiegla, N., K. Gohl, and G. Uenzelmann-Neben (2008), The Agulhas Plateau: structure and evolution of a Large Igneous Province, *Geophysical Journal International*, *174*(1), 336–350, doi:[10.1111/j.1365-246X.2008.03808.x](https://doi.org/10.1111/j.1365-246X.2008.03808.x).
- Pérez-Díaz, L., and G. Eagles (2014), Constraining South Atlantic growth with seafloor spreading data, *Tectonics*, *33*(9), 1848–1873, doi:[10.1002/2014TC003644](https://doi.org/10.1002/2014TC003644).
- Pérez-Gussinyé, M., C. R. Ranero, and T. J. Reston (2003), Mechanisms of extension at nonvolcanic margins: Evidence from the Galicia interior basin, west of Iberia, *Journal of Geophysical Research*, *108*(B5), 2245–2263, doi:[10.1029/2001JB000901](https://doi.org/10.1029/2001JB000901).
- Peron-Pinvidic, G., and G. Manatschal (2010), From microcontinents to extensional allochthons: witnesses of how continents rift and break apart?, *Petroleum Geoscience*, *16*(3), 189–197, doi:[10.1144/1354-079309-903](https://doi.org/10.1144/1354-079309-903).
- Peron-Pinvidic, G., G. Manatschal, and P. T. Osmundsen (2013), Structural comparison of archetypal Atlantic rifted margins: A review of observations and concepts, *Marine and Petroleum Geology*, *43*, 21–47, doi:[10.1016/j.marpetgeo.2013.02.002](https://doi.org/10.1016/j.marpetgeo.2013.02.002).
- Phethean, J. J., L. M. Kalnins, J. van Hunen, P. G. Biffi, R. J. Davies, and K. J. McCaffrey (2016), Madagascar's escape from Africa: A high-resolution plate reconstruction for the Western Somali Basin and implications for supercontinent dispersal, *Geochemistry, Geophysics, Geosystems*, *17*, 2825–2834, doi:[10.1002/2016GC006624](https://doi.org/10.1002/2016GC006624).
- Polteau, S., A. Mazzini, O. Galland, S. Planke, and A. Malthe-Sørensen (2008), Saucer-shaped intrusions: Occurrences, emplacement and implications, *Earth and Planetary Science Letters*, *266*(1-2), 195–204, doi:[10.1016/j.epsl.2007.11.015](https://doi.org/10.1016/j.epsl.2007.11.015).
- Radhakrishna, M., D. Twinkle, S. Nayak, R. Bastia, and G. S. Rao (2012), Crustal structure and rift architecture across the Krishna-Godavari basin in the central Eastern Continental Margin of India based on analysis of gravity and seismic data, *Marine and Petroleum Geology*, *37*(1), 129–146, doi:[10.1016/j.marpetgeo.2012.05.005](https://doi.org/10.1016/j.marpetgeo.2012.05.005).
- Raillard, S. (1990), Les marges de l'Afrique de l'Est et les zones de fracture associées: Chaîne Davie et Ride du Mozambique, Ph.D. thesis, Université Pierre et Marie Curie Paris VI.

- Reeves, C. (2000), The geophysical mapping of Mesozoic dyke swarms in southern Africa and their origin in the disruption of Gondwana, *Journal of African Earth Sciences*, *30*(3), 499–513, doi:[10.1016/S0899-5362\(00\)00035-X](https://doi.org/10.1016/S0899-5362(00)00035-X).
- Reeves, C. (2014), The position of Madagascar within Gondwana and its movements during Gondwana dispersal, *Journal of African Earth Sciences*, *94*, 45–57, doi:[10.1016/j.jafrearsci.2013.07.011](https://doi.org/10.1016/j.jafrearsci.2013.07.011).
- Reeves, C., and M. De Wit (2000), Making ends meet in Gondwana: Retracing the transforms of the Indian Ocean and reconnecting continental shear zones, *Terra Nova*, *12*(6), 272–280, doi:[10.1046/j.1365-3121.2000.00309.x](https://doi.org/10.1046/j.1365-3121.2000.00309.x).
- Reeves, C. V., J. P. Teasdale, and E. S. Mahanjane (2016), Insight into the Eastern Margin of Africa from a new tectonic model of the Indian Ocean, *Geological Society, London, Special Publications*, *431*(1), 1–24, doi:[10.1144/SP431.12](https://doi.org/10.1144/SP431.12).
- Reichert, C., and S. Neben (2008), Research Cruise BGR07 - MOBAMASIS - Marine Geophysical Investigations offshore Central Mozambique, *Cruise report*, Federal Institute for Geosciences and Natural Resources, Hanover, Germany.
- Reznikov, M., Z. Ben-Avraham, C. Hartnady, and T. M. Niemi (2005), Structure of the Transkei Basin and Natal Valley, Southwest Indian Ocean, from seismic reflection and potential field data, *Tectonophysics*, *397*(1-2), 127–141, doi:[10.1016/j.tecto.2004.11.002](https://doi.org/10.1016/j.tecto.2004.11.002).
- Riedel, S., J. Jacobs, and W. Jokat (2013), Interpretation of new regional aeromagnetic data over Dronning Maud Land (East Antarctica), *Tectonophysics*, *585*, 161–171, doi:[10.1016/j.tecto.2012.10.011](https://doi.org/10.1016/j.tecto.2012.10.011).
- Roeser, H., C. Steiner, B. Schreckenberger, and M. Block (2002), Structural development of the Jurassic Magnetic Quiet Zone off Morocco and identification of Middle Jurassic magnetic lineations, *Journal of Geophysical Research: Solid Earth*, *107*(B10), 1–23, doi:[10.1029/2000JB000094](https://doi.org/10.1029/2000JB000094).
- Roeser, H. A., J. Fritsch, and K. Hinz (1996), The development of the crust off Dronning Maud Land, East Antarctica, *Geological Society, London, Special Publications*, *108*(1), 243–264, doi:[10.1144/GSL.SP.1996.108.01.18](https://doi.org/10.1144/GSL.SP.1996.108.01.18).
- Rudnick, R. L., and D. M. Fountain (1995), Nature and composition of the continental crust: A lower crustal perspective, *Reviews of Geophysics*, *33*(3), 267–309, doi:[10.1029/95RG01302](https://doi.org/10.1029/95RG01302).

- Sæther, B. (1997), Improved Estimation of Subsurface Magnetic Properties using Minimum Mean-Square Error Methods, Ph.D. thesis, NTNU Trondheim.
- Sahu, B. K. (2000), Aeromagnetism of selected continental areas flanking the Indian Ocean: with implications for geological correlation and reassembly of Central Gondwana, Ph.D. thesis, Cape Town.
- Saki, T., Y. Tamura, T. Kodato, I. Mizukoshi, and H. Amano (1987), Preliminary report of geological and geophysical surveys off Queen Maud Land, East Antarctica, in *Proceedings of the NIPR Symposium on Antarctic Geosciences, No. 1*, edited by Y. Yoshida, pp. 23–40, National Institute of Polar Research, Tokio.
- Salazar, M. U., D. Baker, M. Francis, D. Kornpohl, and T. West (2013), Frontier exploration offshore the Zambezi Delta, Mozambique, *First Break*, *31*(6), 135–144.
- Salman, G., and I. Abdula (1995), Development of the Mozambique and Ruvuma sedimentary basins, offshore Mozambique, *Sedimentary Geology*, *96*(1-2), 7–41, doi:[10.1016/0037-0738\(95\)00125-R](https://doi.org/10.1016/0037-0738(95)00125-R).
- Saltus, R. W., and R. J. Blakely (2011), Unique geologic insights from "non-unique" gravity and magnetic interpretation, *GSA Today*, *21*(12), 4–11, doi:[10.1130/G136A.1](https://doi.org/10.1130/G136A.1).
- Sandwell, D. T., R. D. Müller, W. H. F. Smith, E. Garcia, and R. Francis (2014), New global marine gravity model from CryoSat-2 and Jason-1 reveals buried tectonic structure, *Science*, *346*(6205), 65–67.
- Scheinert, M., F. Ferraccioli, J. Schwabe, R. Bell, M. Studinger, D. Damaske, W. Jokat, N. Aleshkova, T. Jordan, G. Leitchenkov, D. D. Blankenship, T. M. Damiani, D. Young, J. R. Cochran, and T. D. Richter (2016), New Antarctic gravity anomaly grid for enhanced geodetic and geophysical studies in Antarctica, *Geophysical Research Letters*, *43*(2), 600–610, doi:[10.1002/2015GL067439](https://doi.org/10.1002/2015GL067439).
- Schlindwein, V., and W. Jokat (1999), Structure and evolution of the continental crust of northern east Greenland from integrated geophysical studies, *Journal of Geophysical Research*, *104*(B7), 15,227–15,245, doi:[10.1029/1999JB900101](https://doi.org/10.1029/1999JB900101).
- Schmidt, S., H. Götze, C. Fichler, J. Ebbing, and M. R. Alvers (2007), 3D Gravity, FTG and Magnetic Modeling: the new IGMAS+ Software, in *EGM 2007 International Workshop*, pp. 1–4, European Association of Geoscientists and Engineers, Capri.

- Schmidt-Aursch, M. (2003), The crustal structure of the East Greenland Fjord Region between the Precambrian shield and the recent mid-oceanic ridges: Results from seismic and gravity modelling, Ph.D. thesis, Bremen.
- Schön, J. (1983), *Petrophysik. Physikalische Eigenschaften von Gesteinen und Mineralien*, 45–61 pp., Enke, Stuttgart.
- Schreckenberger, B., H. Roeser, and P. Symonds (1992), Marine magnetic anomalies over the Lord Howe Rise and the Tasman Sea: Implications for the magnetization of the lower continental crust, *Tectonophysics*, *212*, 77–97, doi:[10.1016/0040-1951\(92\)90141-R](https://doi.org/10.1016/0040-1951(92)90141-R).
- Sclater, J. G., M. Munsch, R. L. Fisher, P. Weatherall, S. C. Cande, P. Patriat, H. Bergh, and R. Schlich (1997), Geophysical synthesis of the Indian/Southern Oceans: Part 1, The Southwest Indian Ocean, *Scripps Institution of Oceanography Reference Series*.
- Segev, A. (2001), Flood basalts, continental breakup and the dispersal of Gondwana: evidence for periodic migration of upwelling mantle flows (plumes), *Stephan Mueller Special Publication Series*, *2*, 171–191, doi:[10.5194/smsps-2-171-2002](https://doi.org/10.5194/smsps-2-171-2002).
- Segoufin, J. (1978), Anomalies magnétiques mésozoïques dans le bassin de Mozambique, *Comptes Rendus de l'Académie des Sciences, Série D*, *287*(D), 109–112.
- Shannon, P. M., A. W. B. Jacob, B. M. O'Reilly, F. Hauser, P. W. Readman, and J. Makris (1999), Structural setting, geological development and basin modelling in the Rockall Trough, *Petroleum Geology of Northwest Europe: Proceedings of the 5th Conference on the Petroleum Geology of Northwest Europe*, pp. 421–431, doi:[10.1144/0050421](https://doi.org/10.1144/0050421).
- Sigurdsson, H., B. Houghton, S. McNutt, H. Rymer, and J. Stix (2015), *The encyclopedia of volcanoes*, 2 ed., 395–403 pp., Academic Press, pp. 395-403.
- Simpson, E., J. Sclater, B. Parsons, I. Norton, and L. Meinke (1979), Mesozoic magnetic lineations in the Mozambique Basin, *Earth and Planetary Science Letters*, *43*(2), 260–264, doi:[10.1016/0012-821X\(79\)90209-7](https://doi.org/10.1016/0012-821X(79)90209-7).
- Simpson, E. S. W., R. Schlich, J. Gieskes, W. A. Girdley, L. Leclaire, B. Vaughn Marshall, C. Moore, C. Müller, J. Sigal, T. L. Vallier, S. M. White, and B. Zobel (1974), Site 249, in *Initial Reports of the Deep Sea Drilling Project*, *25*, edited by E. S. W. Simpson and R. Schlich, pp. 287–346, U.S. Government Printing Office, doi:[10.2973/dsdp.proc.25.110.1974](https://doi.org/10.2973/dsdp.proc.25.110.1974).

- Sinha, M. C., K. E. Loudon, and B. Parsons (1981), The crustal structure of the Madagascar Ridge, *Geophysical Journal International*, *66*(2), 351–377, doi:[10.1111/j.1365-246X.1981.tb05960.x](https://doi.org/10.1111/j.1365-246X.1981.tb05960.x).
- Talwani, M. (1962), Gravity Measurements on HMS ACHERON in South Atlantic and Indian Oceans, *Geological Society of America Bulletin*, *73*(9), 1171–1182, doi:[10.1130/0016-7606\(1962\)73\[1171:GMOHAI\]2.0.CO;2](https://doi.org/10.1130/0016-7606(1962)73[1171:GMOHAI]2.0.CO;2).
- Thybo, H., and I. M. Artemieva (2013), Moho and magmatic underplating in continental lithosphere, *Tectonophysics*, *609*, 605–619, doi:[10.1016/j.tecto.2013.05.032](https://doi.org/10.1016/j.tecto.2013.05.032).
- Tikku, A. A., K. M. Marks, and L. C. Kovacs (2002), An Early Cretaceous extinct spreading center in the northern Natal valley, *Tectonophysics*, *347*(1-3), 87–108, doi:[10.1016/S0040-1951\(01\)00239-6](https://doi.org/10.1016/S0040-1951(01)00239-6).
- Tominaga, M., M. A. Tivey, and W. W. Sager (2015), Nature of the Jurassic Magnetic Quiet Zone, *Geophysical Research Letters*, *42*(20), 8367–8372, doi:[10.1002/2015GL065394](https://doi.org/10.1002/2015GL065394).
- Tucholke, B. E., R. E. Houtz, and D. M. Barrett (1981), Continental crust beneath the Agulhas Plateau, southwest Indian Ocean, *Journal of Geophysical Research*, *86*(B5), 3791–3806, doi:[10.1029/JB086iB05p03791](https://doi.org/10.1029/JB086iB05p03791).
- Ueda, K., J. Jacobs, R. J. Thomas, J. Kosler, M. S. Horstwood, J.-A. Wartho, F. Jourdan, B. Emmel, and R. Matola (2012), Postcollisional High-Grade Metamorphism, Orogenic Collapse, and Differential Cooling of the East African Orogen of Northeast Mozambique, *The Journal of Geology*, *120*(5), 507–530, doi:[10.1086/666876](https://doi.org/10.1086/666876).
- Uenzelmann-Neben, G. (2005), Southeastern Atlantic and southwestern Indian Ocean: reconstruction of the sedimentary and tectonic development since the Cretaceous AISTEK-1: Agulhas Transect, *Cruise report*, Alfred Wegener Institute, Helmholtz Centre for Polar and Marine Research, Bremerhaven, Germany.
- van der Meijde, M., I. Fadel, P. Ditmar, and M. Hamayun (2015), Uncertainties in crustal thickness models for data sparse environments: A review for South America and Africa, *Journal of Geodynamics*, *84*, 1–18, doi:[10.1016/j.jog.2014.09.013](https://doi.org/10.1016/j.jog.2014.09.013).
- Vening Meinesz, F. A. (1941), *Gravity expeditions at sea, 1934-1939 Vol. III*, vol. 111, 1–100 pp., Drukkerij Waltman, Delft.
- Viola, G., I. H. C. Henderson, B. Bingen, R. J. Thomas, M. A. Smethurst, and S. de Azavedo (2008), Growth and collapse of a deeply eroded orogen: Insights

- from structural, geophysical, and geochronological constraints on the Pan-African evolution of NE Mozambique, *Tectonics*, *27*(5), 1–31, doi:[10.1029/2008TC002284](https://doi.org/10.1029/2008TC002284).
- Virlogeux, P. (1987), Geologie de la marge nord-Mozambique et de la chaine Davie (9S à 21S): campagne MD40-MACAMO, Ph.D. thesis, Université Pierre et Marie Curie Paris VI.
- Voss, M., and W. Jokat (2007), Continent-ocean transition and voluminous magmatic underplating derived from P-wave velocity modelling of the East Greenland continental margin, *Geophysical Journal International*, *170*(2), 580–604, doi:[10.1111/j.1365-246X.2007.03438.x](https://doi.org/10.1111/j.1365-246X.2007.03438.x).
- Watts, A. B. (2001), Gravity anomalies, flexure and crustal structure at the Mozambique rifted margin, *Marine and Petroleum Geology*, *18*(4), 445–455, doi:[10.1016/S0264-8172\(00\)00079-9](https://doi.org/10.1016/S0264-8172(00)00079-9).
- Watts, A. B., and J. D. Fairhead (1999), A process-oriented approach to modeling the gravity signature of continental margins, *The Leading Edge*, *18*(2), 258–263, doi:[10.1190/1.1438270](https://doi.org/10.1190/1.1438270).
- Weatherall, P., K. M. Marks, M. Jakobsson, T. Schmitt, S. Tani, J. E. Arndt, M. Rovere, D. Chayes, V. Ferrini, and R. Wigley (2015), A new digital bathymetric model of the world’s oceans, *Earth and Space Science*, *2*(8), 331–345, doi:[10.1002/2015EA000107](https://doi.org/10.1002/2015EA000107).
- White, R. S., and L. K. Smith (2009), Crustal structure of the Hatton and the conjugate east Greenland rifted volcanic continental margins, NE Atlantic, *Journal of Geophysical Research: Solid Earth*, *114*(B2), 305–332, doi:[10.1029/2008JB005856](https://doi.org/10.1029/2008JB005856).
- White, R. S., D. McKenzie, and R. K. O’Nions (1992), Oceanic crustal thickness from seismic measurements and rare earth element inversions, *Journal of Geophysical Research*, *97*(B13), 19,683–19,715, doi:[10.1029/92JB01749](https://doi.org/10.1029/92JB01749).
- Zelt, B. C. (2004), ZP - Software for plotting & picking seismic refraction data in SEG-Y format, v1.02a, Hawaii Institute of Geophysics and Planetology, School of Ocean and Earth Science and Technology, University of Hawaii, Honolulu.
- Zelt, C. A. (1999), Modelling strategies and model assessment for wide-angle seismic traveltimes data, *Geophysical Journal International*, *139*(1), 183–204, doi:[10.1046/j.1365-246X.1999.00934.x](https://doi.org/10.1046/j.1365-246X.1999.00934.x).

- Zelt, C. A., and R. B. Smith (1992), Seismic travelttime inversion for 2-D crustal velocity structure, *Geophysical Journal International*, *108*(1), 16–34, doi:[10.1111/j.1365-246X.1992.tb00836.x](https://doi.org/10.1111/j.1365-246X.1992.tb00836.x).
- Zhang, X., A. V. Luttinen, D. H. Elliot, K. Larsson, and K. A. Foland (2003), Early stages of Gondwana breakup: The $^{40}\text{Ar}/^{39}\text{Ar}$ geochronology of Jurassic basaltic rocks from western Dronning Maud Land, Antarctica, and implications for the timing of magmatic and hydrothermal events, *Journal of Geophysical Research: Solid Earth*, *108*(B9), 1–19, doi:[10.1029/2001JB001070](https://doi.org/10.1029/2001JB001070).

Acknowledgements

There are a couple of people, which supported and helped me to prepare this thesis.

At this point I want to use the opportunity to express my thanks.

First of all, thanks to **Cornelia Spiegel** and **Wilfried Jokat** for reviewing my doctoral thesis.

Special thank goes to **Wilfried Jokat** for giving me the opportunity to prepare my thesis at AWI and for participating a research cruise with you as chief scientist.

Furthermore, thanks for supervising my research, long discussions and debates, constructive criticism, signatures and sometimes sending me even at the weekend or late-night your reviews.

Bernd Schreckenberger und **Dieter Franke** is thanked for the assistance with the magnetic data and inspiring discussions from a different point of view.

This work would have not been possible without any data. Therefor, I want to thank the entire **ship's and science crew** of cruise SO230. Additional thanks go to **Schlumberger Multiclient** and **INP** for providing insights into magnetic and seismic reflection data.

I acknowledge the help of **Thomas Bohlen** and **Tilman Metz** for their help with the software SOFI2D and a nice week in Karlsruhe with tropical temperatures. For their continuous support with IGMAS+, I want to thank **Hajo Götze** und **Sabine Schmidt**.

Many thanks to **Tabea Altenbernd** and **Graeme Eagles** for proofreading my manuscripts and improving the content and grammar. An additional thank goes to **Kerstin Kretschmer** for proofreading this thesis.

Thanks go to **Maren Vormann** and **Claudia Schimschal** for the discussions and sharing the same problems in the first 2 1/2 years.

Special thanks to the Digga-Nigga everything service company and the gentlemen's club with its permanent members **Jude Castelino** and **Max Fischer**. Furthermore thanks to the lunch crew for all the great off-topic drivel.

Thanks to all people of the **geophysics section** and the **badminton team** for trying to understand my Saxonian accent and the nice time in Bremerhaven.

Thanks to my **family** for the by now 30 years support! Especially at the beginning ;)

LINDA – Nothing better could happen to me than you.

Appendix A

Example of a parameter file for the generation of synthetic FD OBS-seismograms with SOFI2D

Modified output of a calculation with the following parameters is shown in Figure 4.9. A general explanation of the parameters can be found in [Bohlen et al. \(2015b\)](#). An explanation of the used values for the generation of the synthetic OBS-seismograms is given in section 4.4.2.

```
#-----  
# JSON PARAMETER FILE FOR SOFI2D  
#-----  
# description:  
# description/name of the model: Profile 20140010 station 22 model 7.0  
#  
  
{  
"Domain Decomposition" : "comment",  
  "NPROCX" : "4",  
  "NPROCY" : "4",  
  
"FD order" : "comment",  
  "FDORDER" : "4",  
  "MAXRELEROR" : "1",  
  
"2-D Grid" : "comment",  
  "NX" : "15000",  
  "NY" : "1400",
```

"DH" : "25",

"Time Stepping" : "comment",
"TIME" : "30.00",
"DT" : "0.001",

"Source" : "comment",
"SOURCE_SHAPE" : "1",
"SOURCE_SHAPE values: ricker=1;fumue=2;from_SIGNAL_FILE=3;SIN**3=
4" : "comment",
"SIGNAL_FILE" : "signal_mseis.tz",

"SOURCE_TYPE" : "1",
"SOURCE_TYPE values (point_source): explosive=1;force_in_x=2;force_in_y=
3;custom_force=4" : "comment",

"SRCREC" : "1",
"SRCREC values : read from SOURCE_FILE=1, PLANE_WAVE=2 (internal)" :
"comment",

"SOURCE_FILE" : "./sources/source_20140010_obs22.dat",
"RUN_MULTIPLE_SHOTS" : "0",

"PLANE_WAVE_DEPTH" : "0.0",
"PLANE_WAVE_ANGLE" : "0.0",
"TS" : "0.2",

"Model" : "comment",
"READMOD" : "1",
"MFILE" : "model/20140010_70_rev",
"WRITE_MODELFILES" : "2",

"Q-approximation" : "comment",
"L" : "1",
"FL1" : "5.0",

```
"TAU" : "0.00001",

"Boundary Conditions" : "comment",
"FREE_SURF" : "1",
"BOUNDARY" : "0",

"FW" : "10",
"ABS_TYPE" : "1",
"ABS_TYPE values : CPML-Boundary=1; Damping-Boundary=2" :
"comment",

"Parameter for CPML (ABS_TYPE=1)" : "comment",
"NPOWER" : "4.0",
"K_MAX_CPML" : "1.0",
"VPPML" : "8100.0",
"FPML" : "5.0",

"Parameter for ABS_TYPE=2" : "comment",
"DAMPING" : "8.0",

"Snapshots" : "comment",
"SNAP" : "2",
"TSNAP1" : "1e-3",
"TSNAP2" : "30.00",
"TSNAPINC" : "0.5",
"IDX" : "2",
"IDY" : "2",
"SNAP_FORMAT" : "2",
"SNAP_FILE" : "./snap/obs22ch1_30s_visco_70_rev",

"Receiver" : "comment",
"SEISMO" : "2",
"READREC" : "0",
"REC_FILE" : "./receiver/receiver_20140010.dat",
"REFRECX, REFRECY" : "0.0 , 0.0",
```

"XREC1,YREC1" : "0.0 , 50.0",
"XREC2,YREC2" : "375000.0 , 50.0",
"NGEOPH" : "6",

"Receiver array" : "comment",
"REC_ARRAY" : "0",
"REC_ARRAY_DEPTH" : "50.0",
"REC_ARRAY_DIST" : "150.0",
"DRX" : "6",

"Seismograms" : "comment",
"NDT" : "1",
"SEIS_FORMAT" : "1",
"SEIS_FILE" : "./su/obs22ch1_30s_visco_70_rev",

"Monitoring the simulation" : "comment",
"LOG_FILE" : "log/obs22ch1_30s_visco_70_rev",
"LOG" : "1",
"OUT_TIMESTEP_INFO" : "10000",

"Checkpoints" : "comment",
"CHECKPTREAD" : "0",
"CHECKPTWRITE" : "0",
"CHECKPT_FILE" : "tmp/checkpoint_sofi2D_model_7.0"

Appendix B

OBS stations of profile AWI-20140010 and ray tracing results

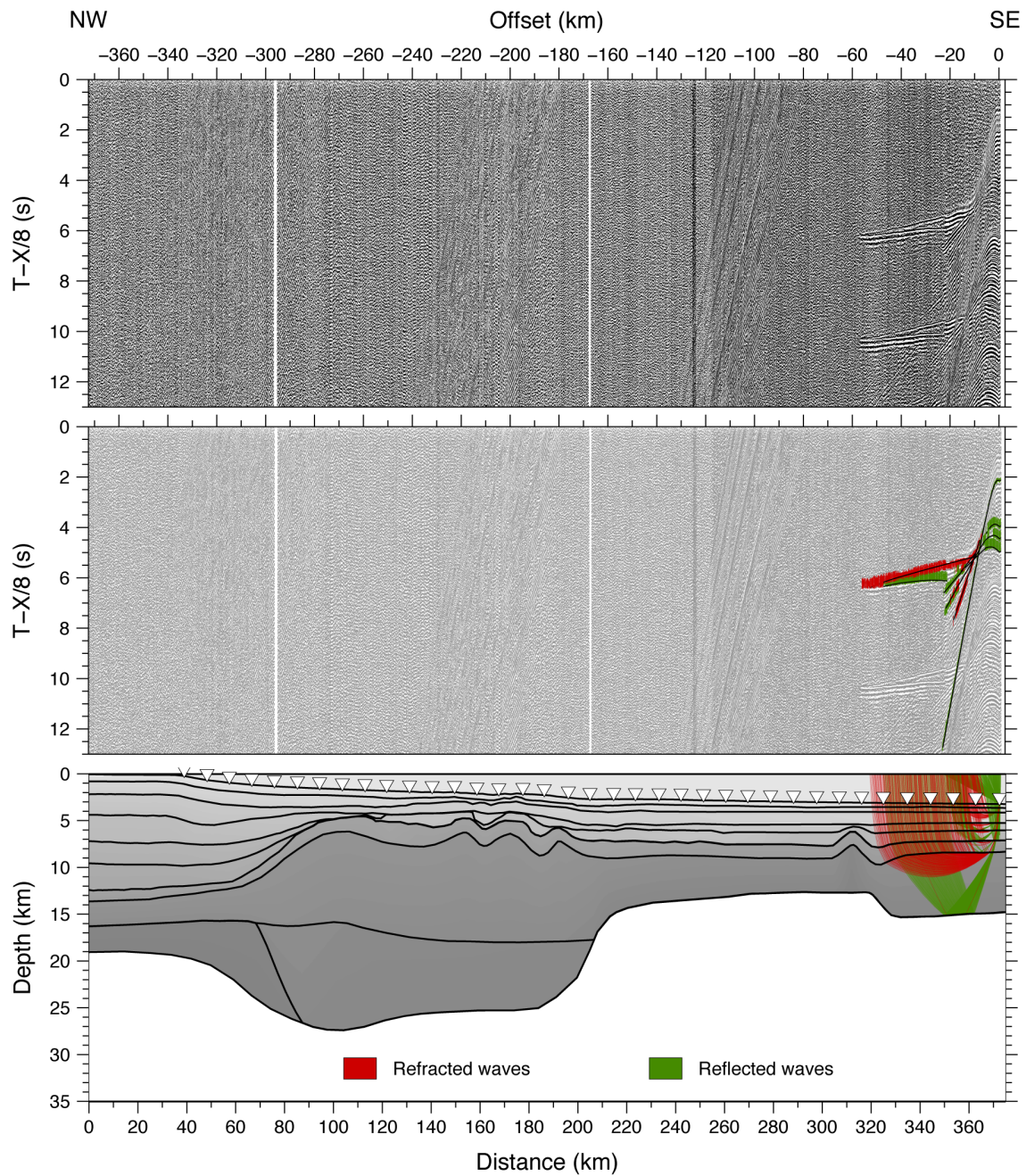


Figure B.1: Seismic section of OBS 11 (hydrophone channel) with a bandpass filter of 4-13.5 Hz (upper panel). A reduction velocity of 8 km/s is applied to the travel time. In the middle panel, picked phases are shown as error bars. Refracted arrivals are plotted in red, reflected arrivals in green. Modelled arrivals are displayed as black lines. Lower panel shows the modelled ray paths for the picks presented in the middle panel.

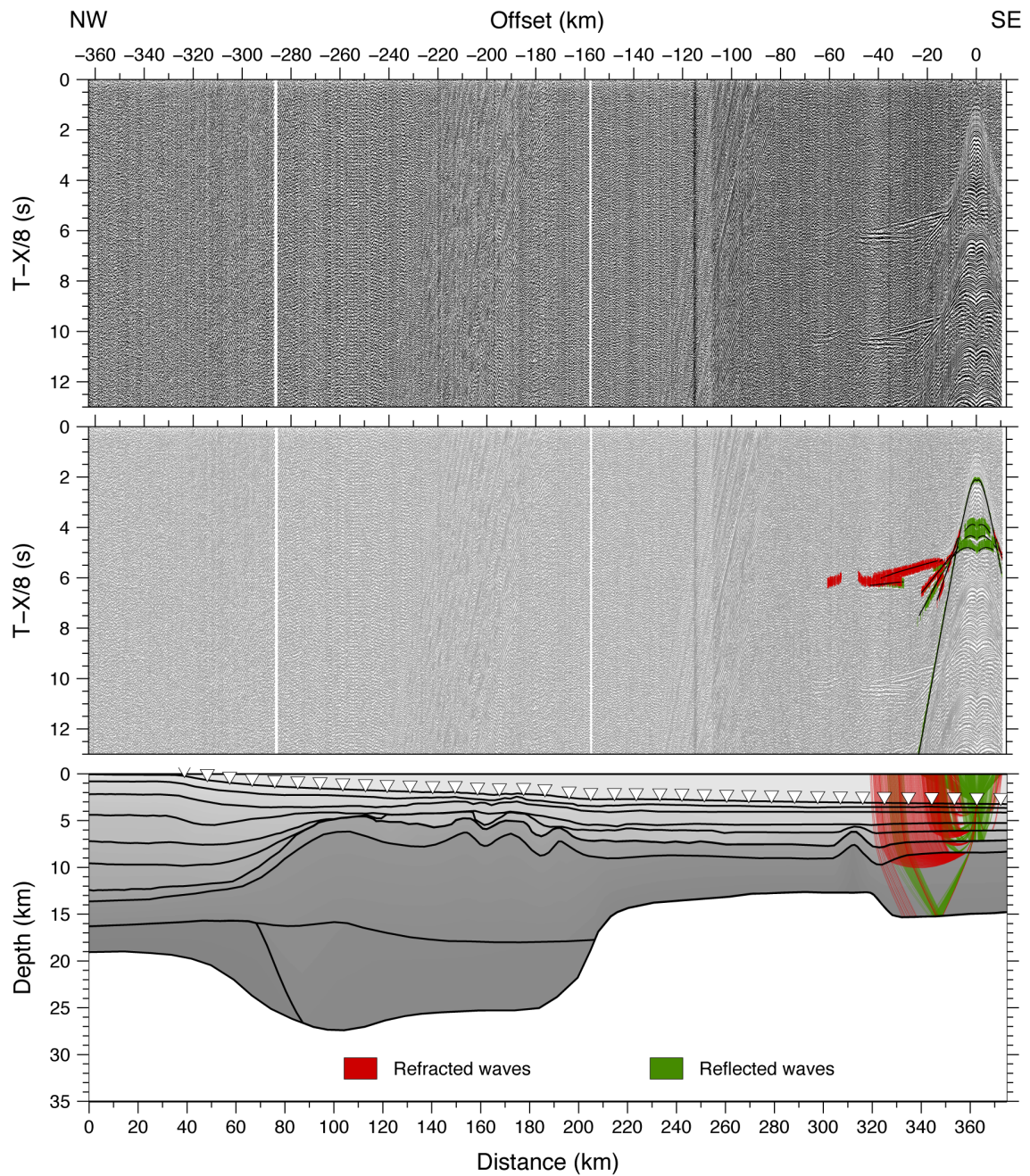


Figure B.2: Seismic section of OBS 12 (hydrophone channel) with a bandpass filter of 4-13.5 Hz (upper panel). A reduction velocity of 8 km/s is applied to the travel time. In the middle panel, picked phases are shown as error bars. Refracted arrivals are plotted in red, reflected arrivals in green. Modelled arrivals are displayed as black lines. Lower panel shows the modelled ray paths for the picks presented in the middle panel.

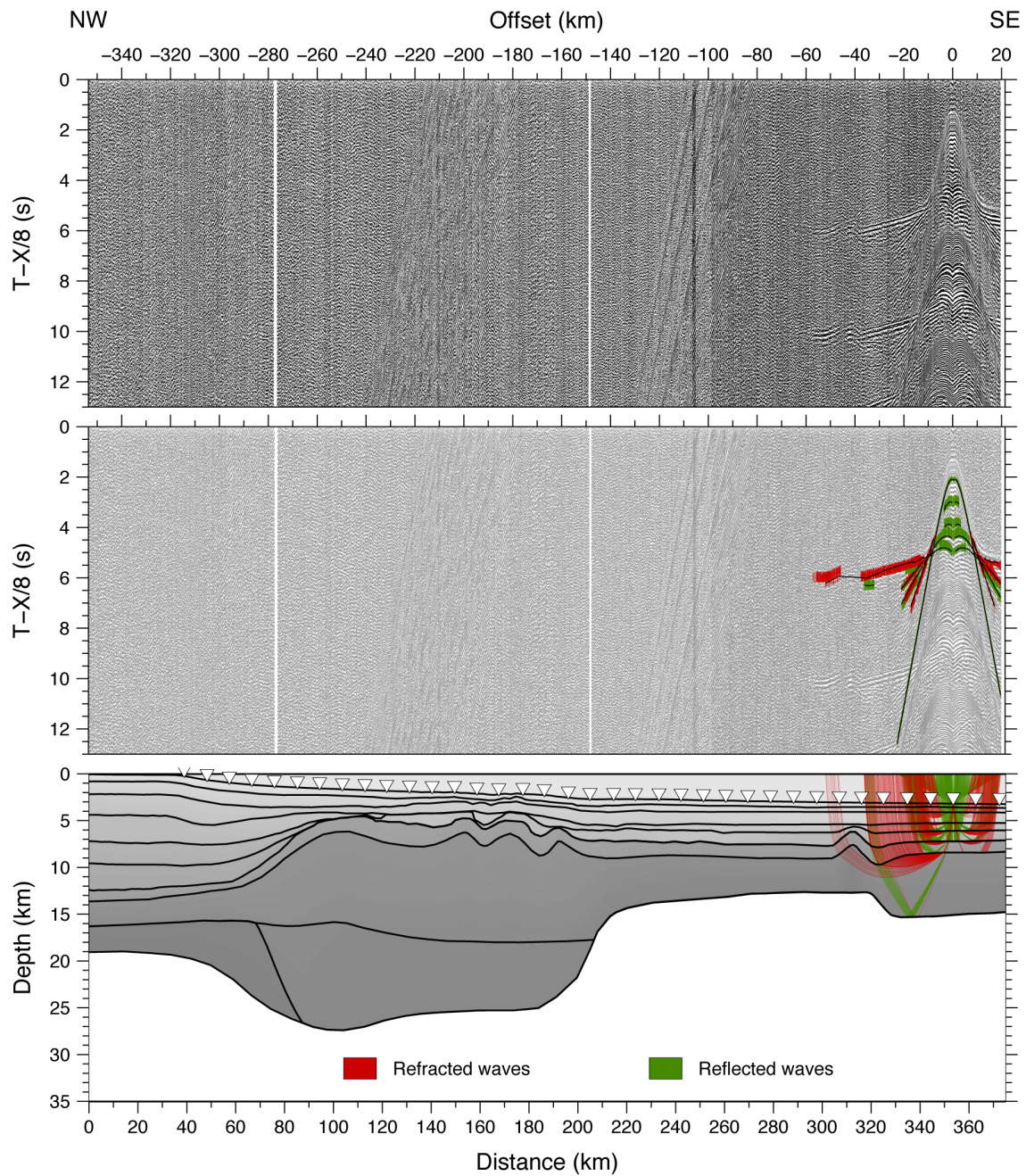


Figure B.3: Seismic section of OBS 13 (hydrophone channel) with a bandpass filter of 4-13.5 Hz (upper panel). A reduction velocity of 8 km/s is applied to the travel time. In the middle panel, picked phases are shown as error bars. Refracted arrivals are plotted in red, reflected arrivals in green. Modelled arrivals are displayed as black lines. Lower panel shows the modelled ray paths for the picks presented in the middle panel.

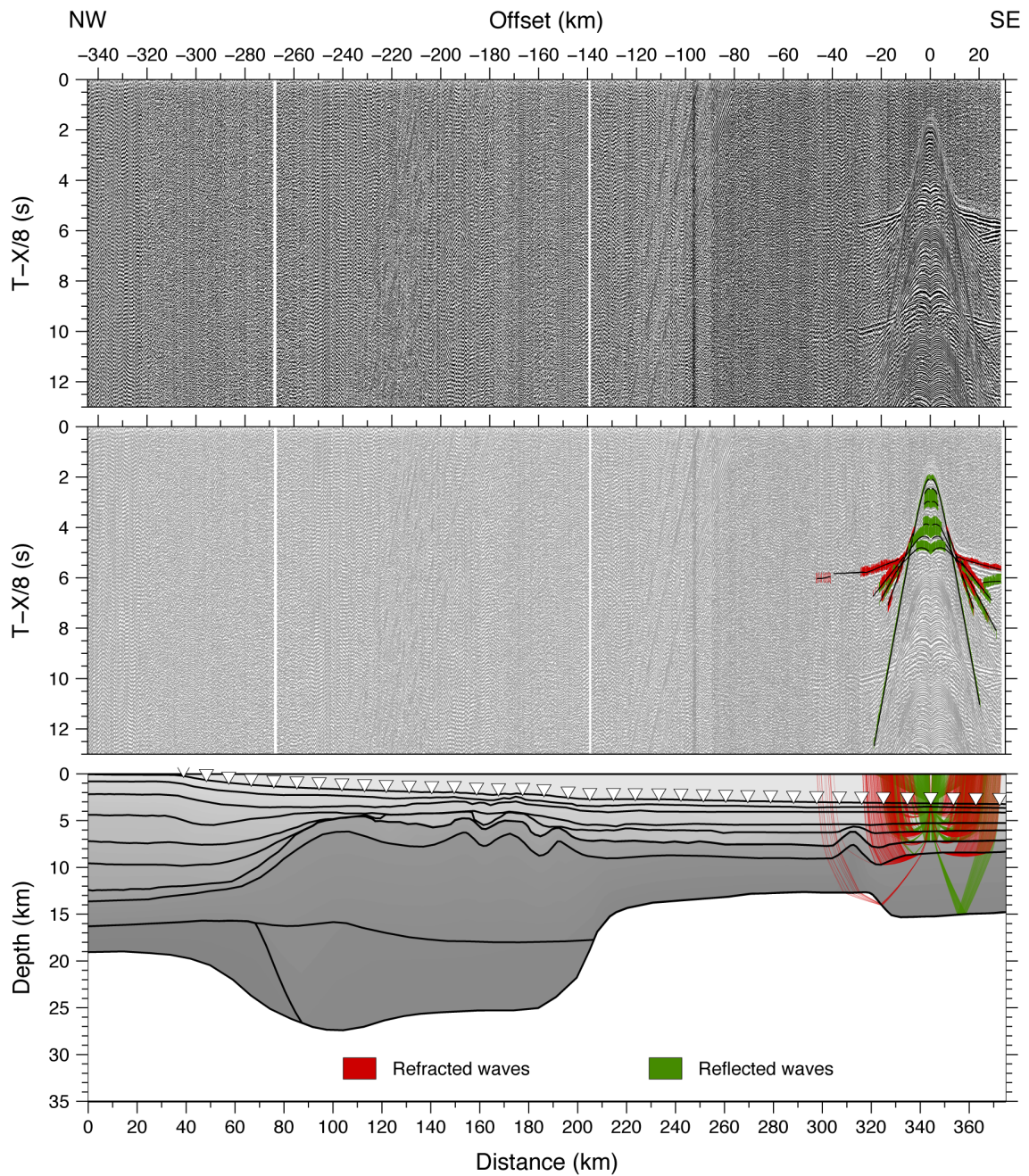


Figure B.4: Seismic section of OBS 14 (hydrophone channel) with a bandpass filter of 4-13.5 Hz (upper panel). A reduction velocity of 8 km/s is applied to the travel time. In the middle panel, picked phases are shown as error bars. Refracted arrivals are plotted in red, reflected arrivals in green. Modelled arrivals are displayed as black lines. Lower panel shows the modelled ray paths for the picks presented in the middle panel.

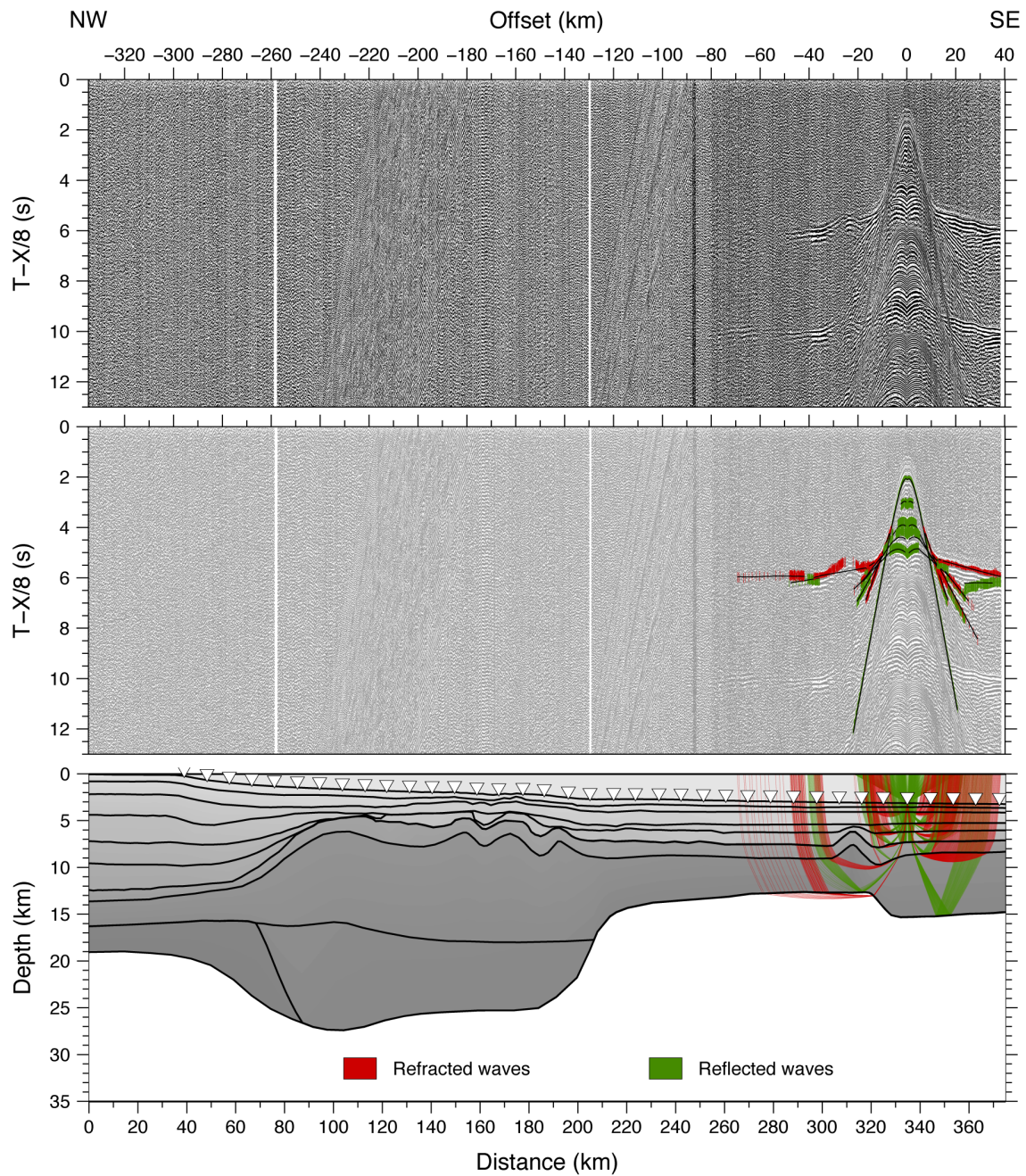


Figure B.5: Seismic section of OBS 15 (hydrophone channel) with a bandpass filter of 4-13.5 Hz (upper panel). A reduction velocity of 8 km/s is applied to the travel time. In the middle panel, picked phases are shown as error bars. Refracted arrivals are plotted in red, reflected arrivals in green. Modelled arrivals are displayed as black lines. Lower panel shows the modelled ray paths for the picks presented in the middle panel.

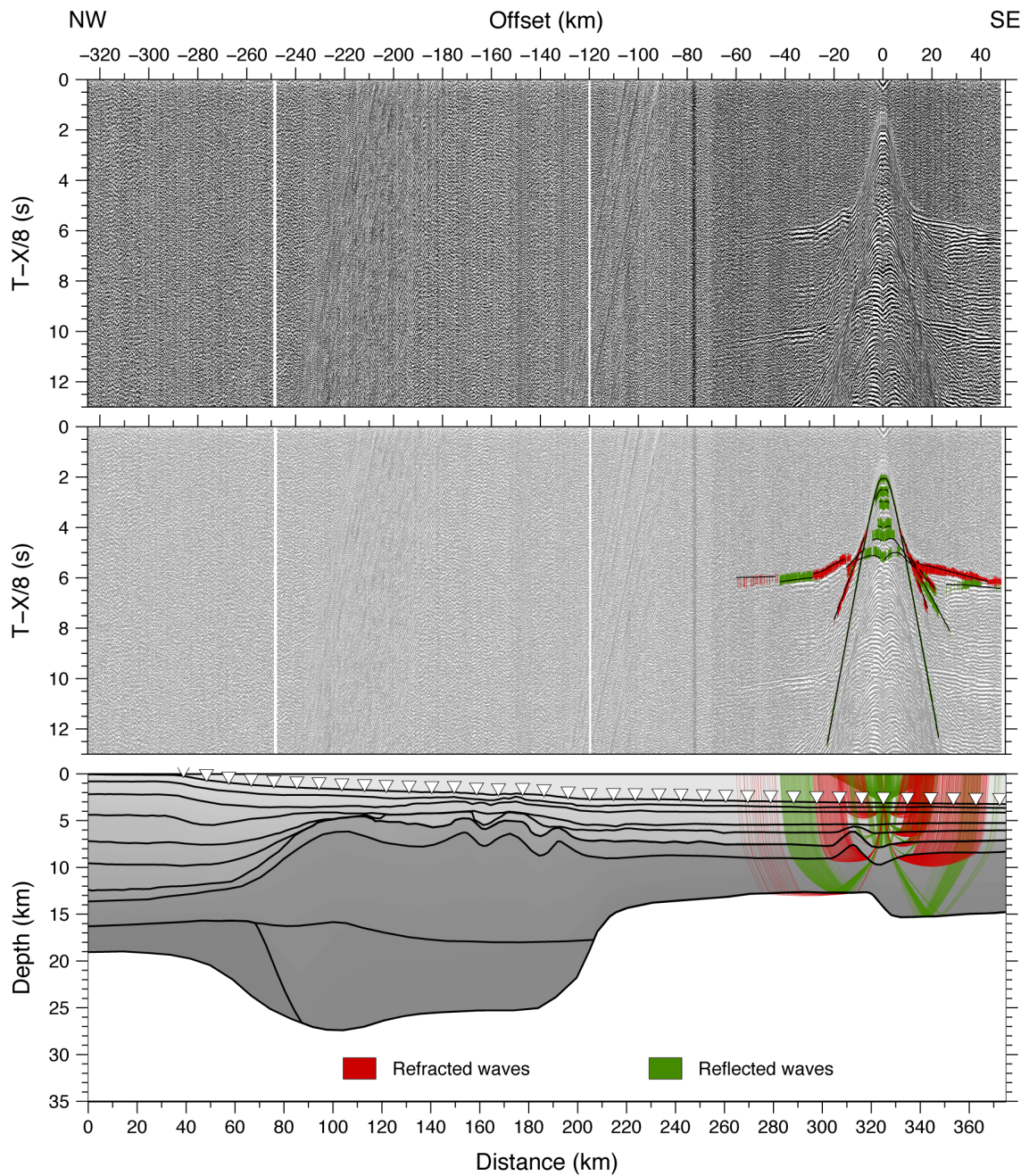


Figure B.6: Seismic section of OBS 16 (hydrophone channel) with a bandpass filter of 4-13.5 Hz (upper panel). A reduction velocity of 8 km/s is applied to the travel time. In the middle panel, picked phases are shown as error bars. Refracted arrivals are plotted in red, reflected arrivals in green. Modelled arrivals are displayed as black lines. Lower panel shows the modelled ray paths for the picks presented in the middle panel.

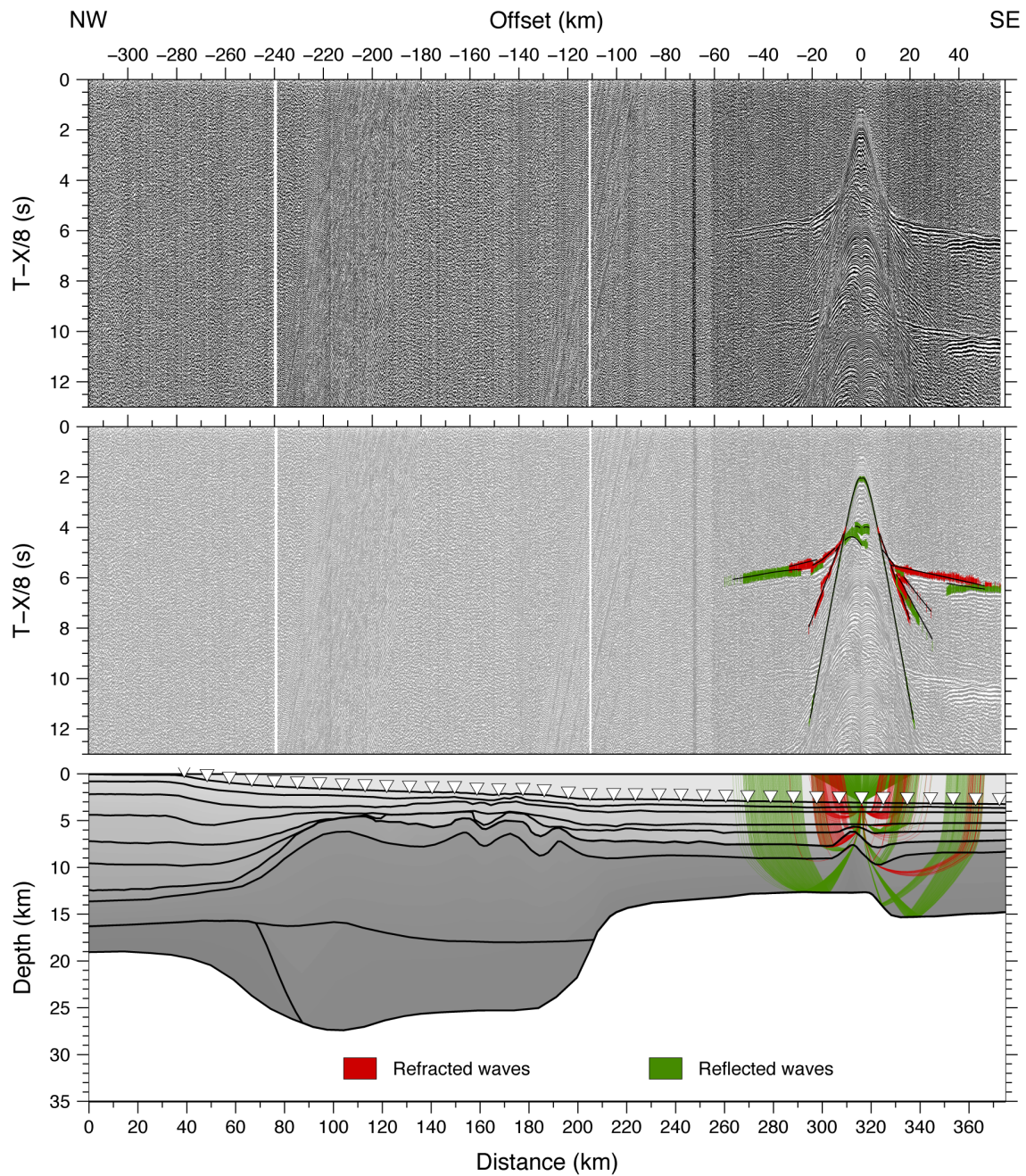


Figure B.7: Seismic section of OBS 17 (hydrophone channel) with a bandpass filter of 4-13.5 Hz (upper panel). A reduction velocity of 8 km/s is applied to the travel time. In the middle panel, picked phases are shown as error bars. Refracted arrivals are plotted in red, reflected arrivals in green. Modelled arrivals are displayed as black lines. Lower panel shows the modelled ray paths for the picks presented in the middle panel.

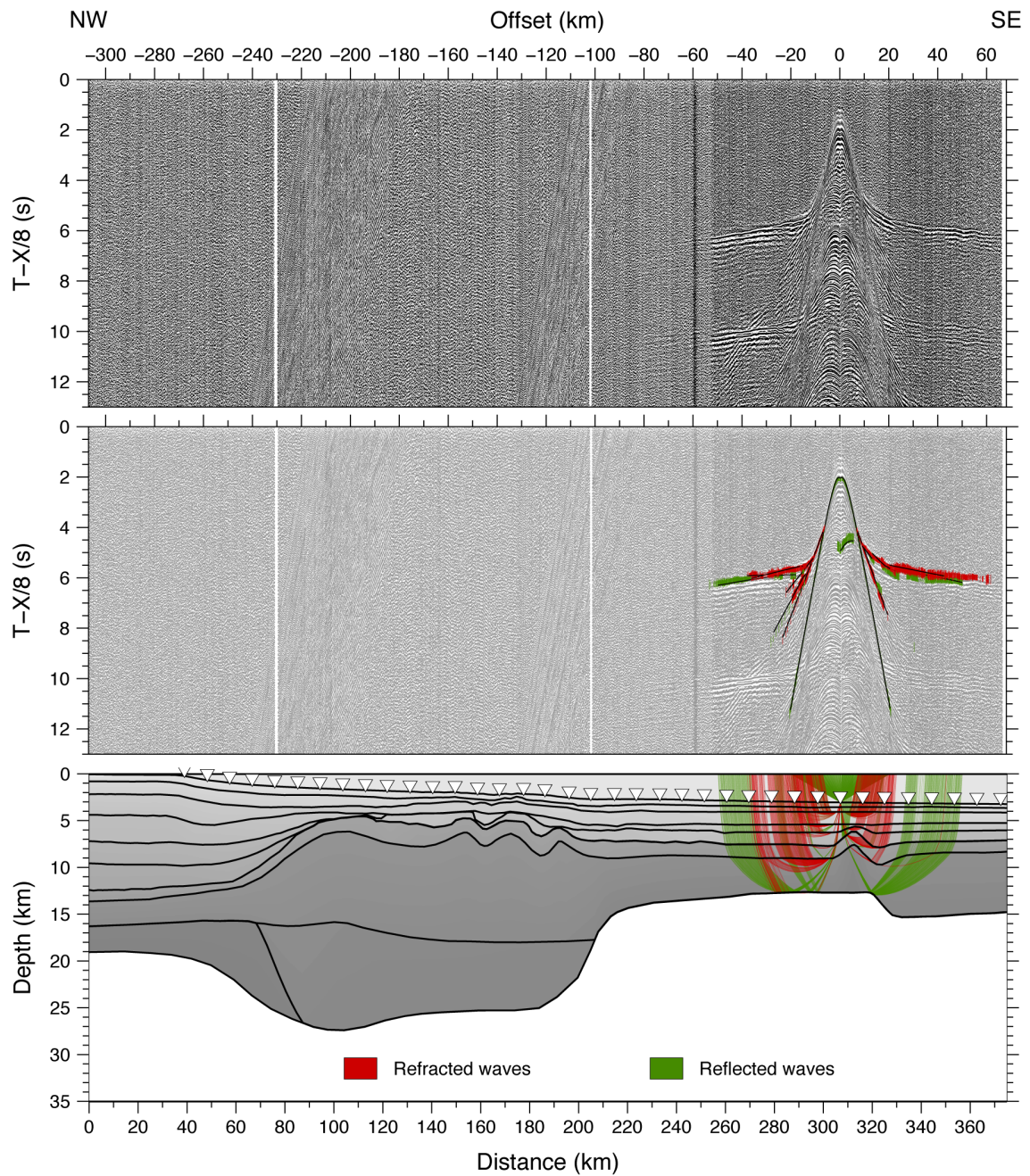


Figure B.8: Seismic section of OBS 18 (hydrophone channel) with a bandpass filter of 4-13.5 Hz (upper panel). A reduction velocity of 8 km/s is applied to the travel time. In the middle panel, picked phases are shown as error bars. Refracted arrivals are plotted in red, reflected arrivals in green. Modelled arrivals are displayed as black lines. Lower panel shows the modelled ray paths for the picks presented in the middle panel.

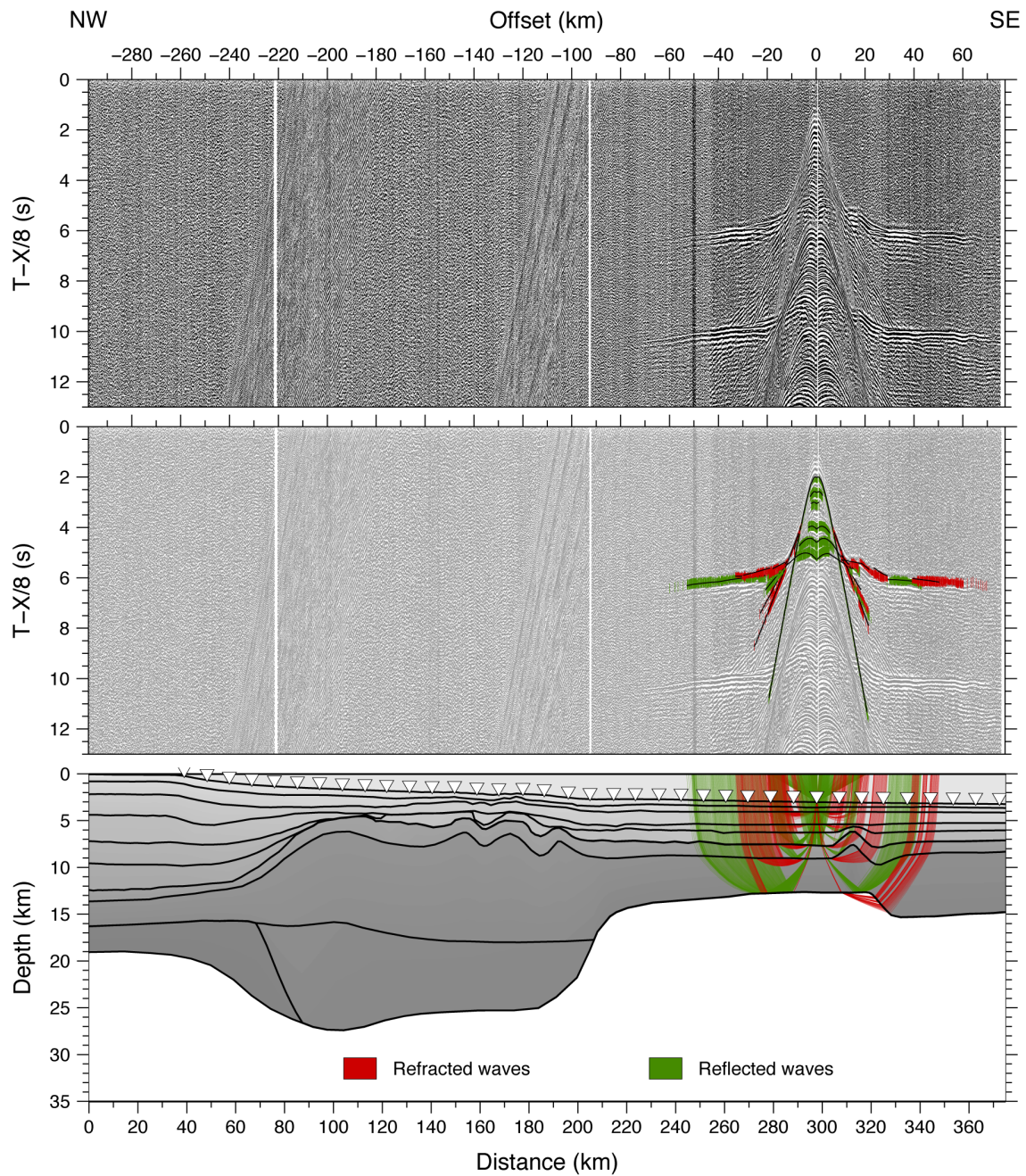


Figure B.9: Seismic section of OBS 19 (hydrophone channel) with a bandpass filter of 4-13.5 Hz (upper panel). A reduction velocity of 8 km/s is applied to the travel time. In the middle panel, picked phases are shown as error bars. Refracted arrivals are plotted in red, reflected arrivals in green. Modelled arrivals are displayed as black lines. Lower panel shows the modelled ray paths for the picks presented in the middle panel.

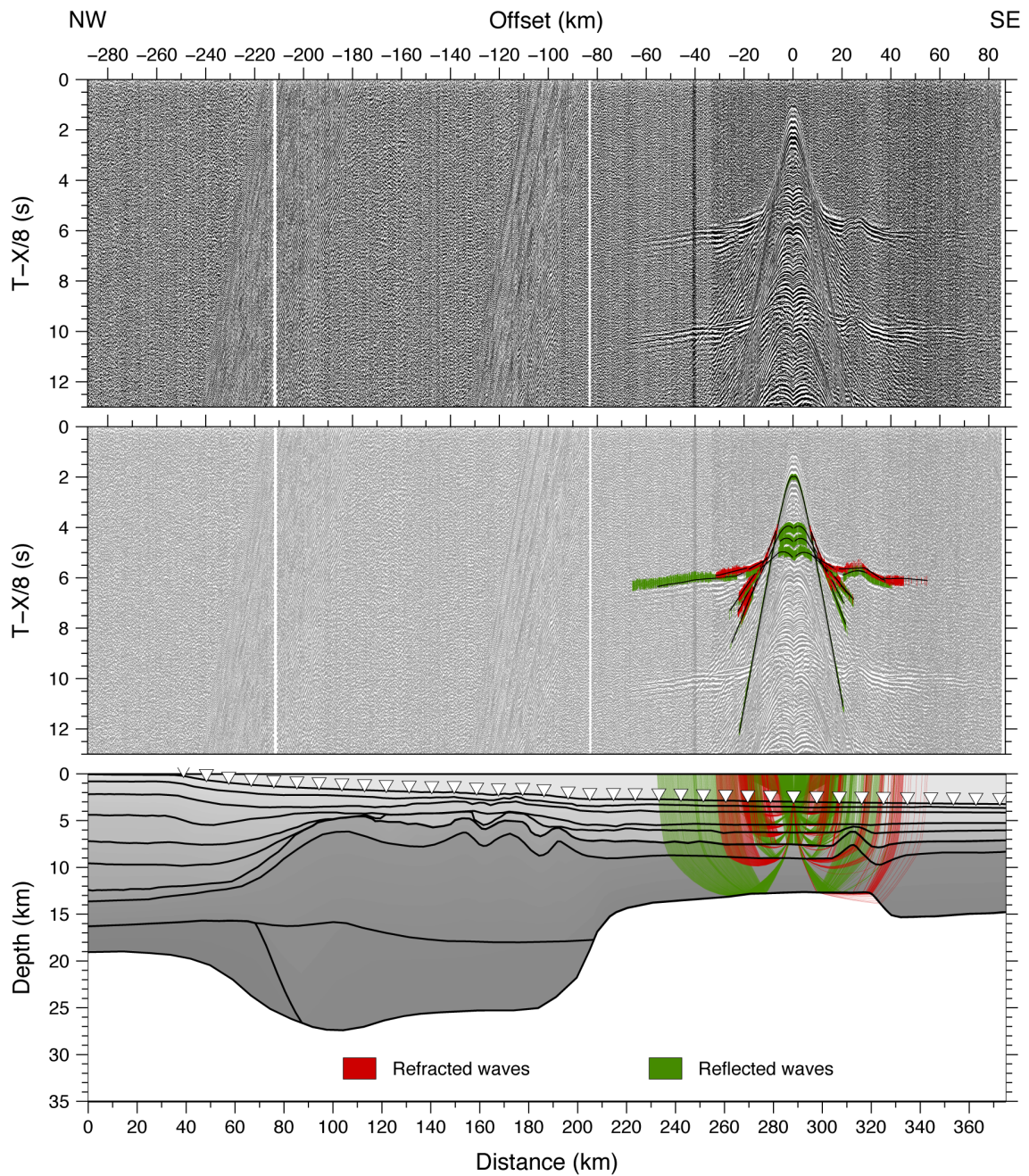


Figure B.10: Seismic section of OBS 20 (hydrophone channel) with a bandpass filter of 4-13.5 Hz (upper panel). A reduction velocity of 8 km/s is applied to the travel time. In the middle panel, picked phases are shown as error bars. Refracted arrivals are plotted in red, reflected arrivals in green. Modelled arrivals are displayed as black lines. Lower panel shows the modelled ray paths for the picks presented in the middle panel.

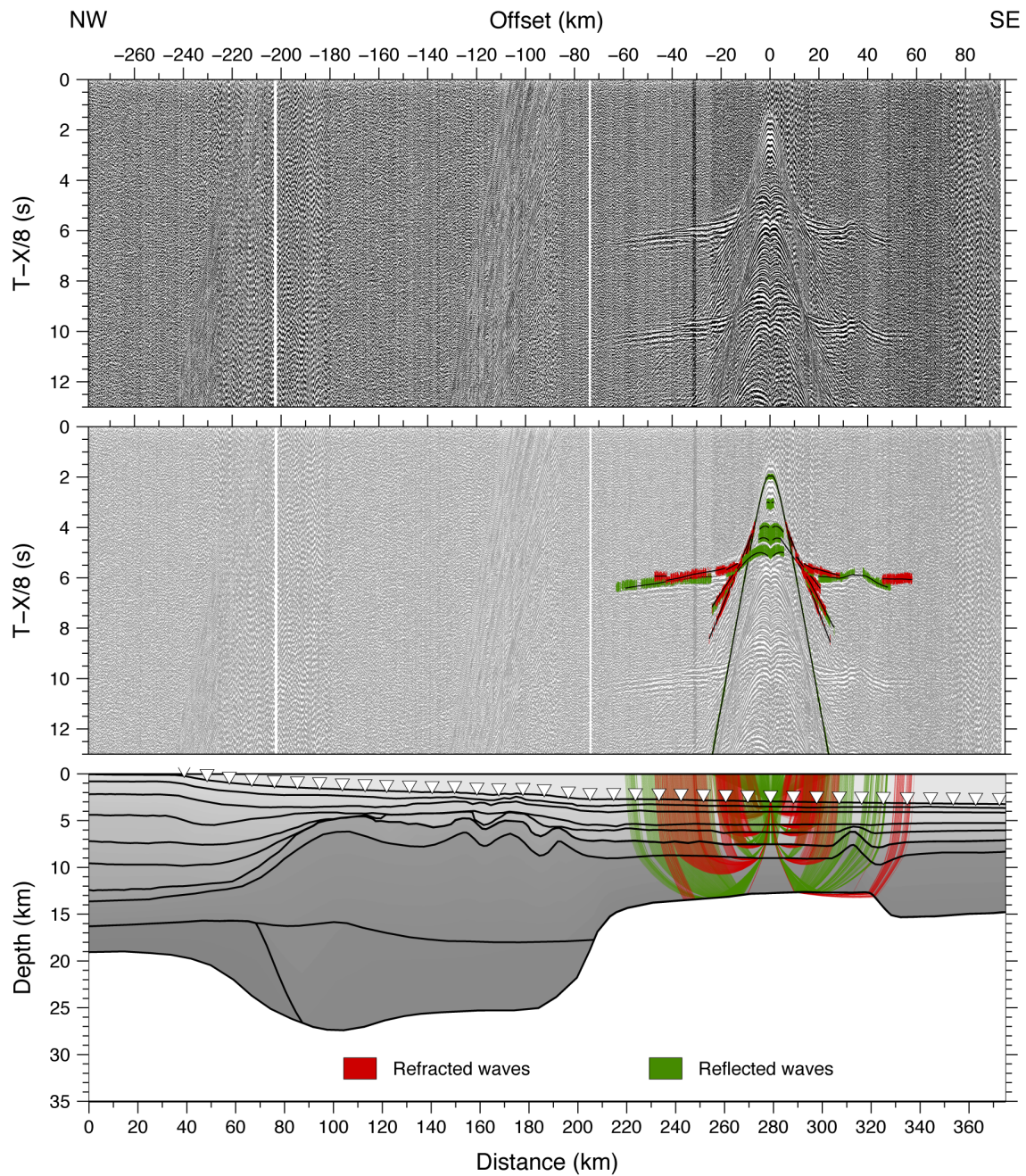


Figure B.11: Seismic section of OBS 21 (hydrophone channel) with a bandpass filter of 4-13.5 Hz (upper panel). A reduction velocity of 8 km/s is applied to the travel time. In the middle panel, picked phases are shown as error bars. Refracted arrivals are plotted in red, reflected arrivals in green. Modelled arrivals are displayed as black lines. Lower panel shows the modelled ray paths for the picks presented in the middle panel.

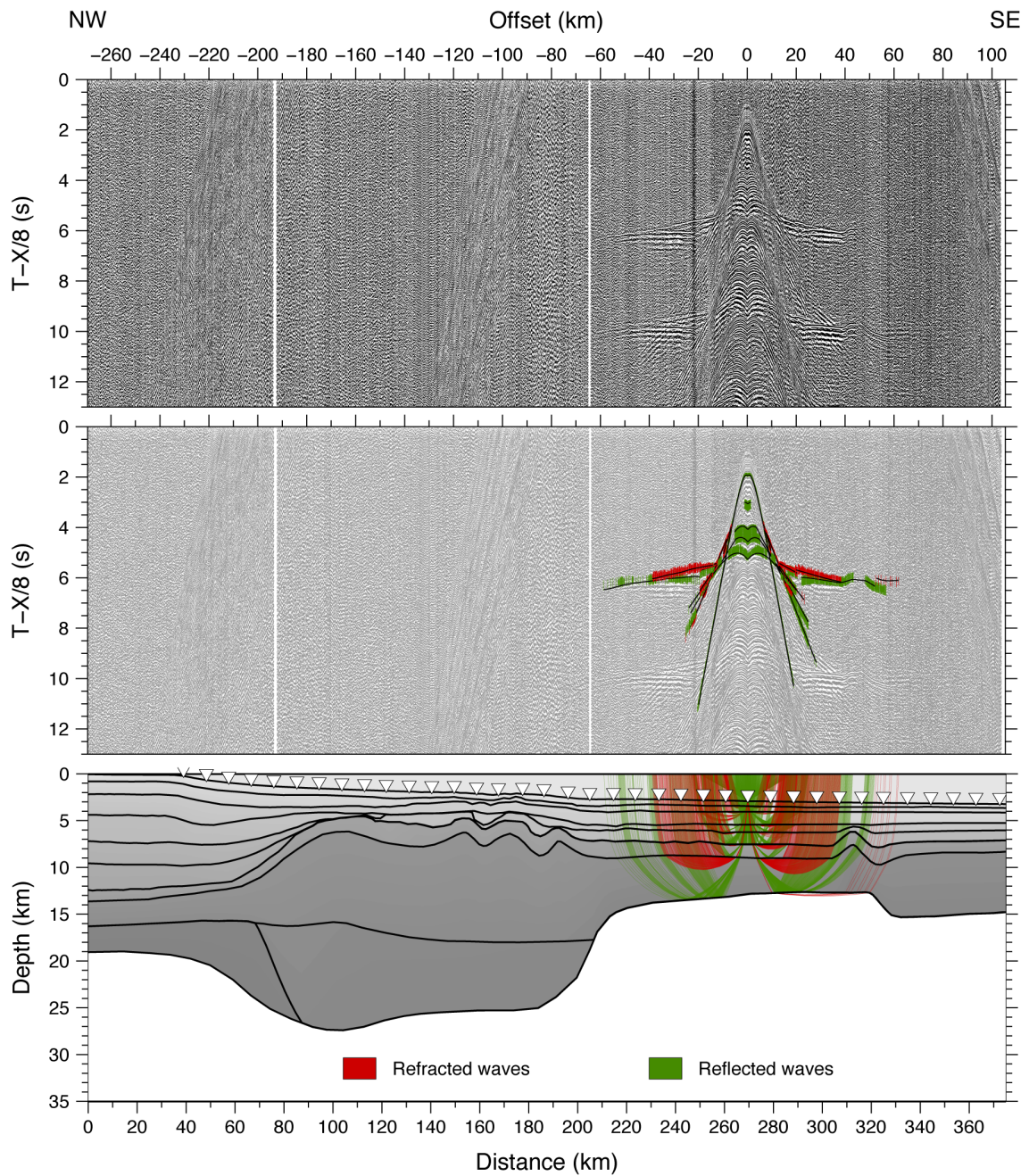


Figure B.12: Seismic section of OBS 22 (hydrophone channel) with a bandpass filter of 4-13.5 Hz (upper panel). A reduction velocity of 8 km/s is applied to the travel time. In the middle panel, picked phases are shown as error bars. Refracted arrivals are plotted in red, reflected arrivals in green. Modelled arrivals are displayed as black lines. Lower panel shows the modelled ray paths for the picks presented in the middle panel.

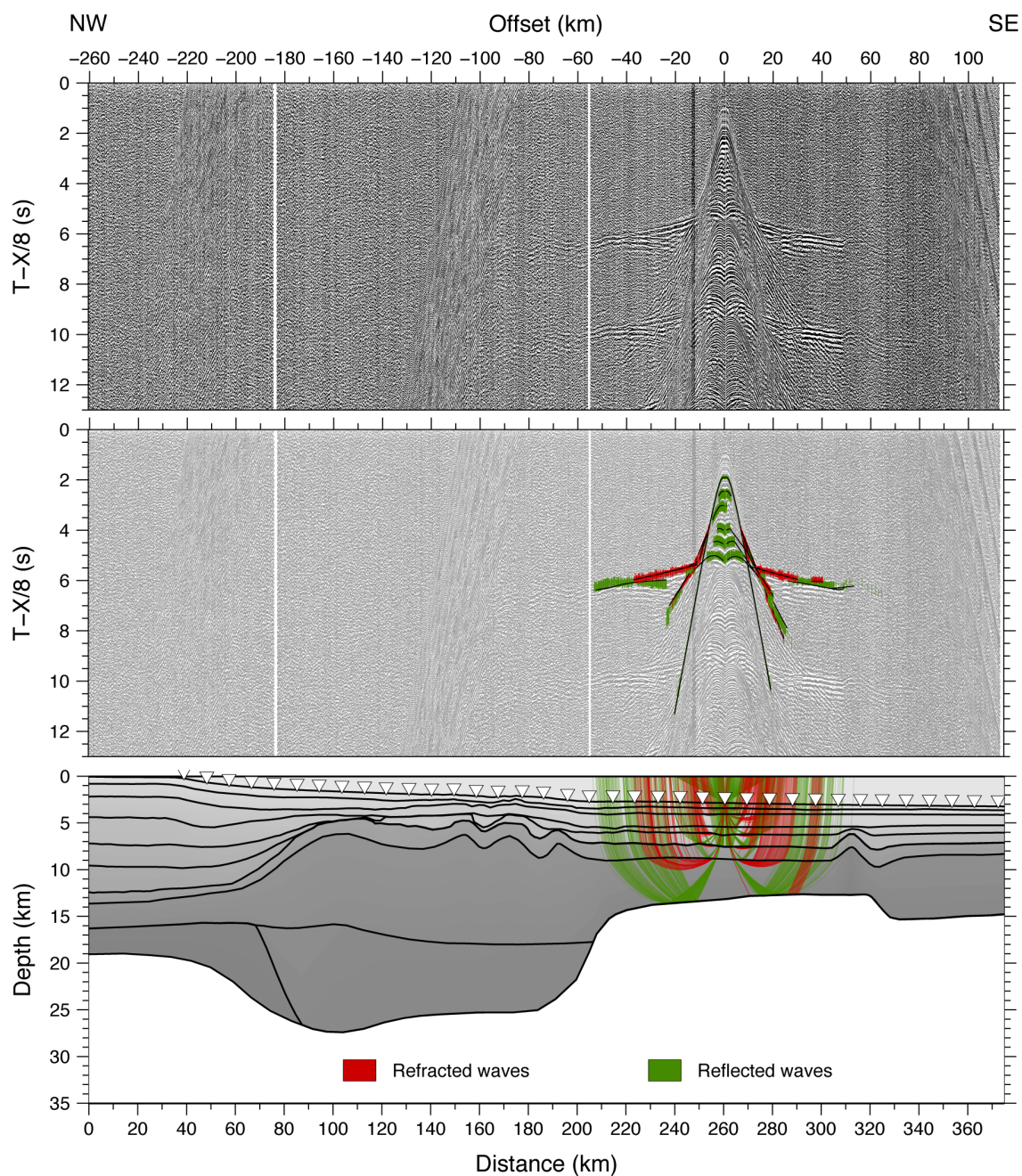


Figure B.13: Seismic section of OBS 23 (hydrophone channel) with a bandpass filter of 4-13.5 Hz (upper panel). A reduction velocity of 8 km/s is applied to the travel time. In the middle panel, picked phases are shown as error bars. Refracted arrivals are plotted in red, reflected arrivals in green. Modelled arrivals are displayed as black lines. Lower panel shows the modelled ray paths for the picks presented in the middle panel.

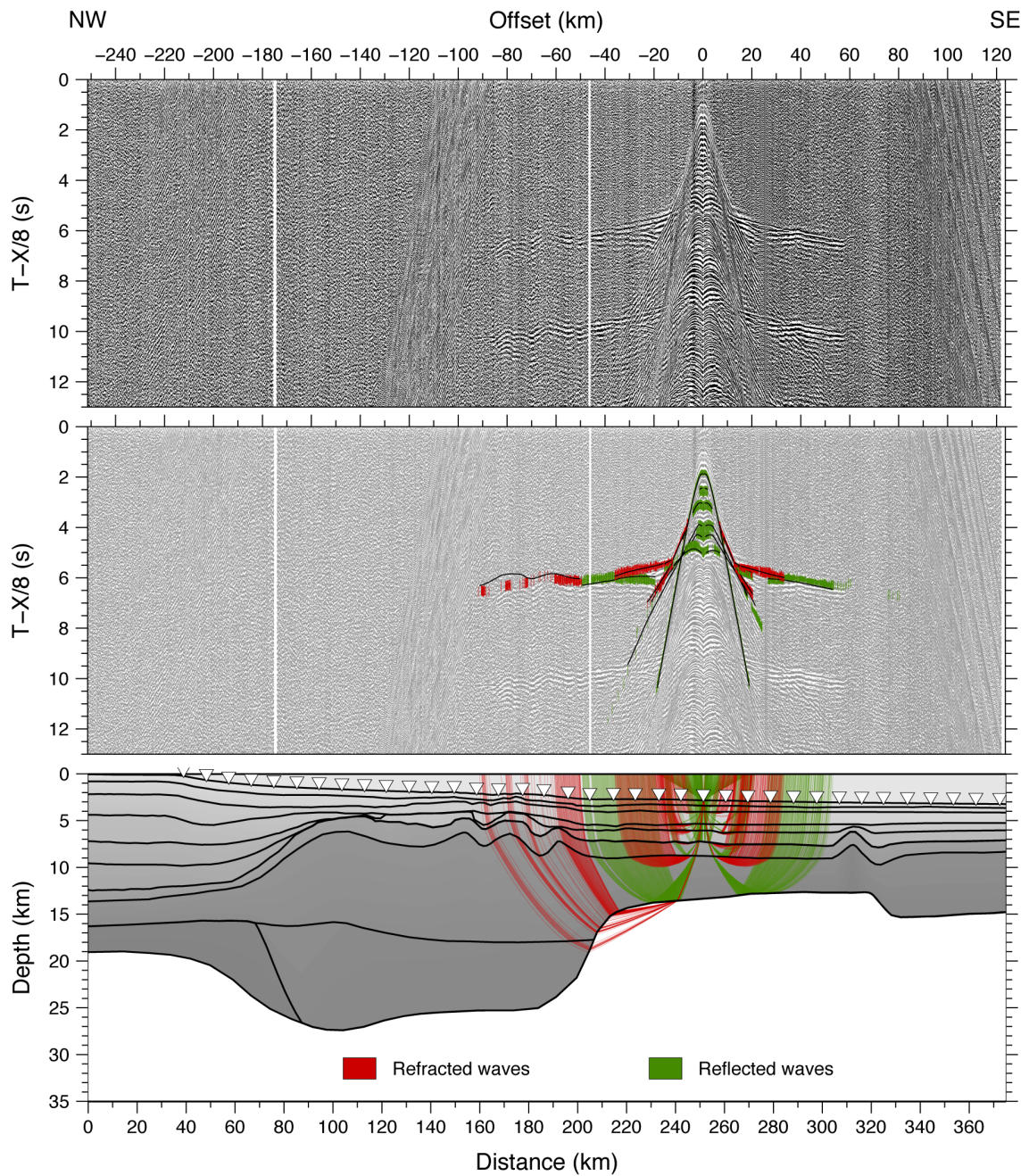


Figure B.14: Seismic section of OBS 24 (hydrophone channel) with a bandpass filter of 4-13.5 Hz (upper panel). A reduction velocity of 8 km/s is applied to the travel time. In the middle panel, picked phases are shown as error bars. Refracted arrivals are plotted in red, reflected arrivals in green. Modelled arrivals are displayed as black lines. Lower panel shows the modelled ray paths for the picks presented in the middle panel.

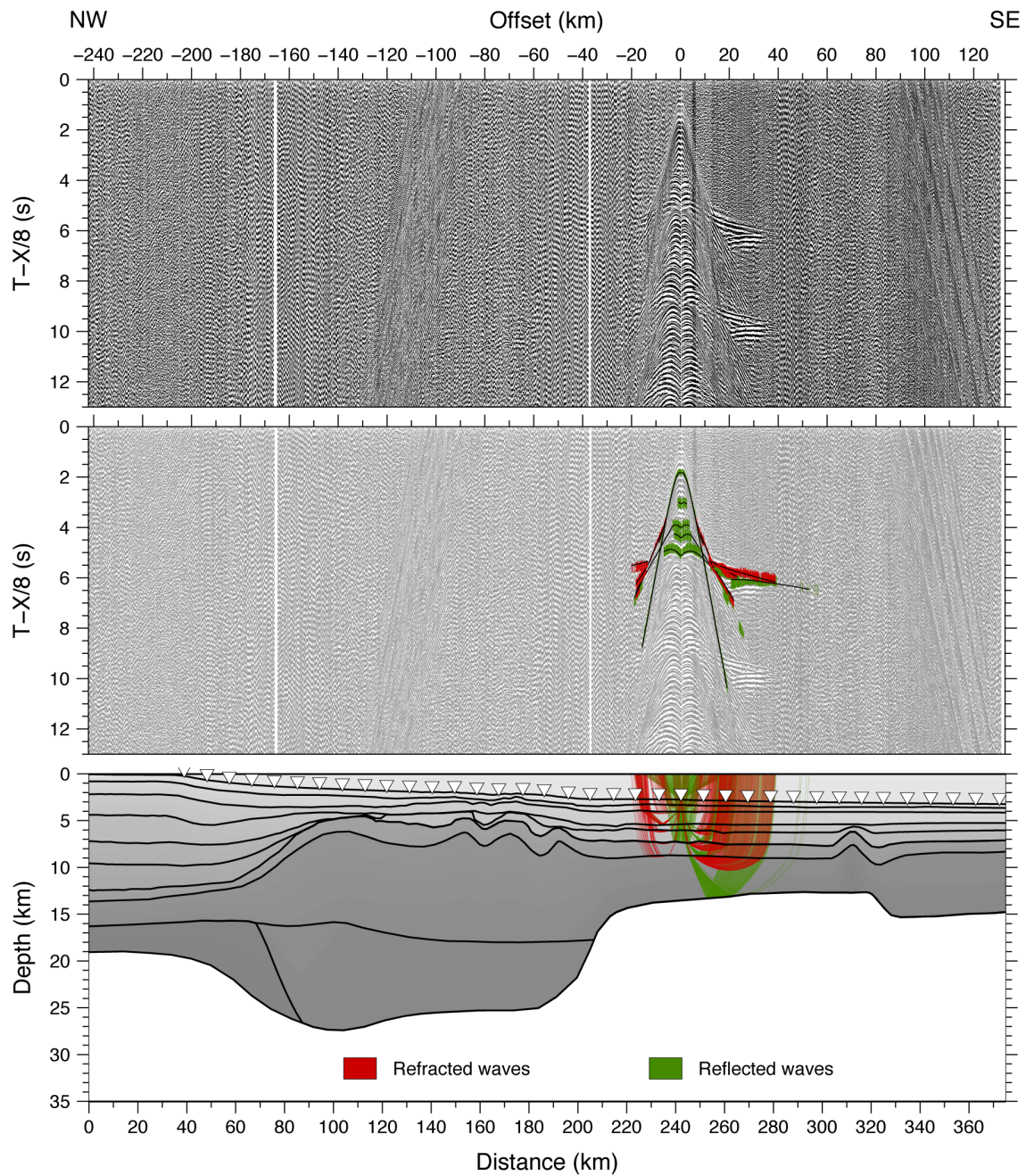


Figure B.15: Seismic section of OBS 25 (hydrophone channel) with a bandpass filter of 4-13.5 Hz (upper panel). A reduction velocity of 8 km/s is applied to the travel time. In the middle panel, picked phases are shown as error bars. Refracted arrivals are plotted in red, reflected arrivals in green. Modelled arrivals are displayed as black lines. Lower panel shows the modelled ray paths for the picks presented in the middle panel.

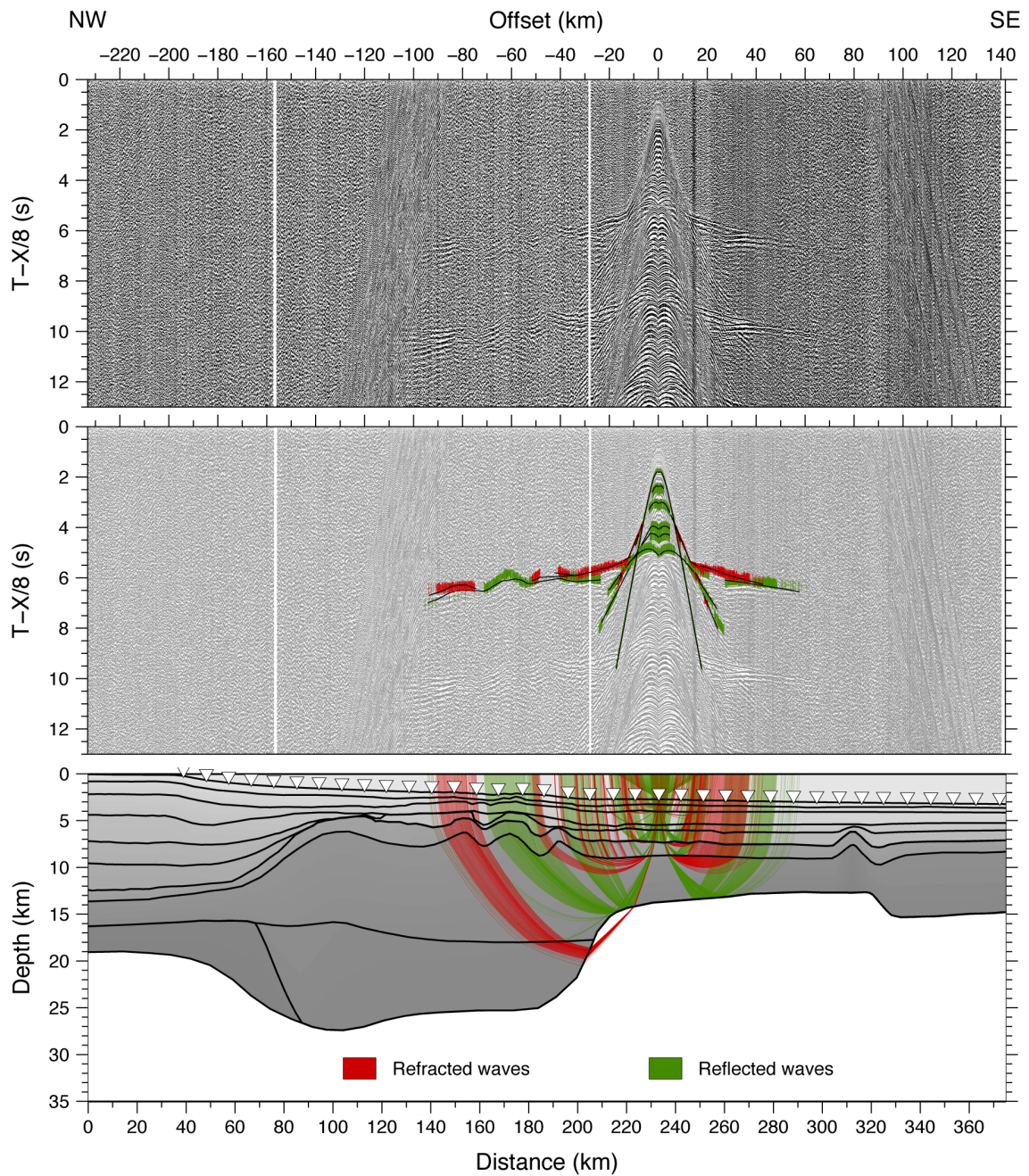


Figure B.16: Seismic section of OBS 26 (hydrophone channel) with a bandpass filter of 4-13.5 Hz (upper panel). A reduction velocity of 8 km/s is applied to the travel time. In the middle panel, picked phases are shown as error bars. Refracted arrivals are plotted in red, reflected arrivals in green. Modelled arrivals are displayed as black lines. Lower panel shows the modelled ray paths for the picks presented in the middle panel.

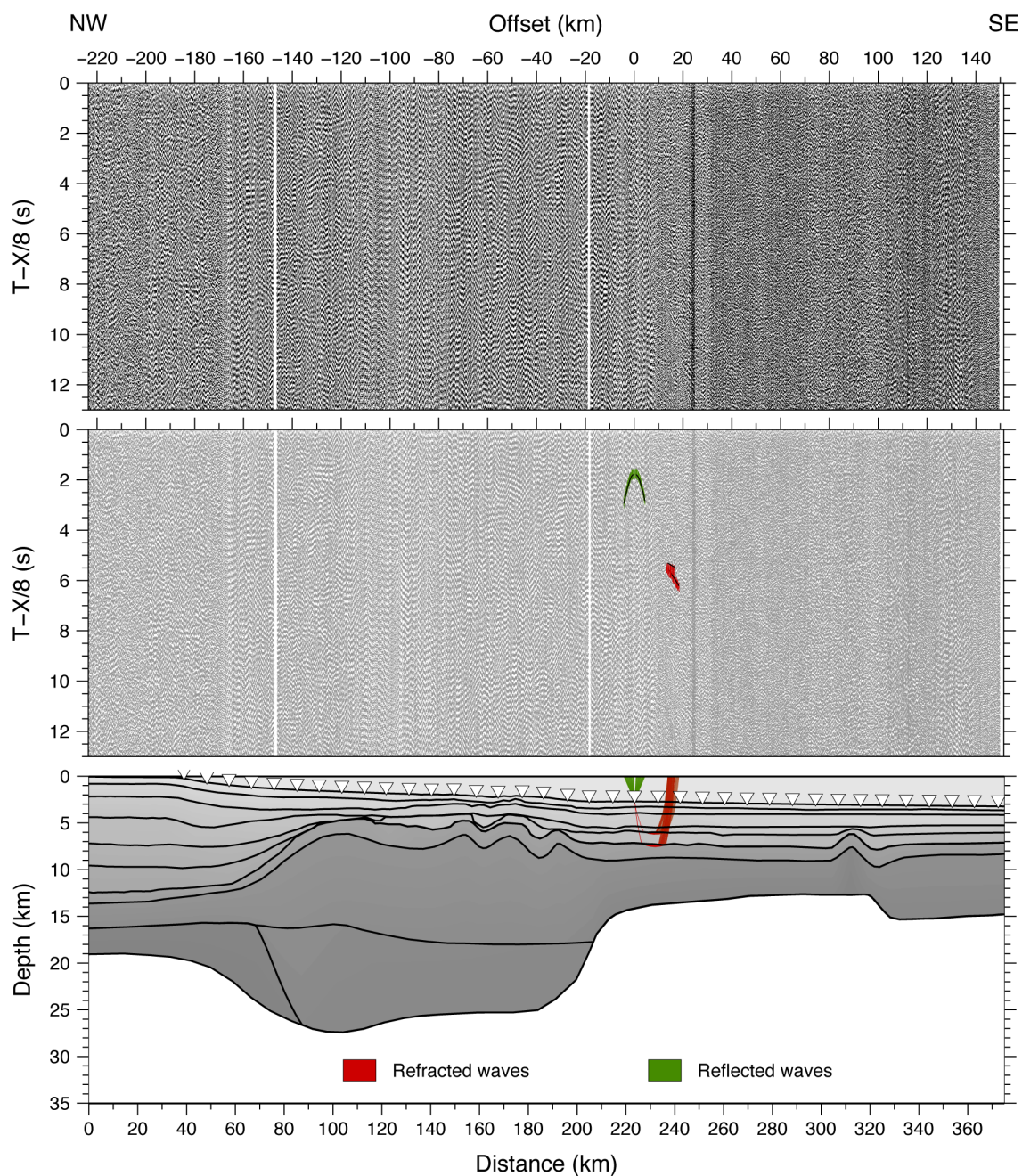


Figure B.17: Seismic section of OBS 27 (hydrophone channel) with a bandpass filter of 4-13.5 Hz (upper panel). A reduction velocity of 8 km/s is applied to the travel time. In the middle panel, picked phases are shown as error bars. Refracted arrivals are plotted in red, reflected arrivals in green. Modelled arrivals are displayed as black lines. Lower panel shows the modelled ray paths for the picks presented in the middle panel.

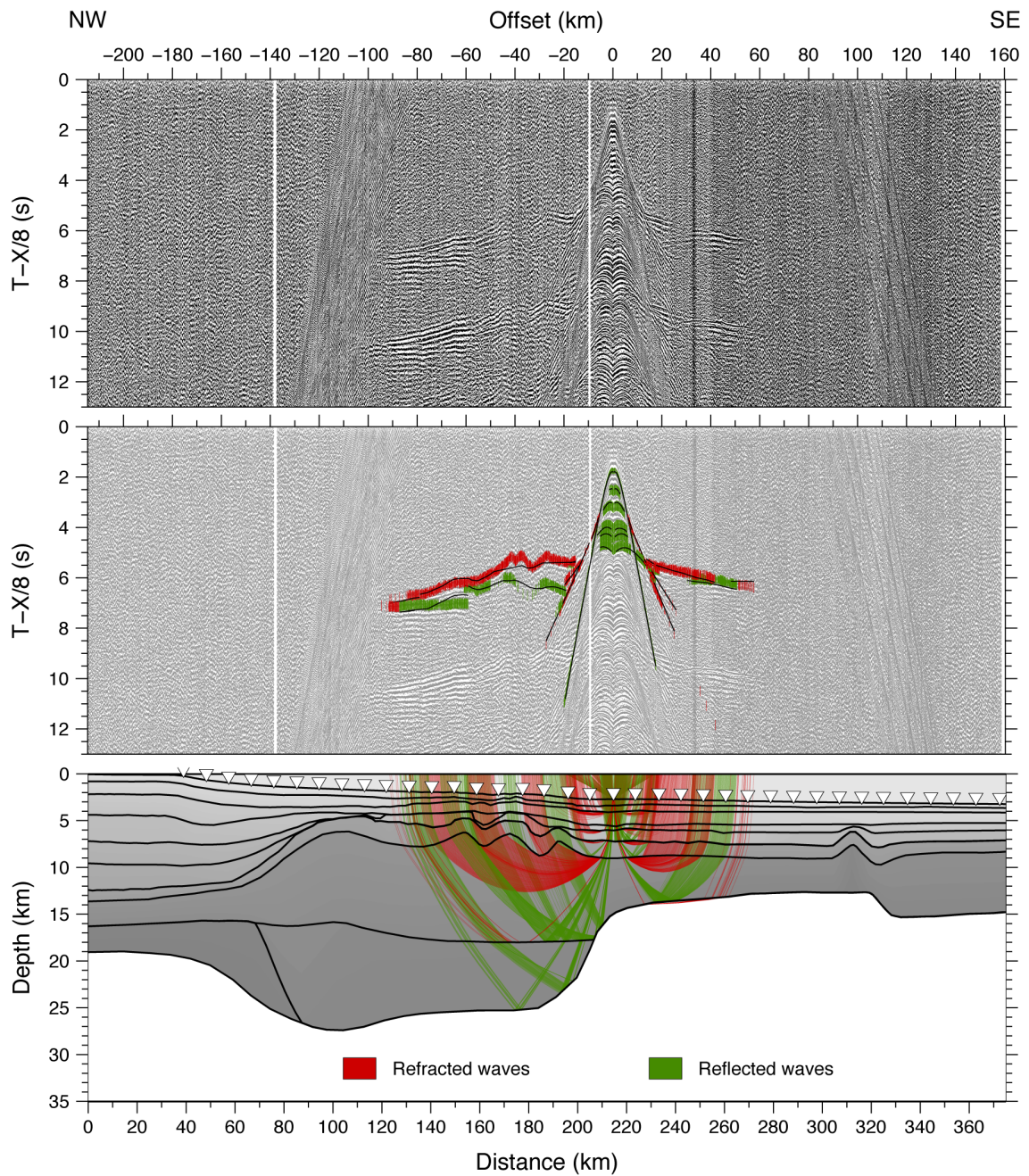


Figure B.18: Seismic section of OBS 28 (hydrophone channel) with a bandpass filter of 4-13.5 Hz (upper panel). A reduction velocity of 8 km/s is applied to the travel time. In the middle panel, picked phases are shown as error bars. Refracted arrivals are plotted in red, reflected arrivals in green. Modelled arrivals are displayed as black lines. Lower panel shows the modelled ray paths for the picks presented in the middle panel.

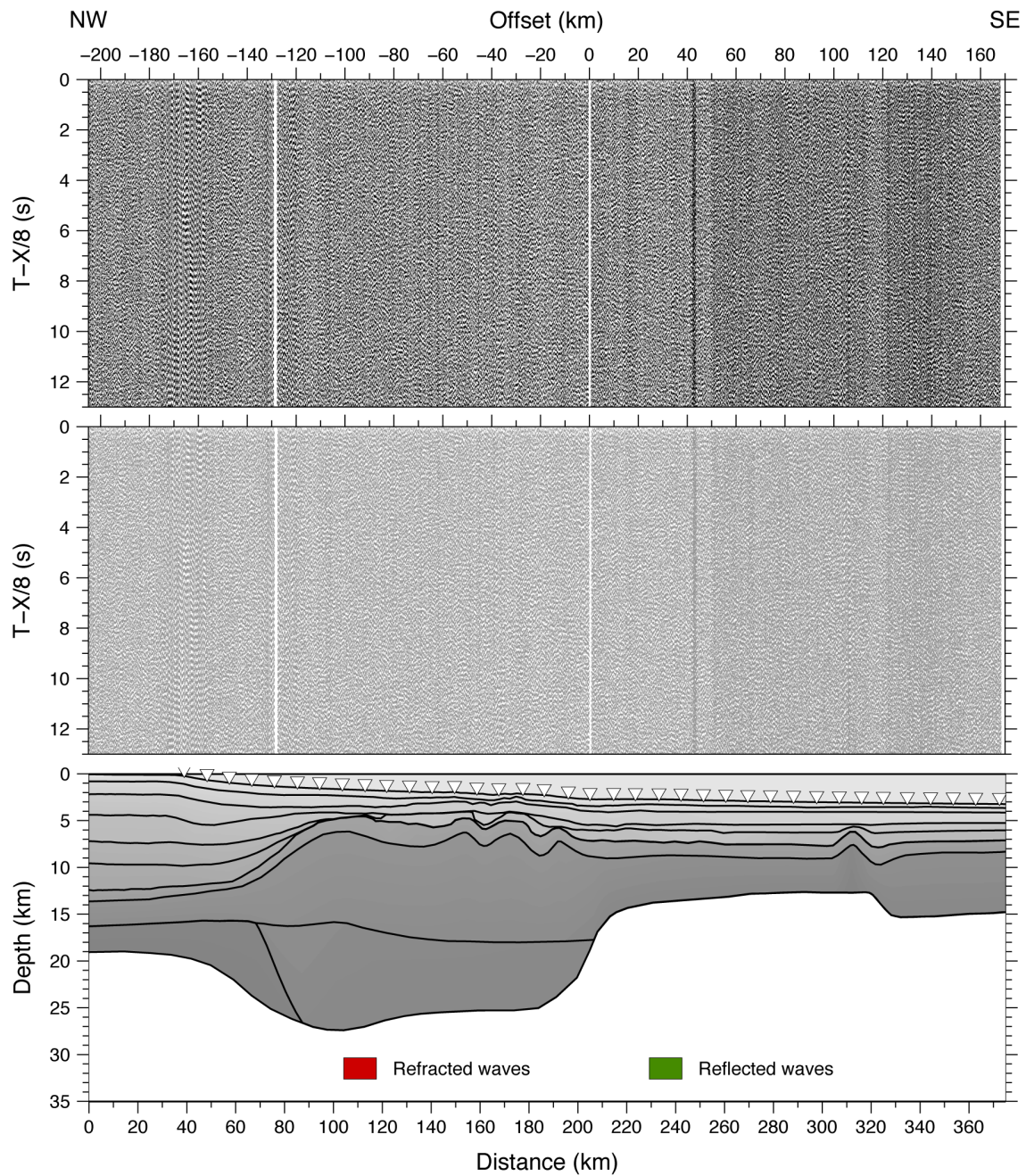


Figure B.19: Seismic section of OBS 29 (hydrophone channel) with a bandpass filter of 4-13.5 Hz (upper panel). A reduction velocity of 8 km/s is applied to the travel time. In the middle panel, picked phases are shown as error bars. Refracted arrivals are plotted in red, reflected arrivals in green. Modelled arrivals are displayed as black lines. Lower panel shows the modelled ray paths for the picks presented in the middle panel.

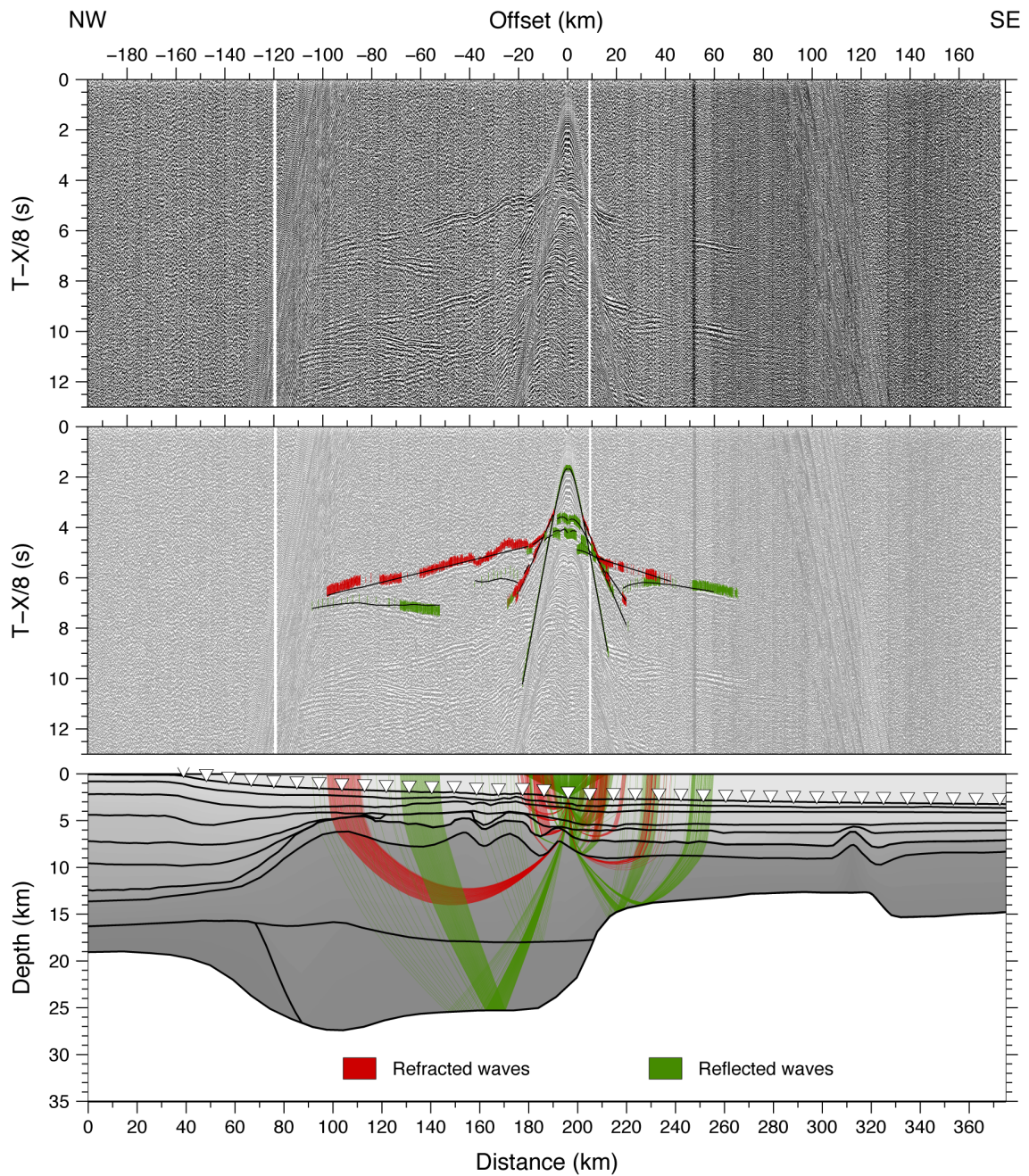


Figure B.20: Seismic section of OBS 30 (hydrophone channel) with a bandpass filter of 4-13.5 Hz (upper panel). A reduction velocity of 8 km/s is applied to the travel time. In the middle panel, picked phases are shown as error bars. Refracted arrivals are plotted in red, reflected arrivals in green. Modelled arrivals are displayed as black lines. Lower panel shows the modelled ray paths for the picks presented in the middle panel.

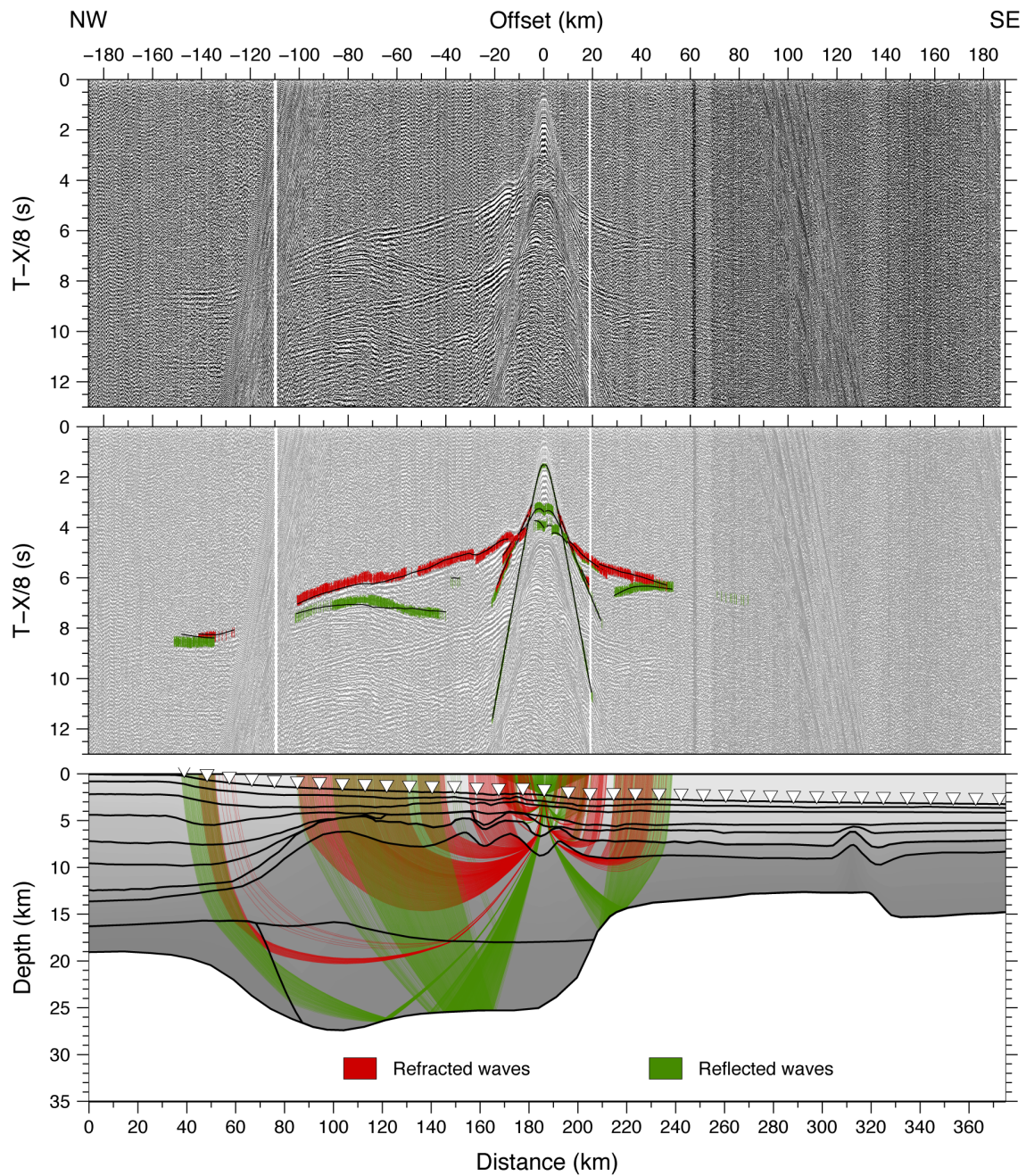


Figure B.21: Seismic section of OBS 31 (hydrophone channel) with a bandpass filter of 4-13.5 Hz (upper panel). A reduction velocity of 8 km/s is applied to the travel time. In the middle panel, picked phases are shown as error bars. Refracted arrivals are plotted in red, reflected arrivals in green. Modelled arrivals are displayed as black lines. Lower panel shows the modelled ray paths for the picks presented in the middle panel.

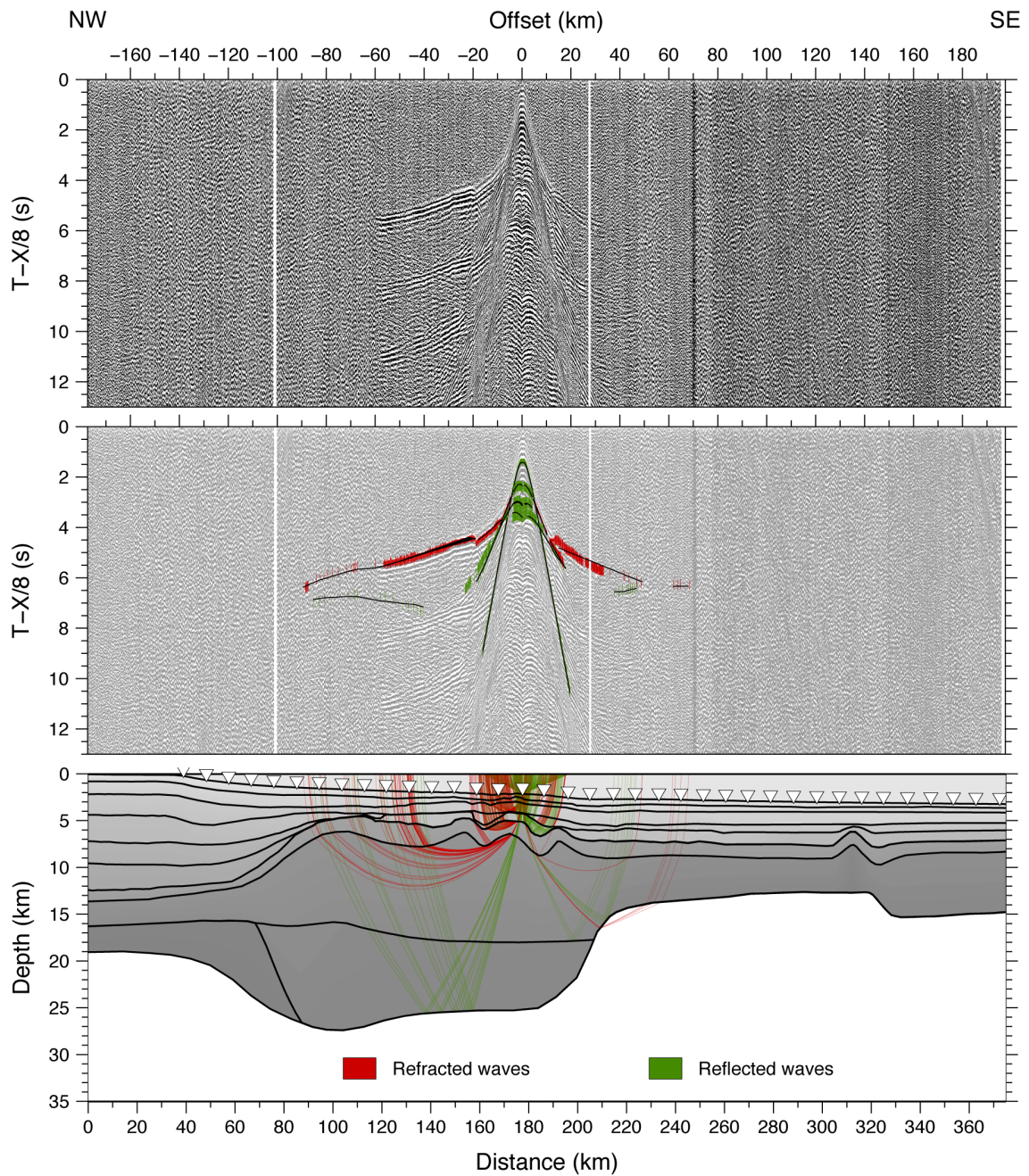


Figure B.22: Seismic section of OBS 32 (hydrophone channel) with a bandpass filter of 4-13.5 Hz (upper panel). A reduction velocity of 8 km/s is applied to the travel time. In the middle panel, picked phases are shown as error bars. Refracted arrivals are plotted in red, reflected arrivals in green. Modelled arrivals are displayed as black lines. Lower panel shows the modelled ray paths for the picks presented in the middle panel.

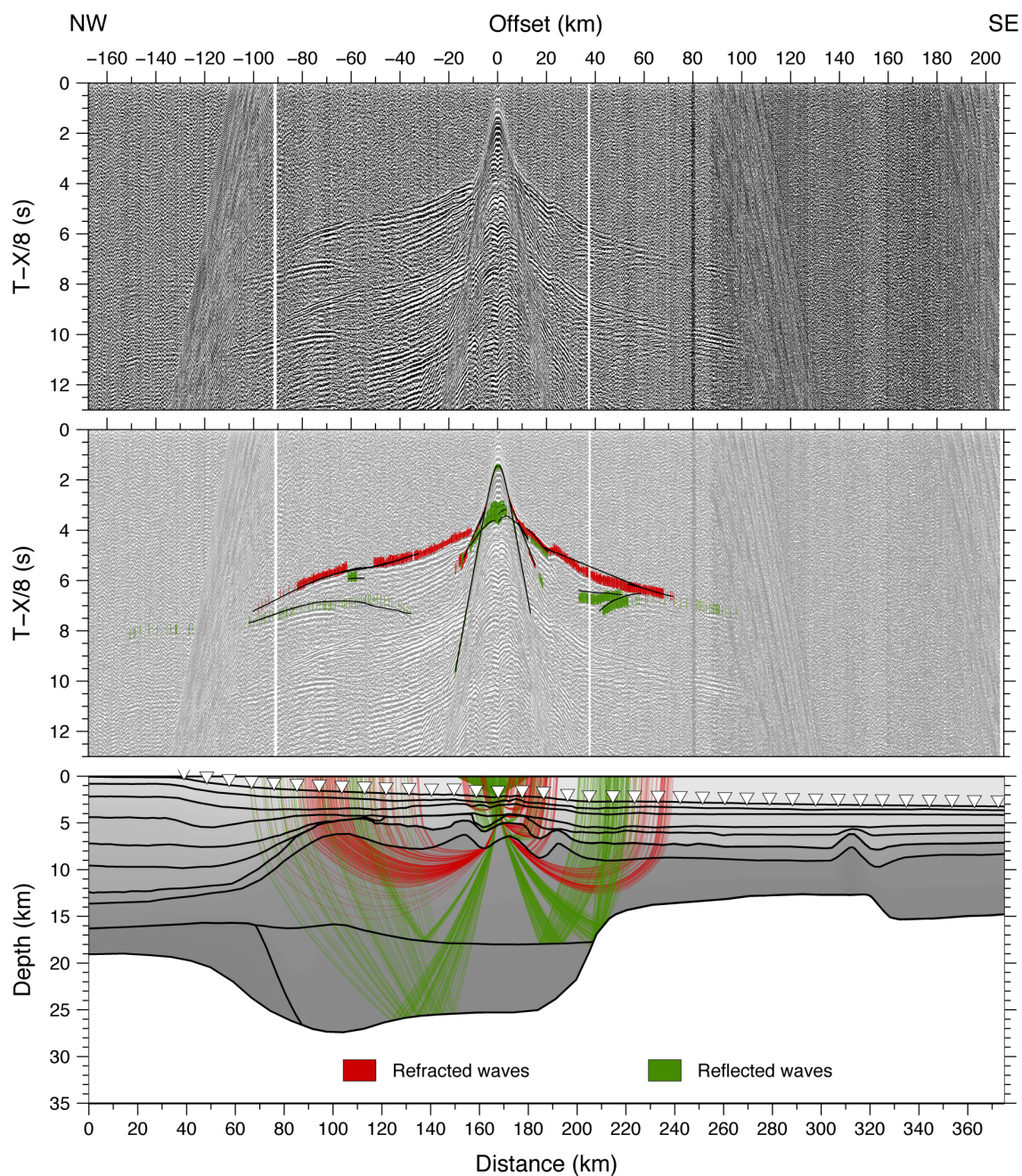


Figure B.23: Seismic section of OBS 33 (hydrophone channel) with a bandpass filter of 4-13.5 Hz (upper panel). A reduction velocity of 8 km/s is applied to the travel time. In the middle panel, picked phases are shown as error bars. Refracted arrivals are plotted in red, reflected arrivals in green. Modelled arrivals are displayed as black lines. Lower panel shows the modelled ray paths for the picks presented in the middle panel.

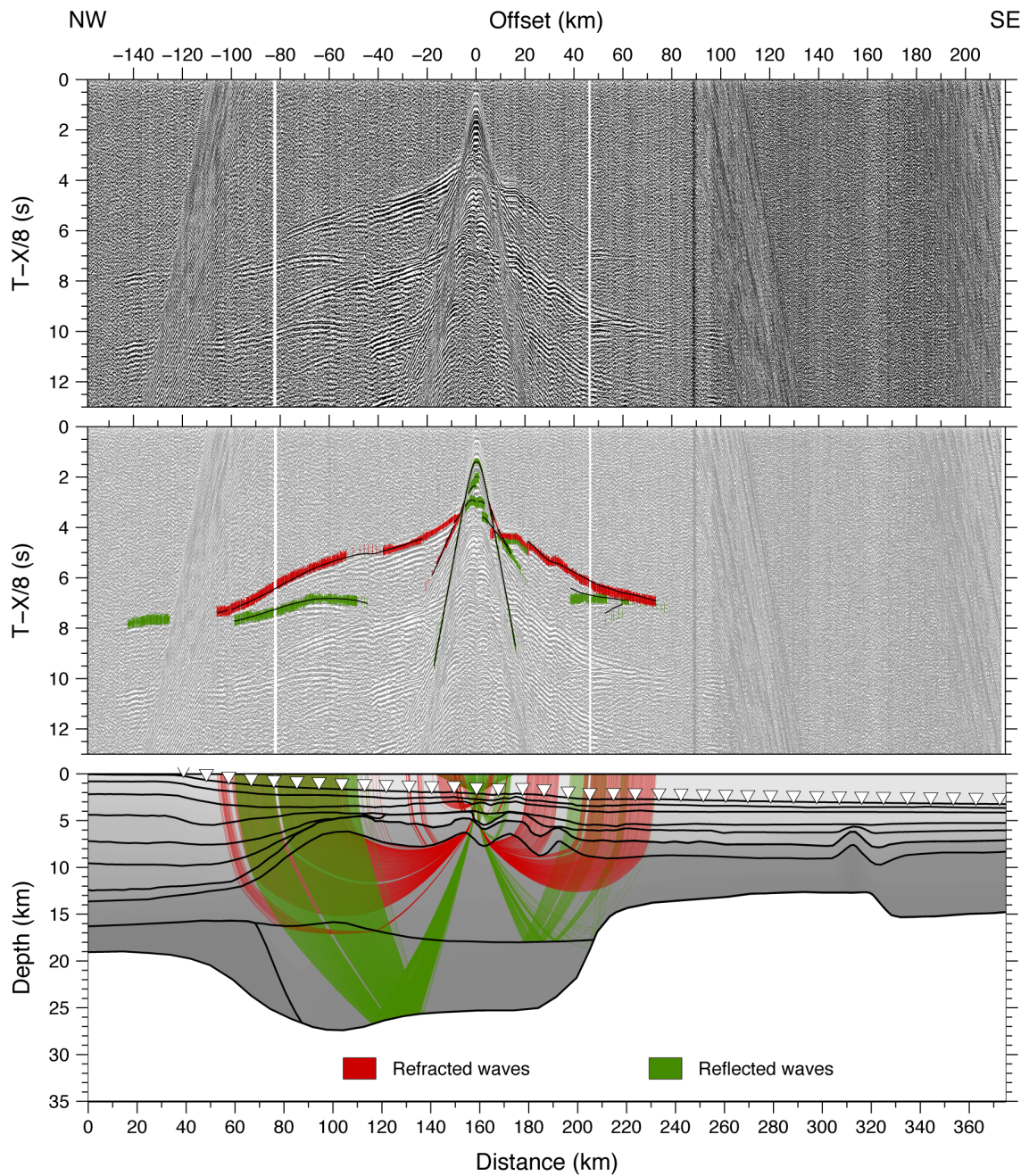


Figure B.24: Seismic section of OBS 34 (hydrophone channel) with a bandpass filter of 4-13.5 Hz (upper panel). A reduction velocity of 8 km/s is applied to the travel time. In the middle panel, picked phases are shown as error bars. Refracted arrivals are plotted in red, reflected arrivals in green. Modelled arrivals are displayed as black lines. Lower panel shows the modelled ray paths for the picks presented in the middle panel.

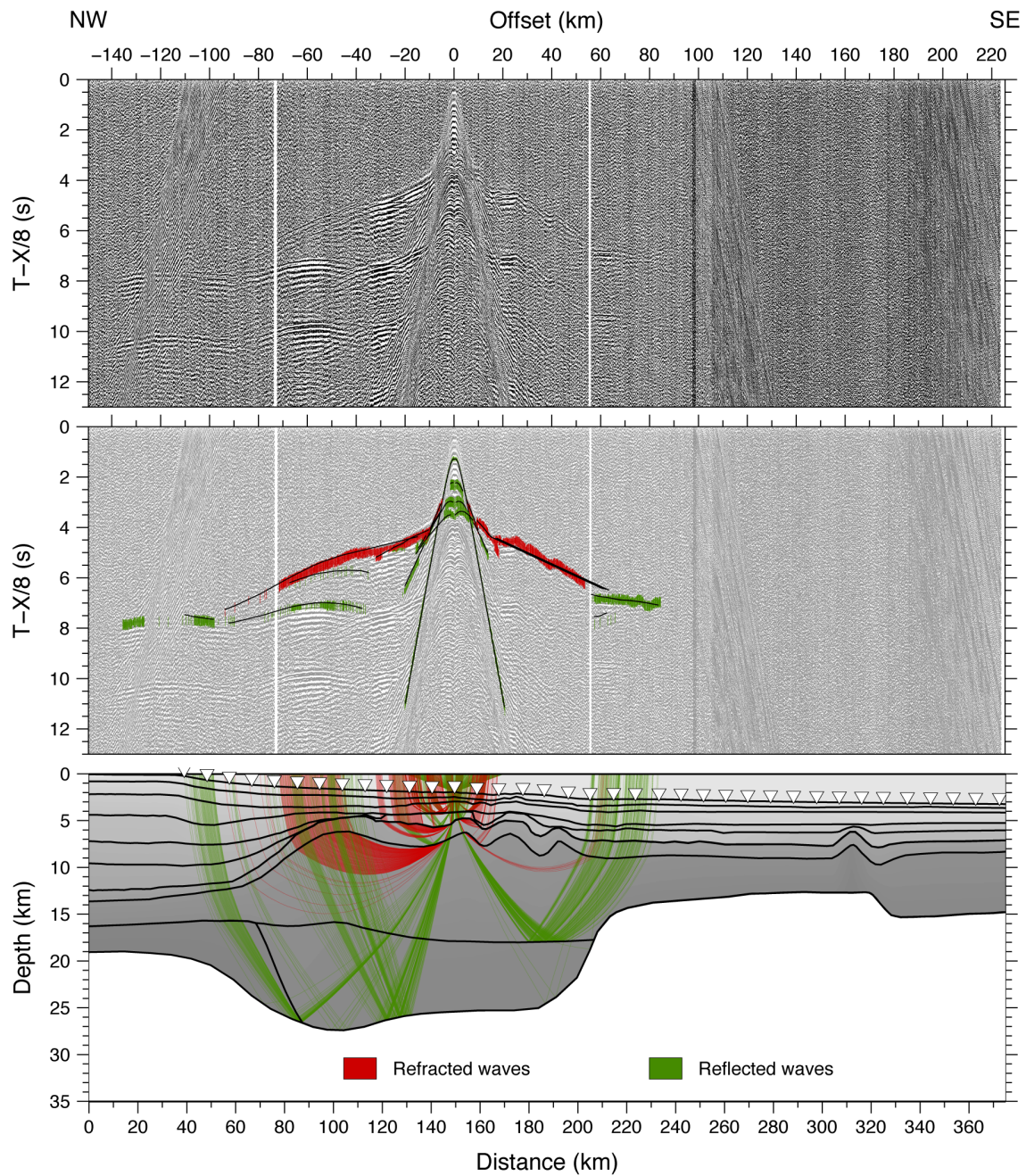


Figure B.25: Seismic section of OBS 35 (hydrophone channel) with a bandpass filter of 4-13.5 Hz (upper panel). A reduction velocity of 8 km/s is applied to the travel time. In the middle panel, picked phases are shown as error bars. Refracted arrivals are plotted in red, reflected arrivals in green. Modelled arrivals are displayed as black lines. Lower panel shows the modelled ray paths for the picks presented in the middle panel.

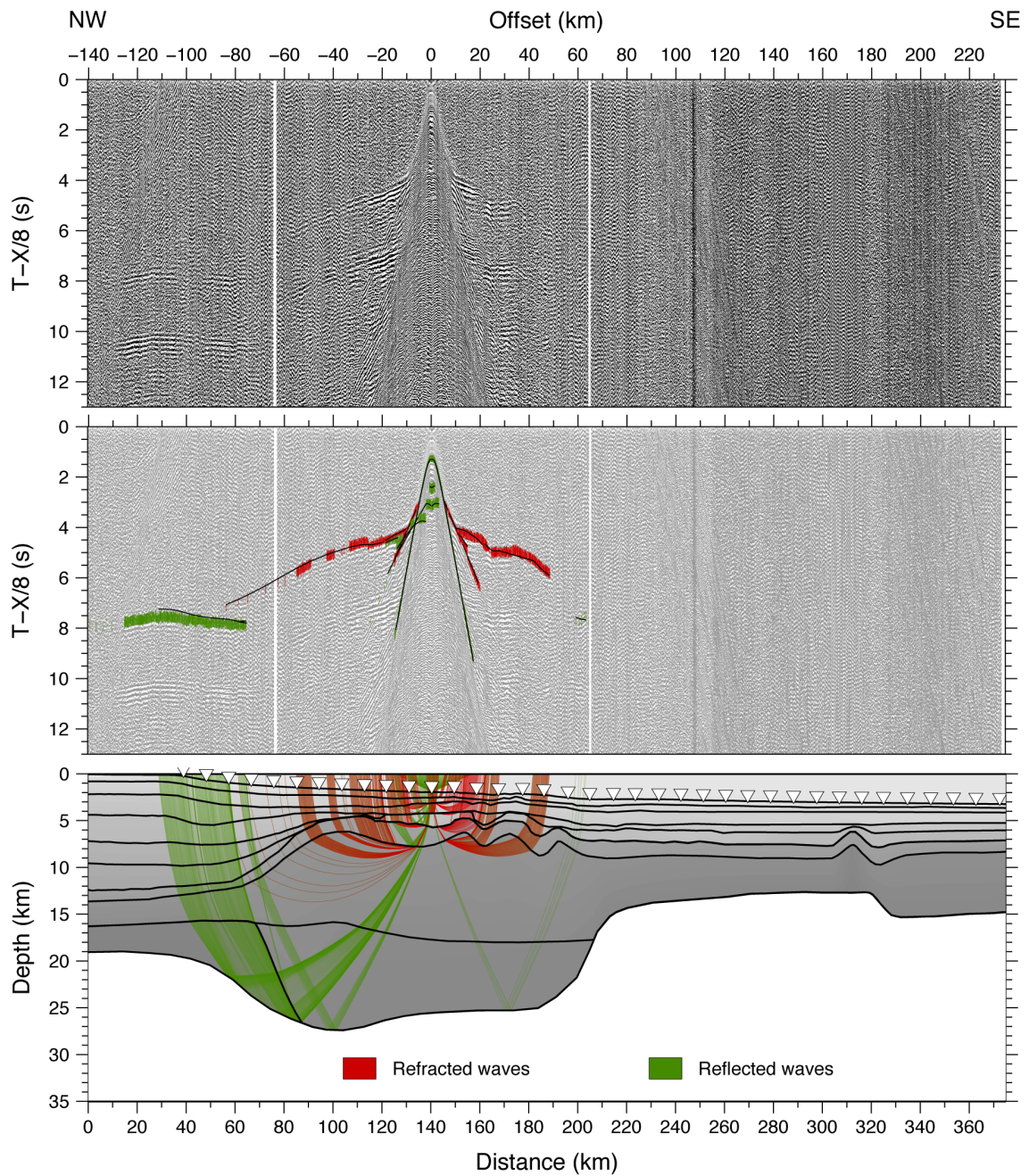


Figure B.26: Seismic section of OBS 36 (hydrophone channel) with a bandpass filter of 4-13.5 Hz (upper panel). A reduction velocity of 8 km/s is applied to the travel time. In the middle panel, picked phases are shown as error bars. Refracted arrivals are plotted in red, reflected arrivals in green. Modelled arrivals are displayed as black lines. Lower panel shows the modelled ray paths for the picks presented in the middle panel.

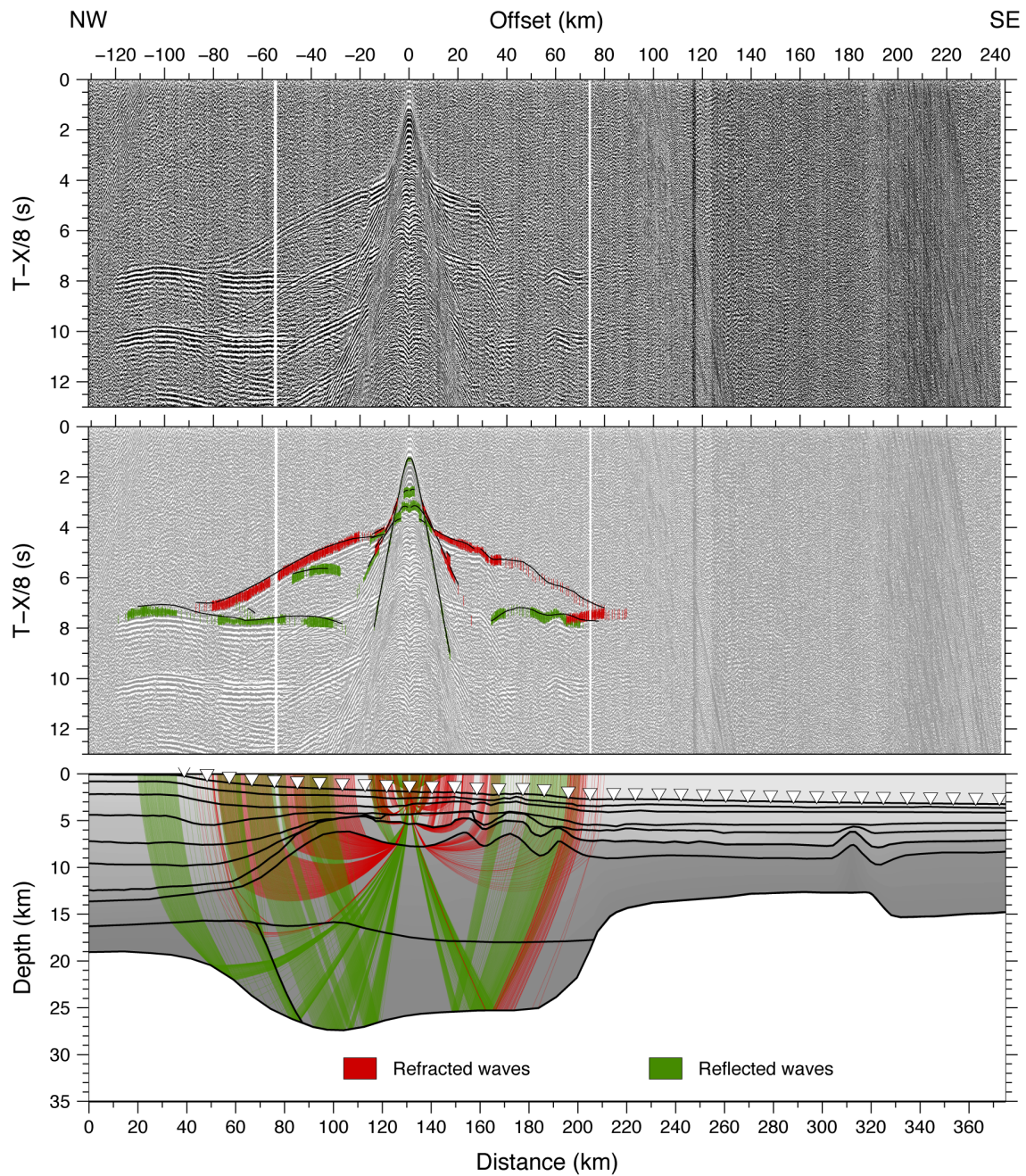


Figure B.27: Seismic section of OBS 37 (hydrophone channel) with a bandpass filter of 4-13.5 Hz (upper panel). A reduction velocity of 8 km/s is applied to the travel time. In the middle panel, picked phases are shown as error bars. Refracted arrivals are plotted in red, reflected arrivals in green. Modelled arrivals are displayed as black lines. Lower panel shows the modelled ray paths for the picks presented in the middle panel.

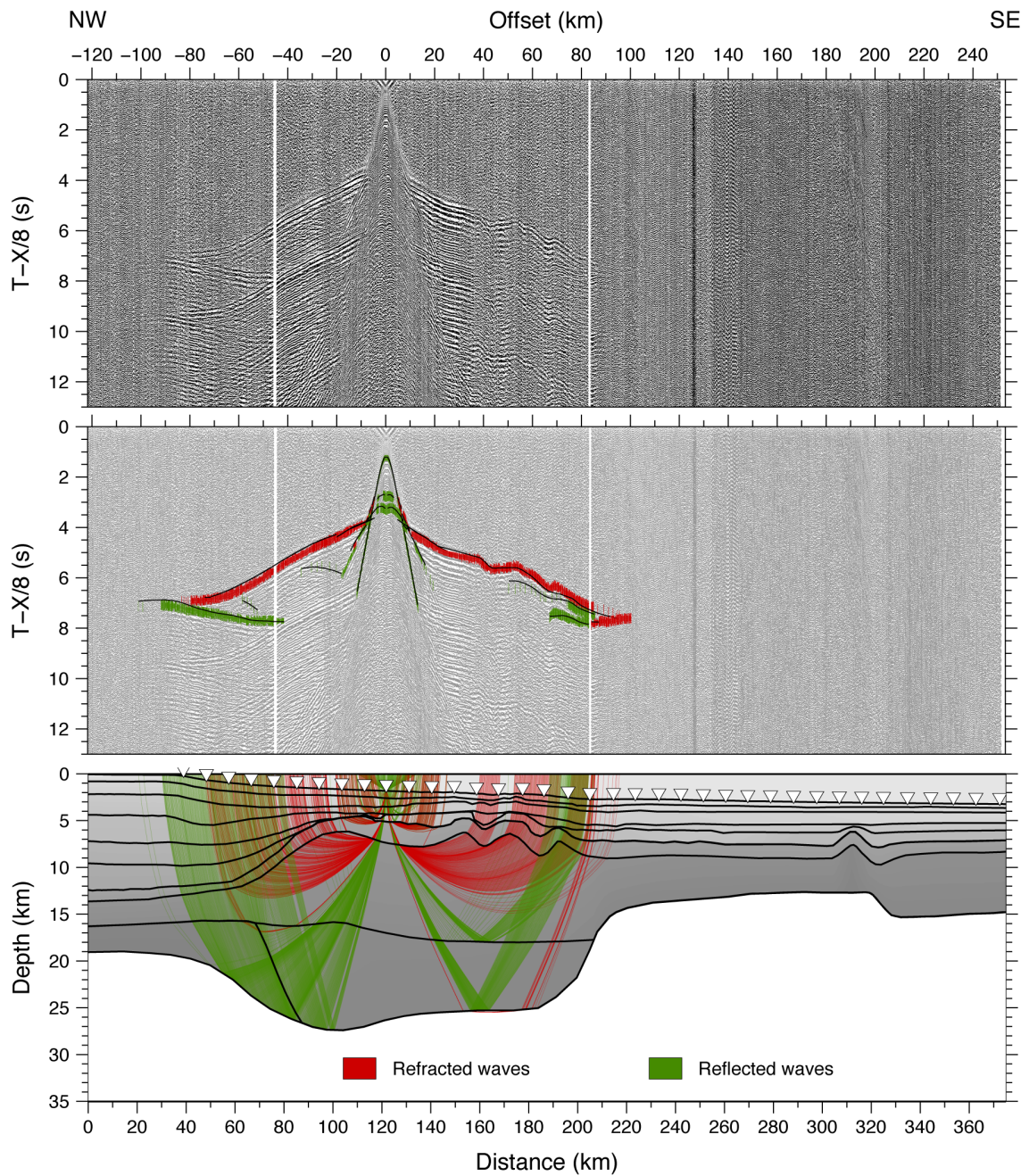


Figure B.28: Seismic section of OBS 38 (vertical seismometer component) with a bandpass filter of 4-13.5 Hz (upper panel). A reduction velocity of 8 km/s is applied to the travel time. In the middle panel, picked phases are shown as error bars. Refracted arrivals are plotted in red, reflected arrivals in green. Modelled arrivals are displayed as black lines. Lower panel shows the modelled ray paths for the picks presented in the middle panel.

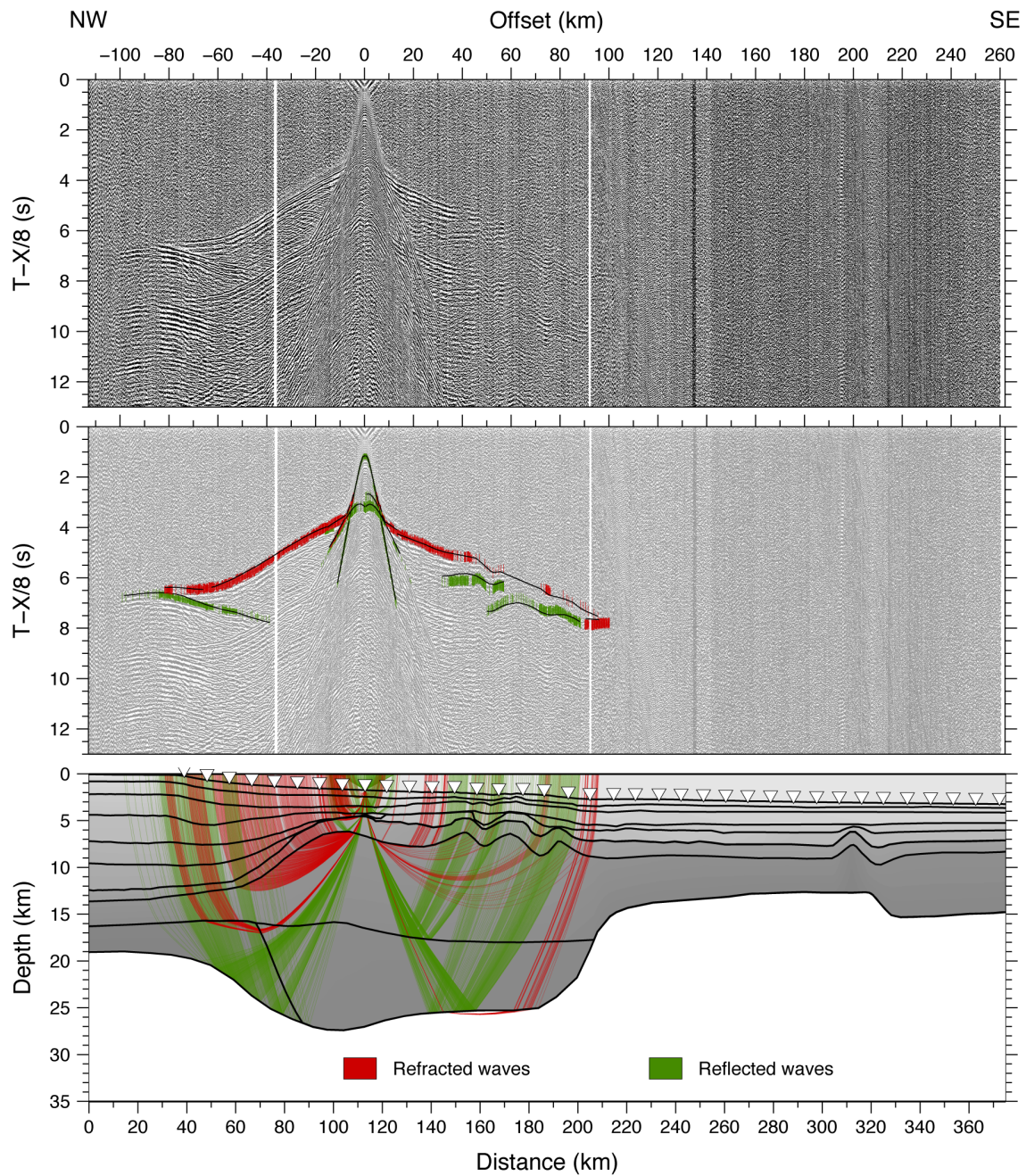


Figure B.29: Seismic section of OBS 39 (vertical seismometer component) with a bandpass filter of 4-13.5 Hz (upper panel). A reduction velocity of 8 km/s is applied to the travel time. In the middle panel, picked phases are shown as error bars. Refracted arrivals are plotted in red, reflected arrivals in green. Modelled arrivals are displayed as black lines. Lower panel shows the modelled ray paths for the picks presented in the middle panel.

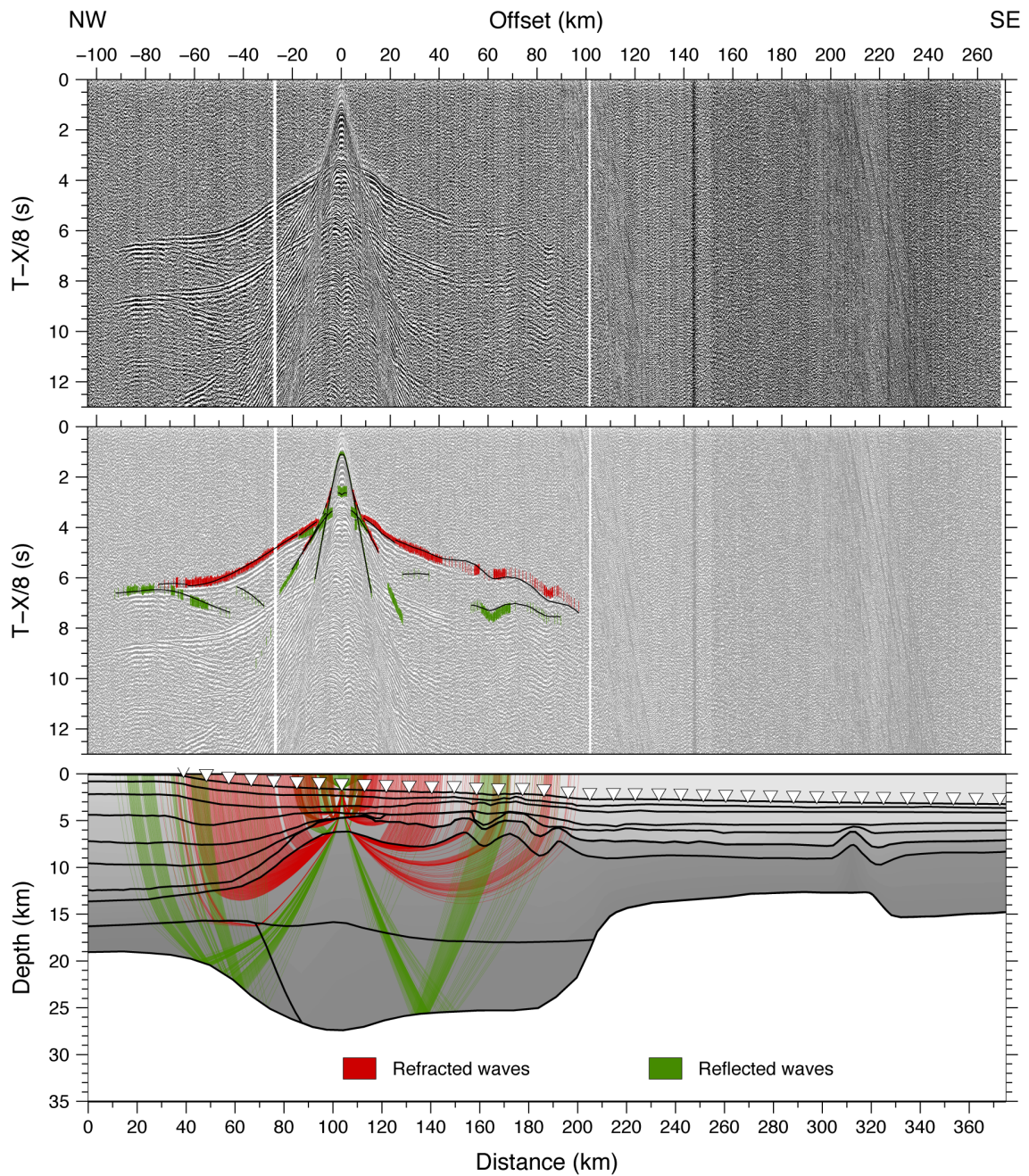


Figure B.30: Seismic section of OBS 40 (hydrophone channel) with a bandpass filter of 4-13.5 Hz (upper panel). A reduction velocity of 8 km/s is applied to the travel time. In the middle panel, picked phases are shown as error bars. Refracted arrivals are plotted in red, reflected arrivals in green. Modelled arrivals are displayed as black lines. Lower panel shows the modelled ray paths for the picks presented in the middle panel.

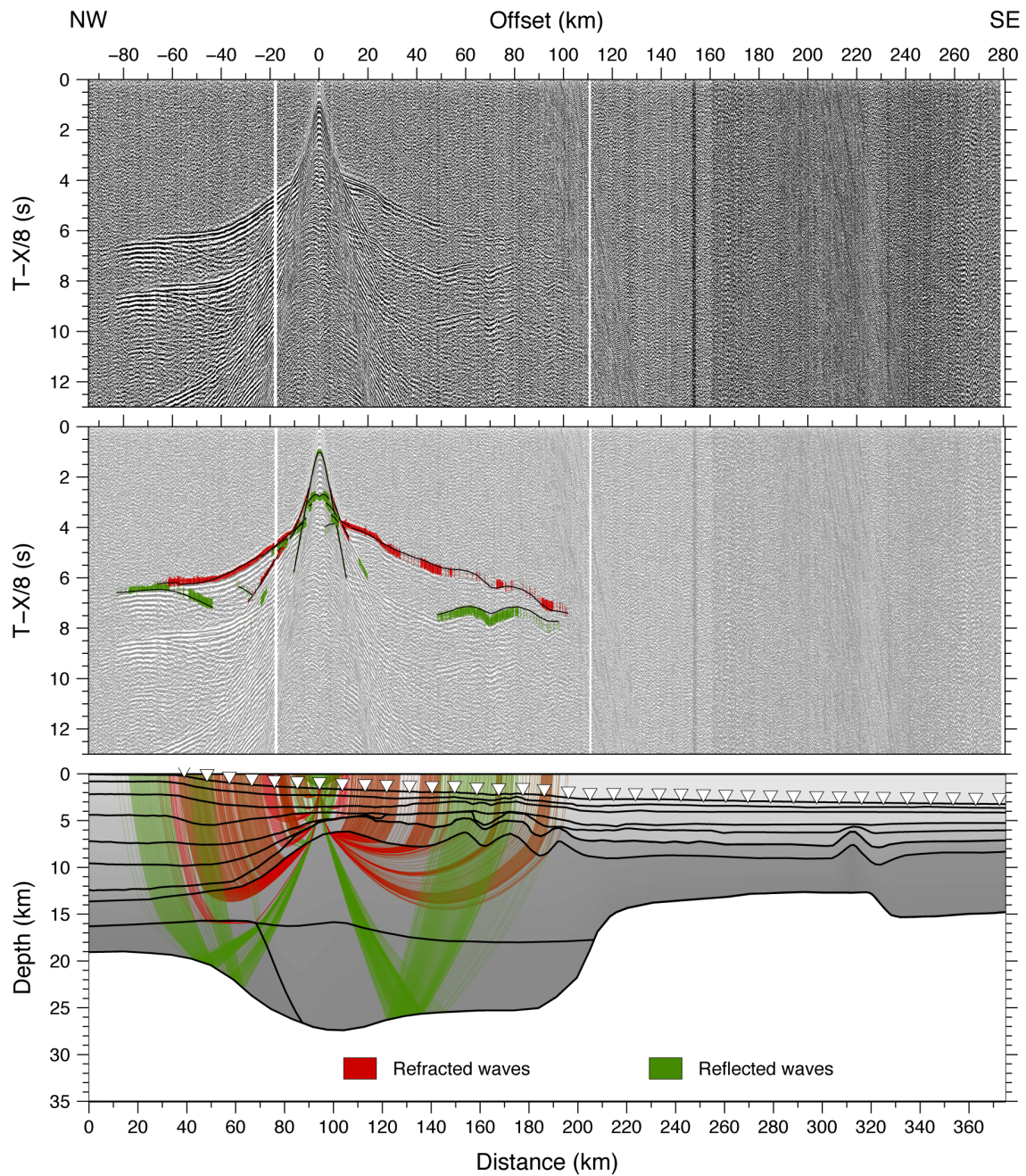


Figure B.31: Seismic section of OBS 41 (hydrophone channel) with a bandpass filter of 4-13.5 Hz (upper panel). A reduction velocity of 8 km/s is applied to the travel time. In the middle panel, picked phases are shown as error bars. Refracted arrivals are plotted in red, reflected arrivals in green. Modelled arrivals are displayed as black lines. Lower panel shows the modelled ray paths for the picks presented in the middle panel.

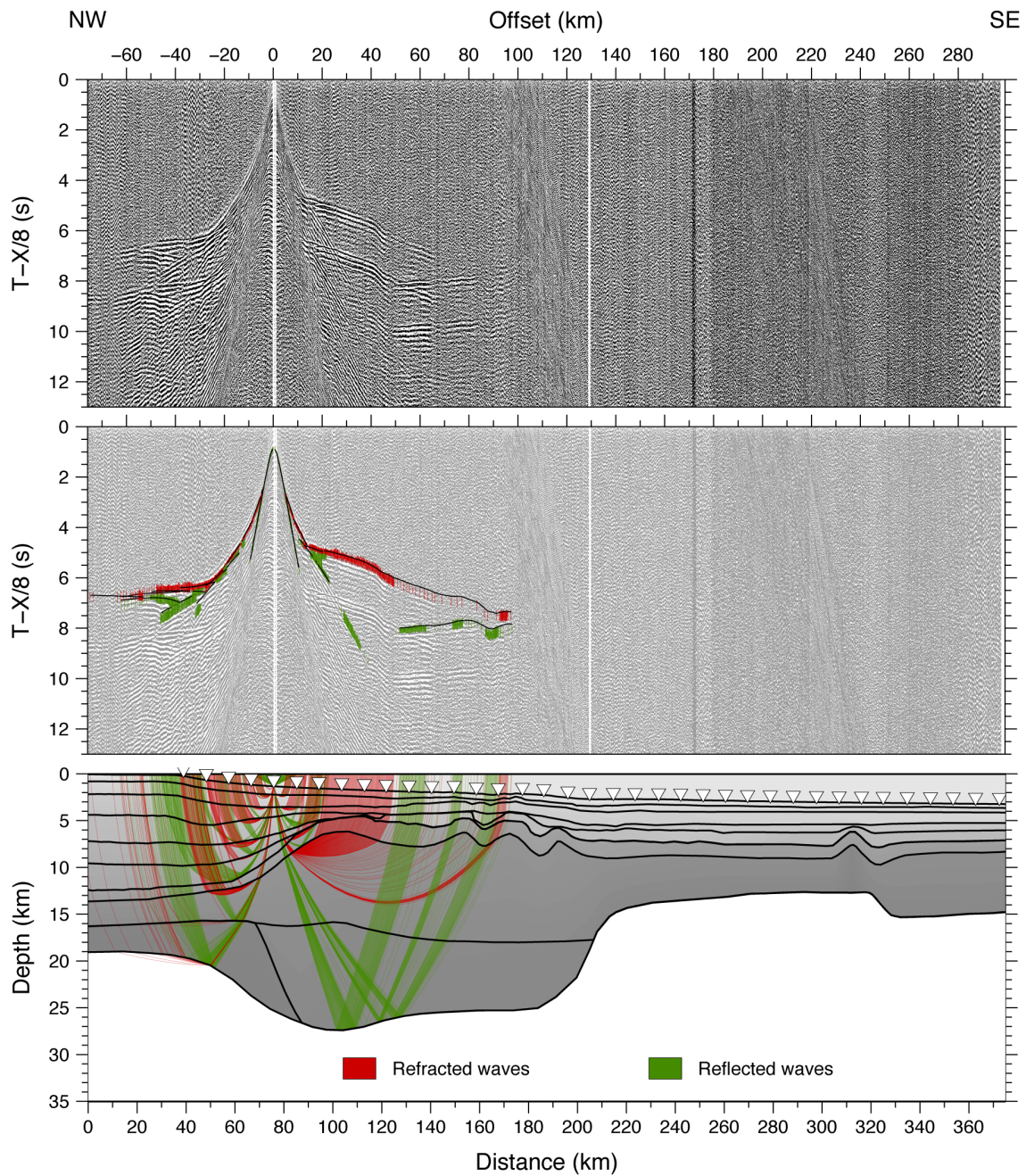


Figure B.32: Seismic section of OBS 43 (hydrophone channel) with a bandpass filter of 4-13.5 Hz (upper panel). A reduction velocity of 8 km/s is applied to the travel time. In the middle panel, picked phases are shown as error bars. Refracted arrivals are plotted in red, reflected arrivals in green. Modelled arrivals are displayed as black lines. Lower panel shows the modelled ray paths for the picks presented in the middle panel.

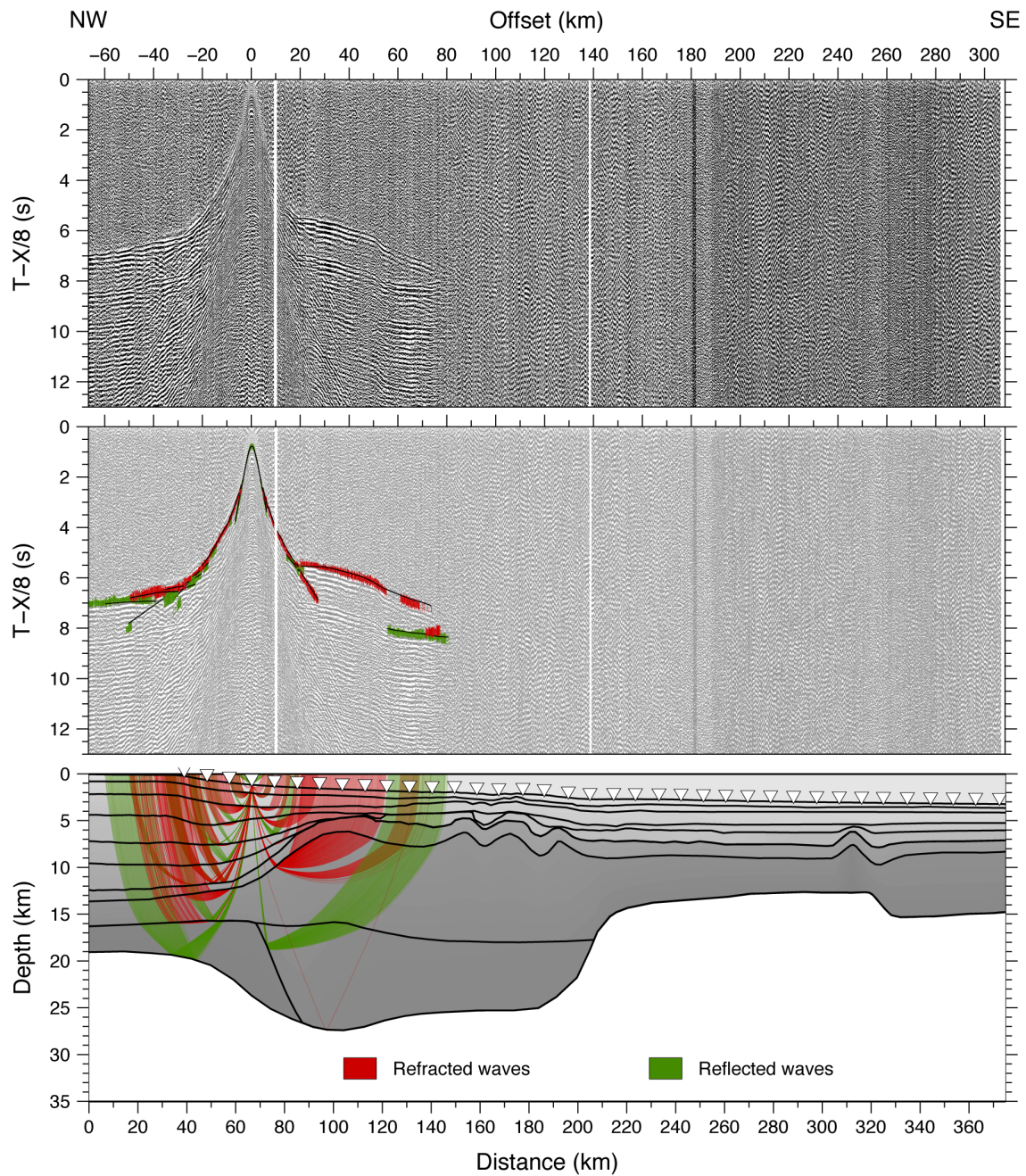


Figure B.33: Seismic section of OBS 44 (vertical seismometer component) with a bandpass filter of 4-13.5 Hz (upper panel). A reduction velocity of 8 km/s is applied to the travel time. In the middle panel, picked phases are shown as error bars. Refracted arrivals are plotted in red, reflected arrivals in green. Modelled arrivals are displayed as black lines. Lower panel shows the modelled ray paths for the picks presented in the middle panel.

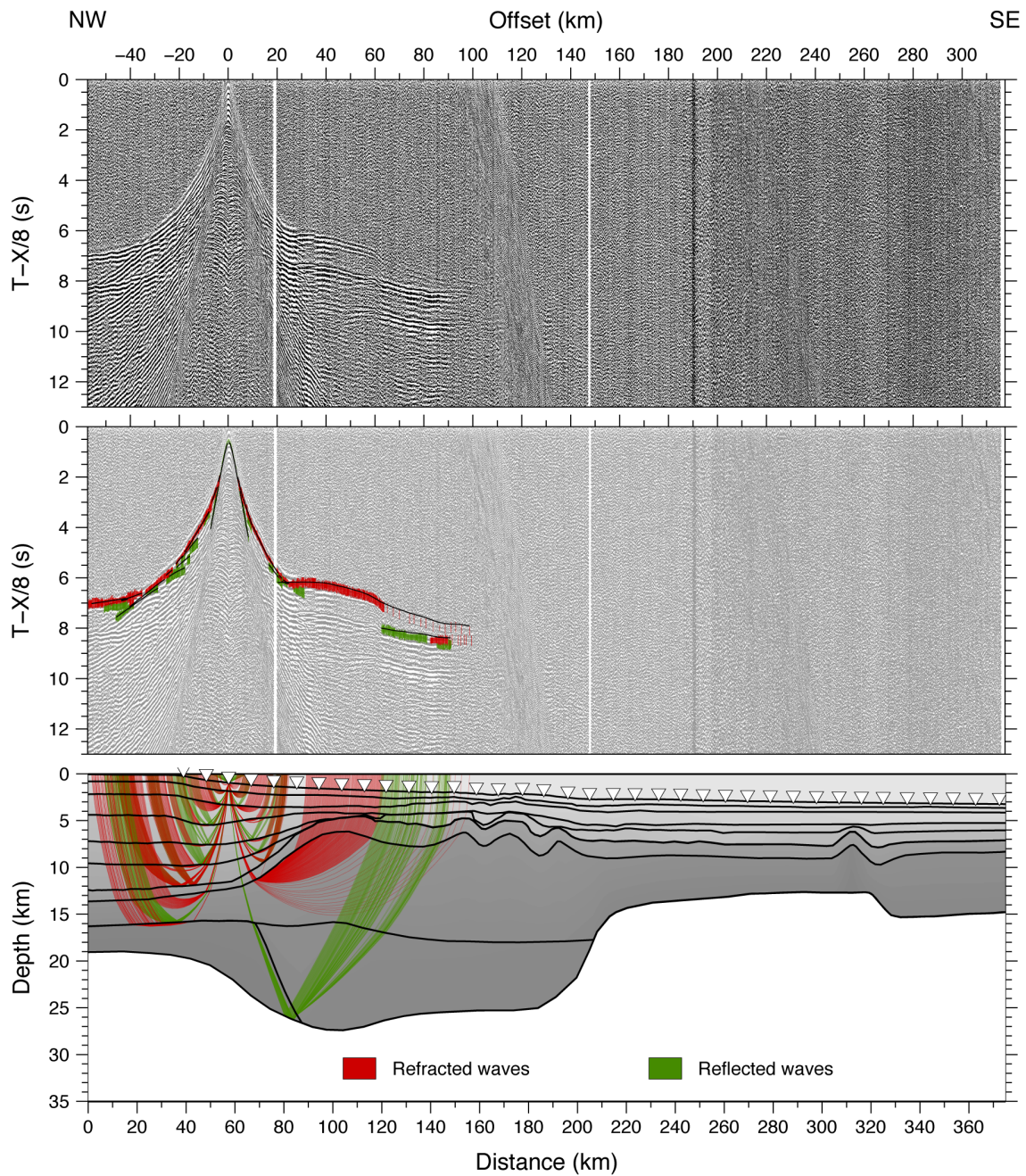


Figure B.34: Seismic section of OBS 45 (hydrophone channel) with a bandpass filter of 4-13.5 Hz (upper panel). A reduction velocity of 8 km/s is applied to the travel time. In the middle panel, picked phases are shown as error bars. Refracted arrivals are plotted in red, reflected arrivals in green. Modelled arrivals are displayed as black lines. Lower panel shows the modelled ray paths for the picks presented in the middle panel.

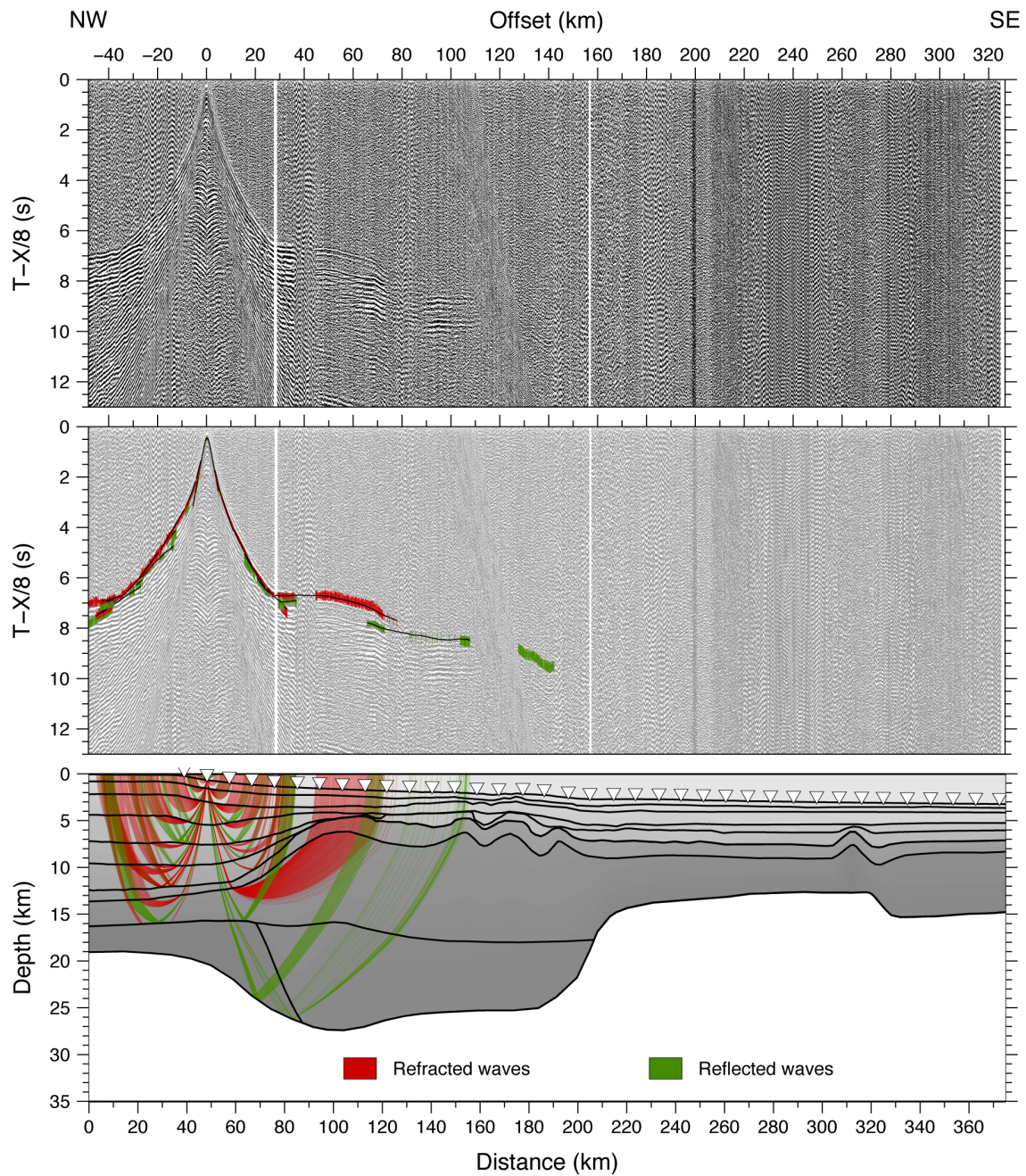


Figure B.35: Seismic section of OBS 46 (hydrophone channel) with a bandpass filter of 4-13.5 Hz (upper panel). A reduction velocity of 8 km/s is applied to the travel time. In the middle panel, picked phases are shown as error bars. Refracted arrivals are plotted in red, reflected arrivals in green. Modelled arrivals are displayed as black lines. Lower panel shows the modelled ray paths for the picks presented in the middle panel.

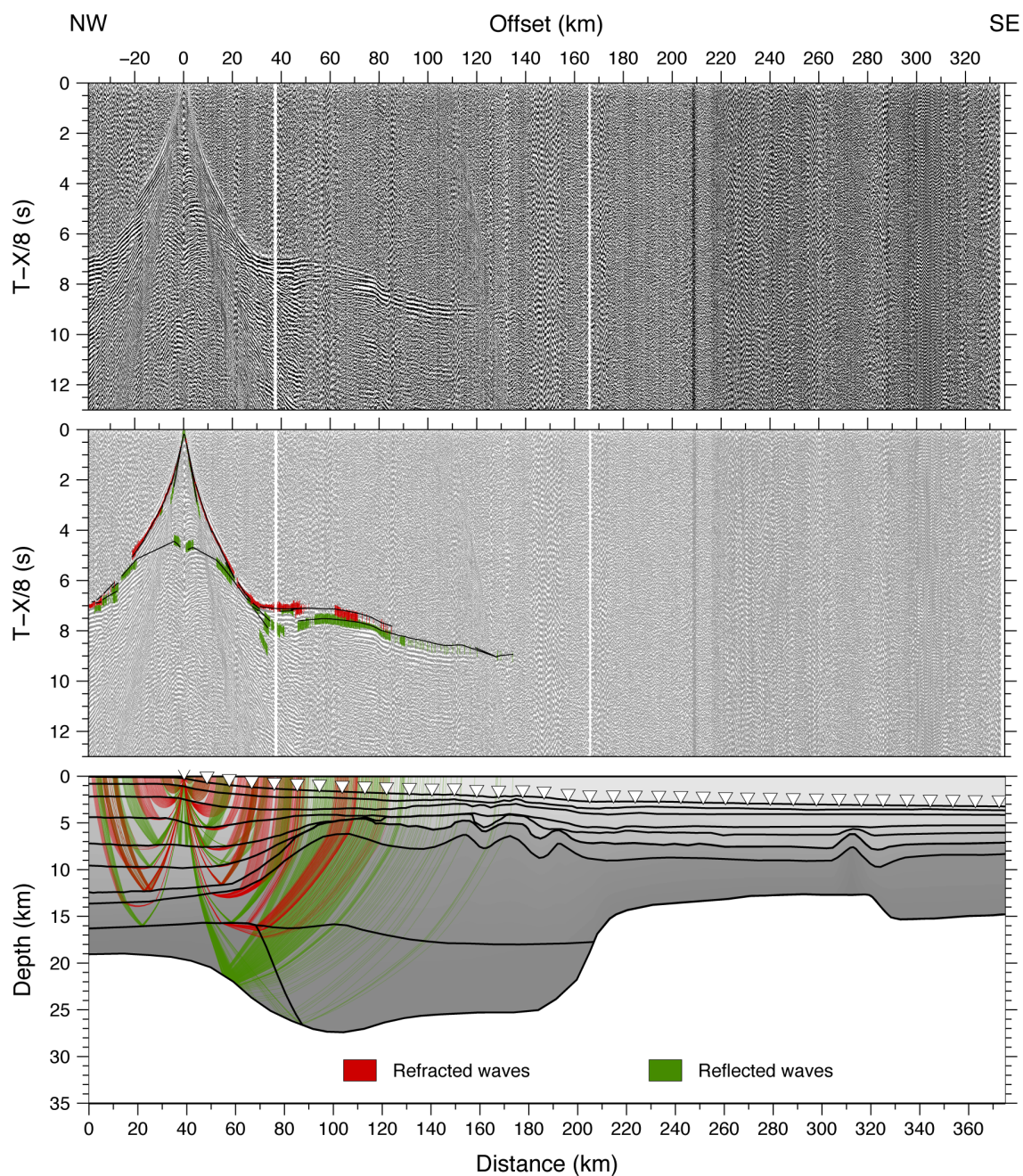


Figure B.36: Seismic section of OBS 47 (hydrophone channel) with a bandpass filter of 4-13.5 Hz (upper panel). A reduction velocity of 8 km/s is applied to the travel time. In the middle panel, picked phases are shown as error bars. Refracted arrivals are plotted in red, reflected arrivals in green. Modelled arrivals are displayed as black lines. Lower panel shows the modelled ray paths for the picks presented in the middle panel.